National Library of Canada

Acquisitions and Bibliographic Services Branch

395 Wellington Street
Ottawa, Ontario
K1A 0N4

Bibliothèque nationale du Canada

Direction des acquisitions et des services bibliographiques

395, rue Wellington
Ottawa (Ontario)
K1A 0N4

Your file Votre référence

Our file Notre référence

NOTICE

The quality of this microform is heavily dependent upon the quality of the original thesis submitted for microfilming. Every effort has been made to ensure the highest quality of reproduction possible.

If pages are missing, contact the university which granted the degree.

Some pages may have indistinct print especially if the original pages were typed with a poor typewriter ribbon or if the university sent us an inferior photocopy.

AVIS

La qualité de cette microforme dépend grandement de la qualité de la thèse soumise au microfilmage. Nous avons tout fait pour assurer une qualité supérieure de reproduction.

S'il manque des pages, veuillez communiquer avec l'université qui a conféré le grade.

La qualité d'impression de certaines pages peut laisser à désirer, surtout si les pages originales ont été dactylographiées à l'aide d'un ruban usé ou si l'université nous a fait parvenir une photocopie de qualité inférieure.

Canada

National Library
of Canada

Acquisitions and
Bibliographic Services Branch

395 Wellington Street
Ottawa, Ontario
K1A 0N4

Bibliothèque nationale
du Canada

Direction des acquisitions et
des services bibliographiques

395, rue Wellington
Ottawa (Ontario)
K1A 0N4

Your file Votre référence

Our file Notre référence

ISBN 0-612-07802-7

Canada

UNIVERSITÉ D'OTTAWA
UNIVERSITY OF OTTAWA

À mon épouse Denise et ma fille Stéphanie

en espérant pouvoir aider à faire de ce monde

un meilleur endroit à croître et à vivre.

ACKNOWLEDGEMENTS

I would like to thank my research supervisor Professor Christian Detellier for his dynamic enthusiasm and exemplary pedagogy which have made my studies an enjoyable and stimulating experience. I am also grateful to the rest of the Detellier research group (Jinhua Bai, Johan Blixt, Zhigang Cheng, Ivo Dellavia, Harouna Dramé, Helen Graves-Smith, Hongbai Lao, Laila Raki, Ravi M. Sarma, Andrew Szabo and James Tunney) for the stimulating discussions and social rapports which came about during the past years. Special thanks is extended to Johan Blixt for expert help in computer matters.

I would like to thank all of the support staff whose skills were instrumental for the development of this research: Corrine Bensimmon (X-ray fluorescence and elemental analysis), Ron Conlon (X-ray diffraction, Carleton University), John Loop (ICP, Dept. of Geology, U. of Ottawa) and Drs. Glenn Facey and John Ripmeester (solid state NMR). I would also like to express my thanks for Dr. B.M. Choudary for useful discussions concerning the smectite aspects of this research, as well as to Professors Sandro Gamboratta and Darrin Richeson (and their research groups) for their insights and constructive criticisms of this work.

I wish to extend my most sincere appreciations to my parents Pierre and Lucienne and to my siblings Paul, Adèle and Lise to whom I have always looked up as inspirational models of academic success and excellence.

My deepest recognitions go my spouse Denise Grenier-Mercier, whose emotional support, visionariness and commitment to excellence where indispensible for the burgeoning

of my scientific career. I am also eternally indebted to my one-year old daughter Stéphanie, whose joyful presence in my life has reinforced in me the aspiration to work in making this world a better place to live.

Finally, I gratefully acknowledge the much needed financial support of the following organizations which has made the work presented in this thesis possible: the University Research Incentive Fund (URIF), the Institute for Chemical Science and Technology (ICST), the Natural Sciences and Engineering Research Council of Canada, the Government of Ontario (OGS Scholarship) and the University of Ottawa (Scholarship).

ABSTRACT

Tetraalkylammonium cation intercalation into smectites was found to be a useful tool for the study of many aspects of smectite chemistry, including the determination of their internal surface areas and the identification of the mineral composition of Alberta oil sands bitumen. The adsorption of aromatic molecules to these organoclays has given useful insights about the nature of the interlamellar pore systems of these compounds.

The grafting of organic moieties to the interlayer surface of montmorillonite was achieved by the reaction of the acidified clay with 3-chloropropyltrimethoxysilane. Nucleophilic substitution of the Cl for chelating functionalities (SH and SCH_2CH_2SH) has resulted in highly effective heavy metal adsorbents, particularly for Pb and Hg. The adsorbents could be easily regenerated by leaching out the metal with HCl. Similar materials were prepared using the layered silicates magadiite and kenyaite, but were found to be ineffective for the removal of metal ions from solution because of the congestion of the interlamellar region of these minerals by the organic functionalities which has prevented the access of the metal ions to the chelating sites.

Alcohols and diols were found to condense onto the the interlamellar silanols of H-magadiite and H-kenyaite upon thermal treatment. The techniques used to characterize these compounds provided strong evidence of the formation of Si-O-C linkages between the mineral template and the organic groups. The nanocomposites thus formed were found to be stable to well beyond 400 °C, but did not show appreciable microporosity. The grafting

of diols into magadiite and kenyaite has given useful insight about the nature of the interlamellar region of these silicates, whose crystal structures are still unknown.

The preparation of clay-based catalysts for nitric oxide decomposition was attempted by the cointercalation of organic and metal cations into montmorillonite and by the doping of Al-pillared montmorillite by metal ions. The resulting compounds were found to promote the *ortho* nitrosylation of phenol in the presence of NO gas, but only in very low yield (3%). Static variable temperature studies have failed to show any catalytic decomposition of nitric oxide in the presence of these materials.

TABLE OF CONTENTS

LIST OF FIGURES

LIST OF TABLES

ABBREVIATIONS

APM	Alumina-pillared montmorillonite
BG	1,4-Butanediol
BTP	Bilayer to pseudotrimolecular
CEC	Cation exchange capacity
CP	Cross-polarization
CPDMS	3-Chloropropyldimethylchlorosilane
CPK	Corey-Pauling precision molecular model
CPTMS	3-Chloropropyltrimethoxysilane
d_{001}	Interlayer distance
DD	Dipolar dephasing
DMF	*N,N*-Dimethylformamide
DMSO	Dimethylsulfoxide
EG	Ethylene glycol
FTIR	Fourier transform infrared spectroscopy
MAS	Magic angle spinning
MPTMS	3-Mercaptopropyltrimethoxysilane
MTB	Monolayer to bilayer
NBu_4^+	Tetrabutylammonium
NEt_4^+	Tetraethylammonium
$NHep_4^+$	Tetraheptylammonium

$NHex_4^+$	Tetrahexylammonium
NMe_4^+	Tetramethylammonium
NMF	*N*-Methylformamide
NMR	Nuclear magnetic resonance
NPe_4^+	Tetrapentylammonium
NPr_4^+	Tetrapropylammonium
$NOct_4^+$	Tetraoctylammonium
PentG	1,5-Pentanediol
PG	1,3-Propanediol
POM	Polar organic molecule
PSA	Particle size analysis
Q^3	$(SiO)_3SiOH$
Q^4	$(SiO)_4Si$
S_i	Internal surface area
SAz-1	Montmorillonite from Cheto, Arizona
SCa-3	Montmorillonite from Otay, California
SHCa-1	Hectorite from San Bernadina, California
STx-1	Montmorillonite from Llano, Texas
SWa-1	Nontronite from Grant County, Washington
SWy-1	Montmorillonite from Clay Spur, Wyoming
TGA	Thermogravimetric analysis
TMA	Tetramethylammonium

TMMyrA	Trimethylmyristylammonium
TMS	Trimethylchlorosilane
TPA	Tetrapropylammonium
TPP	Tetraphenylphosphonium
UHV	Ultra-high vacuum
XRD	X-ray diffraction
XRF	X-ray fluorescence

No man ever wetted clay and then left it,

as if there would be bricks by chance and fortune.

Plutarch, 46-120 A.D.

1. INTRODUCTION TO LAYERED MINERALS

In this section, a general overview of the synthesis, structure, physical properties, chemical reactivity and applications of phyllosilicates will be presented. Although the total volume of work on this topic is much too enormous to be exhaustively discussed within the context of a thesis, this chapter should contain the necessary information to introduce the fundamental aspects of phyllosilicate chemistry. Topics of current interest with regards to these minerals will also be introduced so that the reader can place the results presented in subsequent chapters within the context of industrial and environmental importance.

1.1 Phyllosilicates

The origin of the word "phyllosilicate" stems from the Greek word Φυλλων ("phyllon"), meaning leaf (afficionados of Middle Eastern cuisine will recognize the origins of the expression *filo pastry* from this root). Thus, phyllosilicates can be defined as a class of minerals consisting of a stacked arrangement of leaf-like silicate layers, sometimes with cations and/or water located in between these layers (in the area called the *interlayer* or *interlamellar space*).

There are many type of existing compounds which assume a layered conformation: aluminum phosphates (ALPO), layered double hydroxides (LDH), chalcohalogenides and graphite are well-known and widely studied layered materials. Phyllosilicates can be distinguished from these species in that they possess, though usually not exclusively, silica (SiO_2) as a fundamental structural unit. Of course, there also exists many silicate compounds which are not layered, including quartz, zeolites, and a myriad of other minerals, both natural and synthetic.

Table 1.1 shows a classification scheme for phyllosilicates which has been approved by the AIPEA[a] Nomenclature Committee and by the IMA[b] Commission on New Minerals and Mineral Names[1] with the exception of layered silicates, which were included in this work as a third phyllosilicate layer type. These minerals can be subdivided into three general types: the 1:1 type (also refered to as kandites), the 2:1 type and layered silicates. These types differ from each other in the structures of their layers, the 1:1 minerals consisting of

---

[a]Association Internationale pour l'Étude des Argiles

[b]International Mineralogical Association

an octahedral Al_2O_3 sheet fused to a tetrahedral SiO_2 sheet, the 2:1 minerals consisting of an octahedral Al_2O_3, MgO or Fe_2O_3 sheet sandwiched between two SiO_2 sheets, and the layered silicates being composed solely of SiO_2 tetrahedra. Figure 1.1 depicts schematic representations for each of these three phyllosilicate forms.

Thus, the layer structure of 1:1 phyllosilicates can be viewed as a stack of three hexagonally packed oxygen planes (labeled A,B and C) with Si atoms located in the interstitial tetrahedral cavities between planes A and B, and metal ions (Al, Mg or Fe) in the octahedral cavities between planes B and C. The plane C oxygens all bear hydrogens in order to maintain the electroneutrality of the layer. Likewise, the 2:1 phyllosilicate layer structure consists of four oxygen planes stacked in an ABCA manner, with Si atoms in the tetrahedral cavities of the AB and AC planes, and the other metal atoms (Al, Mg or Fe) in the octahedral sites between the B and C planes. In both of these types of layer structures, one third of the oxygens in the A planes are removed, resulting in an array of six-member oxygen rings each with a vacant hexagonal "hole" or cavity.

Table 1.1 Classifiation of phyllosilicates (L.S. denotes layered silicates).

Type	Interlayer	Group	Subgroup	Species
1:1	None or H_2O	Serpentine-kaolin	Serpentines	Chrysotile, lizardite, amesite, berthierine, cronstedtite, etc.
			Kaolins	Kaolinite, dickite, nacrite, halloysite
2:1	None	Talc-pyrophyllite	Talcs	Talc, willemseite
			Pyrophyllites	Pyrophyllite, ferripyrophyllite
	Hydrated cations	Smectite	Saponites	Saponite, **hectorite**, sauconite, stevensite, etc.
			Montmorillonites	**Montmorillonite**, beidellite, nontronite, volkonskoite, etc.
		Vermiculite	Trioctahedral vermiculites	Trioctahedral vermiculite
			Dioctahedral vermiculites	Dioctahedral vermiculite
	Non-hydrated cations	True mica	Trioctahedral true micas	Phlogopite, biotite, lepidolite, zinnwaldite, annite, etc.
			Dioctahedral true micas	Muscovite, illite, glauconite, tobelite, paragonite, etc.
		Brittle mica	Trioctahedral brittle micas	Clintonite, bityite, anandite, kinoshitalite
			Dioctahedral brittle micas	Margarite
	Hydroxide sheet	Chlorite	Trioctahedral chlorites	Clinochlore, chamosite, nimite, pennantite, baileychlore
			Dioctahedral chlorites	Donbassite
			Di,trioctahedral chlorites	Cookeite, sudoite
L.S.	Hydrated cation	Layered silicate	-	**Magadiite**, **kenyaite**, makatite, kanemite, illerite
	None or H_2O	Layered silicic acid	-	Silhydrite

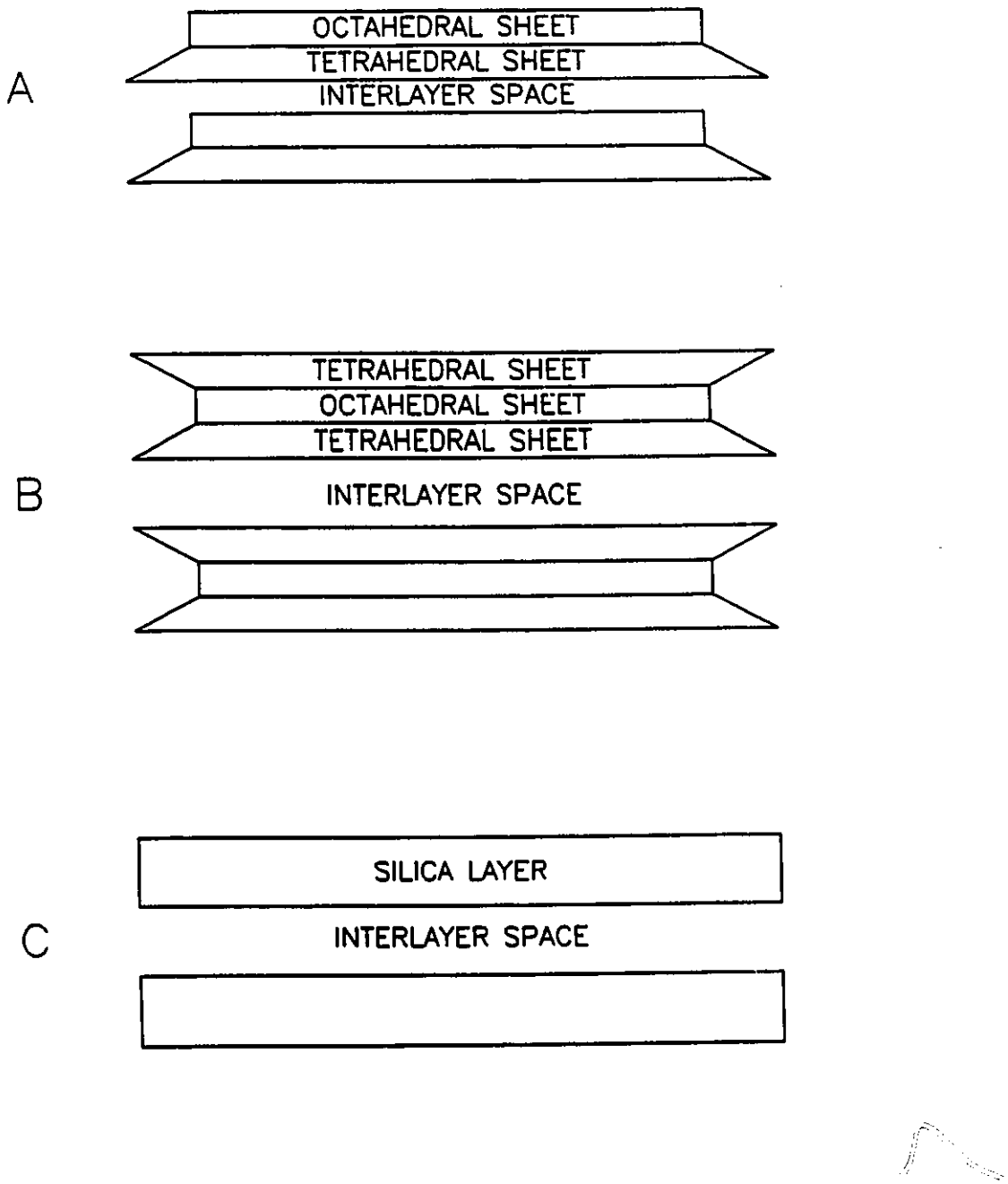

Figure 1.1 Representation of the three types of phyllosilicates: (a) 1:1 phyllosilicates, (b) 2:1 phyllosilicates and (c) layered silicates.

1.1.1 1:1 phyllosilicates

1:1 phyllosilicates include the minerals chrysotile (with octahedral Mg) and kaolinite (octahedral Al). Their interlayer spaces are usually devoid of water, owing to very strong hydrogen bonding of the alumina hydroxyls to the silica oxygens of adjacent layers. Because of this property, such minerals are said to be *non-swelling*.

1.1.2 2:1 phyllosilicates

2:1 phyllosilicates include the groups of talcs, smectites, vermiculites, micas and chlorites. Specific mineral species of this type include montmorillonite, hectorite, saponite, nontronite, muscovite and sudoite, to name but a few.

Minerals of this type are said to be *dioctahedral* if two thirds of the octahedral sites are occupied by a metal atom: this situation is expected when the octahedral metal species is trivalent (*i.e.* Al^{3+}, Fe^{3+}). 2:1 minerals are said to be *trioctahedral* if all of the octahedral sites (three thirds) are occupied: this occurs if the octahedral metal is divalent (*i.e.* Mg^{2+}, Fe^{2+}). For example, montmorillonite is a dioctahedral phyllosilicate, with Al^{3+} as the predominant octahedral metal; hectorite, on the other hand, is trioctahedral, with Mg^{2+} occupying most of the octahedral sites.

Another feature of 2:1 phyllosilicates is the phenomenon of *isomorphic substitution*, which refers to the replacement of some of the octahedral ions by different metals. Thus, for dioctahedral minerals, some of the trivalent metal ions (usually Al^{3+}) can be replaced with divalent ions (such as Mg^{2+}), resulting in a net negative charge on the phyllosilicate layer.

This charge must then be compensated by cations (mostly Na^+ , Ca^{2+} or K^+) which reside in the interlayer region of the mineral. Minerals of the talc/pyrophyllite group have little or no isomorphic substitution, so their interlayer spaces are devoid of cations. Minerals of the smectite and vermiculite groups have moderate substitution, resulting in the presence of hydrated interlayer cations which are rather loosely associated with the layers and can be easily exchanged with other cations (this key property of smectites will be discussed in greater detail in section 1.2.1): due to their affinity for interlayer water adsorption (via cation hydration), these minerals are said to be *swelling*. Minerals of the mica group have very high isomorphic sustitution and thus possess a large interlayer cation content (usually K^+): because of this high charge, the layers are held together tightly by electrostatic attraction and, as a consequence, the cations are not hydrated (mineral is non-swelling) and are very difficult to exchange. Chlorite group minerals also have very high substitution, but the layer charge is compensated by the presence of positively charged metal hydroxyde sheets instead of cations.

1.1.3 Layered silicates

Layered silicates include the minerals magadiite and kenyaite. These purely siliceous compounds have a negative layer charge compensated by interlayer Na^+. These sodium ions are hydrated, thus affording a limited swellability for these minerals. When leached by dilute acids, the sodium of the layered silicates are exchanged for hydrogens, thus generating layered silicic acids, which are considerable less swelling than smectites due to reasonably strong hydrogen bonding between the hydroxyls of adjacent layers. A more detailed

discussion about the structures, properties and reactivities of these compounds will be given in section 1.3.

1.2 Smectites

Smectites are among the most widely studied classes of phyllosilicate minerals. The word finds its origin from the Greek σμεκτικνς ("smectikos"), an adjective refering to something which has the properties of soap. This rather odd appellation comes from the slippery and "soapy" feel many minerals in this group exhibit when manipulated by hand, a property attributed to the slippage of the lamellae over each other which occurs due to the relatively weak attraction between individual clay layers.

1.2.1 Structure, mineralogy and physical characteristics

1.2.1.1 Structure of smectites

As was previously mentioned, smectites are members of the 2:1 phyllosilicate type and are composed of two tetrahedral silicate sheets sandwiching an octahedral metal oxide sheet. The tetrahedral sheet is composed of SiO_4 units which are linked to each other by the sharing of three oxygens to form infinite two-dimensional array composed of fused six-unit rings (Figure 1.2a and 1.2b). The octahedral sheet is composed of MO_6 octahedra which are laterally fused together by edge-sharing (Figure 1.2c and 1.2d). The unshared fourth corners of the silica tetrahedra are then fused to the octahedral oxygen planes, the process being repeated a second time such that tetrahedral sheets becomes bound to both sides of the

octahedral sheet, forming the complete smectite layer (Figure 1.2e). The thickness of the smectite layer can thus be calculated as being 9.6 Å on the basis of this geometry.

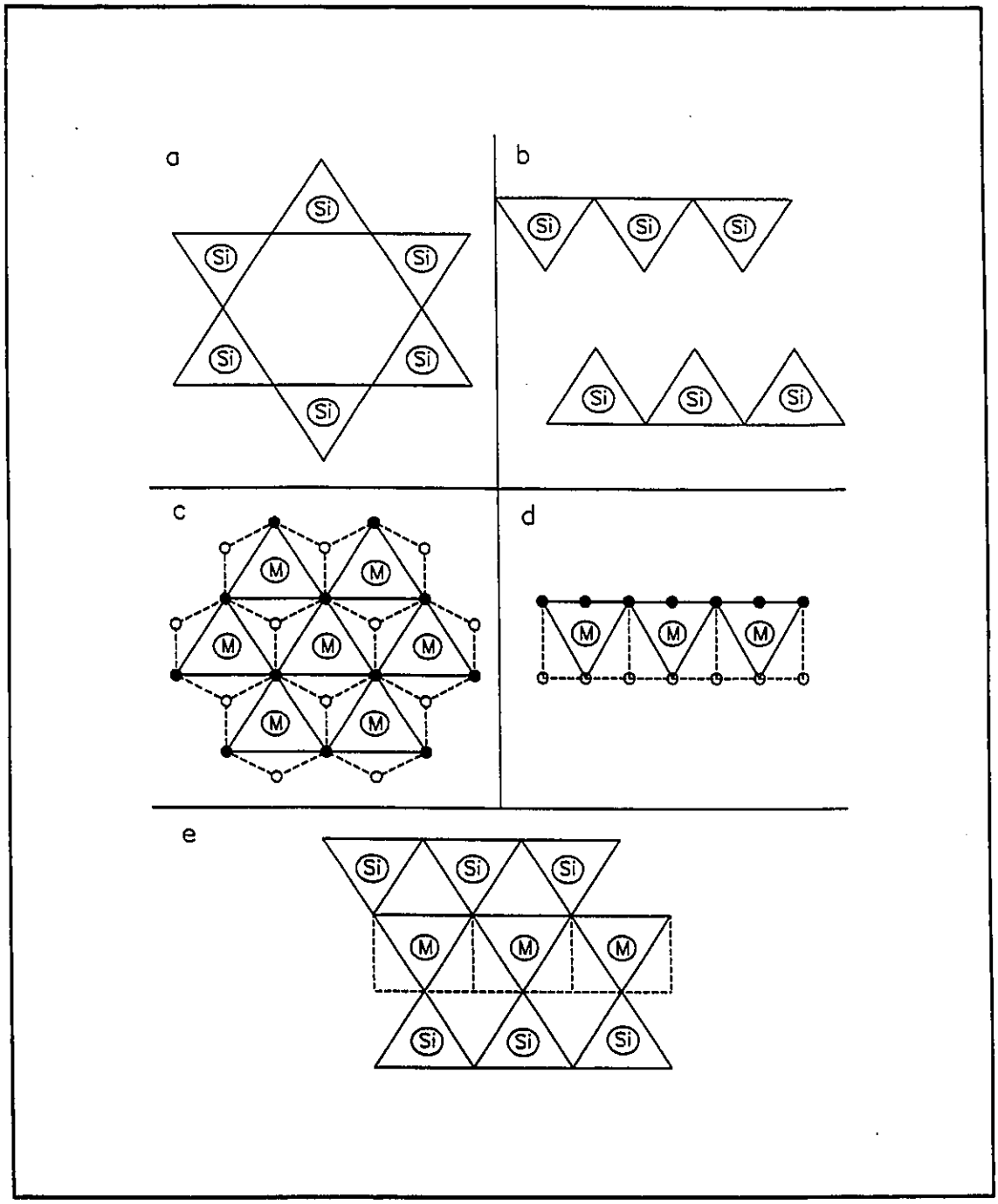

Figure 1.2 Structure of the tetrahedral silicate sheet (top view in (a), cross-sectional view in (b)), the octahedral sheet (top view in (c), cross-sectional view in (d)) and the assembled smectite layer cross-sectional view in (e). In figures (c) and (d), filled circles denote oxygens on the top of the octahedral sheet and hollow circles those on the underside. M denotes octahedral metal ion sites (two thirds occupied for dioctahedral, completely occupied for trioctahedral).

A consequence of the hexagonal geometry of the tetrahedral sheet is that only two thirds of the octahedral oxygens will be connected to silica tetrahedra. The charge imbalance thus occuring because of this forces these oxygens to associate with hydrogen atoms. Therefore, every hexagonal cavity in the silica sheet contains an M-OH group (called a *structural hydroxyl*) which is usually inaccessible for chemical reactions due to the relative small size of the cavity.

The overall *ideal* structural formula for dioctahedral smectites can thus be expressed as $Si_8M_4O_{20}(OH)_4$, where M is a trivalent cation (Al^{3+}, Fe^{3+}, etc.). Likewise, the ideal structural formula of trioctahedral smectites can be written as $Si_8M_6O_{20}(OH)_4$, where M is a divalent cation (Mg^{2+}, Zn^{2+}, etc.). With such formulae, smectites would be expected to be neutral in charge. This is not the case, however, for the vast majority of smectites found in nature since a negative layer charge is almost always found. This is explained by the replacement of the octahedral (and, usually to a lesser extent, the tetrahedral) cations with lower valence species during the genesis of the mineral, causing a net negative charge to appear on the structure. This important property of clay minerals is called *isomorphic substitution* and will be discussed in more detail in a following paragraph. To maintain electroneutrality, this negative charge is balanced by hydrated cations which are located between the clay layers. Figure 1.3 depicts the complete three-dimensional structure of a smectite layer, including all of the smectite features previously discussed.

The general chemical formula for dioctahedral smectites can thus be generalized by the formulation

$$(Si_{8-x}T^{3+}_x)M^{3+}_{4-y}X^{2+}_yO_{20}(OH)_4Q^+_{x+y}$$

where T is a trivalent cation substituting tetrahedral Si, X a divalent cation substituting the predominant octahedral M ion, and Q the charge-balancing interlamellar counter cation.

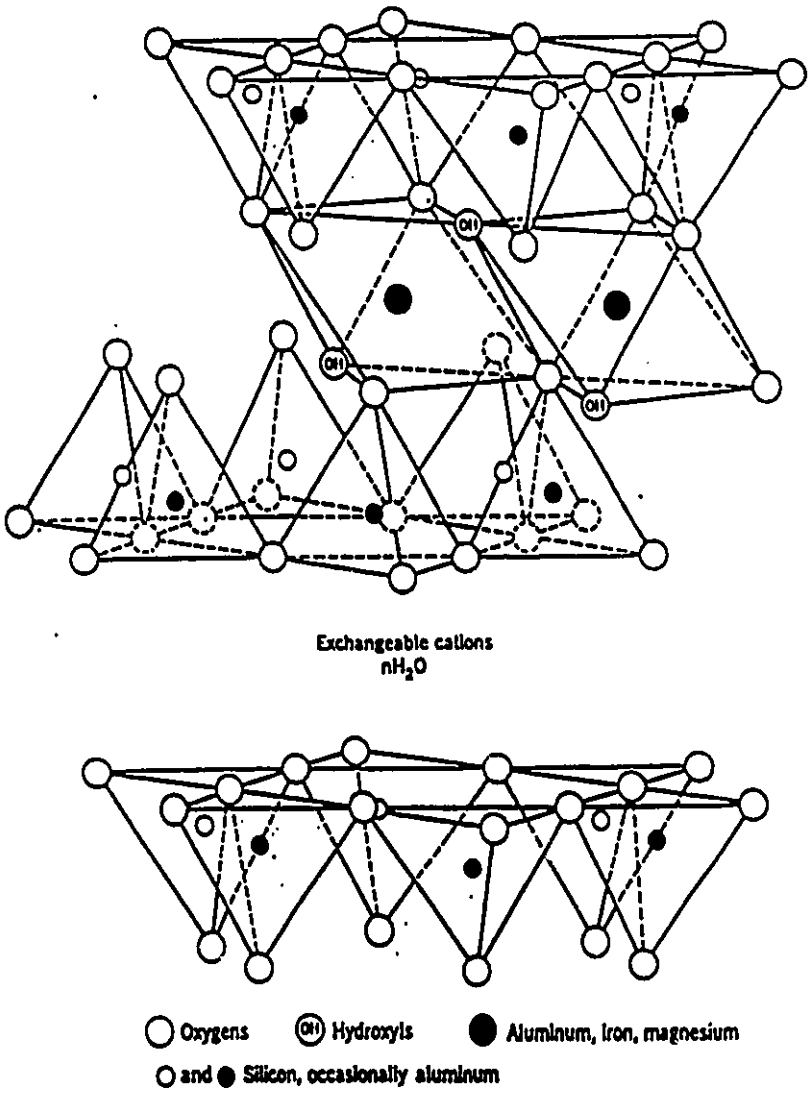

Figure 1.3 Three-dimensional structure of smectite minerals.

Similarly, the general formula for trioctahedral smectites can be written as

$$(Si_{8-x}T^{3+}_x)M^{2+}_{6-y}X^{+}_y\square_zO_{20}(OH)_4Q^{+}_{x+y+2z}$$

where $\square$ represents a vacant octahedral site. Note that, in this case, the negative layer charge results from the substitution of divalent metals for monovalent metals (usually Li^+) or by the vacancy of some octahedral sites.

1.2.1.2 Isomorphic substitution and layer charge on smectites

In dioctahedral smectites, the negative layer charge occurs primarily due to the replacement (or isomorphic substitution) of some of the trivalent octahedral cations for divalent cations. For instance, in the case of montmorillonite, where the predominant octahedral species is Al(III), Mg(II) substitution is the major source of the negative charge.

In trioctahedral smectites, the origin of the negative charge can be related to the exchange of divalent octahedral cations for Li^+, or to the total abstraction of some cations, resulting in a vacant octahedral site. The mineral laponite is an example of a trioctahedral smectite that has both Li^+ substitution and vacant octahedral sites contributing to its layer charge.[2]

In all smectites, isomorphic substitution can also occur in the tetrahedral sheets, where Si atoms could be substituted for trivalent ions (mostly Al, but also Fe, Cr and V), thus further increasing the negative charge on the clay layers. In some minerals the tetrahedral sheet charge is actually greater than that of the octahedral sheet, such as in the cases of beidellite, nontronite, volkonskoite, saponite and sauconite. In the most

predominant smectite species, however, a higher octahedral sheet charge is usually observed, as in the cases of montmorillonite and hectorite.

1.2.1.3 Classification and natural variability of smectites

Because of the wide variety of conditions which can be imagined possible during the formation of smectite minerals during the history of the Earth, it is not surprising that a tremendous number of chemically distinct smectite minerals exist in nature. In fact, the actual number of these clays is likely to be virtually limitless. It is therefore necessary to classify these minerals according to certain arbitrary characteristics which may permit some kind of adequate distinction between similar smectite clays. Such distinguishing factors can include the type of octahedral sheet (di- or trioctahedral), the predominant octahedral cation, the extent of the layer charge and the location of the layer charge (tetrahedral or octahedral substitution).

The smectite group has been subdivided into two subgroups, saponites and montmorillonites, based on the nature of the octahedral sheet (see Table 1.1). The saponite subgroup includes all of the trioctahedral smectites (with the predominant octahedral cation being Mg^{2+} and/or occasionally Fe^{2+}, Zn^{2+}, Co^{2+} or Mn^{2+}) and comprises the minerals hectorite (octahedral Mg), saponite (Mg), stevensite (Mg) and sauconite (Zn). The montmorillonite subgroup encompasses the dioctahedral smectites (with predominant octahedral cations Al^{3+} and/or Fe^{3+}, occasionally Cr^{3+}, V^{3+} or Ti^{3+}) and includes the minerals montmorillonite (Al^{3+}), beidellite (Al^{3+}), nontronite (Fe^{3+}) and volkonskoite (Cr^{3+}).

Montmorillonite and beidellite, both having Al^{3+} as their predominant octahedral cation, can be distinguished from each other by the fact that the layer charge of montmorillonite results primarily from octahedral substitution (Al for Mg) whereas that of beidellite stems predominantly from tetrahedral substitution (Si for Al). A similar distinction can be made between hectorite (octahedral substitution of Mg for Li) and saponite (tetrahedral substitution of Si for Al). Table 1.2 lists examples of chemical formulae for various smectites minerals, highlighting the composition of the their tetrahedral and octahedral sheets as well as their layer charges (represented as the number of interlayer cations per unit formula).

Table 1.2 Tetrahedral, octahedral and interlayer cation compositions of selected smectite minerals.

Smectite	Location (code)	Cations per $O_{20}(OH)_4$ formula		
		Tetrahedral	Octahedral	Interlayer
Montmorillonite[3]	Crook County, Wyoming (SWy-1)	$Si_{7.8}Al_{0.2}$	$Al_{3.28}Mg_{0.38}Fe_{0.34}$	$Na_{0.62}$
Nontronite[4]	Garfield, Washington (SWa-1)	$Si_{6.94}Al_{1.06}$	$Fe_{3.96}Mg_{0.02}Ti_{0.02}$	$Na_{0.96}$
Beidellite[5]	Black Jack Mine, Idaho	$Si_{6.96}Al_{1.04}$	$Al_{3.96}Mg_{0.01}Fe_{0.03}$	$Na_{0.90}$
Volkonskoite[6]	Okhansk, Siberia	$Si_{7.34}Al_{0.66}$	$Cr_{2.36}Mg_{1.56}Fe_{0.54}$	$Ca_{0.50}$
Hectorite[7]	Hector, California (SHCa-1)	Si_8	$Mg_{5.30}Li_{0.66}Al_{0.04}$	$Na_{0.62}$
Saponite[8]	Average formulation	$Si_{7.06}Al_{0.94}$	$Mg_{5.84}Fe_{0.04}Al_{0.06}$	$Na_{0.96}$
Sauconite[9]	Saucon Valley, Pennsylvania	$Si_{6.68}Al_{1.22}$	$Zn_{3.90}Fe_{1.16}Al_{0.34}Mg_{0.24}$	$Na_{0.66}$

1.2.1.4 Layer stacking

Now that the structure of individual smectite layers has been established, discussion may proceed to the arrangement of these layers with respect to each other as they stack together to form discreet smectite particles. Thus, three fundamental layer stacking modes can be observed in the case of smectite minerals.[10] The first is "regular stacking", the second "semi-random stacking" and the third "turbostratic stacking".

Regular stacking involves the superposition of the smectite layers such that the positions of the metal and oxygen atoms result in a perfect three-dimensional periodicity in the structure. This situation can be analogized by a deck of cards containing, for example, 52 identical cards (for examples, the ace of spades) where all of the cards are neatly stacked in the same direction (such that the spades are all pointing in the same direction).

In semi-random stacking, the layers are stacked with a random 60, 120, 180 or 240° rotation with respect to each other. In this case, the hexagonal cavities of the tetrahedral layers still form a perfect stacking array, but the rest of the layer becomes shifted with respect to the adjacent layers by an angle of n x 60°, where n is a random integer.

Turbostratic stacking (from the Latin *turbare* - to disturb - and *stratum* - spread, bed) represents layers which are stacked onto one another in a completely random arrangement. Using the deck of cards analogy previously mentioned, this situation would be akin to throwing the deck on a table, resulting in a disordered pile of cards.

In the majority of cases, smectites adopt a turbostratic stacking mode because of the relatively weak interaction between the clay layers.[10] It was observed, however, that the

inclusion of large monovalent cations such as K^+ or Cs^+ in the interlayer region has the effect of creating, in certain smectites, some increase in the stacking order which was attributed to the coordination of these cations to the hexagonal cavities of two adjacent layers, thus forcing the layers into a semi-random stacking mode.[11,12] Smaller cations (Na^+, for instance) would likely be too small to coordinate in such a manner.

Other factors which can influence the stacking conformation of smectite layers include the hydration of the interlayer cation and of the clay surface. Thus, the relative atmospheric humidity can affect the extent of the water content in the interlayer region of the clay. The layer charge density and distribution is also an important consideration, as it is likely to direct the position of the interlayer cations within the smectite framework. As was demonstrated in the previous paragraph, the nature of the interlayer cation has critical effects on the smectite layer structure.

1.2.1.5 Cation exchange capacity (CEC)

This most important characteristic of clay minerals is actually another way of expressing the layer charge of smectites. The cation exchange capacity (CEC) is defined as the amount of interlayer cation per unit mass of the smectite which can be exchanged by another type of cation. The CEC of a given smectite sample is therefore a function of its layer charge (which is implicitly related to the amount of interlayer cation), the nature of the interlayer cation and that of the exchange cation.

Different types of cations have different affinities for the clay surfaces, thus a cation with a weak interaction with the smectite layers can be easily displaced by one with a greater binding affinity with the clay. Conversely, ion exchange of strongly interacting cations for weaker exchange ions would be difficult. Although a systematic relationship between ion exchange and the nature of the cations is difficult to establish, it is observed as a general trend (with great emphasis on the word *general*) that monovalent cations are more weakly bound to the clays than divalent ions, with the ease of cation replaceability decreasing in the following order:[13,14] $Na^+ > K^+ > NH_4^+ > Mg^{2+} > Ca^{2+} > H^+$.

1.2.2 Chemistry of smectites

1.2.2.1 Ion exchange

By far, the most widely exploited reaction process involving smectite clays is that of ion exchange. In this process, the parent clay mineral (usually in its Na^+ form) is treated with a solution containing the desired exchange cation so that a new clay material is obtained with novel chemical properties bestowed by the included cation.

The ion exchange of organic cations in smectite minerals forms the widely studied class of compounds known as *organoclays*. Materials of this type, first introduced by the early work of Gieseking in 1939[15-18] and other authors,[19-21] were found to be very stable as the organic cations were very strongly adsorbed by clay minerals and difficult to replace by smaller inorganic cation. Also, small organic cations were found to be more easily replaced

by larger organic cations, suggesting that Van der Waals interactions of the cations to the clay surface play an important role in the ion exchange process. Such organoclays were found to be hydrophobic in nature and thus devoid of interlamellar water. This property results in the formation of stable microporous cavities in the interlayer region of such smectites, a feature which has led to an extensive studies of the gas adsorption/separation applications of organoclays by Barrer[22-32] and other authors.[33,34] Organic cation-clay interactions have also found widespread applicability for the characterization of the charge density of smectites[35-49]

1.2.2.2 Pillaring[50-67]

As an alternative to organic cations, large *inorganic* oligocations such as $Al_{13}O_4(OH)_{24}^{7+}$ or $Zr_4(OH)_{16-x}^{x+}$ can instead be intercalated into the clay interlayers by ion exchange. Calcination of these species results in the dehydroxylation of the pillars and the formation of thermally stable pillared clays which have found great use as catalysts and adsorbents.[68]

The pillars in such materials are found to be very acidic, confering them with useful catalytic abilities.

1.2.2.3 Grafting of smectites

In the 1940's Deuel reported the covalent fixation of acetate, alcohol, amine and phenyl groups to the interlayer surface of montmorillonite through, seemingly, condensation of hydroxyl groups.[69-73] This evidence led this author to postulate that the surface of montmorillonite layers was covered by hydroxyl groups, a conclusion consistent with an alternate structure for the smectite layer proposed by Edelman and Favejee.[74] The Edelman-Favejee model, however, is now considered inaccurate and hence the grafting mechanism proposed by Deuel has been refuted.[75]

Despite this, similar reactions are still being performed today resulting in tenaciously bound molecular species on the surfaces of smectite minerals which would seemingly involve condensation to Si-OH groups. The work of Choudary, for instance, has shown that the fixation, or anchoring, of organosilyl,[76-78] phosphine[79-81] or alkyl[79] moieties does indeed occur and may indicate the presence of some Si-OH groups in the interlamellar region of smectites due to defects or structural anomalies, particularly when the clay is acid-treated prior to the grafting reaction.

The two pathways taken by this group to achieve grafting involve (1) acid treatment of the clay followed by treatment with an organosilane or (2) treatment of the clay with thionyl chloride followed by treatment with an organophosphine or an alkyllithium compound. Figure 1.4 shows a proposed reaction scheme for these processes.

Although the exact mechanism for this type of reaction is still poorly understood, the undeniable formation of stable organo-smectite materials via such pathways should be regarded as a challenge for chemists in future research efforts.

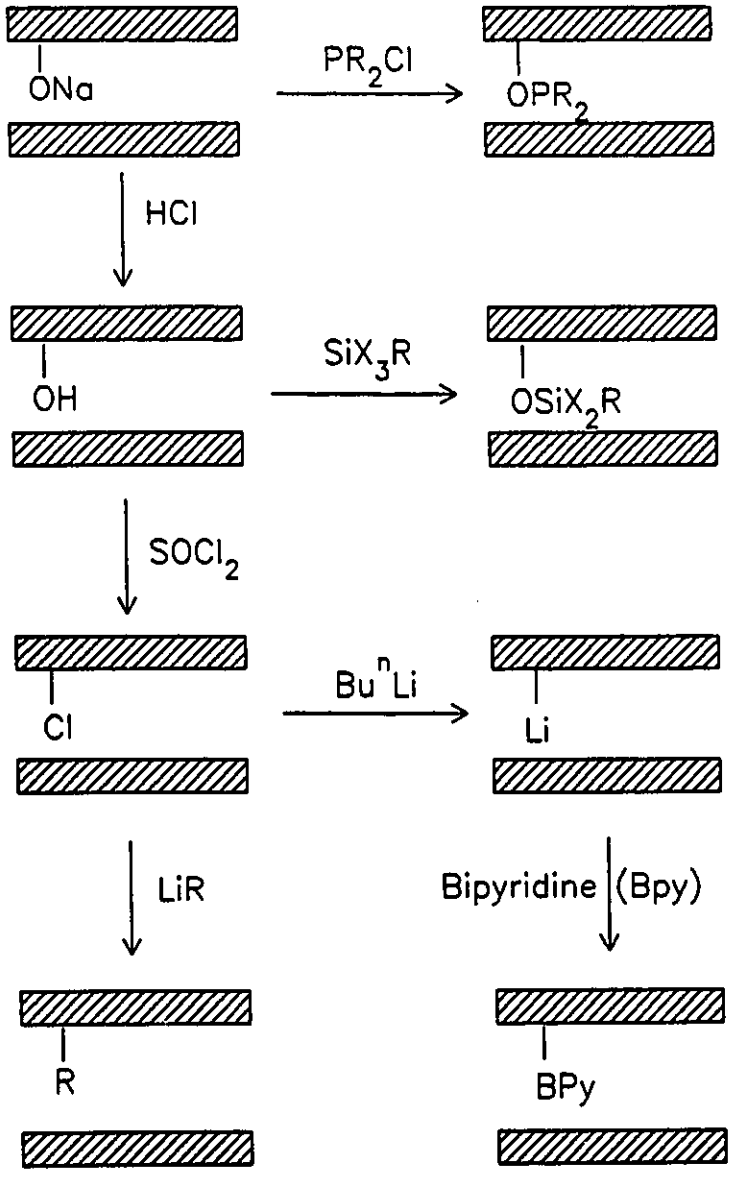

Figure 1.4 Proposed reaction scheme outlining various smectite anchoring strategies, according to the work of Choudary.[76-82]

1.2.3 Applications of smectites

Clays minerals possess many properties which make them useful for technological applications, stemming from their low cost, natural abundance, small particle sizes, large reactive surface areas and especially from their particular intercalative properties. This section will briefly discuss some of the more important practical uses of clays in the contemporary world.

1.2.3.1 Catalysis

The first important industrial application of clays was the use of acidified smectites as a petroleum cracking catalyst, a method which was extensively used until the 1960's when they were replaced by more effective zeolite catalysts.[68] Since then, clays have been exploited as effective catalyst carriers, where suitable catalytic species could be intercalated into the structure, resulting in solid-phase structures with catalytic centres dispersed in a microporous cavity network. Such catalysts have the distinct advantage of avoiding the use of large volumes of solution phase reagents often required in homogeneous catalysis, thus curtailing the waste and environmental damage of workup residues, such as acid or toxic metal effluents.[83,84] Another key feature of intercalated catalysts is that of their geometrically confined environments which can be exploited for reaction selectivity and molecular recognition.[85,86]

The direct ion-exchange of catalytically-active molecules can be made in order to generate new solid state catalysts. An example of this is given by the enhanced decomposition efficiency of peroxides by diaminostilbene when the latter is intercalated into montmorillonite.[87]

A more widespread approach to the design of clay catalysts involves the use of pillared clay compounds, thus exploiting the acidity and large internal surface area confered by the oxide pillars. Examples of reaction systems involving such catalysts include the alkylation of aromatic compounds,[83] O-Me bond cleavage of anisoles,[88] oxidation of aromatics[84] and sulphides,[89] and the cracking and selective disproportionation of alkylbenzenes.[90]

The catalytic applications of grafted smectites have been extensively studied by Choudary, involving the covalent anchoring of catalytic species in the interlamellar region of montmorillonite. This group has found these grafted-clay catalysts to be effective in promoting olefin hydrogenation,[79-82,91] knoevenagel condensation,[78] phase-transfer catalysis[77] and olefin oxidation.[76]

1.2.3.2 Environmental applications of clays

There has been much attention put on clays with respect to their interaction with environmental pollutants because of the ubiquitous presence of these minerals as soil components with strong adsorption capacities. For instance, pesticides and herbicide use has generated in recent decades a strong interest in understanding the fate of these harmful

compounds in the environment: their interaction with clay minerals is thus an important part of this goal.[92,93]

The sorption properties of clay minerals and their chemically modified derivatives for organic molecules have also been extensively explored with the goal of generating effective new technologies for the removal of toxic pollutants from the environment. Molecules targeted for removal using clays, organoclays and/or pillared clays include aromatics,[94-100] chlorophenols,[99,101-103] chlorinated hydrocarbons,[98,100,104,105] dioxin[106] and N-heterocyclic compounds.[107]

The adsorption of metal ions to smectites has also been examined with a similar environmental objective as that of organic pollutants. In light of the Chernobyl reactor accident, the application of smectites as radionucleide scavengers has been explored.[108,109] The removal of other heavy metals, particularly toxic species such as Pb, Hg and Cd, has been studied using both the natural clays,[110,111] pillared clays[112] and sulfurized clays.[113]

1.2.3.3 Other applications

Organoclays have been used for gas chromatographic separation of gases,[33,34,114] exploiting the selective recognition properties of these compounds for small molecules derived from the size of the interlayer micropores.

A promising new generation of membranes has recently been in the working, involving the incorporation of modified clays in polymer matrices.[115-117] Thus, the well-

defined microporosity and adsorptive character of such materials can now be exploited in membrane separation processes.

1.3 Layered silicates

After 1:1 and 2:1 minerals, the third and final class of phyllosilicates is that of layered silicates. These purely siliceous compounds are only rarely found in nature since they require exceptionally high alkaline conditions for their syntheses. Localities where naturally occuring layered silicates have been found thus far are shown in Figure 1.5, including Central and East Africa and Northwestern U.S.A. These materials can, however, be conveniently prepared in the laboratory, producing minerals with exceptional intracrystalline reactivity. In this section, the mineralogy, synthesis, structure and reactivity of layered silicates will be introduced.

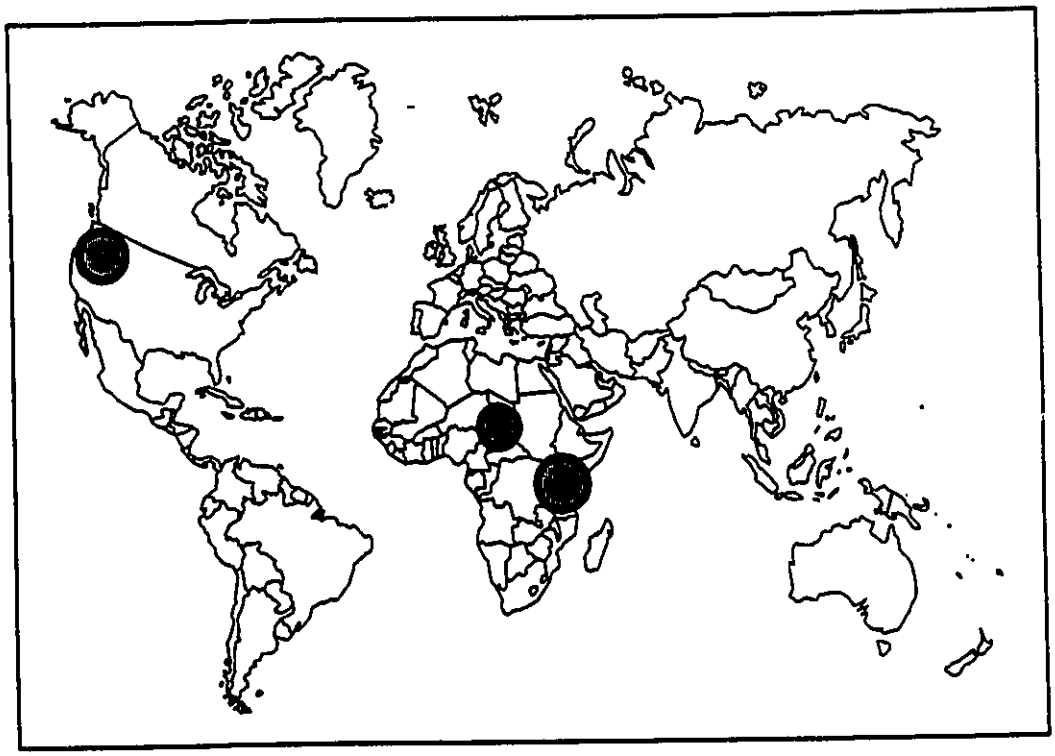

Figure 1.5 Geographic locations of known layered silicate deposits.

1.3.1 Mineralogy and synthesis

1.3.1.1 Historical perspective

A curious irony in the development of the field of layered silicates is that such compounds had already been reported many decades *prior* to their discovery by Eugster in 1967![118] As early as 1905, Tschermak reported a new silicate species obtained by the leaching of albite with dilute hydrochloric acid.[119] Crystalline silicic acids were first prepared by Schwarz in the 1920's,[120] but it was only in the 1950's with the advent of X-ray diffraction technology that the structures of these compounds could be determined.

Magadiite and *kenyaite* were the first naturally occuring layered silicates species discovered in the deposits of Lake Magadi, Kenya in 1967.[118] The characteristic aspect of this area is the high alkalinity of the lake water: this causes high amounts of silica to be dissolved and then precipitate as the crystalline minerals.[118,121,122] Alkaline lakes in other parts of the world were also found to contain similar mineral phases, namely Trinity County (California),[123] Alkali Lake and Rome (Oregon),[124,125] Wyoming,[126] and Kanem (Tchad).[127] Later, other layered silicates were identified from these deposits: *makatite*,[128] *silhydrite*[129] and *kanemite*.[127] In 1952, *sodium octosilicate* became the first synthetic layered silicate ever prepared[130] (unbeknownst to the author at the time, he had also managed to synthesize magadiite and kenyaite, 15 years before their discovery!).

1.3.1.2 Mineralogy

The key aspect of the areas where layered silicates are found is the high alkalinity of the lake water causing high amount of silica to be dissolved.[118,121,122] Subsequent evaporative concentration results in the precipitation of the silicate species. The scarcity of layered silicates in nature thus stems from the fact that the occurence of lakes which are both highly alkaline and evaporative is, indeed, quite rare.

The formation of silicates from such solutions can be explained by the sol-gel co-condensation of dissolved silica monomers (SiO_4^{4-}) to form three-dimensional polymers.[131] Product formation under such cirumstances is highly dependant upon the relative water, base and silica content of the reaction system, and is also driven by the nature of the cations and anions present in the solution.[132]

The chemical compositions of layered silicates are given in Table 1.3, along with their layer spacings (d_{001}). It is evident from this list that an increase in layer spacing is associated with increasing Si content (with respect to a Na + H content of 2), which leads to the hypothesis that the silicate layers of these different species are composed of a variable number of silicate sheets fused to each other. These structural aspects will elaborated upon in more detail in a following section.

Table 1.3 Composition and basal spacings of some layered silicates

MINERAL	Na	H	Si	O	H_2O	d_{001} (Å)	REF.
Kanemite	1	1	2	5	3	10.2	133
Makatite	2	0	4	9	5	9.0	128
Octosilicate	2	0	8	17	11	11.0	134
Magadiite	2	0	14	29	11	15.8	135
Silhydrite	0	2	14	29	4	14.5	136
Kenyaite	2	0	22	45	10	19.7	137

Another important class of compounds is obtained by reacting these sodium silicates with acids: under such treatment, sodium ions are leached out of the interlamellar space and replaced with hydrogen ions,[118,123,138] producing what are refered to as *layered silicic acids*. The silicic acid corresponding to magadiite and kenyaite will thus be termed simply as H-magadiite and H-kenyaite, respectively, as no other system of nomenclature has yet been devised for these species. Note that the mineral silhydrite (see Table 1.1) is actually a naturally occuring form of H-magadiite.

1.3.1.3 Synthesis

Layered silicates can be readily synthesized by simple hydrothermal process. McCulloch[130] was the first to prepare such a compound (octosilicate) by heating 15 parts silica gel, 3.6 parts sodium hydroxide and 30 parts water in sealed ampoules at 100°C for 4 weeks. The synthesis of magadiite was first reported by Lagaly, *et al.*,[135] who obtained the mineral by heating 9 moles SiO_2, 2 moles NaOH and 75 moles H_2O for 4 weeks. Kenyaite was also synthesized following a similar procedure but with longer reaction times and changing the relative SiO_2:NaOH:H_2O ratio in favour of higher Si content.[137]

Eugster proposed that kenyaite formation occured by a preliminary magadiite precipitation followed by an alteration to the kenyaite structure (given proper temperature/composition conditions)[139], and continued thermal treatment would cause the mineral to condense into quartz. The following progression was therefore be established:

silica solution → magadiite → kenyaite → quartz

This hypothesis was verified by numerous experimental results[137] which have permitted the construction of phase diagrams describing the behaviour of the SiO_2-NaOH-H_2O system (Figure 1.6). Thus, by controlling the relative quantities of silica, water and base in the hydrothermal system, one may selectively obtain magadiite or kenyaite.

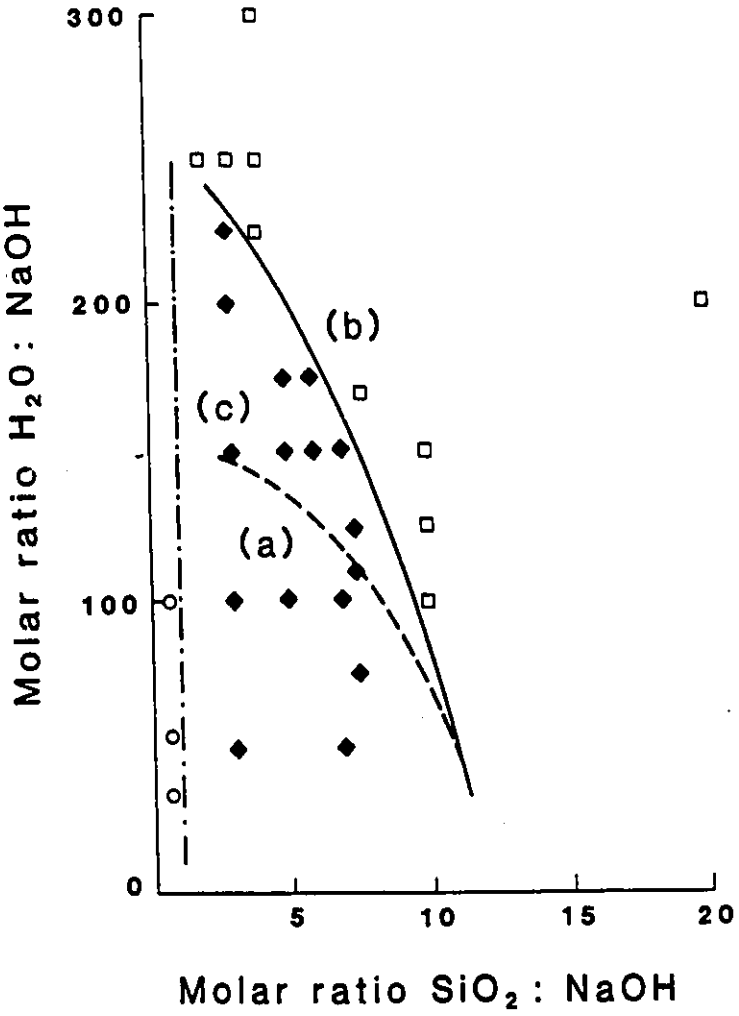

Figure 1.6 Layered silicate compositional phase diagram at 150°C (diamonds denote magadiite, squares kenyaite and circles solution)

Another important feature in layered silicate synthesis is the reaction temperature: raising it by only a few tens of degrees can dramatically decrease the reaction time. At 100 °C, magadiite was formed in 4 weeks,[135] but raising the temperature to 150 °C reduced the reaction time to 3 days.[132] Futher increasing the temperature to 175 °C resulted in the formation of magadiite in 19 hours.[140]

It has been shown that the presence of foreign anions can affect the outcome of the reaction[132]. By replacing two-thirds of the NaOH with equimolar amounts of the sodium salt of another anion, one obtains magadiite for Br^-, I^- and SO_4^{2-}, and kenyaite for F^-, Cl^- and CO_3^{2-}. Introducing borate into the mixture seemed to prevent crystallization altogether. Using sodium carbonate as base instead of sodium hydroxide generally favoured the formation of kenyaite for most silica:base:water ratios.

Changing the alkali cation of the base employed has also been found to exert a profound effect on the synthesized material. Replacing NaOH with KOH (under synthetic conditions that would expect to yield magadiite) was found to favour the formation of a potassium silicate with a structure analogous to that of kenyaite.[141] By stopping the reaction at a shorter time, the potassium silicate analog of magadiite was obtained.[142c] Interestingly, the reactivity (ion-exchange and swelling) of these silicates and their corresponding silicic acids was found to be greater than that of their sodium analogs,[142] as will be discussed in a further section.

---

[c]Magadiite and kenyaite are defined as the sodium varieties of the layered silicates. Distinction is normally made between these minerals and their potassium analogs.

1.3.2 Structural elucidation

Electron diffraction and X-ray powder data have revealed that magadiite has a monoclinic unit cell with parameters a=b=7.25Å, c=15.69 and ß=96.8°.[143]

Because of the microcrystalline aspect of layered silicates, no single crystal X-ray diffraction studies of these minerals were possible. Thus, no definite crystal structures for layered silicates are at present known, with the exception of makatite.[144] One must therefore rely on a combination of less direct spectroscopic evidence in order to elucidate the structural features of the silicate layers and arrive at a plausible structural model for the minerals. Techniques used for this purpose include ^{29}Si NMR spectroscopy, powder X-ray diffraction, infrared spectroscopy, thermal analysis and ^{1}H NMR.

1.3.2.1 Nature of the interlameliar region

As was previously mentioned, the structure of magadiite consists of silicate layers separated by an interlayer space. The basal spacing is defined as the distance from the top of one layer to the top of a subsequent layer, or the sum of the thickness of a layer and the interlayer space. This distance varies according to the type of interlayer cation present and the extent of hydration of the mineral. Table 1.4 shows the spacing of magadiite under various conditions, as determined by X-ray powder diffraction[143]. What this experiment demonstrates is that, when magadiite is converted to H-magadiite, there is a reduction of the basal spacing resulting from the partial dehydration of the interlamellar region. Upon

heating H-magadiite above 100 °C, the interlamellar region becomes devoid of water and the layers collapse. Thus, when magadiite is in its fully hydrated 15.6 Å form, a bilayer of water molecules is expected to reside in the interlayer region. Upon acid treatment, the leaching of interlayer sodium ions reduces the hydration capacity of the mineral such that only a monolayer of water molecules remains which, upon heating the material, is easily expelled from the structure.

Table 1.4 Basal spacings of various magadiite species.

LAYERED SILICATE	d_{001} (Å)
Magadiite (hydrated)	15.6
H-magadiite (hydrated)	13.7
Magadiite (dehydrated)	13.5
H-magadiite (dehydrated)	11.2

Both infrared and ^{1}H-NMR studies have shown that there are 2 types of OH groups on the layers of H-magadiite:[145] the first are strongly hydrogen bonded to hydroxyls on the adjacent layers (FTIR band at 3450 cm^{-1}) and disappear upon heating between 300 and 500°C due to condensation, the second are isolated OH groups (FTIR band at 3660 cm^{-1}) which are eliminated between 500 and 1000°C. Proton NMR results have indicated that the H-bonded hydroxyls are separated by 2.2-2.9 Å and the free ones by 4.3-5.2 Å: these latter

groups were said to point into hexagonal cavities of the next layer (recall the smectite tetrahedral sheet structure, section 1.2.1.1), thus not interacting with hydroxyls on the adjacent layer. Thermogravimetric studies have found that the OH surface density is of about 3.5 OH's/100Å^2, a value which is consistent with a new chemical formula for H-magadiite: $H_4Si_{14}O_{30}$.[145] This formula can account for the two types of protons observed in the IR and NMR spectra. An outcome of this result is the writing of a new formula for magadiite (in the sodium form): $Na_2H_2Si_{14}O_{30}$.

1.3.2.2 Structural models

Many suggestions as to the crystal structure of magadiite (and other layered silicates) were attempted,[146-150] mostly by correlating previous experimental results with high-resolution solid state ^{29}Si NMR data, all yielding interesting but very conjectural hypotheses which are not without discrepancy. The following describes five suggested structural models for layered silicates.

Schwieger model[146]

This group was the first to exploit ^{29}Si NMR spectroscopy for the study of layered silicates. Their working hypothesis was that layers of these silicates were composed of multiple makatite sheets connected together. The known makatite structure is essentially composed of a two-dimentional arrangement of a single layer of silica tetrahedra. Thus,

Schwieger *et al.* have proposed that the octosilicate layer consists of two fused makatite sheets, magadiite of three fused sheets (shown in Figure 1.7a), and kenyaite of five.

^{29}Si NMR spectra of the synthetically prepared layered silicates featured a Q^3 signal (Si atoms bound to OH groups, *viz* $(SiO)_3SiOH$) at -101 ppm and Q^4 signals (Si atoms completely surrounded by other SiO_4 tetrahedra, *viz* $(SiO)_4Si$) around -112 ppm for each of the three silicates. The Q^4/Q^3 peak intensity ratios were 0.89, 2.07 and 4.07 for octosilicate, magadiite and kenyaite, respectively. These values were in very good agreement with the values of 1, 2 and 4 expected on the basis of their proposed structure.

The basal spacings calculated for magadiite and kenyaite on the basis of this model (19.14 and 29.18 Å, respectively), however, greatly differed from the observed value of 15.6 and 19.7 Å for the respective layered silicates. This model is therefore inadequate for the description of the magadiite and kenyaite layers, however palatable the empirical trend it offers may be.

Pinnavaia model[147]

An alternative structural model proposed by Pinnavaia *et al.*, depicted in Figure 1.7b, suggests that magadiite (synthetically prepared) be composed of two sheets of silica fused together by the sharing of apical oxygens, with some of the tetrahedra being "flipped over" to point into the interlamellar region, forming the Q^3 sites of the mineral. Such a layer, consisting of five oxygen planes, would have a thickness consistent with the observed 11.2 Å of fully collapsed H-magadiite. Moreover, the Q^4:Q^3 ratio was measured by ^{29}Si NMR to be 3:1, suggesting that one out of every four silica tetrahedra would be flipped.

Rojo model[148]

This model is essentially the same that of Pinnavaia *et al.*, both works having been simultaneously published. The only differences between both studies were that natural magadiite (Trinity County, California) was used here and the relative Q^4:Q^3 ratio was found to be close to 2:1, as measured by ^{29}Si NMR. Thus, they have concluded that 1 out of every three silica tetrahedra in the magadiite layer were flipped, as shown in Figure 1.7c.

Brandt model[149]

Figure 1.7d shows a structural model for magadiite proposed by Brant *et al.* once again suggesting, as in the Schwieger model, that magadiite is composed of three makatite-like sheets fused together. This model does fit quite well with the NMR results (Q^4:Q^3 ratio of 2:1), but, again like the Schwieger model, overestimates the layer thickness, which was calculated according to the model as 12.84 Å.

The structural model proposed for kenyaite, however, fares much better than the preceding Schwieger model,[146] this time consisting of four makatite sheets fused together and resulting in a sheet structure composed of 9 oxygen planes. The layer thickness calculated on the basis of this model was 17.12 Å, which is in good agreement with the observed spacing of fully collapsed H-kenyaite (17.3 - 17.7 Å).[137]

Garcés model[150]

This group has proposed a model based on a zeolite dachiardite framework structure, where the magadiite layer structure would consist of pentagonal rings of silica tetrahedra

fused together as shown in Figure 1.7e. This model was found to give a calculated XRD pattern with a very good match to the experimentally measured patterns, but faltered from the point of view of the relative Q^4:Q^3 ratio which would be 1:1 on the basis of the proposed structure.

Out of the five models proposed for magadiite, the Pinnavaia and Rojo models seem to be the most consistent with all of the experimental data thus far acquired. The Brandt model seems adequate for the description of the kenyaite layer. One must bear in mind, however, that the evidences presented are not by any means sufficient to conclusively demonstrate the actual structure of this class of minerals. Moreover, the variability observed between the ^{29}Si NMR spectra and chemical compositions for different batches of magadiite suggest that, although indistinguishable from the point of view of powder X-ray diffraction, substantial structural permutations can exist between them.[151] The question of the layered silicate structures thus remains open...

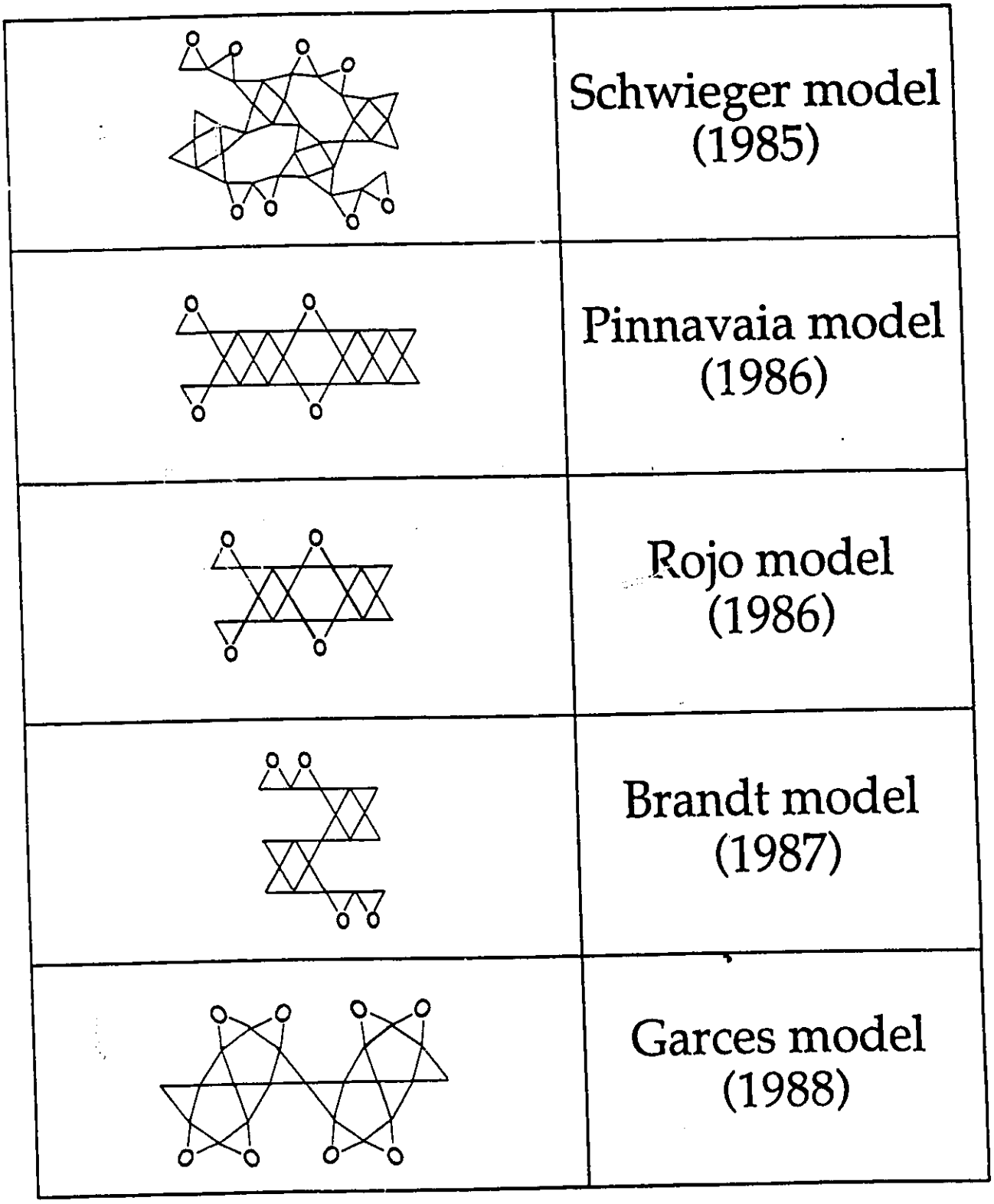

Figure 1.7 Proposed layer structures for magadiite. Triangles represent silica tetrahedra, with oxygens at the apices. Circles denote OH groups (Q^3 tetrahedra).

1.3.3 Interlayer reactions of layered silicates

There has been much interest in studying the intracrystalline reactivity of layered silicates, particularly for the purpose of designing organophilic or microporous minerals. Such reactions may be divided into three categories: ion exchange, intercalation of polar organic molecules and covalent grafting. In this section, reactions performed by these routes will be discussed.

1.3.3.1 Ion exchange reactions

This type of reaction involves the exchange of interlayer alkali metal ions with another cation. The first such reaction performed with magadiite has already been discussed above, namely the exchange with hydrogen ions to produce the layered silicic acid H-magadiite.[138] This process is reversible: treatment of silicic acids with sodium hydroxide restores the parent sodium silicate.

$$\text{magadiite} \underset{\text{NaOH}}{\overset{\text{H}^+}{\rightleftarrows}} \text{H-magadiite}$$

Exchange of organic cations into magadiite was achieved by reacting magadiite with relatively concentrated aqueous or aqueous-ethanolic (10% ethanol maximum) quaternary ammonium cation solutions at pH 7.5-8.0.[135,152] With such a procedure, various alkylammonium, trimethylalkylammonium, dimethyldialkylammonium and alkylpyridinium cations were inserted into magadiite. Such compounds are air-stable, yet generally collapse when washed in water due to exchange for hydrogen ions produced by the dissociation of water molecules.[135]

1.3.3.2 Intercalation of polar organic molecules

Since 1961, potassium acetate and urea were found to expand the layers of kaolinite.[153-156] Similar intercalates were also observed in H-magadiite, the hydrogen-exchanged form of magadiite, using short chain fatty acid amides, urea derivatives, S-oxides, N-oxides and P-oxides.[120,138] What is required for a molecule to be intercalatable in the interlamellar space of silicic acids is its ability to break the hydrogen bonds between adjacent layers: it must therefore have a high dipole moment (>3.5 debyes) and strong hydrogen bond acceptor sites.[120] Bases with $pKb<9$ are often also intercalated, including pyridine derivatives and alkylamines.[120,138] This type of inclusion phenomenon provides the doorway by which covalent grafting of silanes onto the H-magadiite surface can be achieved, as the expansion of the interlayer space makes the hydroxyl groups accessible for reaction. Preferred molecules for such purposes include N-methylformamide (which increases H-

magadiite's basal spacing to 15.9Å), N,N-dimethylformamide (basal spacing = 16.7Å) and dimethylsulfoxide (basal spacing = 15.6Å).[138]

1.3.3.3 Covalent grafting

Grafting of trimethylsilane groups into the interlamellar OH's have been achieved by refluxing trimethylchlorosilane or hexamethyldisilazane (or a mixture of both) with DMSO or NMF magadiite complex in dioxane.[157,158] The resulting material was shown to have an interlayer spacing of 8.2Å (basal spacing = 19.4Å). Other silanes moieties which were grafted in such a manner are $-Si(CH_3)_2CH_2Cl$ and $-Si(CH_2CH_3)_3$. Bulkier groups such as $-Si(CH_3)_2C_6H_5$ and $-Si(C_6H_5)_3$ were found to graft only on the external surface of the mineral, as they were seemingly too large to diffuse into the rather tight interlamellar space.[158] This problem was later remedied by grafting the silanes onto dodecyltrimethylammonium exchanged magadiite, which has a very high basal spacing of 29.4Å, rather than NMF-magadiite:[152,159] in such a way, diphenylmethylchlorosilane was successfully grafted into magadiite.

1.3.3.4 Pillaring

In a manner similar to pillared montmorillonite (section 1.2.2.2), aluminum Keggin ions were intercalated into magadiite and the resulting pillared silicate calcined to produce an aluminum oxide-pillared silicate.[160] Although strongly disordered, the pillared compound

had a surface area comparable to that of pillared montmorillonite (about 260 m^2/g) and proved to be a good solid acid catalyst.

Silica pillared magadiite was also prepared via the condensation of silicate clusters obtained from the hydrolysis of tetraethylorthosilicate.[161] Highly microporous materials were thus obtained (480-670 m^2/g).

In an attempt to control the pore sizes in pillared magadiite, clusters of hydrolyzed phenyltrichlorosilane were grafted to the interlamellar region of H-magadiite.[140] The removal of the organic part of the pillars by calcination afforded a reasonably well-defined pore network, although the lack of uniformity between the pillars precluded the narrow pore size distribution (zeolite-like) network sought for.

2. DESIGN STRATEGIES AND CHARACTERIZATION METHODS OF SORBENTS

2.1 The need for new types of adsorbents

2.1.1 Environmental perspective

Metals as priority pollutants

In today's post-industrial society, there is great public demand and environmental need for finding solutions to the multitude of pollution problems which potentially threaten human health and livelihood. Contaminants of organic (pesticides, petroleum waste, PCBs, etc.) as well as inorganic (heavy metals, mining effluent, etc.) nature are particularly of concern, as they are often ubiquitous in the environment, being rapidly distributed by air, water and through the food chain. Organic contaminants often have relatively short lifetimes in the environment, as they may be subjected to photodegradation and biological metabolization. Inorganic species, however, are permanent nuisances in the biosphere; in fact, some processes which contribute to the natural destruction of organic pollutants may react with metallic ions to produce even more toxic organometallic derivatives. Thus, the only possible solution to the inorganic contaminant problem is the development of new technologies to directly remove the target compounds from the environment.

Origins of metal pollution

The class of inorganic compounds with greatest environmental concern is without doubt that of heavy metals, including mercury, lead and cadmium (among many others). Anthropogenic sources of heavy metal pollution usually involve inefficiencies in industrial

basins treated with base and/or coagulation agents (alum, ferric sulphate or hydroxide, for example).

Currently exploited adsorption technologies for heavy metal removal are principally limited to activated charcoal, which adsorbs relatively low amounts of metal (1 mg/g for Hg at pH 4)[165] and is unselective to the type of metal. The development of more effective adsorption systems are thus of great importance for wastewater treatment.

Government guidelines and goals

The Canadian Federal Government has established in 1977 the following maximum monthly mean concentrations for metal mining liquid effluents: 0.5 ppm for As, 0.3 ppm for Cu, 0.2 ppm for Pb, 0.5 ppm for Ni, 0.5 ppm for Zn and background concentrations for Cd and Hg. These stringent guidelines reflect the public interest in taking aggressive action in order to combat abuse of the environment.

In the United States, current EPA priorities rank waste separation and treatment, respectively, as its third and fourth most important goals, after recycling (second) and waste reduction (top priority).[166] Although reduce-reuse-recycle strategies are well on their way to becoming mainstream in both the private and public sectors, separation and treatment methods are in a continuing state of evolution. The need for the development of such technologies remains a fruitful and highly coveted field.

2.1.2 Economic perspective

Although environmental concerns are the primary concern when it comes to heavy metal recuperation, economic benefits can also arise from such processes. By considering demand growth and the rate of metal reserve depletion, industrial demand for most mined metals are expected to far exceed their known reserves by the year 2100.[167] This makes the development of metal adsorption technologies for the goal of recuperation an economically viable strategy for resource conservation. The reserve depletion rate, with respect to industrial demand, was found to be particularly critical for cadmium, lead, mercury and zinc. In combination with the environmental risk aspect of many of these metals, it becomes evident that the development of adsorption technologies for these four metal species is desirable from both environmental and economic considerations.

Moreover, many rare precious metal catalysts are used by industries, such as platinum, palladium and rhodium. The recovery of these most expensive elements could also be a tenable goal of new adsorbent materials.

2.1.3 Attributes for adsorbents

From the point of view of heavy metals, the ultimate purpose of any adsorption technology is to concentrate the species so that it can be safely disposed of or reused in an industrial process. From both the environmental and economic perspectives, the development of adsorbents for heavy metals is a useful approach to achieve this goal. Such materials would optimally have the following properties:

1. *Strong adsorptivity*: the materials should have the capacity to strongly retain a reasonably large amount of metal per unit mass of adsorbent.
2. *Selectivity*: the materials should bind selectively to certain target metals.
3. *Cost effectiveness*: the materials should be reasonably inexpensive to produce.
4. *Regenerateness*: there should be a way to extract the adsorbed metals and reuse the adsorbent.

In this thesis, the preparation of phyllosilicate-based adsorbents for the recovery of heavy metals will be endeavoured, with a focus on the priority species Hg, Pb, Cd and Zn.

2.2 Phyllosilicates as base compounds for new adsorbents

Minerals such as smectite clays, kaolinite and layered silicates make up a unique family of compounds which are ideal candidates for the design of new adsorbents because of their lamellar structure which bestows on them a much higher surface area than non-lamellar structures of similar dimensions. Since classical surface chemistry principles state that adsorptivity is a function of available surface area, layered minerals have a clear advantage over most other compounds as precursors for new adsorbents (thus in part satisfying criterion 1 from section 2.1.3). Clays are also cheap and abundantly available in nature, making them quite cost effective (criterion 3).

Clays are known to be adsorptive materials towards a myriad of compounds, as was described in Chapter 1. Their intercalation, ion-exchange and grafting properties are well suited for attracting guest molecules into their interlamellar space. By such routes, chemical modification of the minerals can be achieved so that novel materials with vastly improved adsorptive capacities can be developed. These capacities can be tuned such that selective 0adsorption (criterion 2) and strong binding ability (criterion 1) would be promoted by the new materials.

2.3 Strategies for sorbent synthesis

The modification of phyllosilicates in order to produce new varieties of sorbents can follow three pathways, as shown in Figure 2.1.

The first (middle in Figure 2.1) involves the direct ion-exchange of interlayer cations for organic cations, a method which can be used to intercalate specific functionalities in the material and can provide specific interlamellar geometries by tuning the size of the included cation. The major drawbacks of such compounds are their low chemical and thermal stability (included moieties can easily be burned off or leached out of the interlayer space).

The second pathway (left on Figure 2.1) involves the inclusion of polymetallic cations into the structure, followed by calcination to produce metal oxide pillared layered compounds, characterized by large porosities and high thermal stability. The disadvantages of such materials are their lack of well-defined chemical functions, which would preclude them from the rational design of chemically selective adsorbents.

The third pathway (right on Figure 2.1) will be the primary (although not the exclusive) focus of this thesis, involving the covalent functionalization of the smectite interlayers. The general principle behind the preparation of a metal-selective adsorbent by this method involves the reaction of phyllosilicate with a chemical species which can covalently bind to the hydroxyl groups on the minerals layers. Suitable species for this purpose include silanes, which can spontaneously condense onto hydroxyl groups to give a covalent linkage: such grafted species would be impervious to leaching under ambient conditions so that the adsorbent is expected to possess great chemical stability. The grafting

molecule must also bear a functional group which has the desired chelation properties for the selective binding of heavy metal species. Thus, by tuning the functional group, it should be possible to obtain adsorbents with selectivities for distinct metal species.

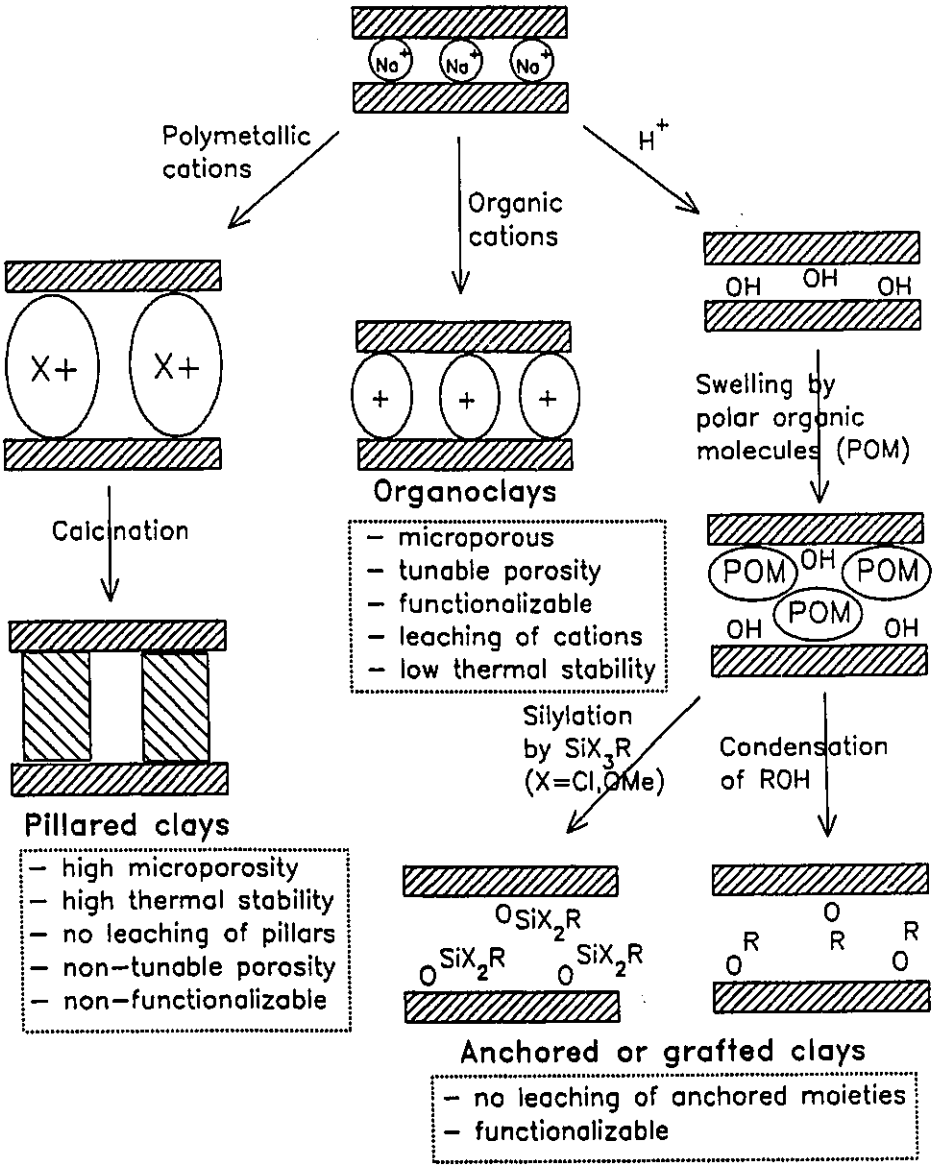

Figure 2.1 Strategies for sorbent synthesis.

2.4 Characterization techniques

In this section, the techniques used to characterize phyllosilicate adsorbents will be presented, including some details about the principle of each method, apparatus description, sample preparation, and data interpretation.

2.4.1 X-ray diffraction (XRD)

Principle

X-rays are a form of high energy electromagnetic radiation characterized by a wavelength of 0.1 to 4.5 Å. Since such wavelengths are within the range of interatomic distances in a crystal lattice, it was found that crystals could serve as grating for the diffraction of X-rays.[168,169] Subsequently, W.L. Bragg found that X-rays of a given wavelength will diffract from a crystal only at certain incidence angles which depended on the wavelength and the distance between the atomic planes in the crystal lattice.[170] This phenomenon has been explained by the reflection of X-rays off parallel atomic planes of a crystal which constructively interfere, producing a diffraction line. Thus, as illustrated in Figure 2.2, X-rays impinging upon a plane undergo reflection at point A, while other X-rays penetrate to a deeper plane and reflect at point B. If the difference between the path lengths of the X-rays reflecting at points A and B is equal to an integral number of the X-ray wavelengths, constructive interference will occur. Similarly, the difference in path length between the X-rays reflected at points A and C must also be equal to integral values of the

incident wavelength. In order to observe a diffraction signal, the following condition must therefore be met:

$$n\lambda = 2d\mathrm{Sin}\theta \qquad (1)$$

where λ is the incident X-ray wavelength, θ the angle of incident X-rays, d the distance separating two planes in a crystal lattice and n an integer. This relationship is known as the Bragg equation.

When n=1, a diffraction line will be observed when X-rays impinge at a certain angle of incidence θ_1 from which the interplanar distance d can be calculated using equation (1): such a line is refered to as the *first order reflection* line. When n=2, another diffraction line (the *second order reflection* line) will occur at an angle of incidence θ_2 , where $\mathrm{Sin}(\theta_2) = 2\mathrm{Sin}(\theta_1)$, from which d can also be calculated. Thus, the X-ray diffraction pattern of a crystal consisting of repeating planes will appear as a series of lines (consisting of the multiple order reflections) appearing at various angles of incidence. For each of these lines, a d value can be calculated using equation (1), *viz.* $d = \lambda/(2\mathrm{Sin}\theta)$ (note that n=1 is always used for this calculation as no *a priori* assignment of the reflection order is being made).

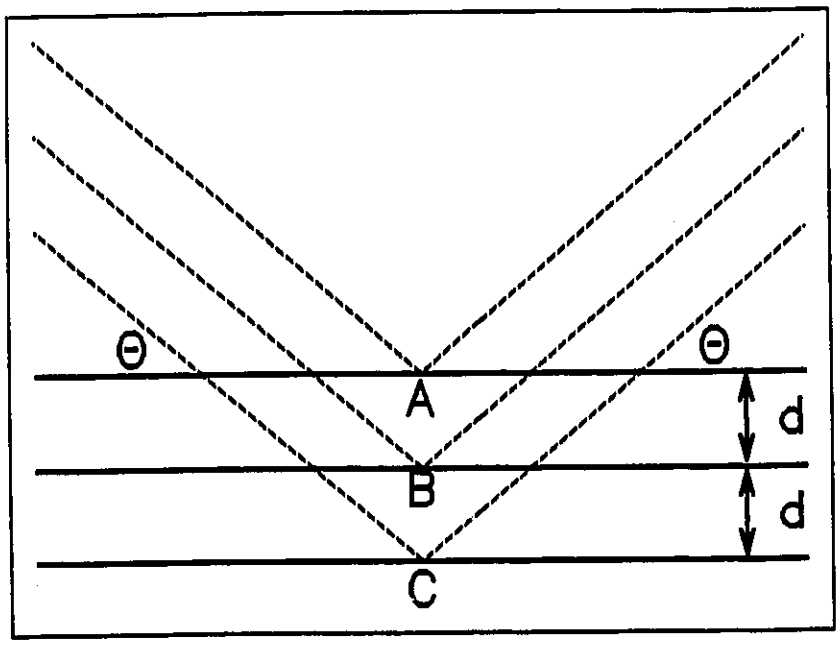

Figure 2.2 Explanation of the Bragg diffraction phenomenon by the reflection of X-rays from different planes of a crystal lattice.

XRD and phyllosilicates

Since phyllosilicates consist of a stacked arrangement of layers, XRD can be used for the determination of the distance between two adjacent layers, also known as the interlayer distance or basal spacing. The first order diffraction line in the XRD pattern of a phyllosilicate is refered to as the d_{001} line and directly gives the basal spacing of the mineral. The second order diffraction line, observed at higher angle of X-ray incidence, is denoted as the d_{002} line. If one were to apply the Bragg equation to the corresponding angle value of this line, one would calculate a d value equal to one half that of the d_{001} spacing (using that n=1 for the calculation). For higher order reflections, the spacings calculated from the resulting d_{00n} lines would therefore be equal to the d_{001} spacing divided by n. The following relationship can thus be written:

$$\text{basal spacing} = d_{001} = 2d_{002} = 3d_{003} = 4d_{004} = \ldots = nd_{00n}$$

From all of the visible d_{00n} lines, it is possible to calculate an average basal spacing value by using the following expression:

$$\text{average basal spacing} = 1/n \sum nd_{00n}$$

An example illustrating the calculation of the basal spacing of a mica is shown in Figure 2.3. Thus, the averaging of all of the d_{00n} contributions permits the calculation of an interlayer distance of 10.2 Å.

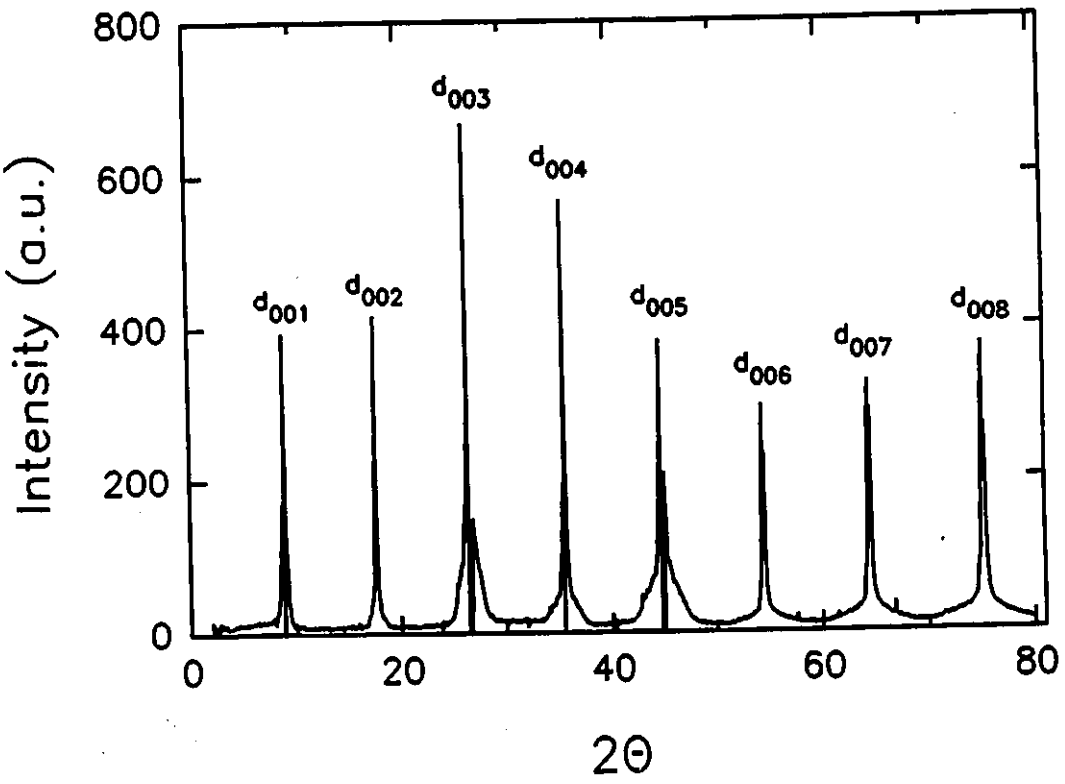

Figure 2.3 XRD pattern for mica, showing the assignments and distances of the multiple reflection orders.

Apparatus

An X-ray diffractometer consists of an X-ray source, a goniometer which measures the diffraction angle and a detector which measures the intensity of the X-rays diffracted off the sample. The source thus shines X-rays on the sample at an angle of incidence θ, while both the sample holder and detector rotate about the goniometer axis at different rates such that the angle between the incident beam and the recorder is 2θ (*i.e.* the recorder rotates at twice the angular velocity as the sample). Figure 2.4 shows a schematic representation of a diffractometer, depicting the way it functions. At θ values that satisfy the Bragg diffraction condition (equation 1), a diffraction peak will be recorded by the detector. The resulting XRD pattern is thus presented as the number of X-ray counts plotted as a function of the angle 2θ.

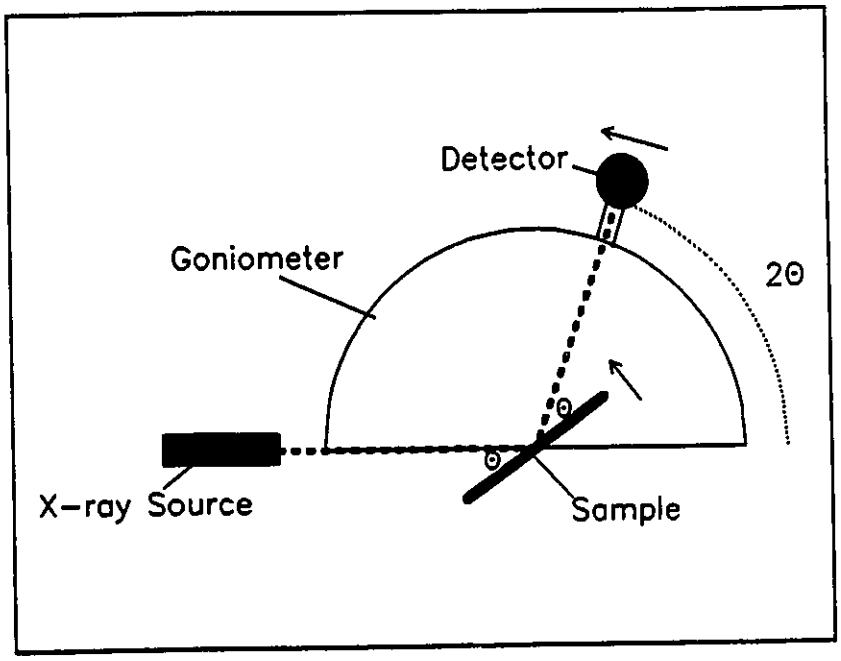

Figure 2.4 Schematic representation of an X-ray diffractometer.

Sample preparation and scanning parameters

Typically, phyllosilicate samples were dispersed in water or other suitable solvents in which the material can be suspended. The mixture was then dropped onto a glass slide and allowed to air-dry. The slide was then mounted to the sample holder of the diffractometer and the XRD pattern recorded from 2θ values of 2 to 50° with a scanning speed of about 3 degrees per minute.

For the case of smectites dispersed in water, the samples were found to have *preferred orientation*, meaning that the clay platelets have settled on the slide such that most of the layers were lying flat (recall the "deck of cards" analogy). This had the effect of enhancing the d_{00n} reflection intensities when compared with samples without such orientations.

In contrast, magadiite samples, having large nodular morphologies, cannot adopt such conformations and do not exhibit preferred orientation. In such a case, the XRD patterns are expected to be identical, regardless of the sample slide preparation method.

2.4.2 Solid-state NMR

2.4.2.1 ^{29}Si NMR

Being the primary element of phyllosilicate minerals, Si is an obvious choice as an "observation centre" for such materials and their derivatives. ^{29}Si NMR spectroscopy would thus be a useful tool in their investigation.

The ^{29}Si nucleus

^{29}Si is a dipolar nucleus (I=1/2) with 4.7% natural abundance and a receptivity with respect to ^{13}C of 2.09.[171] These properties makes the NMR characterization of this nucleus very useful for the study of siliceous compounds, particularly for the probing of the local chemical environments for distinct Si sites in phyllosilicates.

The chemical shifts of this nucleus, measured using neat tetramethylsilane (TMS) reference, range from 0 to -150 ppm. ^{29}Si is a very slow relaxing nucleus with T_1 times ranging from 5 to 150 s. The resonance frequency (referred to the ^{1}H TMS resonance at 100 MHz) is 19.867 MHz.

Two NMR techniques are of particular interest for the study of this nucleus, the first being MAS (magic-angle spinning) NMR and the second being CP-MAS (Cross-polarization MAS) NMR.

MAS NMR

This technique is the basic solid-state pulse NMR experiment, involving a 90 degree pulse to excite the ^{29}Si nuclei and allowing the spin vector to decay while recording the FID of the relaxation process. The pulse sequence of this experiment is shown in Figure 2.5a. Of course, being in the solid state, the studied samples must be spun at the 54.7° "magic angle" so that the solid state spectrum can appear as a high resolution liquid state spectrum.

The MAS NMR experiment would thus give signals whose integration would give quantitative estimation about the relative number of Si atoms residing in every site. Of course, a sufficiently long delay time must be allowed between pulses to permit the complete relaxation of all the nuclei, especially considering the very long T_1 values associated with this nucleus.

CP-MAS NMR

This technique involves the magnetization transfer of ^{1}H nuclei to spatially proximate ^{29}Si nuclei, resulting in the enhancement of their signal intensities as well as hastening their relaxation rate with respect to the more distant nuclei. The pulse sequence of this technique (Figure 2.5b) involves the application of a 90° pulse to both the ^{1}H and ^{29}Si magnetization vectors and both spins are "locked" together by the application of spin locking fields for both nuclei whose magnitudes satisfy the Hartmann-Hahn condition. Under this "matching" situation, the dilute ^{29}Si spins adopt the more favourable spin distribution of the ^{1}H nuclei, resulting in a transfer of the proton magnetization to the nearby Si nuclei.

The common repetition rate in such an experiment is 4 s and thus the CP-MAS spectra of this nucleus will usually show only signals of Si atoms which are close to H atoms (considering that the proton magnetization transfer effect is proportional of the inverse cubic distance between H and Si atoms). Si magnetizations from atoms which are distant from hydrogens will usually not have sufficient time to significantly decay during the 4 s recycle time, and thus such sites would not be seen in the CP-MAS spectra.

The CP-MAS technique can thus be useful in discriminating between various Si sites in phyllosilicates according to their relative proximity to H sources. Thus, the quantitative information obtained by MAS NMR can complement the data obtained by CP-MAS NMR (which can show, for example, Si-OH groups) such that structural information about the compounds can be obtained.

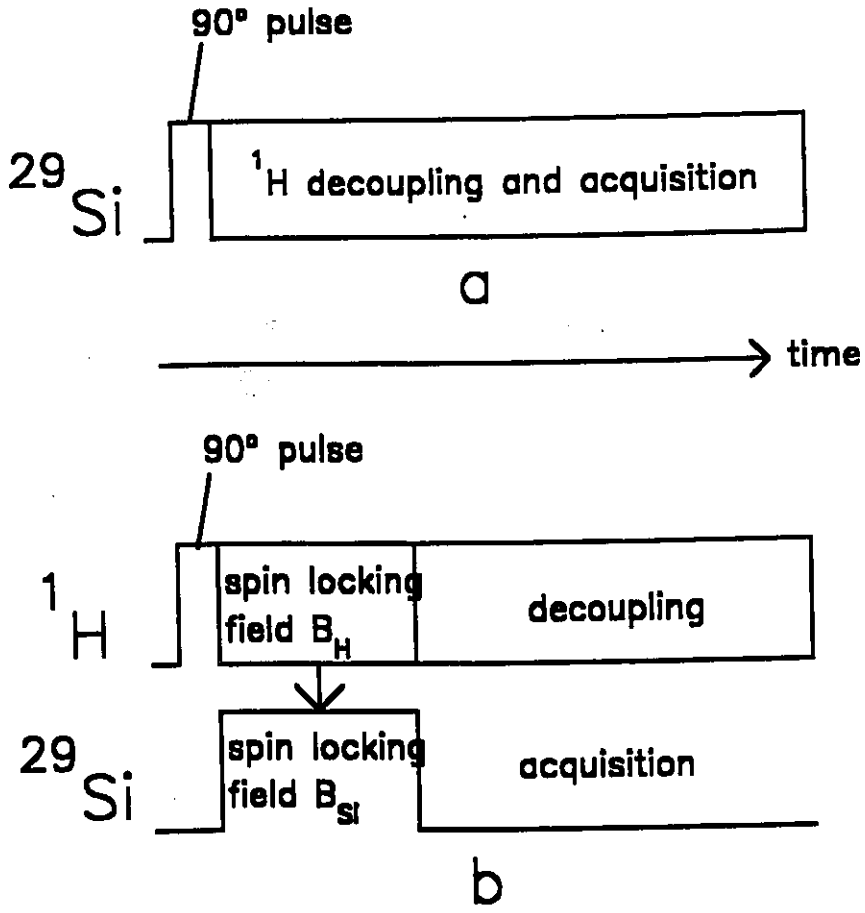

Figure 2.5 Pulse sequences for (a) MAS NMR and (b) CP-MAS NMR

2.4.2.2 ^{13}C NMR

Since modification of phyllosilicates for the preparation of adsorbents involve the inclusion of organic moieties, ^{13}C NMR should be important for the characterization of the nancomposites. The CP-MAS experiment can provide structural data about these systems, while the dipolar dephasing could give dynamic information.

CP-MAS NMR

As was described for the ^{29}Si case, this sequence enhances the signals of carbons which are coupled to hydrogens, especially if these are directly bound to the carbon atoms. Since this is almost always the case in organic molecules, the CP-MAS experiment is the commonly used method for recording ^{13}C spectra, as their signals would benefit from a much greater signal-to-noise ratio with respect to those which would be obtained by MAS NMR alone.

In the context of this thesis, ^{13}C CP-MAS is used as a simple identification tool such that the included or grafted organic species can be unambiguously identified.

Dipolar dephasing NMR

^{13}C-^{1}H dipolar interactions represent an important relaxation mechanism for ^{13}C signals. In the liquid state, such interactions are negligeable due to fast motional averaging. In the solid state, however, the rigid conformations adopted by the C-H bonds can result in a significant dipolar relaxation mechanism for the ^{13}C signals.

This dipolar dephasing pulse sequence (Figure 2.6) is similar to that of CP-MAS, except that a dephasing time is applied between the cross-polarization and acquisition steps. Thus, after the application of the 90° pulse, both spin vectors are locked together for a certain time (usually 1 ms) to allow the $^{1}H \rightarrow ^{13}C$ magnetization tranfer and evolve the ^{13}C signal typical of the regular CP-MAS experiment. Following this step, the spin locking fields are turned off for a period of time (called the *dephasing time*, usually in the order of 0 to 100 μs), during which the ^{13}C magnetization is attenuated by the C-H dipolar interactions. The subsequent acquisition step would result in a spectrum with ^{13}C signals with diminished intensities when compared to that of a standard CP-MAS spectrum (without dipolar dephasing). Thus, more rigid molecules would be expected to have greater signal attenuation than more mobile ones. The ^{13}C dipolar dephasing experiment is therefore useful for monitoring the rigidity of organic molecules in the solid state.

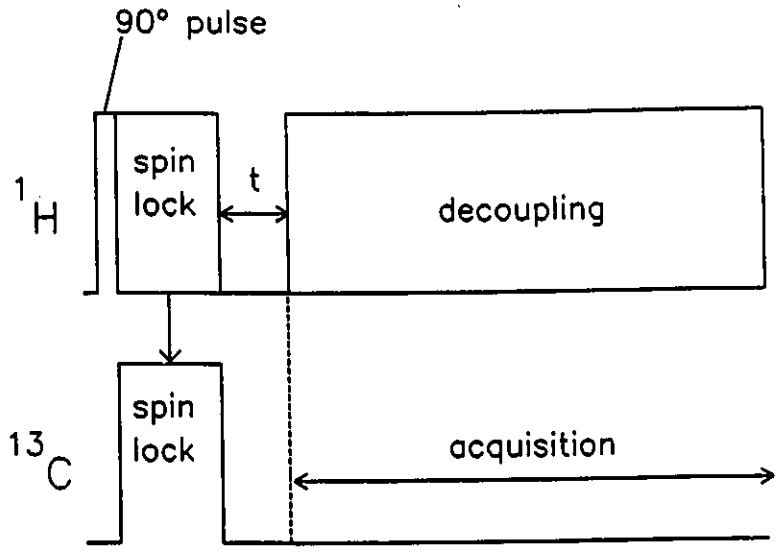

Figure 2.6 Pulse sequence for dipolar dephasing ^{13}C NMR.

2.4.3 Thermogravimetric analysis (TGA)

This technique is used to monitor the thermal behaviour of compounds. A sample of the studied material (about 10-20 mg) is heated in an alumina crucible from room temperature to 1200 °C, typically at a heating rate of 20 °C per minute. The mass of the sample can then be plotted as a function of the temperature to give the TGA profile of the material.

From the obtained curve, quantitative estimates of the various volatile phases can be made. The thermal stability of the material can also be evaluated on the basis of the TGA profile.

2.4.4 Infrared spectroscopy

Samples are typically prepared in the form of KBr pellets. Thus, a 0.5% mixture of the compound with dry FTIR grade KBr (Aldrich, stored in a desiccator) is finely ground and pressed into a pellet (5 mm diameter, 0.5 mm thickness) using a manual KBr press. The pellet is then mounted on a sample holder and the FTIR spectra recorded from 400 to 4000 cm^{-1} using 10 scans at a resolution of 4 cm^{-1}.

FTIR spectroscopy is typically used to identify key functional groups present in the sample.

2.4.5 Particle size analysis

Particle size analysis (PSA) uses the principle of sedimentation in order to determine the diameter of particles in a suspension. Thus, Stoke's law can be applied to relate the diameter D of a spherical particle to its velocity v as it sinks through a fluid medium by the action of gravitational force (the "sinking velocity"):

$$D = [(18\ \eta\ v)/(g\ (\rho-\rho_0))]^{½}$$

where η is the viscosity of the fluid, ρ_0 the density of the fluid, ρ the density of the particle and g the acceleration of gravity. In practice, however, particles are not usually spherical and can adopt a large variety of irregular shapes: this is especially true for smectites, whose particles have lamellar morphologies. The diameter of the above equation thus refers to the "Stoke's diameter" or "equivalent spherical diameter" for such particles, representing the mean diameter of a sphere which would be composed of the same material and that would have the same mass as the particle in question.

The velocity v can be further expressed as the distance h fallen by the particle during a period of time t, and the Stoke equation can be reformulated as:

$$D = [(18\ \eta\ h)/(g\ t\ (\rho-\rho_0))]^{½}$$

Thus, after a time t, all the particles larger than the corresponding diameter D will have fallen below a given distance h. This principle thus permits the relation between the sedimentation time t_i and the mass concentration C_i of particles with diameters inferior to D_i, as measured from a fixed distance h from the surface of the suspension. The weight percent (P_i) of particles finer than D_i can be expressed as

$$P_i = 100\ (C_i/C_0)$$

where C_0 is the inital concentration of the material (at t=0).

In the particle size analysis experiment, a suspension of a material is allowed to settle in a cell through which a collimated X-ray beam is passed (at a fixed position). The intensity of the X-rays is reduced as they pass through the suspension and the X-ray transmittance T_i can be related to the particle mass concentration C_i in the beam's path. Thus, the particle size distribution can be expressed as

$$P_i = 100\ (\ln T_i / \ln T_0)$$

where T_0 is the X-ray transmittance of the initial suspension.

The P_i values measured by X-ray transmittance can therefore be plotted as a function of the D_i values obtained from the sedimentation time to give the particle size distribution graph for the studied material. This is most often presented as a cumulative mass plot, where the percentage of particles with larger mass is plotted as a function of particle size.

The percentage of particles found in different size intervals can likewise be determined. The use of X-rays as scattering light in such an experiment can permit the particle size analysis of materials with an equivalent spherical diameter range of 100 to 0.1 μm.

2.4.6 Elemental analysis

2.4.6.1 X-ray fluorescence

Principle

High energy X-rays can interact with atoms and cause core electrons to be ejected from the irradiated atoms. Electrons from higher energy levels can then drop to fill the vacant core electron site by process of fluorescence, thus releasing a photon of energy equal to the difference in both energy levels. This emitted photon (in the X-ray part of the electromagnetic spectrum) is expected to have an energy which is characteristic of the element from which it came. This is the basis of X-ray fluorescence spectroscopy.

Sample analysis

The sample to be analyzed (about 100 mg, finely ground) is packed in a cuvette and broad-range X-ray radiation is shone upon it. The fluorescence radiation emitted from the sample is then detected by scanning the range of frequencies where the fluorescence peaks of the elements in the sample are expected. The intensities of the observed peaks (each representing a given element) can then be related to the relative concentration of that element

in the sample. XRF can only detect elements of atomic number 13 (Al) or higher since smaller elements do not exhibit sufficient fluorescence characteristics to be detectable.

This technique thus gives the relative molar ratios of the different elements detected in the sample, providing that each studied element has first been referenced to samples of precisely known composition containing that element. For the analyses of the compounds prepared in this thesis, Si, Al, Pb and Fe were referenced to their oxides (99.999%, Aldrich), S to the elemental form and Cl to NaCl (99.999%, Aldrich).

A complicating factor in XRF analysis is the occurence of *matrix effect*. Thus, the presence of a certain element in a sample can sometimes alter the signal of another in the same sample by adsorbing some of its emitted fluorescence energy. Matrix effects can be compensated by adding the culprit element to the reference standard so that the resulting mixture can "mimic" the composition of the sample. In the case of the phyllosilicate materials studied in this thesis (see Chapter 3), a matrix effect was observed when carbon was present with silicon whereby the Si content became seriously underestimated. In order to counteract the effect, leucine was added to the SiO_2 standard, which resulted in a corrected estimation of the Si content.

2.4.6.2 C,H and N analyses

Standard C, H and N analyses can be performed on the samples to quantitate the amount of grafted organic species in the adsorbents. Since combustion is the chemical process used to isolate these elements for detection (the C,H and N in the sample is burned off into CO_2, H_2O and N_2), such analyses become complicated by the formation of residual black carbonaceous residues in the sample which can be attributed to moieties in the interlayer space of the phyllosilicates which are inaccessible to combustion. This effect can be minimized by adding to the sample copious amount of tungsten oxyde (WO_2) as an oxidant to aid the combustion of the interlayer organic species.

2.5 Synopsis of sorbent design approach

The working strategy of this thesis is the generation of adsorbents through the covalent anchoring of functional groups onto the interlamellar surface area of phyllosilicate minerals (specifically, smectites and layered silicates). The grafted groups would be selected on the basis of their chemical reactivity towards particular target species which may be of environmental concern. Chelating functionalities, for instance, would be suitable for the generation of adsorbents which may be used for the capture of heavy metals.

Thus, a suitable organosilane would be grafted to the hydroxyls present on the interlamellar surfaces of the phyllosilicate species. The organic part of the anchored moiety would then be functionalized with a chemical unit tuned for the selective adsorption of toxic molecules such as heavy metals. Alternatively, the thermal condensation of alcohols to these hydroxyls could be considered as an alternative means of preparing such adsorbents.

Phyllosilicates are useful base compounds for the design of such adsorbents since they have large accessible surface areas and thus have the potential of generating microporous structures upon the inclusion of guest species in the interlamellar region.

3. SMECTITE SORBENTS

In this chapter, the preparation, characterization and applications as adsorbents of chemically modified smectites will be discussed. Although the main focus of this chapter will be on the grafting of functional units with the purpose of designing heavy metal adsorbents, some discussion about the ion exchange of ammonium cations will also be featured, along with some of their potential applications.

3.1 Purification of smectites

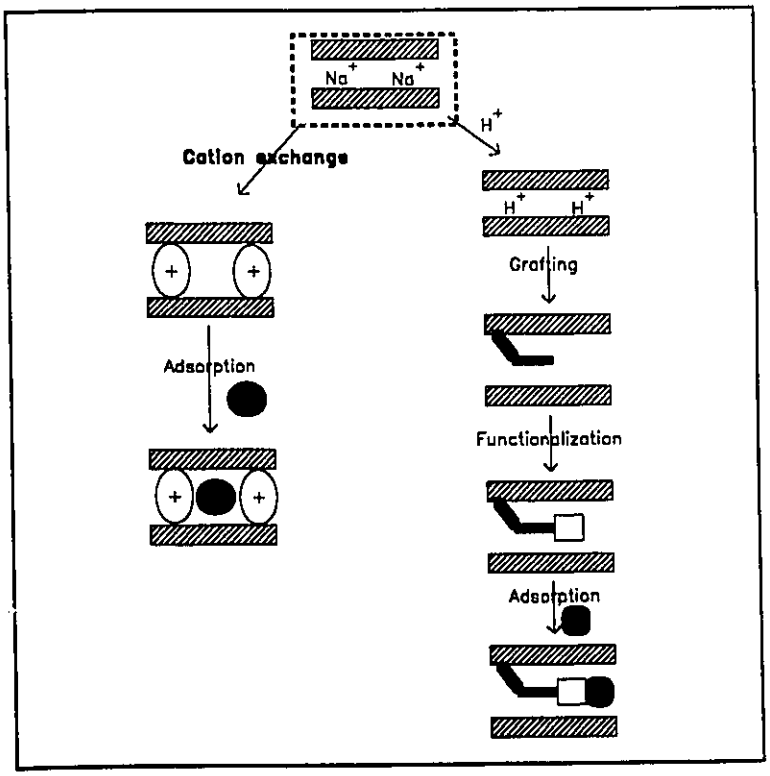

3.1.1 Method

The purification procedure for smectites involves the following steps: (1) sedimentation to recover the finer clay particles ($< 2.0\ \mu m$) and eliminate mineral impurities (sand, gravel etc.), (2) homoionization with sodium chloride to produce a fully sodium-exchanged clay, and (3) isolation of the purified material by dialysis to remove excess salt followed by freeze-drying. In this section, the purification and characterization of the following smectites were performed: SWy-1 (Clay Spur, Wyoming), SHCa-1 (San Bernadino, California), STx-1 (Llano, Texas) SAz-1 (Cheto, Arizona), SCa-3 (Otay, California) and SWa-1 (Grant County, Washington). Each of these smectites were obtained from the Clay Source Repository of the University of Missouri and all belonged to the montmorillonite mineral sub-group except for SHCa-1 (hectorite) which is formally classified in the saponite sub-group.

Sedimentation

30 g of crude smectite were stirred for 18 hours in 400 ml of distilled water with a mechanical stirrer. The pH was adjusted to 10 (NaOH 0.1 M) then carefully acidified to pH 3.5 (HCl 1 M) in order to destroy carbonates. This process often resulted in a significant thickening of the solution so that the addition of water was needed to make the suspension stirrable (up to a total volume of about 800 ml). The suspension was then centrifuged, the supernatant liquid discarded, and the clay washed and centrifuged one or two times with dilute HCl (pH 3.5). The clay was then redispersed with about 800 ml distilled water in a 1 L beaker and the pH elevated to 8 (NaOH 0.1 M). The suspension was left to stand for

24 hours on a vibration-free surface, thus allowing the large particles to settle to the bottom of the beaker. The suspension was then siphoned into an erlenmeyer flask until the level of the suspension was about 3 cm from the bottom of the beaker, thus preventing the recuperation of the large sedimented particles. The remaining suspension in the beaker was redispersed with water (for a total volume of about 800 ml) and once again allowed to settle overnight, after which the supernatant suspension was collected and added to the first collection.

Homoionization

The fine clay fraction obtained by the above sedimentation step was acidified to pH 3.5 (1 M HCl) and 200 ml of saturated NaCl solution were added. The mixture was allowed to stand until significant flocculation of the clay was attained (24 to 48 hours) and a fully sodium-exchanged smectite was obtained. The supernatant liquid was decanted prior to proceeding with the dialysis step.

Isolation

The NaCl-clay suspension mixture was tranfered into dialysis bags (molecular weight cut-off 12000-14000) and put in a bath of distilled water. The water was replaced with fresh distilled water 3 or 4 times a day for a period of about 1 week, until the wash water tested negative for chloride ions (using the silver nitrate test).

The contents of the dialysis bags were then transfered into a lyophilization flask, frozen onto its sides by means of an acetone-dry ice bath, and freeze-dried under vacuum for 72 hours to give purified flakes of homionic Na^+-smectites.

3.1.2 Characterization

Particle size analysis

The particle sizes of the smectites were determined for both the crude and the purified clays, the cumulative mass plots being shown in Figure 3.1. The effectiveness of the sedimentation process is clearly demonstrated by these plots since in all cases the particle sizes of the purified smectites were considerably smaller than those of the crude clays. Moreover, the target 2 μm maximum particle diameter was achieved in all cases (except for SAz-1) with, in the cases of STx-1, SCa-3 and SWa-1, most particles being much lower than this threshold.

X-ray diffraction

The XRD patterns for smectites were all very similar to each other, essentially featuring only rather broad d_{00n} reflections, as exemplified in Figure 3.2 for the case of SWy-1. This attests to the turbostratic disorder of these minerals, as only the peaks resulting from the c-axis reflections are seen in the XRD pattern. Some quartz impurities were found to remain in the sample, despite the careful sedimentation process.

The basal spacings were between 12 and 13.5 Å, which corresponded to an interlayer distance of 2.4 to 3.9 Å resulting from the hydrated interlamellar region of the smectites.

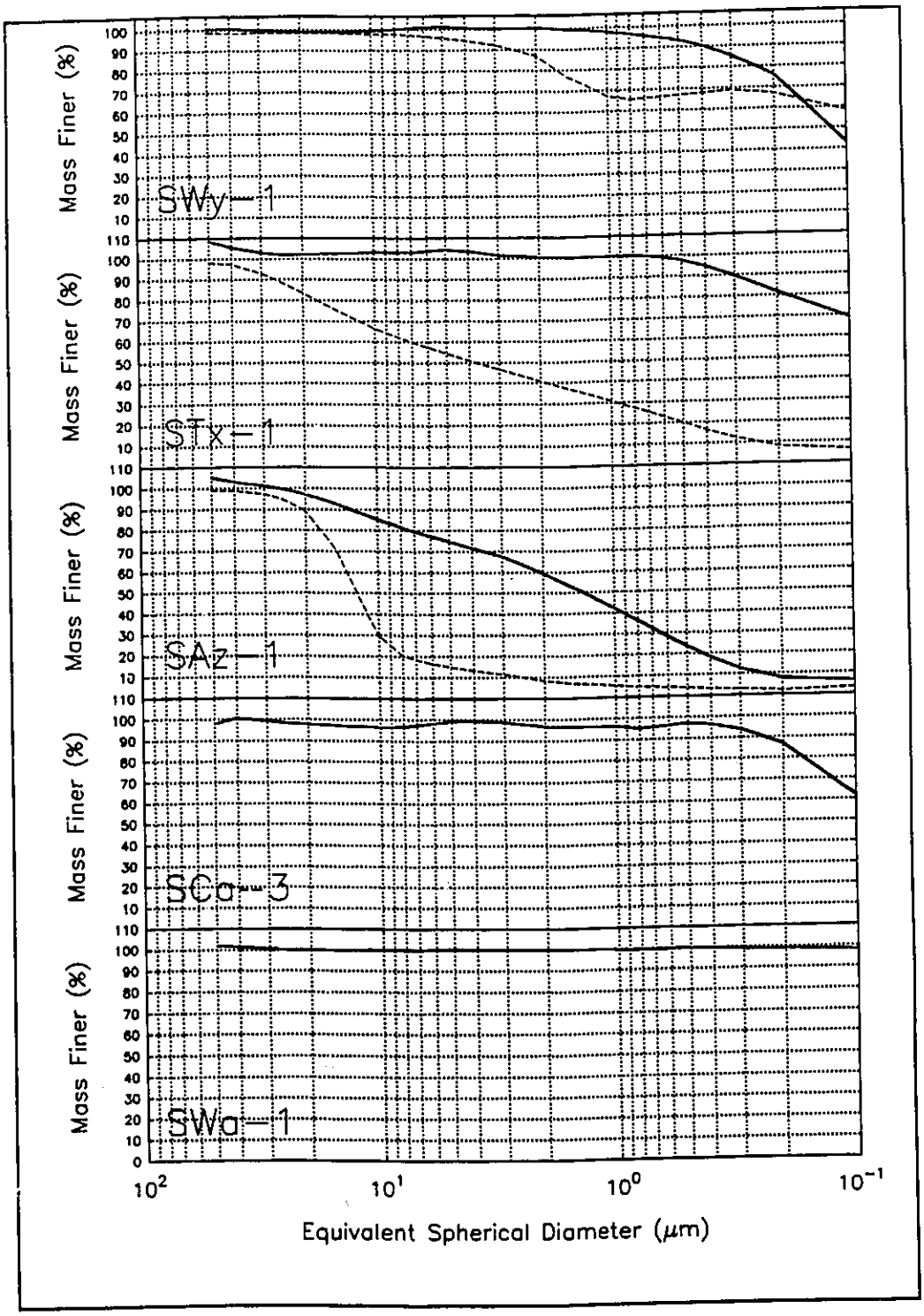

Figure 3.1 Particle size analyses of smectites. Dashed lines denote crude and solid lines purified clays.

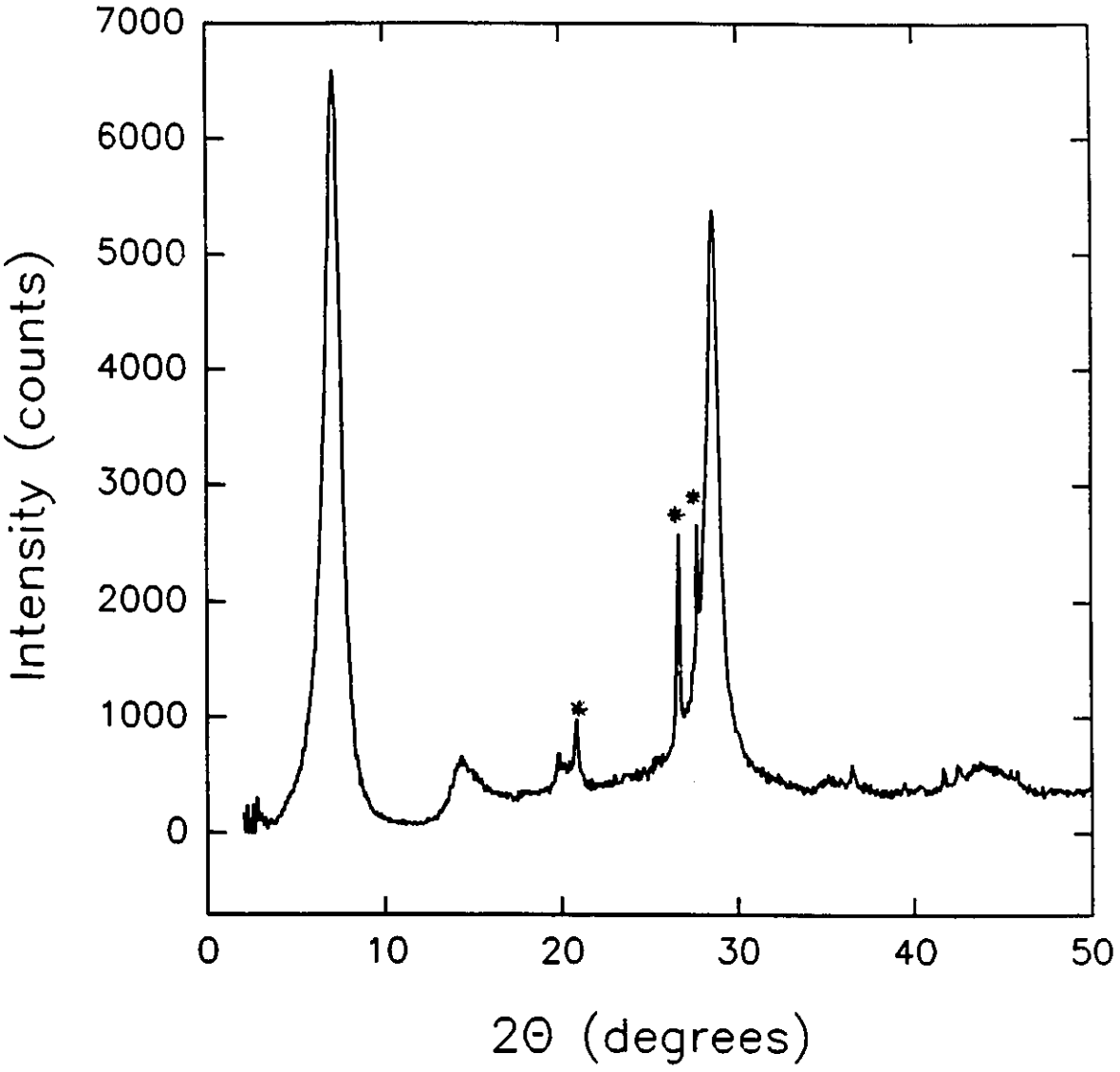

Figure 3.2 XRD pattern for SWy-1 (Asterisks denote quartz impurities).

Infrared spectroscopy

The FTIR spectrum for SWy-1 (Figure 3.3) featured the Si-O-Si vibrational modes between 400 and 1200 cm^{-1}, the water modes at 1630 and 3436 cm^{-1} resulting from the hydrated interlamellar region, and the OH stretching mode at 3630 cm^{-1} attributed to the Al-OH structural units of the smectite.

Thermogravimetric analysis

The TGA curve for SWy-1 (Figure 3.4) featured a 6% mass loss between 60 and 120 °C characteristic of the removal of interlayer water from the structure. This observation corresponds to the collapse of the basal spacing to 9.6 Å when smectite samples are heated beyond 120 °C. A 3% loss is also seen between 610 and 700 °C resulting from the condensation of structural hydroxyl groups inside the clay layer and is consistent with the chemical formulation of SWy-1.

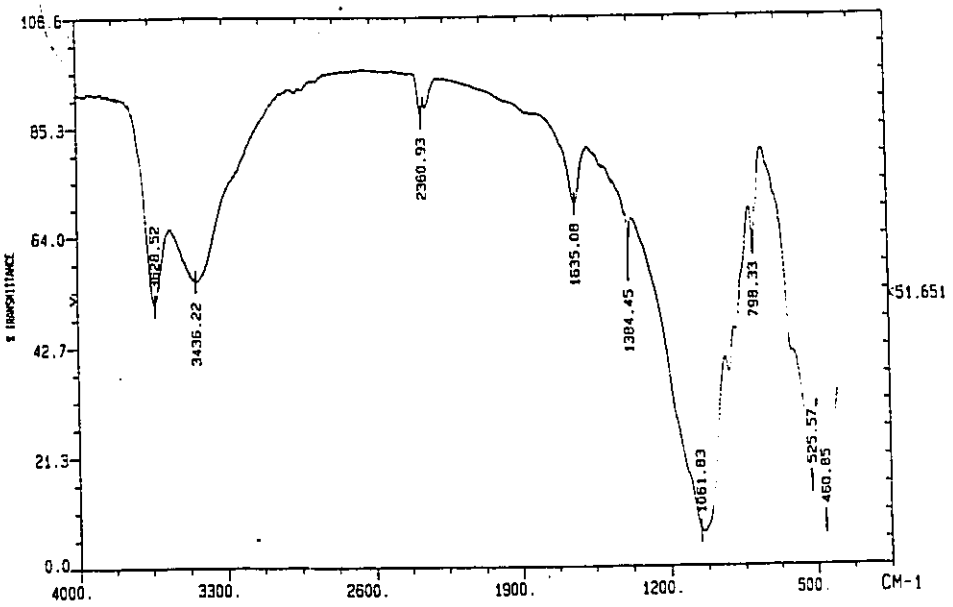

Figure 3.3 FTIR spectrum of SWy-1

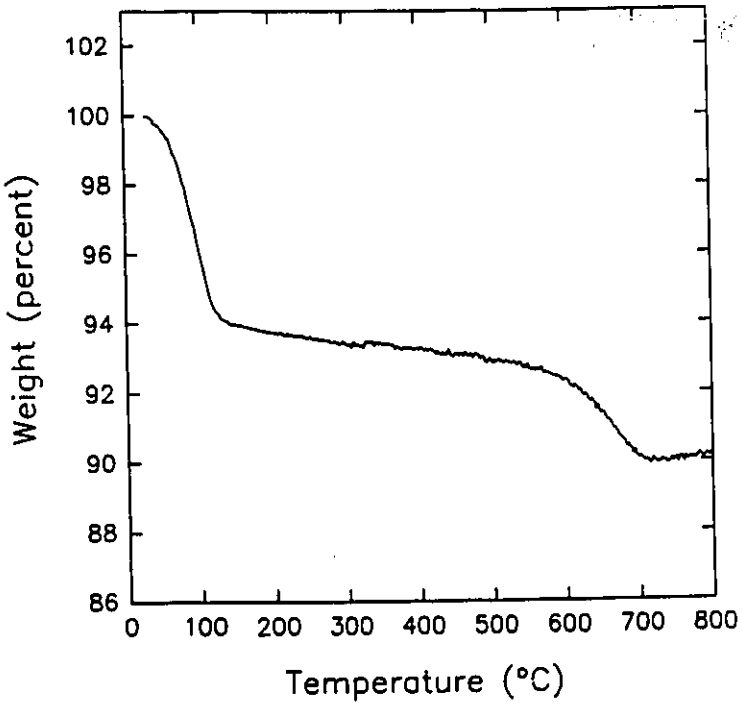

Figure 3.4 TGA curve of SWy-1.

Cation-exchange capacities (CEC)

CEC values for the various clays were determined by the sodium desorption method. Thus, a series of NaCl solutions were prepared ranging from 0.1 to 1.0 mM. A Na^+ electrode was used to measure the potential of each solution. From these results, a standard plot was made relating log [Na^+] to the measured voltage. Tetramethylammonium iodide (TMA, 0.4 mmole) was added to 0.1 g of each clay (accurately weighed) and 50 ml of water was added. The suspension was stirred for 48 hrs at room temperature and centrifuged. 25 ml of the supernatent was diluted with 50 ml water and the potential was measured with the sodium electrode. Using the standard plot, the quantity of Na^+ released from the clay by cation exchange was determined and the CEC calculated. The above procedure was repeated using tetrapropylammonium iodide (TPA) to verify whether or not the exchange was dependent on cation size. Table 3.1 gives the values found for the studied smectites. The CEC values measured by TMA displacement were found to be consistent with those of the literature. Those values measured by TPA displacement, however, were found to be significantly smaller for the higher charge smectites (SCa-3 and SAz-1). This phenomenon will be discussed in greater detail in section 3.2.1.

Table 3.1 Cation exchange capacities for studied smectites.

Smectite	CEC(meq/g) literature values[172]	CEC measured by TMA displacement	CEC measured by TPA displacement
SWy-1	0.79	0.83	0.75
STx-1	0.80	0.85	0.60
SHCa-1	0.46	n.d.	n.d.
SWa-1	n/a	1.04	n.d.
SAz-1	1.20	1.26	0.53
SCa-3	1.53	1.70	0.70

3.2 Ion exchange in smectites

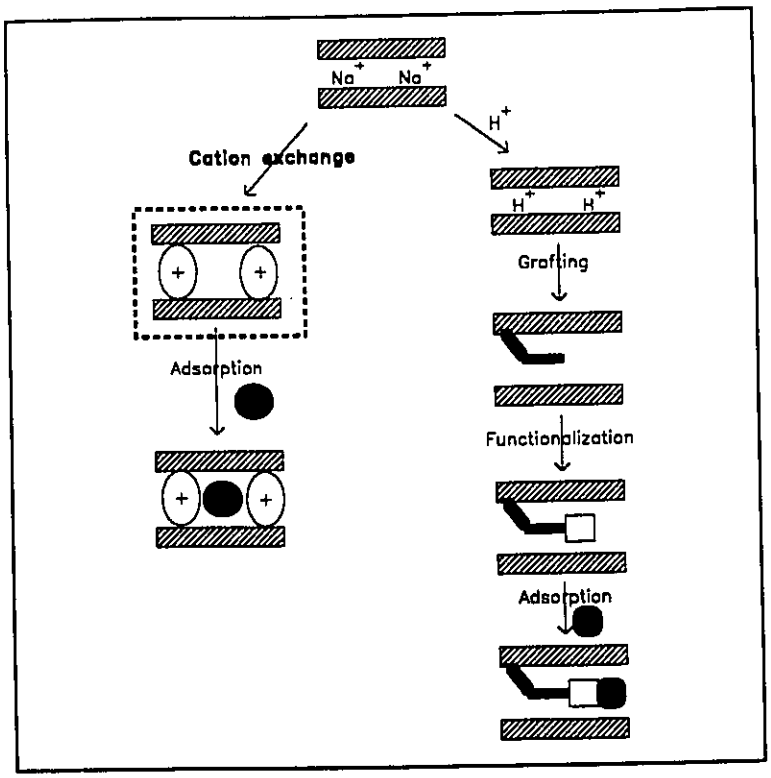

This type of inclusion reaction is by far the most studied and widely used method for the preparation of organoclay derivatives. Although the main scope of this thesis involves the *covalent* fixation of organic species on the surfaces of layered minerals, some studies have been performed in order to further explore the nature of alkylammonium cation intercalation into smectites.

3.2.1 Tetraalkylammonium smectites

Preparation

To 0.1 g samples of clay were added about 0.4 mmol of each tetraalkylammonium salt (bromide or iodide) (ranging from tetramethylammonium to tetraoctylammonium) and about 40 ml of a 70% methanol/water mixture. The samples were stirred for 48 hrs at room temperature and centrifuged, discarding the supernatant liquid. The samples were then washed and centrifuged several times with 70% methanol in order to remove cation adsorbed in excess to the clays' CEC and air dried.

X-ray diffraction

The organoclays were suspended in methanol and spread out on glass slides for XRD analysis. Figure 3.5 shows the interlayer distances for the tetraalkylammonium-smectites, calculated by averaging all of the visible d_{00n} contributions on the diffraction pattern [i.e., $d = (d_{001} + 2d_{002} + 3d_{003} + \ldots + nd_{00n})/n$] and subtracting 9.6 Å (the thickness of a smectite layer).

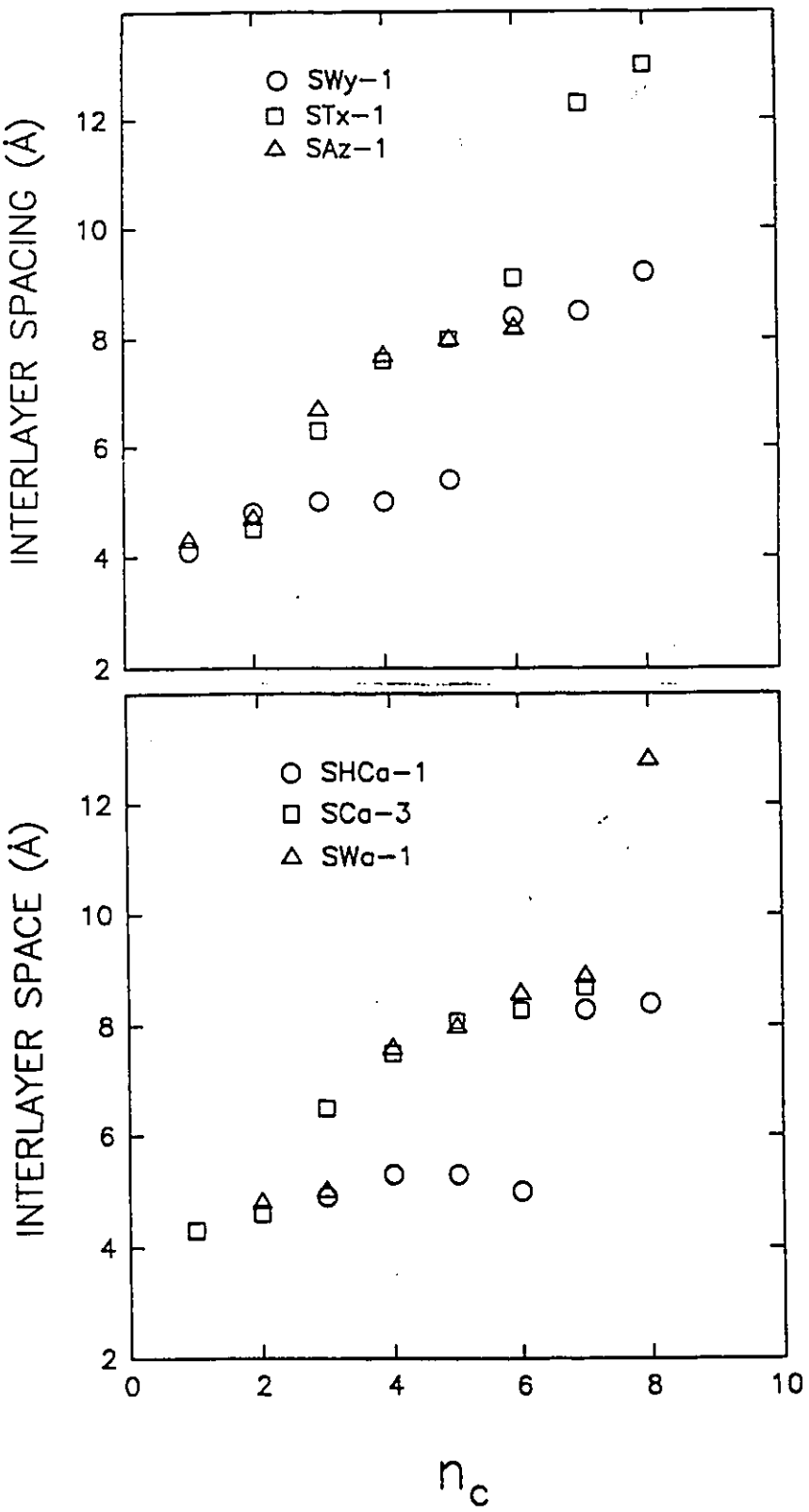

Figure 3.5 Interlayer distance of various organo-smectites as a function of the number of carbons, n_C, of the alkyl groups of intercalated tetraalkylammonium $[^+N((CH_2)_{n-1}CH_3)_4]$ cations.

In most cases, the interlayer spacing increased slightly as larger tetraalkylammonium ions are intercalated. Eventually, a sudden jump in the spacing from 4-5 Å to 8-9 Å is observed which can be attributed to the transition from a monolayer to a bilayer arrangement of the exchanged cations (henceforth denoted as the MTB transition) caused when the intercalated molecules become larger than the area covered by a unit charge on the clay surface. This situation is depicted in Figure 3.6. In the case of SWa-1, a second transition can be observed between n_c=7 and 8 which can be assigned to the formation of a trilayer (or pseudotrimolecular) arrangement of cations from the bilayer state (henceforth denoted as the BTP transition, or bilayer to pseudotrimolecular).

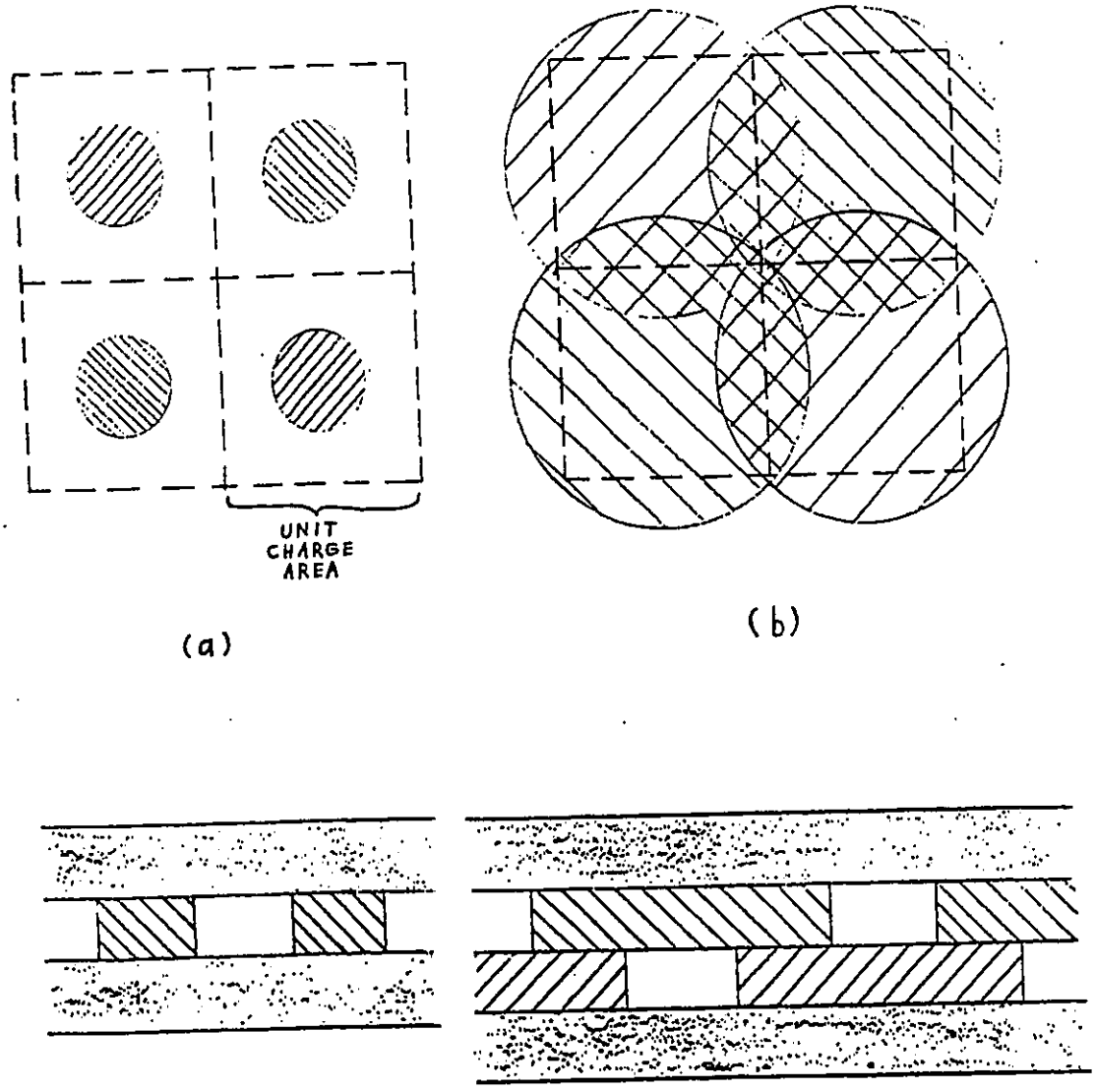

Figure 3.6 Representation of top and cross-sectional views of smectites intercalated with (a) cations smaller than the unit charge area (monolayer situation) and (b) cations larger than the unit charge area (bilayer situation).

Surface area measurements

An important characteristic of smectites with regard to their intercalation properties is the area covered by the interlamellar regions of the clays, known as the internal surface. The current means of measuring the internal surface of expandable clays is by glycerol sorption,[173] a method which involves treating a clay sample with a 10% glycerol solution and heating this smectite complex in a thermoanalyzer at 1°C/min until a region of constant weight is reached. At this point, it is assumed that a stable saturated monolayer glycerol complex exists and, knowing the mass of glycerol adsorbed and the surface area covered by each molecule, the total surface area of the smectite may be calculated. BET measurements using nitrogen on a sample of the same clay must then be done in order to determine the external surface of the clay particles. The internal surface S_i can then be calculated by subtracting the external surface from the total surface. A simpler and quicker method of determining the internal surface (S_i) of smectites can be postulated from the intercalation of tetraalkylammonium cation into their interlamellar regions.

Since tetraalkylammonium cations force an interlayer spacing of 4-5 Å when they assume a monolayer configuration in the smectite interlayers, it can be assumed that they assume the flattest configuration possible, such that the alkyl chains lie parallel to the clay layers due to the compression between the lamellae.[22] Using molecular scale CPK models, the volume of the tetraalkylammonium cations can be determined, from which the surface area covered by their "flat" conformation can be calculated (by dividing the volume by 4.1 Å, the interlayer separation conferred by tetramethylammonium cations). The following

empirical relationship can thus be derived from the measured surface areas, relating the area covered by a tetraalkylammonium cation to the number of carbons in the molecule:

$$\text{Cation area } (A_C) = n_C \times 26 \text{ Å}^2 \tag{3.1}$$

where n_C is the number of carbons in each alkyl chain of the cations.

Thus, as the cations inserted into the clay interlayers get progressively larger by increasing the chain lengths, so does the surface area covered by the alkyl chains within the interlamellar space. At a certain point, the total surface coverage of the cations will exceed that of the available interlamellar space (internal surface) and the monolayer to bilayer (MTB) transition will occur. As even larger cations are inserted, the bilayer to pseudotrimolecular (BTP) transition will be observed, when the total cation area exceeds twice that of the internal surface.

The point of the MTB transition must, therefore, correspond to an organically saturated interlamellar space. In other words, each cation covers the surface area corresponding to a single charge on the clay layers. This surface is known as the unit charge area (S_c) and can be expressed as a function of the internal surface and the CEC by the following relationship:

$$S_C = 1000\, S_i / (\text{CEC}\, N_A) \tag{3.2}$$

where CEC is expressed in mmol/g, S_i in m^2/g, S_C in m^2/eq and $N_A = 6.023 \times 10^{23}$ mol^{-1}.

When observing a MTB transition, the value of S_c must be located between the last monolayer and first bilayer points. The value S_{mb} represents the middle area between these points, where the internal surface would theoretically be entirely covered by the cations. Taking into account that each interlayer cation touches two smectite layers, the following equality exists at full surface coverage: $S_c = S_{mb}$. Thus, S_{mb} may be related to the internal surface by rearrangement of equation 3.2:

$$S_i = CEC \times N_A \times S_{mb} / 1000 \qquad (3.3)$$

The internal surface may likewise be calculated using the BTP transition area, defined as S_{bp}, using the following equation:

$$S_i = CEC \times N_A \times (S_{bp}/2) / 1000 \qquad (3.4)$$

Analogous equations relating cation size, layer charge and smectite surface area were derived using n-alkylammonium cations.[174] In that work, those equations were used to calculate the interlayer charge density using given unit cell parameters and organic cation surface areas. In this study, the reverse was done, the surface areas of the clays being determined by using the the surface areas of intercalated cations and known interlayer charge (considered as being close to the CEC values).

The XRD data of the smectites exchanged with tetraalkylammonium cations (Figure 3.5) showed in most cases evident MTB and BTP transitions with which the internal surfaces

of the smectites could be measured, as shown in Table 3.2. These gave results for SWy-1, STx-1 and SHCa-1 which were in excellent accordance with those obtained from the literature. The measurements for the high charge smectites (SAz-1 and SCa-3), however, had considerable uncertainties in their values and, in the case of SAz-1, did not concur with the previously determined value.

The theory behind the method follows two important assumptions: (1) that all of the exchangeable interlayer sodium cations be replaced with the organic cations of each tetraalkylammonium species (100% exchange), and (2) that the cations be placed in a homogeneous manner within the clay layers.

Table 3.2 Internal surfaces for smectites (in m^2/g). The CEC values used for the calculations were those obtained from TPA exchange, except for SHCa-1 and SWa-1 which used 0.46 and 1.04 meq/g respectively. For SAz-1 and SCa-3, the TMA exchange values were used, for these transitions occurred before the TPA insertion.

Smectite	S_{mb} ($Å^2$)	S_{bp} ($Å^2$)	Calculated S_i	Literature S_i[173]
SWy-1	143 (13)	-	646 (59)	662 (22)
STx-1	169 (13)	-	611 (47)	599 (24)
SHCa-1	169 (13)	-	468 (36)	486 (12)
SWa-1	91 (13)	98 (7)	611 (44)	n.d.
SAz-1	65 (13)	-	493 (99)	820 (18)
SCa-3	65 (13)	-	670 (130)	n.d.

The first assumption was found to be correct in the case of SWy-1, where it has been shown that cation exchange is complete or nearly complete up to the tetraoctylammonium cation.[175] In SAz-1 and SCa-3, however, the cation exchange drops dramatically from the TMA cation to the TPA cation (see Table 3.1). It has indeed been reported that the reactivity of clays with tetraalkylammonium cations decreases with increasing clay layer charge.[47] The large tetraalkylammonium cations thus do not completely exchange the interlayer sodium of high charge clays.[176,177] The proposed method is, therefore, not reliable for high charge smectites (CEC > 1.20 meq/g) such as SAz-1 and SCa-3.

The second assumption is not quite factual, since charge heterogeneity exists in the clay structure because of uneven isomorphic substitutions in the clay layers. A consequence of this is that with insertion of progressively larger alkylammonium cations (of type $R\text{-}NH_3^+$), no sudden MTB or BTP transitions are observed but rather a gradual increase in the interlayer distance is seen in the transition zone.[35-37,39-49,174,178-181] The very sharp transitions of the tetraalkylammonium smectites suggest that the effect of charge heterogeneity is negligible for these species, since the size increase from one such cation to the next larger is much greater than the size increase from one n-alkylammonium cation to the next. An exception to the previous statement is seen in the case of STx-1, where the interlayer space increases very rapidly as the inserted cations get larger, presumably because the very high charge heterogeneity of the smectite results in the agglomeration of cations. The MTB transition for the STx-1 system is assumed to occur at the tetraheptylammonium cation, as this corresponds to the only appreciable jump in interlayer spacing.

Advantages of the discussed method with respect of the glycerol adsorption method are that it is quicker, requires no thermobalance, and the calculations are independent of particle size information, thus not requiring BET measurements. Disadvantages of the tetraalkylammonium method include less precision than the glycerol adsorption method, the requirement of a precise CEC value (especially for the cations near the MTB transition), and the apparent ineffectiveness of the method for high-charged smectites (CEC > 1.20 meq/g).

Qualitative observations seemed to be indicative of the MTB transition: when the substituted SWy-1 samples were washed with 70% methanol, the supernatant wash liquids were clear for the organoclays inserted with cations up to tetrapentylammonium and cloudy for those inserted with larger cations. The formation of an organic bilayer indicates that the entire clay surface is covered with organophilic alkyl chains: thus, there is no contact between the solvent and the mineral clay surface, resulting in a sudden reduction in the flocculation ability of the clay in a largely organic solvent. This same observation is also valid for STx-1.

Thus, precise values for the internal surface of various smectites were calculated from the MTB and BTP transitions observed by exchanging the clays with tetraalkylammonium cations. The method was found to be a simple and quick alternative to the glycerol sorption method. It was, however, ineffective to measure that of smectites with high CEC values (> 1.20 meq/g) since cation exchange was incomplete for these species.

3.2.2 Aromatic compound sorption by tetraalkylammonium smectites

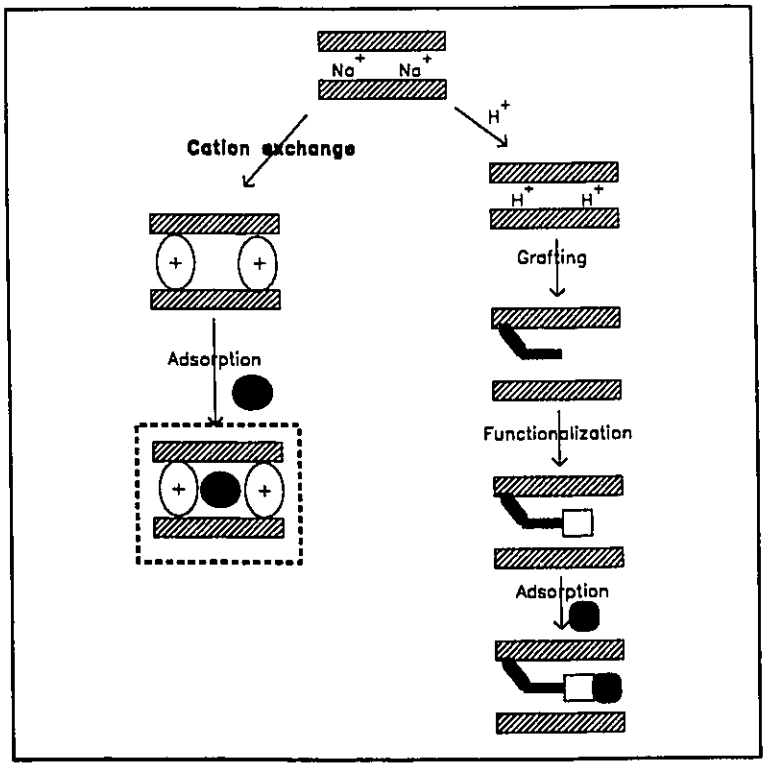

In an attempt to further characterize tetraalkylammonium-exchanged montmorillonite and to delve into the potential applications of such materials as environmental adsorbents, the adsorption of aromatic species (benzene, naphthalene and biphenyl) from water was studied. Thus, saturated solutions of each compound were made by adding copious amounts of the aromatics to distilled water followed by thorough mixing and filtration (in the case of benzene, the solution was allowed to stand overnight and the excess benzene was decanted off). 25 ml aliquots of the solutions were stirred with 0.1 g samples of each tetraalkylammonium-exchanged montmorillonites (using the SWy-1 clay) for 18 hours at

room temperature. The concentrations of the aromatics were measured before and after treatment by UV-visible spectroscopy, following the intensities (I) of the 254 nm band for benzene, the 268 nm band for naphthalene and the 244 nm band for biphenyl. Thus, the ratio of aromatic compound adsorbed by the clay could be expressed as $(I_{before}-I_{treated})/I_{before}$.

In order to relate this adsorption ratio to the clay surface present during the adsorption process, it is necessary to consider that the intercalated tetraalkylammonium ions represent a significant proportion of the mass of the organoclays, particularly in the case of very large cations. It is thus necessary that, in order to make adequate comparisons between the various organoclays, the mass of the exchange ions be subtracted from that of the organoclays used in the experiments, such that the resulting mass will reflect only that of the clay layers themselves.

Tables 3.3, 3.4 and 3.5 show the aromatic adsorption ratios, the mass of clay layers and ratio of these two values for benzene, naphthalene and biphenyl, respectively. Figure 3.7 plots the aromatic adsorption ratios/ g of clay layers as a function of the size of the organoclays' exchange ion. These results show, in all cases, a large increase in adsorptivity going from the NMe_4^+ clay to the NEt_4^+ clay, which could be explained by the increase hydrophobicity (organic character) of the latter material. Following this, a gradual decrease of adsorptivity is observed until the NBu_4^+, plausibly due to the decreasing space available for the aromatics as the larger organic cations begin to stuff the interlamellar region of the clay. It can thus be reasoned that, when SWy-1 is intercalated with NEt_4^+, there exists an optimal situation where the pore dimensions are suitable for the inclusion of all three

aromatic compounds and the size of the cation (relative to NMe_4^+) affords appreciable hydrophobicity.

In the case of organoclays intercalated with NPe_4^+ or larger cations, benzene adsorption gradually increases, a fact which can be explained by the increasing hydrophobicity of the materials. The situation for naphthalene and biphenyl, however, becomes chaotic, with no obvious trend being observable. This can be explained by the competition between two effects: first, the increasing hydrophobicity of the organoclays would favour the increased adsorption of the aromatics (as is the case for benzene), and, second, the congestion of the interlamellar region caused by the inclusion of the large cations would disfavour the adsorption of external species, particularly large adsorbate molecules (such as naphthalene and biphenyl). Note that in the case of biphenyl, the adsorption generally increases, suggesting that hydrophobic interactions may be more significant than the steric repulsion, perhaps owing to the more flexible nature of the molecule. Naphthalene, however, having a rigid structure, may not be flexible enough to adequately accomodated itself into the congested interlayer region of these organoclays so that, as a result, no net increase in adsorptivity is observed.

What is suggested by these results is that, when small cations are intercalated into montmorillonite (assuming a monolayer configuration), they form pillars which are discretely placed in well-defined positions in the interlayer region. The micropores thus formed have well-defined dimensions where only molecules of appropriate dimensions can enter. After the inclusions of larger cations (which force a monolayer to bilayer transition), the alkyl chains of adjacent cations now come in close contact and the interlayer region become

cluttered: in this situation, small or maleable molecules may be able to enter the interlamellar region and occupy void space, but geometric constraints would preclude the inclusion of large rigid species.

Table 3.3 Adsorption of benzene from water by tetraalkylammonium-montmorillonites.

Interlayer cation	Mass of clay layers (g)	ratio of benzene adsorbed	ratio adsorbed / mass of clay layers
$^{+}NMe_4$	0.095	0.39	4.1
$^{+}NEt_4$	0.089	0.43	4.8
$^{+}NPr_4$	0.087	0.39	4.5
$^{+}NBu_4$	0.082	0.35	4.3
$^{+}NPe_4$	0.078	0.38	4.9
$^{+}NHex_4$	0.073	0.39	5.3
$^{+}NHep_4$	0.067	0.38	5.7
$^{+}NOct_4$	0.064	0.41	6.3

Table 3.4 Adsorption of naphthalene from water by tetraalkylammonium-montmorillonites.

Interlayer cation	Mass of clay layers (no cations)	ratio of naphthalene adsorbed	ratio adsorbed / mass of clay layers
$^{+}NMe_4$	0.099	0.45	4.5
$^{+}NEt_4$	0.088	0.55	6.3
$^{+}NPr_4$	0.084	0.43	5.1
$^{+}NBu_4$	0.080	0.29	3.6
$^{+}NPe_4$	0.075	0.42	5.6
$^{+}NHex_4$	0.084	0.24	2.9
$^{+}NHep_4$	0.068	0.28	4.1
$^{+}NOct_4$	0.063	0.40	6.3

Table 3.5 Adsorption of biphenyl from water by tetraalkylammonium-montmorillonites.

Interlayer cation	Mass of clay layers (g)	ratio of biphenyl adsorbed	ratio adsorbed / mass of clay layers
$^{+}NMe_4$	0.097	0.41	4.2
$^{+}NEt_4$	0.092	0.89	9.7
$^{+}NPr_4$	0.085	0.61	7.2
$^{+}NBu_4$	0.082	0.70	8.5
$^{+}NPe_4$	0.076	0.78	10.3
$^{+}NHex_4$	0.072	0.63	8.8
$^{+}NHep_4$	0.085	0.87	10.2
$^{+}NOct_4$	0.063	0.57	9.0

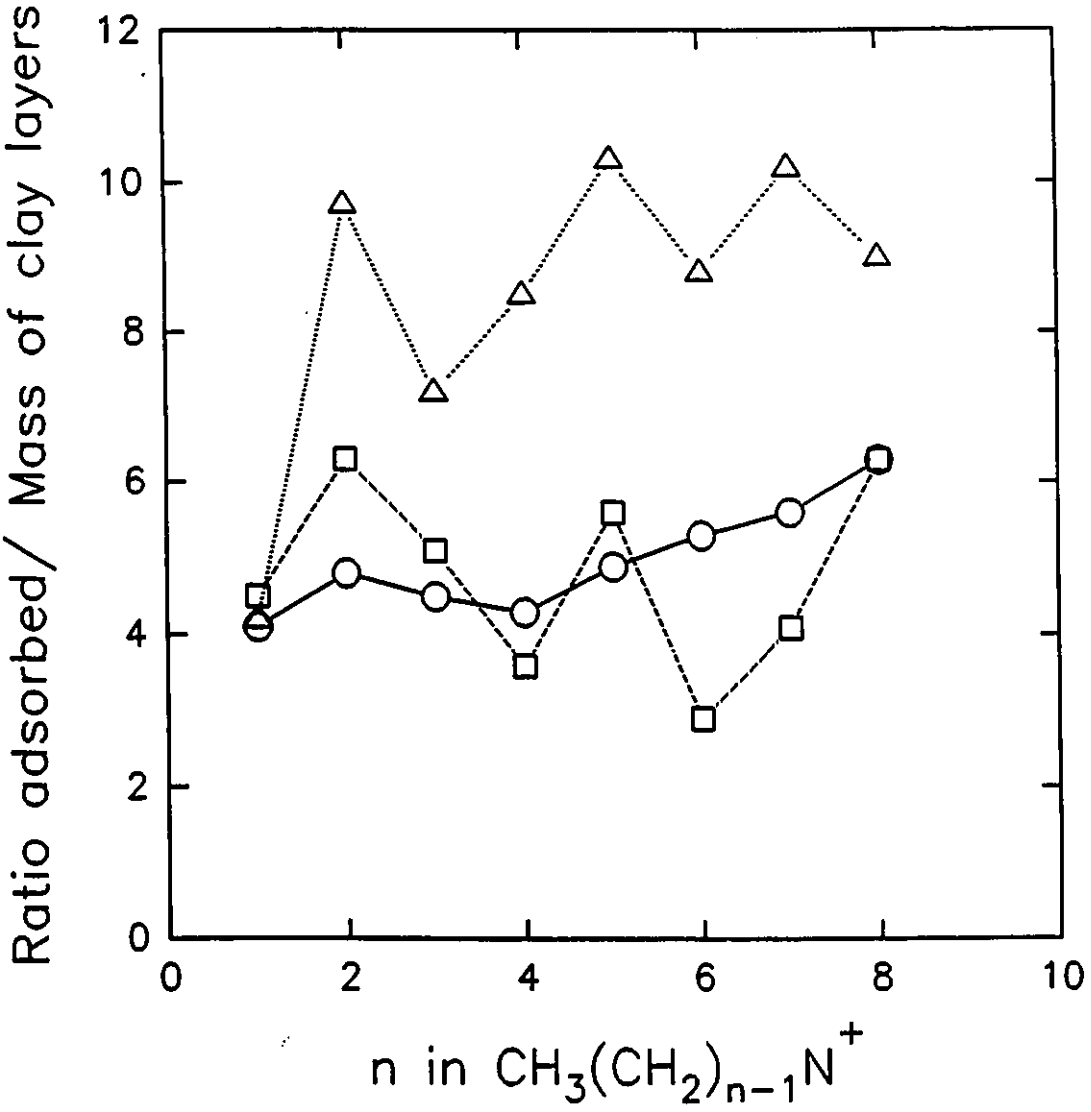

Figure 3.7 Adsorption of aromatic compounds by tetraalkylammonium montmorillonite (SWy-1). Circles denote benzene, squares naphthalene and triangles biphenyl. Note that the y-axis reflects the UV intensity *ratio* of the adsorbed compounds and is not a measure of the *absolute quantity* adsorbed by the organoclays (see text for more precise details).

3.2.3 Investigation of Alberta oil sands tailings

Part of the petroleum refining process in Canada involves the extraction of bitumen from the oil sands where much of Alberta's rich petroleum deposits are found. This bitumen is problematic for two principal reasons: (1) they make the process of petroleum extraction difficult and costly, and (2) the disposal of this toxic sludge results in the spoiling of vast amounts of land. There is therefore much interest in understanding the nature of this sludge and of the mineral components which make up an important part of it.

The stability of this sludge can often be attributed to the the colloidal properties of its component minerals, especially clay minerals. Kaolinite, illite and montmorillonite have been identified as possible components of this bitumen[182] so clay mineral characterization techniques are paramount if one is to gain an understanding about the properties of oil sands tailings sludge. This section will deal with a practical example of the application of characterization techniques described in section 3.1.2 in the study of sediments derived from Alberta oil sands tailings.

Sample preparation

Three fractions of the bituminous mineral sample were supplied, the first centrifuged at 200 g, the second at 500 g and the third at 1500g. The organic fraction of the samples had been removed via toluene extraction prior to delivery.

Each fraction was slurried in about 100 ml distilled water and about 10 g of NaCl were added in order to promote Na^+ homoionization of the clay minerals in the samples.

The fractions were then washed of excess NaCl by dialysis and isolated by freeze-drying, in the manner consistent with the previous purifications of smectites.

CEC measurements

The CEC of each sample fraction was determined by tetrapropylammonium exchange. Thus, accurately weighed samples of each fraction were stirred in 50 ml tetrapropylammonium iodide (TPA) solutions (of known concentrations) for 24 hours. After centrifugation, the TPA concentration of the supernatent solution was measured by colorimetry.[175] This was accomplished by diluting 25 ml of the supernatent to 1 L, then adding to an extraction flask 5 ml of this solution with 5 ml chloroform and 1 ml bromocresol green indicator solution (1 g of bromocresol dissolved in 14.4 ml NaOH 0.1 M and diluted to 250 ml with water): the yellow organic phase (containing the TPA-bromocresol complex) was removed and analyzed by UV-vis spectroscopy. Thus, the absorbance of the TPA-bromocresol complex (λ=417 nm) could be related to the concentration of the cation in the solution. The CEC of the clay fractions could then be calculated by dividing the mmoles of adsorbed TPA by the mass of the samples. Table 3.6 shows the results of these CEC determinations.

Table 3.6 CEC values for bituminous mineral fractions.

fraction	mass of sediment (g)	initial [TPA] (mM)	[TPA] after exchange (mM)	CEC (mmol/g)
200 g	0.1000	2.49	2.41	0.08
500 g	0.0980	1.99	1.84	0.08
	0.1032	2.99	2.78	0.11
	0.1005	3.99	3.70	0.15
1500 g	0.0686	2.49	2.35	0.20

The relatively low CEC values for all of the fractions seem to suggest that there are little or no swelling smectites (such as montmorilionite) in the sample. Moreover, that a concentration dependance is observed for the TPA adsorption (in the case of the 500 g fraction) indicates that TPA is likely being physisorbed to the mineral particles and not intercalated by ion exchange. The CEC values were also found to increase as the particle sizes in the fractions diminished, an observation which corroborates with the statement in the previous sentence since the higher surface area particles would be expected to favour the physisorption of adsorbate species.

X-ray diffraction

The XRD patterns were recorded for the three sample fraction and for the 500 g sample treated with TPA solution (0.1005 g with 50 ml of 3.99 mM TPA) (Figure 3.8). In all cases, the most intense peaks were observed at 7.2 and 3.57 Å and assigned to kaolinite, which is often found as the major mineral species in such sludges.[182] Peaks at 10.2 and 5.0 Å were also found and are likely to indicate the presence of illite in the samples.

After TPA treatment, no changes were observed in the XRD pattern. This result conclusively demonstrates the absence of swelling smectite clays in this bitumen sample.

It was also noted that the relative intensity of the 10.2 Å illite peak increased with respect to the 7.2 Å kaolinite peak as the size fractions became smaller, indicating that illite represents the finest mineral particles of the bitumen.

Infrared spectroscopy

The FTIR spectrum of the 500 g sample (Figure 3.9) was characteristic of kaolinite, featuring well-resolved OH stretching bands at 3698, 3653 and 3622 cm^{-1}. This is consistent with the XRD evidence showing kaolinite to be the most prevalent mineral in the samples.

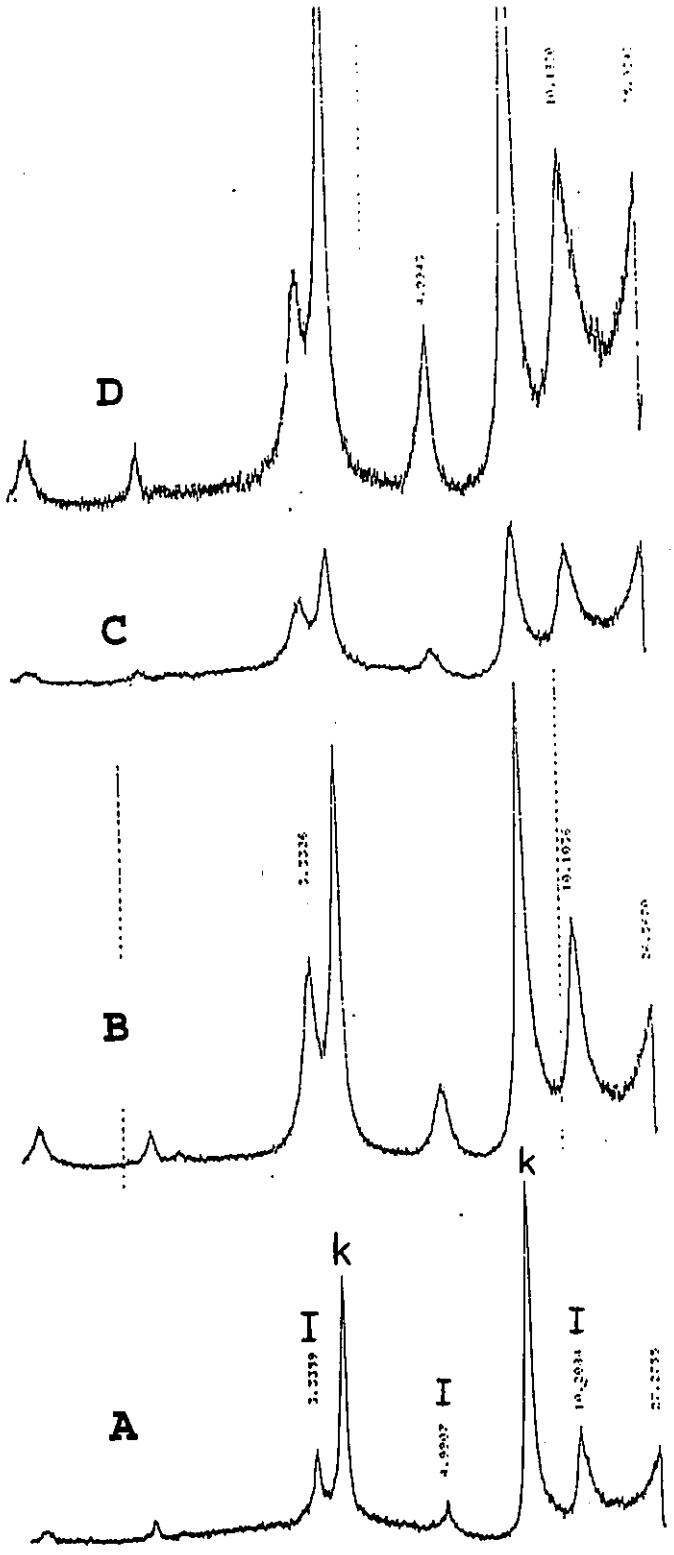

Figure 3.8 XRD patterns for bituminous clay samples: (a) 200 g fraction, (b) 500 g fraction, (c) 1500 g fraction and (d) TPA^+-treated 500 g sample ("K" denotes kaolinite and "I" illite).

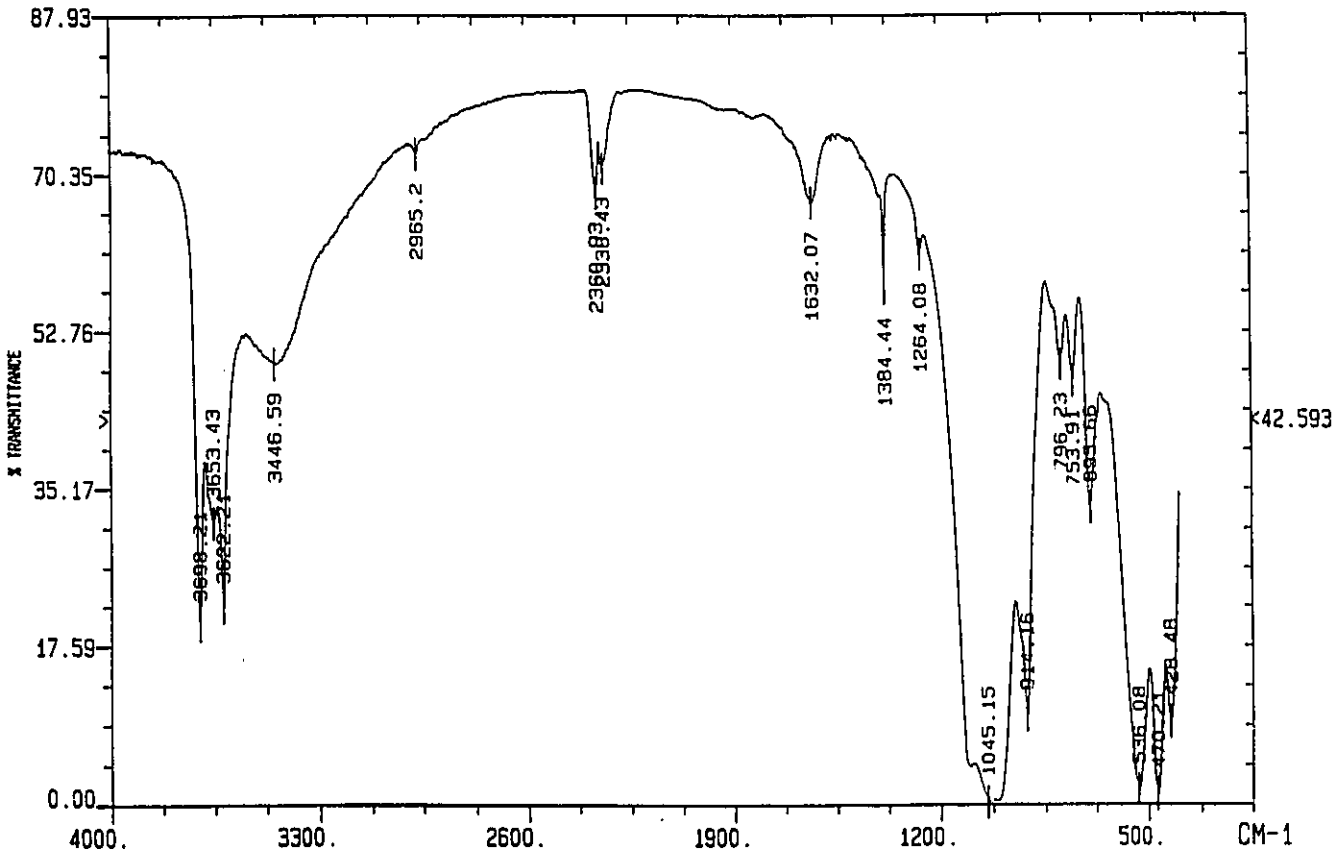

Figure 3.9 FTIR spectrum for 500 g bituminous clay fraction.

The analysis of the bituminous clay samples showed that the prevalent compound was likely to be kaolinite, with the presence a smaller quantity of fine illite particles. The experiments have also conclusively demonstrated that swelling smectites such as montmorillonite were not present in the sample provided.

This case study has therefore shown the utility of the clay analysis techniques in the characterization of a problematic substance in the oil industry. The knowledge of the properties of oil sands sludge is likely to have enormous economic consequences, and these relatively simple techniques can thus be used to further this goal.

3.3 Covalent grafting on smectites

The issue of covalent functionalization of the surfaces of smectites has been a source of debate and controversy among clay chemists for many decades. Deuel's claims of achieving covalent fixation of montmorillonite by acetate, alcohol, amine and phenyl groups[69-73] have been used by this author as conclusive evidence that the structure of montmorillonite follows the Edelman-Favejee model, which had suggested that the silica tetrahedra of the montmorillonite structure were inverted, resulting in an abundantly hydroxylated interlamellar region. Although such a mechanism has since been refuted,[75] mostly due to the lack of acceptance for the Edelman-Favejee model for the smectite layer structure, there nonetheless exists incontrovertible evidence supporting the existence of tenaciously bound molecular species to the surfaces of smectite minerals which would seemingly involve condensation to Si-OH groups.

Since then, all the work done with such grafted clay minerals have focused on their applications, particularly in the field of catalysis.[76-80,82,91,183] Since the inception of this problem almost half a century ago, however, little work has been done to elucidate the fundamental chemical nature of these compounds. It is the purpose of this section to both expand the applicability of these materials for environmental purposes as well as to gain more understanding about these elusive structures.

The preparation of clay based adsorbents with covalently grafted functionalities involves the following steps: (1) *hydrogen exchange* of Na^+-montmorillonite in relatively dilute acid in order to promote the formation of hydroxyl units on the clay surface yet without destroying the lamellar structure of the mineral, (2) *grafting* the H^+-montmorillonite

with an appropriate silane bearing a good leaving group, and (3) *functionalization* of the material by nucleophilic substitution of the grafted silane with a suitable adsorbate functional group.

3.3.1 H-montmorillonite

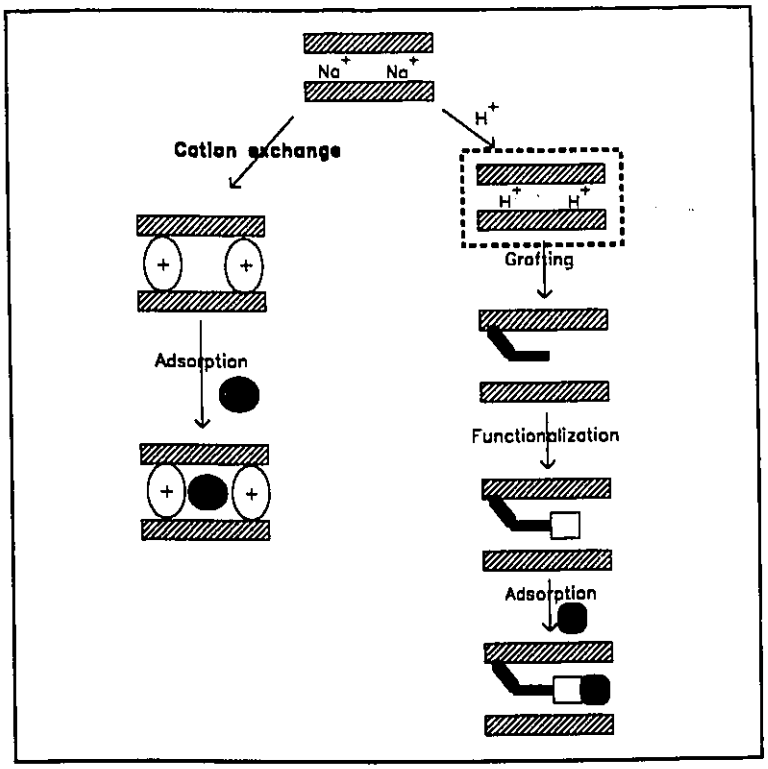

Preparation

10 g of Na^+-montmorillonite (SWy-1, purified according to the procedure described in section 3.1.1) was added to 500 ml of a 0.10 or 1.0 M HCl solution and stirred for 24 hours at room temperature. The suspension was then washed by dialysis (until a negative silver nitrate chloride test was obtained) and freeze-dried to give H^+-exchanged montmorillonite. Alternatively, the acidified suspension could be washed by several cycles of centrifugation, replacing with fresh distilled water until the supernatant tested negative for chloride ions.

Characterization

The XRD pattern of H-montmorillonite dried at room temperature was identical to that of Na^+-montmorillonite, featuring a basal spacing of about 13 Å. When dried *in vacuo* at 130 °C, the spacing collapsed to 9.6 Å (the completely dehydrated form). When H-montmorillonite was dried at 130 °C without vacuum, XRD revealed a layer spacing of 11.8 Å (Figure 3.10), suggesting only a partial dehydration of the layers. The d_{001} peak was very symmetric, as ascertained by deconvolution analysis (Figure 3.10), confirming that the layers of H-montmorillonite are stacked with considerable regularity (this observation will be important for the characterization of grafted montmorillonite, as will be shown in section 3.3.2.2).

The TGA profile (Figure 3.11) was also nearly identical to that of the sodium derivative, except for a significant increase in the content of adsorbed water in H-montmorillonite (about 10%, compared to 6% in Na^+-montmorillonite) which may have resulted from the generation of hydroxyl sites in the structure, increasing its hydrophilicity.

The FTIR spectrum for H-montmorillonite featured no discernable differences from that of the parent Na^+-montmorillonite.

All of these results show that the layer structure of the acidified clay is maintained and that there are few discernible macroscopic differences between Na^+-montmorillonite and H-montmorillonite, save for an apparent increase in water adsorptivity. Moreover, all of the H-montmorillonite batches prepared seemed identical to each other, regardless of the concentrations of HCl used in their preparation or of their method of isolation (*i.e.* freeze-drying or centrifugation).

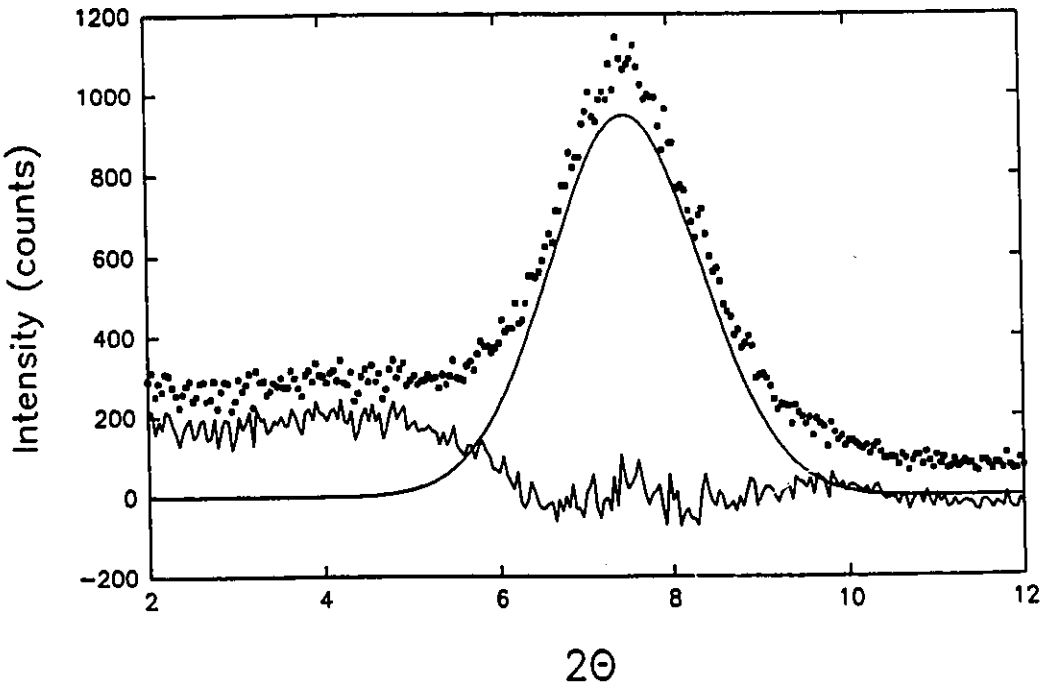

Figure 3.10 XRD pattern for H-montmorillonite dried at 130 °C, featuring the deconvolution of the 11.8 Å peak (solid curve) and the residual pattern (bottom).

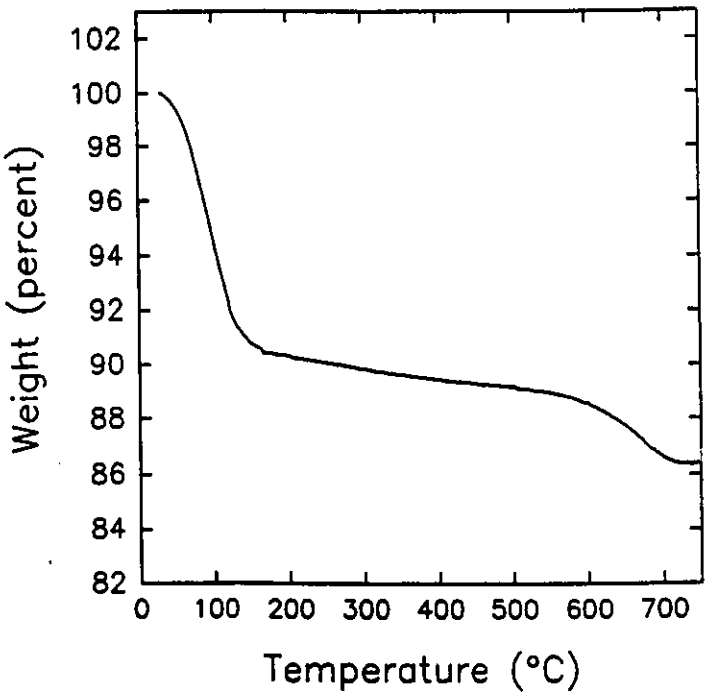

Figure 3.11 TGA curve for H-montmorillonite.

3.3.2 Grafting of 3-chloropropyltrimethoxysilane to H-montmorillonite

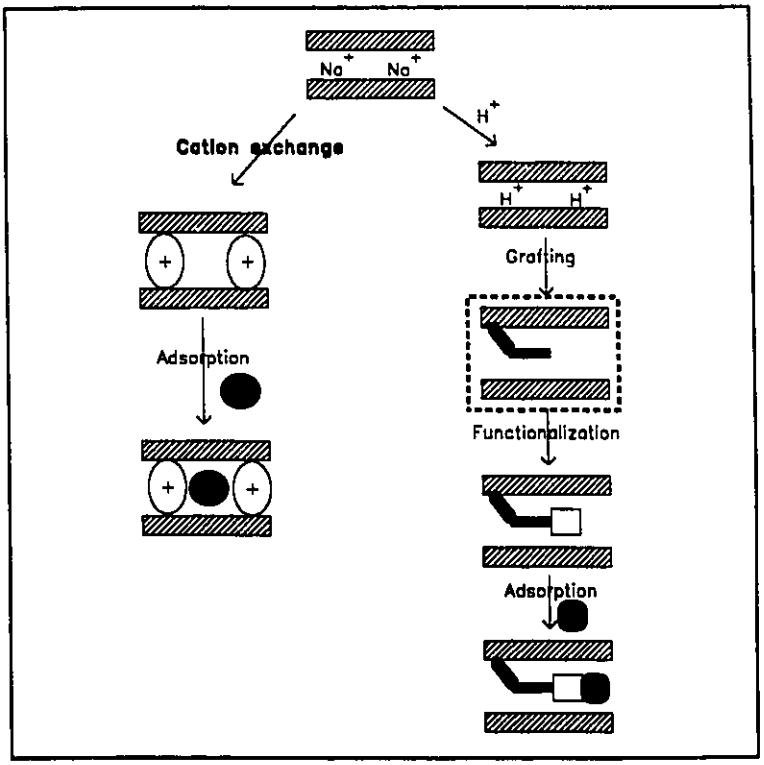

3.3.2.1 Preparation

Five different batches of this compound (annotated A to E) were prepared following similar but slightly varying procedures, the details of which are described as follows (including the details regarding the preparation of the parent H-montmorillonite).

Chloromont A.

Na^+-montmorillonite was treated with 1M HCl for 24 hours, then washed free of excess ions by dialysis and isolated by freeze-drying.

Approximately 2 g of H-montmorillonite were dried in vacuo over P_2O_5 at 110 degrees C and added to 200ml dry toluene with 2-3 ml chloropropyltrimethoxysilane. With a drying tube attached to the condenser, the mixture was refluxed for 2 days. The resulting gray material (chloromont-A) was filtered and washed with dry toluene followed by ether, then dried in vacuo at 60 degrees C overnight.

Chloromont B.

This sample was prepared using the same procedure as sample A except that a much smaller excess of chloropropyltrimethoxysilane was used (0.3 ml).

Chloromont C.

A suspension of H-montmorillonite prepared according to the procedure of sample A was stored for several months awaiting use. It was then retreated with 0.1 M HCl and centrifuged at 4000 rpm for 45 minute periods and water washed six times to remove excess HCl. The resulting gel was then dried in vacuo at 100°C , then ground into a fine powder and once again dried in vacuo at 110°C over P_2O_5 .

2.2 g of H-montmorillonite was refluxed over N_2 in dry toluene with about 1 g chlorpropyltrimethoxysilane for 65 hours.

The chloromont-C thus formed was filtered and treated with Soxhlet extraction using benzene over calcium hydride as wash solvent for 17 hours. The product was then washed with ether and dried in vacuo at 70°C.

Chloromont D.

Purified Na^+-montmorillonite (about 10g) was dispersed in water (500 ml) and concentrated HCl was added to make up a concentration of 0.15 M. The H-montmorillonite thus obtained was then washed free of excess ions (dialysis) and freeze-dried.

The 2 g of H-montmorillonite were dried at 80°C in vacuo over P_2O_5 then refluxed over N_2 in 400ml toluene (freshly distilled over calcium hydride) with about 1 g chloropropyltrimethoxysilane for 65 hours.

The chloromont-D thus formed was filtered and washed by Soxhlet extraction following the same procedure as Chloromont-C.

Chloromont E.

The procedure for this preparation was identical to that of sample D, except that instead of freeze-drying, the H-montmorillonite was isolated by centrifugation for about 5 hours at 4000 rpm, followed by drying in vacuo over P_2O_5 and fine grinding. The finer fraction was isolated by passing the powder through an 80 mesh sieve. Other than this modification, chloromont-E was prepared as its D analog.

3.3.2.2 Characterization[d]

X-ray diffraction

The XRD pattern for chloromont-A (Figure 3.12a) showed a slight increase in the basal spacing after silanation of the clay with respect to the ungrafted clay (12.9 Å for H-montmorillonite, 14.2 Å for chloromont-A, and 13.5 Å for chloromont-B, C, D and E samples), suggesting the presence of included species in the interlamellar region. This result alone, however, is not sufficient to conclusively ascertain the successful anchoring of the silane between the clay layers, as the layer expansion could feasibly reach this value under appropriate hydration conditions, such as upon exposure to high atmospheric humidity. In comparison to that of the Na^+-montmorillonite (Figure 3.12b), the XRD pattern of chloromont featured less intense and broadened d_{00n} peaks, suggesting a loss of crystallinity relative to the parent montmorillonite structure. This observation is suggestive of some interlamellar modification of the mineral.

Since interlayer hydration was problematic to this investigation, the chloromont samples were dried at 130 °C for 24 hours (as was done for H-montmorillonite, see section 3.3.1 and Figure 3.10) in order to remove all the volatile components from the material. The XRD pattern (Figure 3.13) showed, unlike that of H-montmorillonite (Figure 3.10), a highly asymmetric d_{001} reflection, with an intensity maximum at 10.2 Å (corresponding to fully collapsed clay layers) and a strong sloping towards lower θ values. Deconvolution of the

[d]Unless otherwise mentioned, all of the analyses presented in this section refer to the chloromont-D sample.

10.2 Å phase by curve fitting the steeper right side of the peak, followed by spectral subtraction, elucidated a peak at 12.1 Å (Figure 3.13). In contrast, the H-montmorillonite spectrum (figure 3.10) displayed a very symmetric d_{001} peak, with virtually no residual pattern resulting from the spectrum subtracted with the fitted curve.

Two plausible conclusions can be made from these observations. The dissymetric peak may indicate that some form of interstratification exists, resulting in some layers being grafted (the 12.1 Å phase) and others not bearing any grafted species (the 10.2 Å phase). A second possibility, consistent with the reduction of peak intensity, is that the grafting of the layers causes a complete or near complete destruction of the sample crystallinity, thus highlighting residual ungrafted clay particles. The X-ray diffraction evidence clearly shows that the clay-silane interaction has a profound effect on the nanoscale structure of the clay composite.

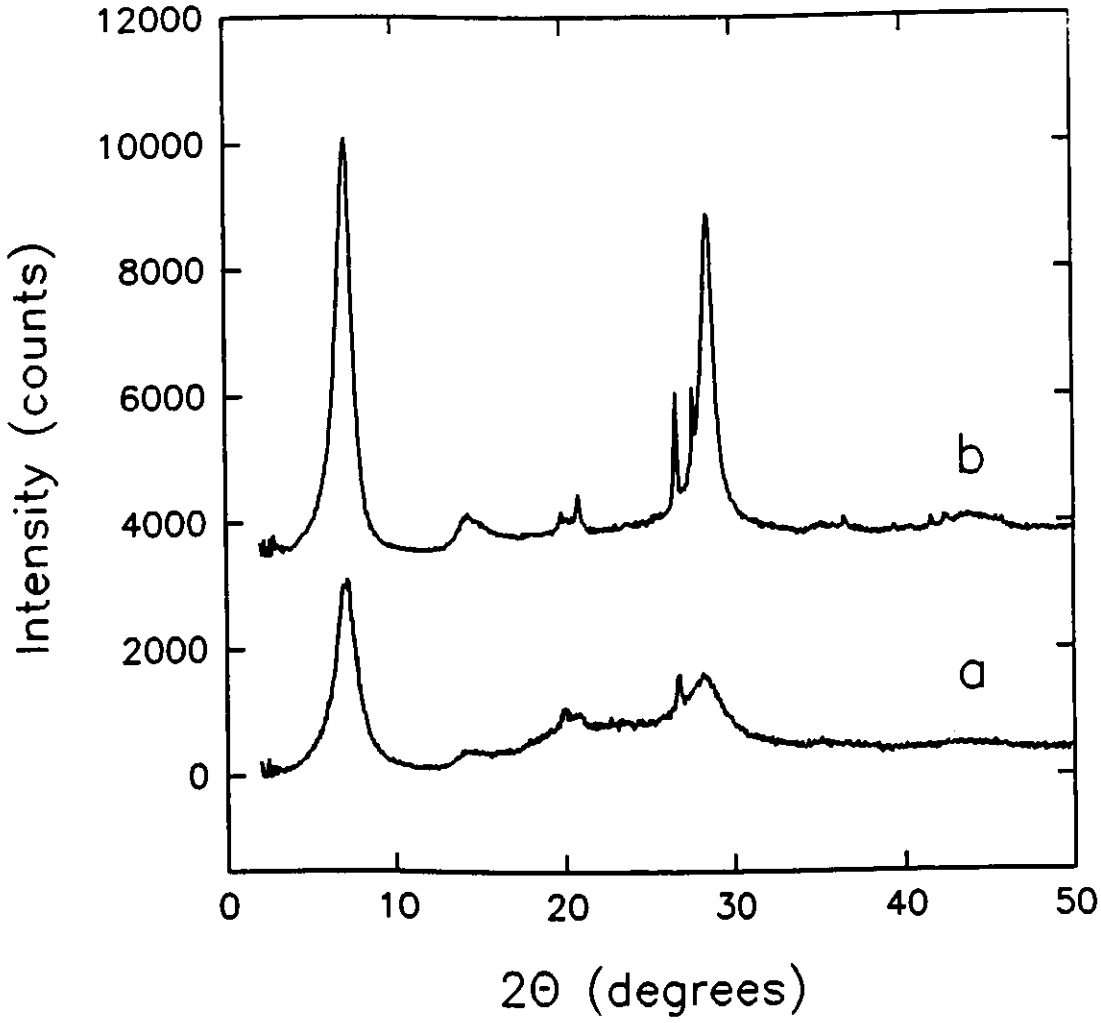

Figure 3.12 XRD pattern for chloromont (a), in contrast to that of Na^+-montmorillonite (b).

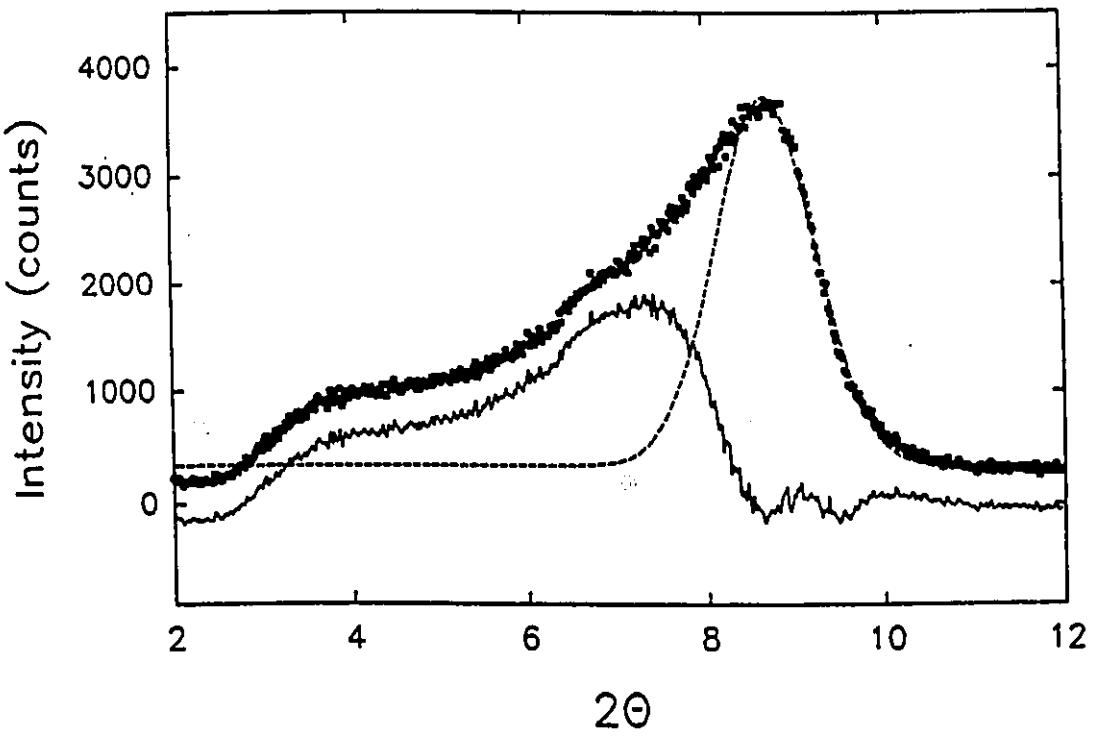

Figure 3.13 XRD pattern for chloromont dried at 130 °C featuring the deconvolution of the 10.2 Å peak (dashed line) and the spectral subtraction (lower curve).

Infrared spectroscopy

New peaks appear in all of the chloromont spectra (Figure 3.14) indicative of the grafting of the chloropropyl moieties: 2940 cm-1, 1440 cm-1 (C-H modes) and 700 cm-1 (C-Cl stretch). These new peaks are most intense in the samples where a large excess of silane was used (chloromont A,C,D and E).

Elemental analysis

The C and H analyses of the chloromont samples are given in Table 3.7. For most samples, the H/C ratio for the grafted moieties (the last column of the table) is reasonably close to 2. To be in accordance with the hypothesis that the grafted species are $Si(OH)_2(CH_2)_3Cl$, that number would have to be 2.67. This deviance can be explained by the possible condensation of Si-OH groups to each other, so that only the hydrogens on the chloropropyl chain are left. Another possibility is that the structural OH groups of montmorillonite are participating in the grafting process, meaning that the subtraction of these hydrogens from the calculation in the last column of the table is an incorrect assumption.

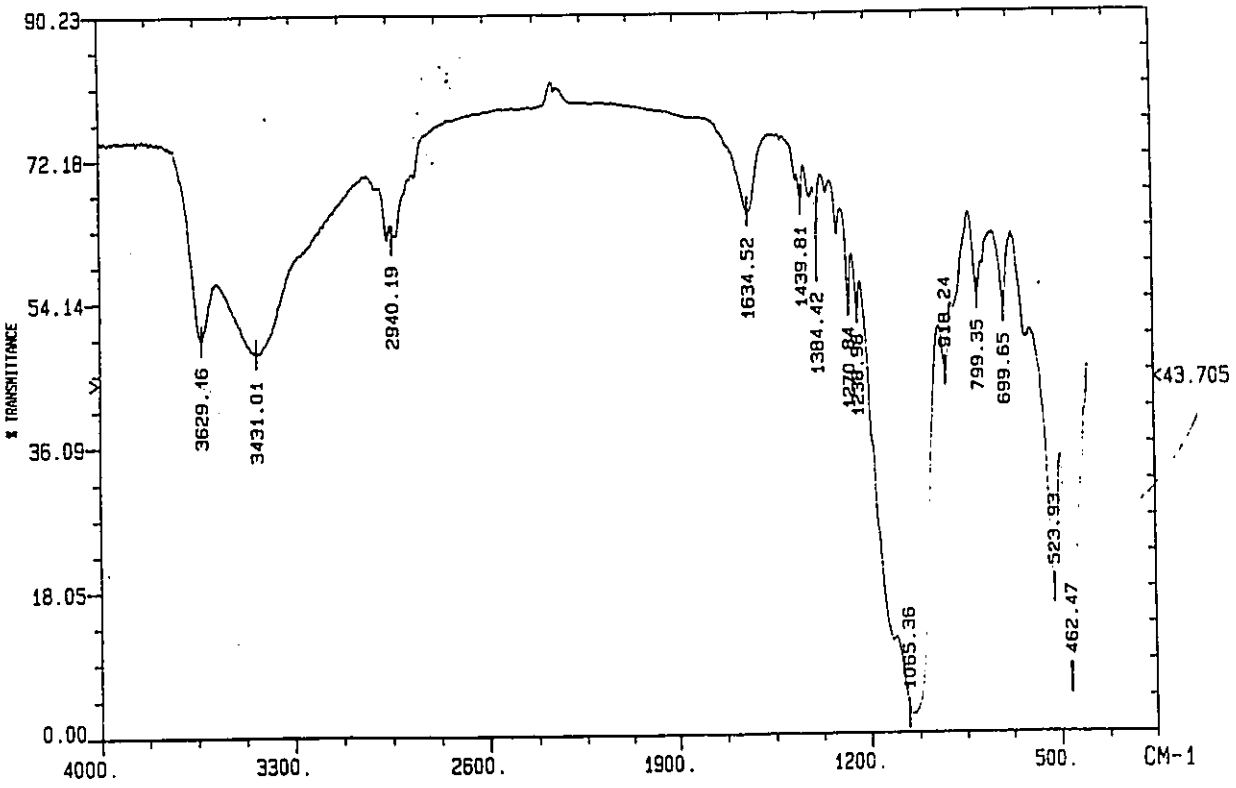

Figure 3.14 FTIR spectrum of chloromont.

Table 3.7 C and H analyses of chloromont samples.

	C (weight %)	H (weight %)	H/C (mole/mole)	H/C[a] (mole/mole)
H-montmorillonite	0.21	0.83	-	-
Chloromont-A	12.76	2.49	2.32	1.94
Chloromont-B	4.44	1.38	3.70	1.87
Chloromont-C	6.97	1.65	2.82	1.79
Chloromont-D	13.31	2.44	2.18	1.83
Chloromont-E	9.93	2.08	2.50	1.89

[a]H/C ratio calculated by subtraction of the structural hydrogens of montmorillonite (0.83%), assuming the presence of $Si(OH)_2(CH_2)_3Cl$ grafted moieties.

3.5. X-ray fluorescence.

X-ray fluorescence analysis gave a Si/Al molar ratio of 2.64 for crude Na^+-montmorillonite, 2.58 for purified Na^+-montmorillonite and 2.38 for H-montmorillonite. All of these results are reasonably consistent with the literature value of 2.77.

Table 3.8 shows the analyses of the chloromont samples for Si, Al, Fe, Ca, P, and Cl.The results for the crude, purified and acidified montmorillonites seem to be reasonably consistent with one another and with literature value, save for an abnormally high P content (this was present in most of the samples analyzed and is probably an artifact of the instrument).

The results ascertained the presence of Cl in the chloromont samples. The Si content in all silylated samples was, as expected, higher than in the parent clays. Moreover, the Cl

content was found to increase in a concomittant manner with that of the Si (that is, the Si content above that of the parent clay). These observations support the presence of the chloropropylsilane moieties in the chloromont samples.

Table 3.8 X-ray fluorescence data for chloromont samples (results expressed in molar ratios)

	Fe	Ca	P	Si	Al	Cl
Literature value (Clemency)	0.131	0.085	0.001	2.76	1.00	-
Crude Na^+-montmorillonite	0.198	0.170	0.151	2.65	1.00	-
Purified Na^+-montmorillonite	0.150	0.043	0.167	2.58	1.00	-
H-montmorillonite	0.150	0.055	0.118	2.39	1.00	-
Chloromont-A	0.129	0.087	0.312	5.16	1.00	1.97
Chloromont-B	0.135	0.081	0.304	4.02	1.00	0.287
Chloromont-C	0.200	0.082	0.254	4.22	1.00	0.625
Chloromont-D	0.175	0.122	0.328	5.61	1.00	1.95
Chloromont-D (1000 °C)	0.245	0.098	0.288	5.97	1.00	-
Chloromont-E	0.241	0.083	0.294	4.65	1.00	1.72

Thermogravimetric analysis

The TGA profile for chloromont-D (Figure 3.15) featured two major mass losses: the first between 350 and 490 °C (12.6%) and the second between 490 and 560 °C (8.3%). There appears to be, therefore, two type of grafted silane moieties, one being more strongly bound (the 8.3% loss) than the other.

The total mass loss (about 21%) was somewhat short of that determined by elemental analysis. This can be attributed to the use of N_2 atmosphere during the analysis resulting in the formation of non-combustible carbonaceous residues in the sample. This hypothesis is supported by the black colour of the material observed after the analysis.

It is interesting to note that the dehydroxylation mass loss (2.7% at 650 °C) of the parent H-montmorillonite is not observed in chloromont. This evidence suggests that a profound modification of the montmorillonite structure has occured as a result of the silane grafting, possibly associated with the involvement of the structural hydroxyls in the grafting process.

^{13}C-NMR spectroscopy

Three signals are observed in the ^{13}C spectrum at 12, 27 and 48 ppm corresponding to the three carbon signals in the chloropropyl chain. No signal was observed, however, for the OCH_3 groups, indicating that these were possibly replaced with OH through hydrolysis with water physisorbed on the parent clay, or by atmospheric humidity. Despite the precautions taken to prevent moisture contamination in the reaction system, it is nonetheless probable that such contamination has occured.

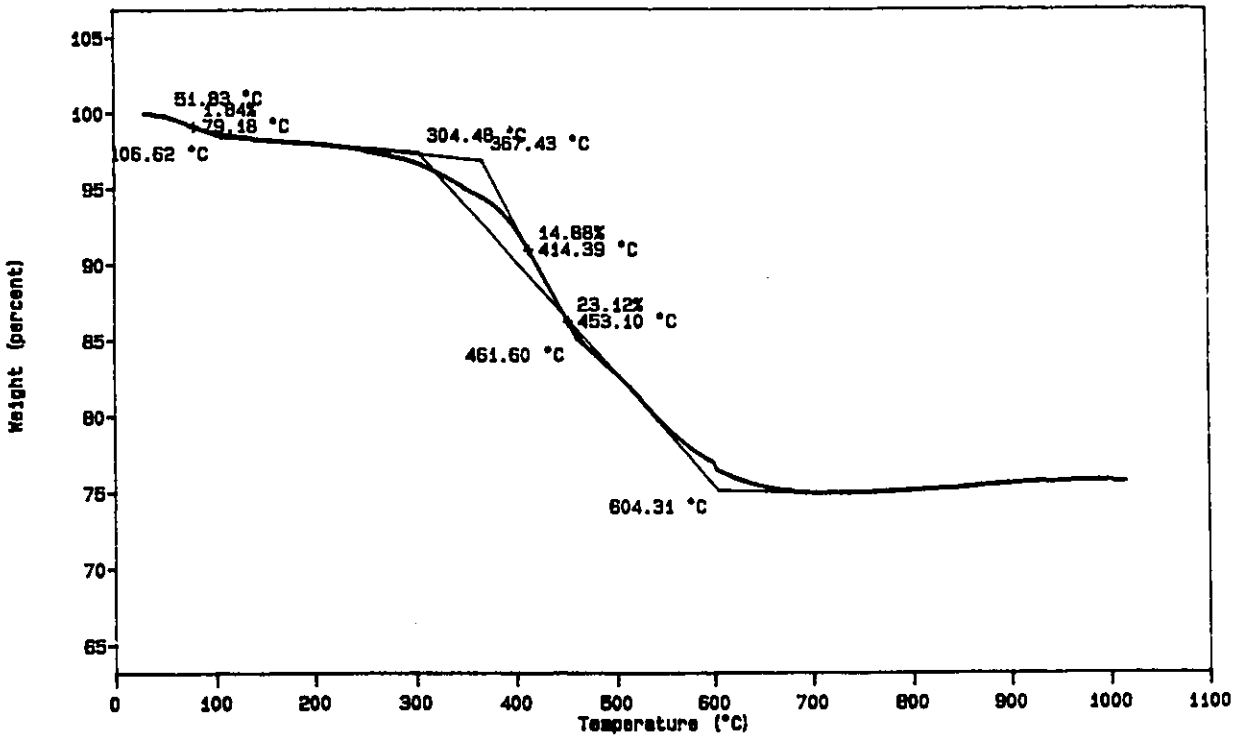

Figure 3.15 TGA profile of chloromont.

The dipolar dephased spectrum of chloromont (recorded with 40 μs dephasing time) showed only a slight reduction in the intensity of the signals, suggesting that much of the silane moities are mobile, plausibly a result of significant grafting to the external region of the clay particles or in the mesoporous cavities of the material.

Combustion study

0.1392 g of chloromont-D was heated at 1000°C for 17 hours over air, resulting in a weight loss of 27.6%, a value which has excellent accordance with the determined 13.31% C content (on the basis of which one could calculate a weight loss of 28.7%, assuming C, H and Cl volatilization), but somewhat higher than the weight loss measured by TGA over nitrogen (19.3%). This, along with the observation that the sample heated under nitrogen atmosphere turned black but the sample combusted over air did not (light yellowish-beige), seems to indicate that much of the carbon in the TGA sample did not evolve into CO_2 (due to lack of oxygen), but probably remained as elemental carbon.

X-ray fluorescence analysis performed on this calcined sample showed the Si/Al ratio to be nearly identical to that of chloromont-D. This is proof that the silicon atoms of the grafted silanes are retained after heating to 1000°C: it can therefore be assumed that the weight loss in the combustion process is due only to loss of C, H and Cl atoms, resulting in a mixture of Si, Al and other metal oxydes (the beige colour of the sample being likely due to the presence of a small amount of iron oxide).

From this information, the following reaction for the combustion process can be postulated:

$$Si_{7.8}Al_{3.3}Fe_{0.3}Mg_{0.4}O_{20}(OH)_4[Si(OH)_2(CH_2)_3Cl]_x$$

$$\downarrow$$

$$Si_{7.8}Al_{3.3}Fe_{0.3}Mg_{0.4}O_{22} + 2\ H_2O + xSiO_2 + x"C_3H_8Cl"$$

By solving the above equation for a weight loss of 27.6%, one can calculate the x stoichiometric parameter. Thus, the chemical formula of chloromont can be calculated as being $Si_{7.8}Al_{3.3}Fe_{0.3}Mg_{0.4}O_{20}(OH)_4 \cdot 4.3[Si(OH)_2(CH_2)_3Cl]$, giving a Si/Cl ratio of 2.81, consistent with X-ray fluorescence data (Si/Cl=2.87).

By considering the hypothesis that the structural OH groups of montmorillonite participate in the silane grafting process (as was suggested by the TGA evidence), the following chemical formula for chloromont can be proposed:

$$Si_{7.8}Al_{3.3}Fe_{0.3}Mg_{0.4}O_{19.7}[OSi(OH)_2(CH_2)_3Cl]_{4.3}$$

Reproducibility of the samples

Samples A,D and E all had similar results in their chemical analyses (elemental analysis and XRF) and had consistent XRD patterns, suggesting that the procedure was quite reproducible when a large excess of silane was used. The drying procedure (*i.e.* air drying or freeze-drying) of the parent H-montmorillonite did not seem to dramatically affect the

outcome of the grafting, save for the fact that a much denser material was obtained from the air-dried H-montmorillonite (the chloromont obtained from the freeze-dried clay retained the flaky aspect of the parent H-montmorillonite). It is notable, however, that the freeze dried H-montmorillonite afforded more highly grafted material than the powdered clay (isolated by centrifugation), plausibly due to the greater mesoporosity associated with the freeze-dried material which may have promoted enhanced access of the silane molecules to grafting sites.

Sample B had few grafted moieties compared to samples A,D and E, as evidenced by the low C and Cl contents measured by elemental analysis and XRF. This is due to the insufficient amount of silane used in the grafting process. Sample C also had a low C and Cl content despite the use of excess silane in its preparation: this could have resulted from the use of an "old" H-montmorillonite batch which was reacidified and washed by centrifugation (instead of dialysis). This lack of rigour in the preparation of the parent H-montmorillonite is thus likely to have resulted in a material somewhat less active to the grafting reaction.

Despite these discrepancies, it is evident that an adequate reproducibility between the various grafted-clay products was obtained, providing that the parent H-montmorillonite is carefully prepared (thoroughly washed free of excess HCl and dried) and that freshly prepared material is used for the grafting reaction.

Structural considerations of chloromont

From the experimental evidence presented above, the following conclusions can be made regrading the structure of chloromont.

Although XRD has clearly shown that grafting has occured in the interlamellar region of montmorillonite, the large amount of grafted silane molecules measured by elemental analysis, XRF, combustion and TGA (about 8 times the CEC of the parent clay) suggests many of these are likely to be grafted on the external region of the clay particles. It can thus be suggested that the two mass losses observed by TGA for thiomont are due to two types of grafted silanes: the low temperature loss ($\sim 12\%$) can be attributed to the externally grafted groups, while the high temperature loss ($\sim 8\%$) can be assigned to moieties grafted in the interlamellar region of the clay. The presence of very mobile carbon chains as shown by ^{13}C dipolar-dephasing NMR further supports the presence of externally grafted chloropropyl chains.

A plausible structure which can take into account all of the observed features of chloromont is shown in Figure 3.16, where the mesoporous cavity walls are grafted, and some of the interlayers have grafted moieties and others not. Thus, the situation is an extremely complex one, requiring the convergence of a multitude of different analytical approaches in order to arrive at a feasible representation of the modified clay.

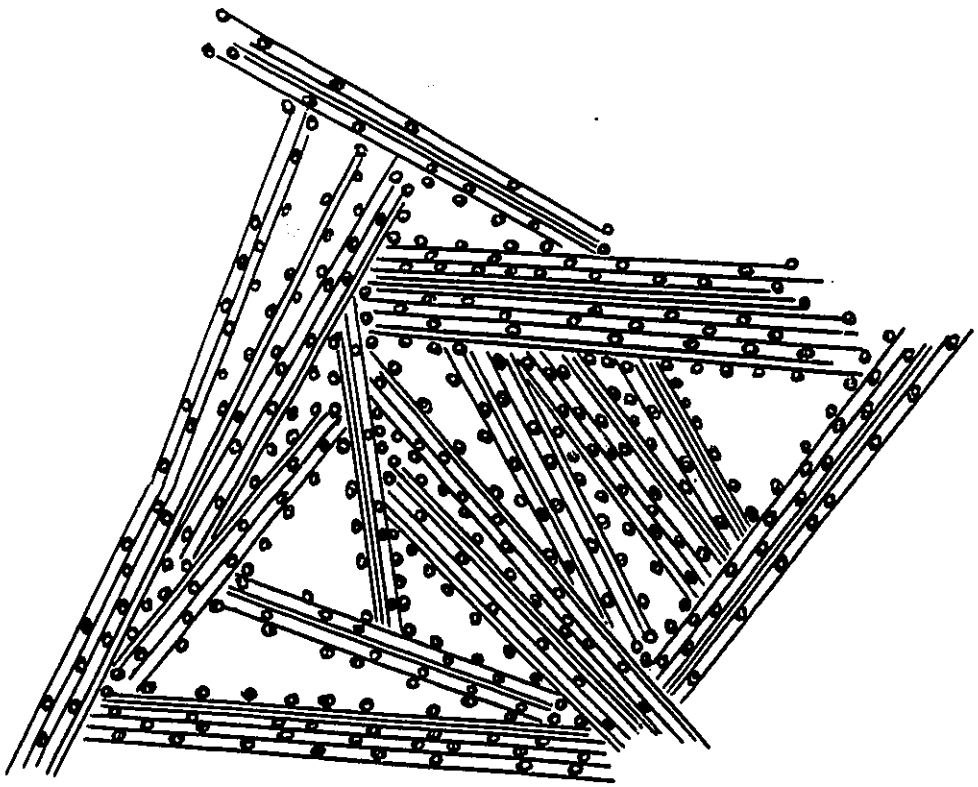

Figure 3.16 Representation of the structure of chloromont. Lines represent the montmorillonite layers and dots denote the chloropropylsilane moieties.

3.3.3 Functionalization of grafted montmorillonite (chloromont)

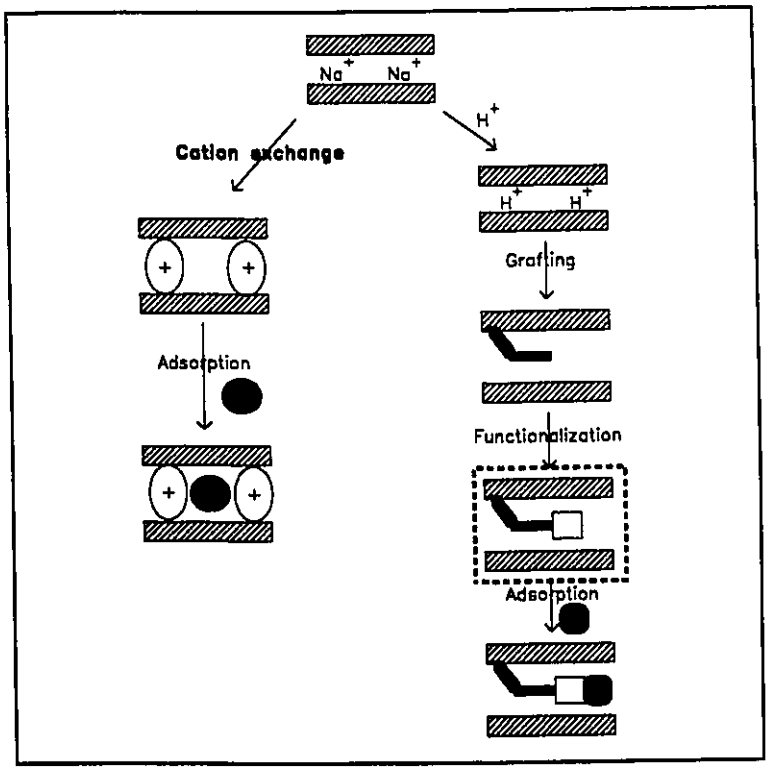

In this section, the functionalization of the grafted montmorillonite will be attempted via the nucleophilic substitution of the Cl on the grafted chloropropyl chain with metal-chelating functionalities, namely the thiol (SH), ethanedithiol (SCH_2CH_2SH) and cyclam-6 ($C_{22}H_{50}N_6$) (an aza-crown) groups.

3.3.3.1 Thiomont: SH functionalization

Preparation

2g of chloromont (samples A, C, D and E) and 4 g of NaSH were stirred in about 75 ml of ethanol and refluxed for 48 hours, forming a greenish-blue compound. The products (labelled as thiomont A, C, D and E, respectively) were filtered, washed with water, ethanol and acetone, and, in the cases of thiomont D and E, further washed by Soxhlet extraction for 24 hours over a 3:1 ethanol/water mixture. It is of interest to note that thiomont samples were blue-green when soaked in ethanol, but became white when dried.

Characterization

Elemental analysis and XRF data for the thiomont samples are shown in Tables 3.9 and 3.10, respectively. These data confirm that Cl was completely substituted for SH by the reaction of NaSH with chloromont. The carbon content was slightly lower in the thiomont samples, possibly due to the hydrolysis of some silane moieties on the clay caused by the refluxing in ethanol.

^{13}C NMR spectroscopy shows three signals at 12, 23, and 40 ppm, corresponding, as in the case of chloromont, to the three carbons of the propyl chains (Figure 3.17a). The dipolar dephasing experiment performed on this compound showed, in contrast to chloromont, a very rigid conformation for the carbon chains since the signals decay significantly upon the application of a 40 μs dephasing time (Figure 3.17b). This

observation, in light of the reduced carbon content in thiomont with respect to chloromont, reinforces the hypothesis that the more mobile externally grafted moieties have indeed been removed and that the thiopropyl chains that remain are located in the more confined internal surface areas of the clay particles.

The TGA profile of thiomont (Figure 3.18) showed, similarly to chloromont, two mass losses above 300 °C. In this case, however, the first loss is only of about 7% (compared to 12% for chloromont), while the second loss is of about 8% (the same as in chloromont). These observations are consistent with the loss of externally grafted carbon chains, which would be expected to have less thermal stability than those present inside the clay structure, while the interlamellar thiopropyl groups have remained intact. It can thus be proposed that the first mass loss observed between 300 and 350 °C corresponds to moieties which are grafted in the mesopore regions of the clay (between the clay particles) and that the second mass loss between 350 and 600 °C corresponds to those located in the more confined interlamellar region.

Thus, because of its analogy with that of chloromont, the approximate chemical formula of thiomont can be deduced as $Si_{7.8}Al_{3.3}Fe_{0.3}Mg_{0.4}O_{20}(OH)_4 \cdot 4[Si(OH)_2(CH_2)_3SH]$, or $Si_{7.8}Al_{3.3}Fe_{0.3}Mg_{0.4}O_{20}[O(Si(OH)_2(CH_2)_3SH]_4$ (by considering that the structural OH groups of montmorillonite participate in the grafting process.

Table 3.9 C and H analyses of chloromont and thiomont samples.

	C (weight %)	H (weight %)	H/C (mole/mole)	H/C[a] (mole/mole)
Chloromont-C	6.97	1.65	2.82	1.79
Chloromont-D	13.31	2.44	2.18	1.83
Thiomont-C	4.09	1.17	3.41	1.38
Thiomont-D	11. 47	2.20	2.29	1.81

[a]H/C ratio calculated by subtraction of the structural hydrogens of montmorillonite (0.83%), assuming the presence of $Si(OH)_2(CH_2)_3Cl$ grafted moieties.

Table 3.10 X-ray fluorescence data for chloromont and thiomont samples (results expressed in molar ratios)

	Fe	Ca	P	Si	Al	Cl	S
Cloromont-A	0.129	0.087	0.312	5.16	1.00	1.97	-
Chloromont-B	0.135	0.081	0.304	4.02	1.00	0.287	0.147
Chloromont-C	0.200	0.082	0.254	4.22	1.00	0.625	0.152
Chloromont-D	0.175	0.122	0.328	5.61	1.00	1.95	0.201
Thiomont-C	n.d.	n.d.	n.d.	2.85	1.00	n.d.	0.393
Thiomont-D	0.211	0.100	0.259	5.32	1.00	-	2.29

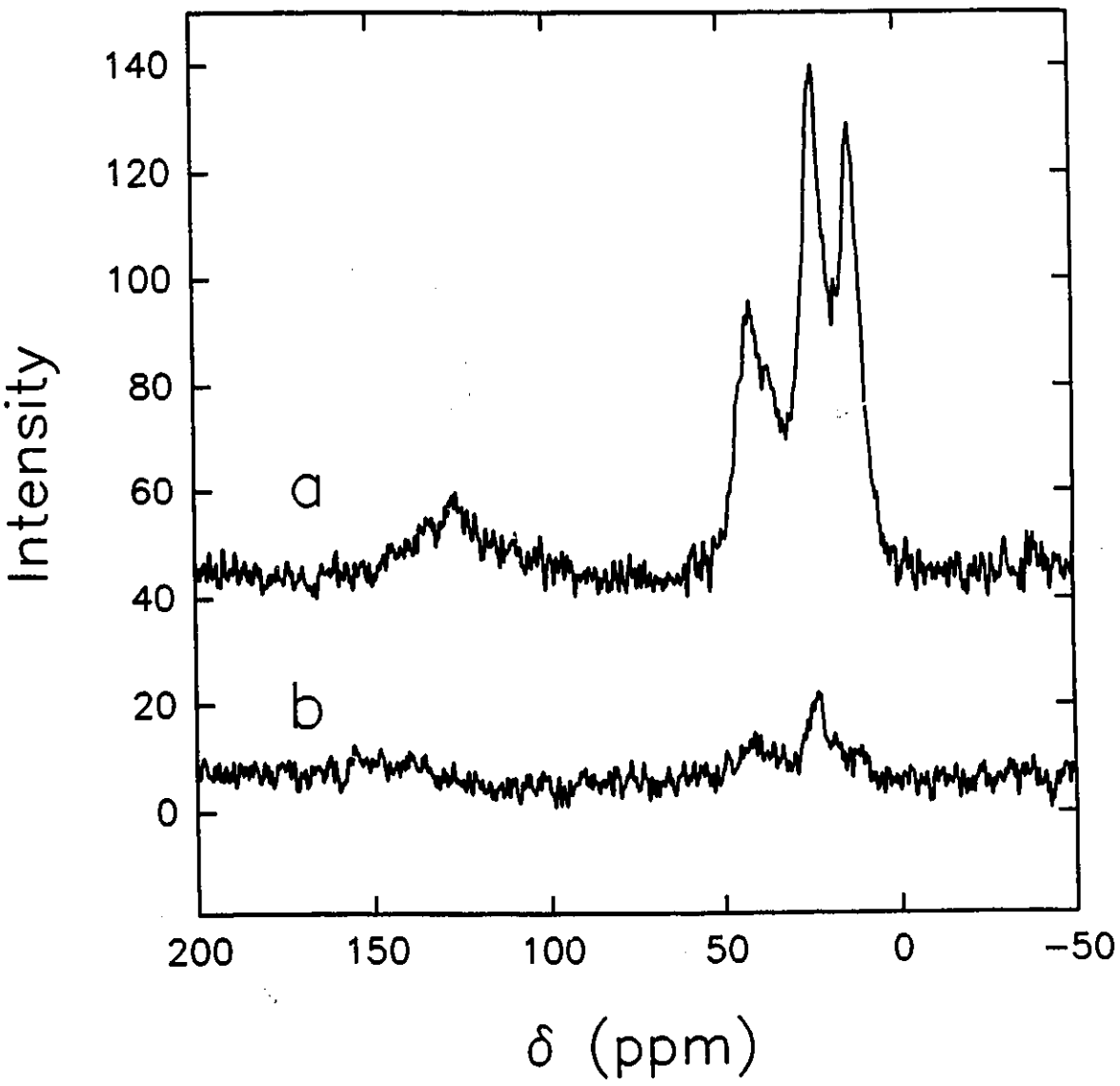

Figure 3.17 ^{13}C NMR spectra of thiomont using (a) CP-MAS (regular spectrum) and (b) dipolar dephasing (t_1 = 40 μs).

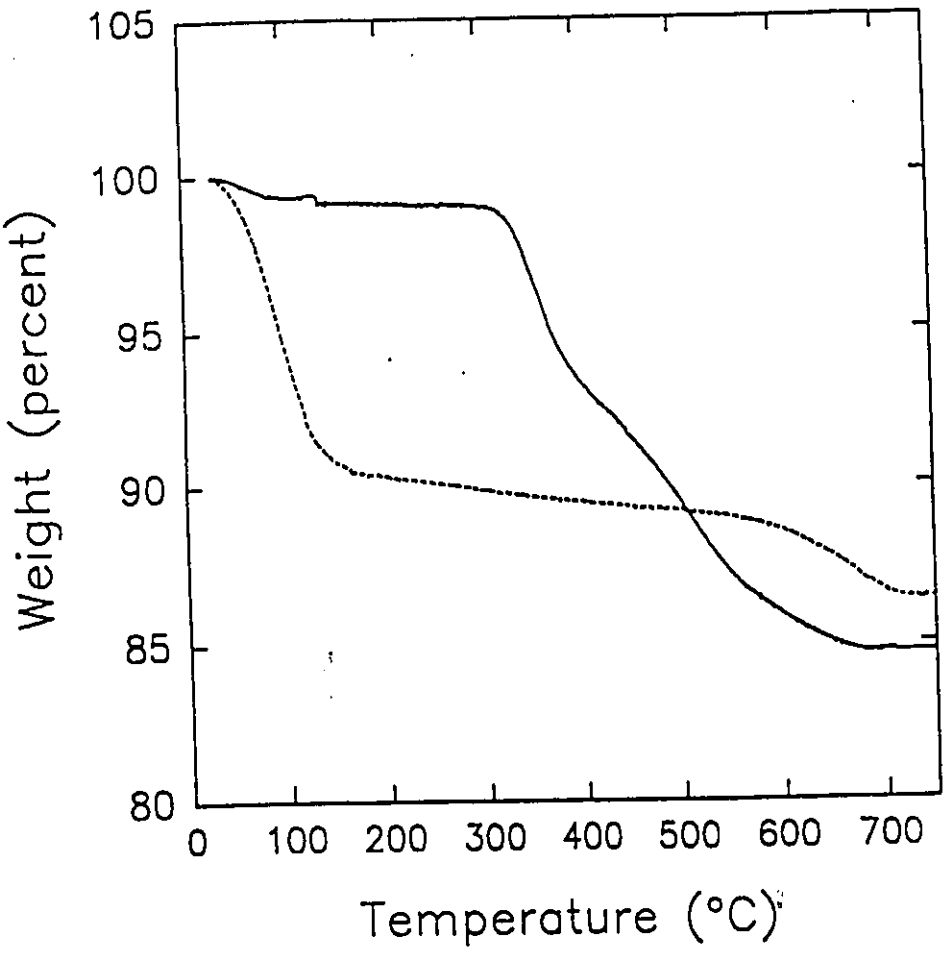

Figure 3.18 TGA profile for thiomont (solid curve), compared with that of H-montmorillonite (dashed curve).

3.3.3.2 Ethanedithiomont: SCH_2CH_2SH functionalization

0.1 g of chloromont-A was refluxed in 15 ml ethanol with 0.5 g ethanedithiol [$HS(CH_2)_2SH$] and 0.21 g NaOH for 72 hours. The product ("ethanedithiomont") was centrifuged and washed several times with water, ethanol and, finally, with acetone.

3.3.3.3 Cyclam-6-mont: cyclic amine functionalization

It has been reported by Izatt *et al.* that the covalent binding of aza-crowns to silica gels afforded materials which were effective for the selective recovery of heavy metals.[184] In this study, the grafting of such a molecule to montmorillonite was attempted.

Cyclam-6 (Figure 3.19) was prepared using the synthetic procedure reported by Bradshaw *et al.*[184-186] 0.2 g of chloromont-A was refluxed in 20 ml acetonitrile with 0.15 g of cyclam-6 for 48 hours. The resulting gold-coloured compound (cyclam-6-mont) was filtered and washed with acetonitrile and acetone.

The TGA profile for cyclam-6-mont was indistinguishable from that of chloromont, showing an identical total mass loss resulting from the combustion of the grafted organic moieties. One would expect, if cyclam-6 molecules were grafted to the material, a significantly greater mass loss compared to that of chloromont due to the very large size of the species. It was thus concluded that the substitution of Cl for cyclam-6 moieties was not successful. The bulky dimensions of the molecule would seem to prevent access to the interlayer grafting sites.

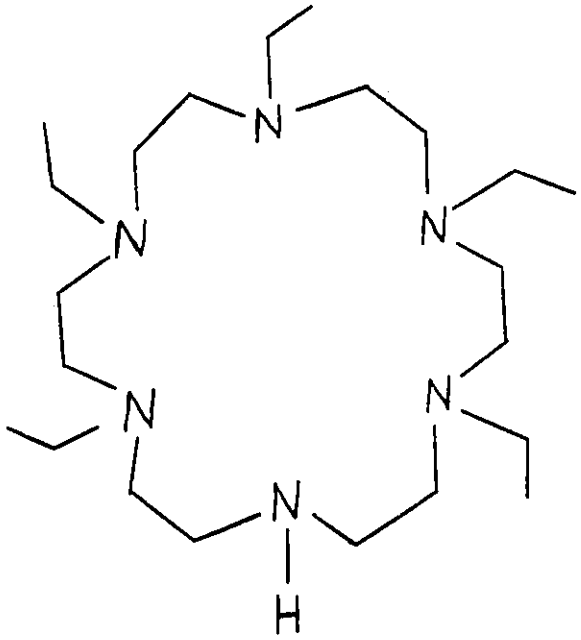

Figure 3.19 Cyclam-6

3.3.4 Environmental application of grafted smectites: heavy metal adsorption

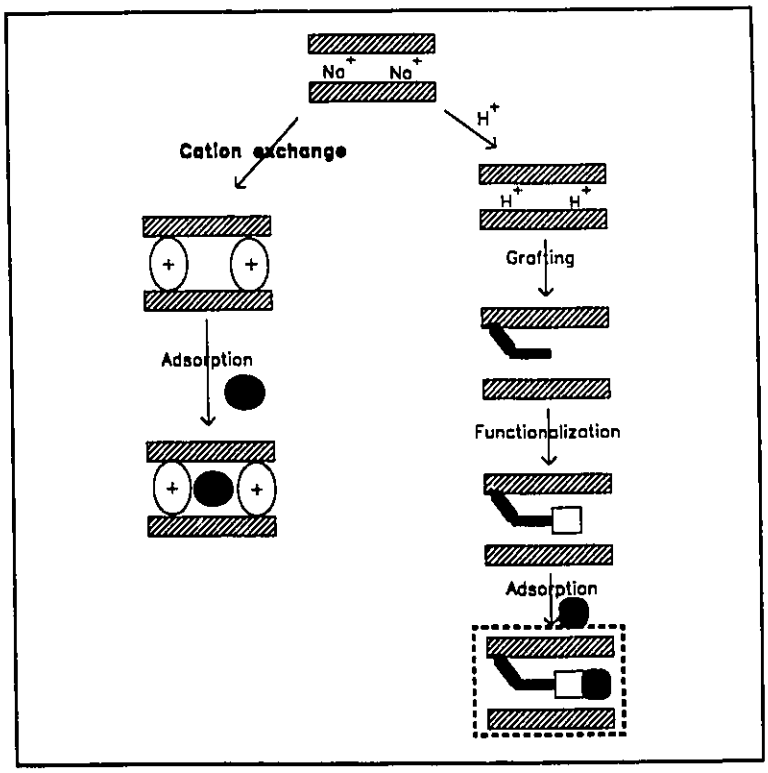

Having been characterized, the grafted clay sorbents can be tested for their affinity for the adsorption of heavy metals. In this section, the interaction of these materials, thiomont in particular, with metals of environmental importance (Pb, Hg, Cd and Zn) is explored. The effects of pH and salinity on these adsorptions will be discussed, as well as how the adsorbents can be regenerated for multiple use.

3.3.4.1 Derivation of heavy metal adsorption isotherm equation

The interaction of metals to the grafted clay adsorbents is expected to involve their chelation to the functional groups anchored to the surfaces of the clay. A Langmuir-type isotherm model can be proposed since, once all of the available adsorption sites become occupied with metal atoms, no further adsorption of the metal would be expected. Also, it is supposed that all of the adsorption sites are equivalent to each other such that no specific site can preferably capture metal ions over another.[187,188]

Thus, after equilibrium, let a fraction of the adsorption sites X/X_m be occupied by a metal ion, where X is the amount of metal bound to the adsorbent under the equilibrium conditions and X_m the maximum loading capacity (the saturation limit) of the adsorbent, both expressed in mg of metal per g of adsorbent. It therefore follows that a fraction of $1-X/X_m$ of the available adsorption sites will not be occupied by a metal ion. The adsorption rate constant will be proportional to the concentration of metal in the solution (C) as well as to the the fraction of available adsorption sites. The rate of adsorption r_a can thus be expressed as

$$r_a = k_a C (1-X/X_m) \quad (1)$$

where k_a is an adsorption rate constant.

The rate of desorption (r_d) is proportional to the fraction of occupied adsorption sites, such that

$$r_d = k_d X/X_m \quad (2)$$

Under equilibrium (steady-state) conditions, $r_a = r_d$, so

$$k_a C (1-X/X_m) = k_d X/X_m \quad (3)$$

Allowing the equilibrium constant k_a/k_d to be written as b, the previous equation can be rearranged as

$$X/(X_m-X) = bC \quad (4)$$

or

$$X = X_m bC/(1+bC) \quad (5)$$

The adsorption isotherm parameters b and X_m can be determined by plotting C as a function of X, where C is the equilibrium metal concentration of a metal solution/ adsorbent system (i.e. the concentration left over after treatment with the adsorbent, in mg/L) and X the amount of metal adsorbed (in mg/g of adsorbent), and fitting the experimental data points to the curve defined by equation (5).

The product of b and X_m can be defined as K_a, a new adsorption equilibrium constant normalized with respect to the maximum adsorption value of the metal-sorbent system. Note that this equilibrium constant is purely phenomenological, with no real physical significance.

Its values can only be used to make relative comparisons between different metal-adsorption processes.

3.3.4.2 Adsorption of heavy metals by grafted clay adsorbents

Methods

0 to 20 ppm solutions of metal nitrate salts (Pb^{2+}, Hg^{2+}, Cd^{2+} and Zn^{2+}) were prepared in distilled water. In the case of $Hg(NO_3)_2$, nitric acid was added to the solution in order to prevent oxide formation, such that the pH of the mother liquor was about 3. Aliquots of these solution (25 or 50ml) were stirred in the presence of accurately weighed amounts of adsorbent (2.5 to 5 mg) at room temperature for 18 hours. The metal concentrations were measured before and after treatment with the adsorbent. Hg and Cd concentrations were determined by ICP emission spectroscopy, whereas Pb and Zn were quantitated using atomic absorption spectroscopy (AAS).

In this manner, the adsorption isotherms of Pb, Hg, Cd and Zn with thiomont (Figure 3.20) were plotted using equation (5) and the data shown in Tables 3.11, 3.12, 3.13 and 3.14. Likewise, adsorption isotherms of Pb and Zn with ethanedithiomont (Figure 3.21) were determined using the data shown in Tables 3.15 and 3.16. As a control experiment, the adsorption isotherm of Pb to chloromont was also plotted using the data from Table 3.17 (Figure 3.22). A summary of all of these adsorption systems, featuring the Langmuir parameters X_m and K_a, is shown in Table 3.18. It is to be noted that the scatter in the data points has resulted in relatively large uncertainties in these parameters, particularly for the

equilibrium constants. The X_m parameters were found to have 10 to 20 % uncertainties associated with their values. Similar values can be calculated by simply averaging the adsorption values of the points located on the maximum adsorption plateau. The Langmuir parameters shown here are intended to give some quantitative feel for the tabulated adsorption processes and are not meant to be viewed as values of utmost statistically precision.

Table 3.11 Adsorption of Pb(II) by thiomont.

C_i(Pb) (mg/L)	C(Pb) (mg/L)	mass of thiomont (mg)	Pb adsorbed (mg)	X(Pb) (mg/g)
0.27	<0.01	20.0	0.27	1
0.94	0.05	5.5	0.89	16
1.05	<0.03	5.3	1.05	20
5.05	0.60	5.2	4.45	86
6.28	2.46	5.0	3.82	76
10.33	7.85	5.0	2.48	50
12.04	7.48	2.2	0.11	52
15.21	10.21	6.0	4.70	78

Table 3.12 Adsorption of Hg(II) by thiomont.

C_i(Hg) (mg/L)	C(Hg) (mg/L)	mass of thiomont (mg)	Hg adsorbed (mg)	X(Hg) (mg/g)
2.1	0.8	2.6	0.03	13
5.7	0.6	2.7	0.13	47
8.9	1.1	2.6	0.20	75
14.4	5.9	2.6	0.21	82
18.0	13.0	2.2	0.13	57
20.9	14.9	2.2	0.15	68

Table 3.13 Cadmium adsorption by thiomont.

C_i(Cd) (mg/L)	C(Cd) (mg/L)	mass of thiomont (mg)	Cd adsorbed (mg)	X(Cd) (mg/g)
2.22	0.89	3.1	0.067	21
6.00	4.28	3.1	0.086	28
14.42	10.23	3.5	0.10	31

Table 3.14 Adsorption of Zn(II) by thiomont.

C_i(Zn) (mg/L)	C(Zn) (mg/L)	mass of thiomont (mg)	Zn adsorbed (mg)	X(Zn) (mg/g)
4.18	2.42	3.0	0.044	15
8.04	6.13	3.4	0.048	14
12.33	10.05	3.7	0.057	15
16.49	14.13	3.7	0.059	16
21.00	17.75	4.3	0.081	19

Table 3.15 Adsorption of Pb(II) by ethanedithiomont.

C_i(Pb) (mg/L)	C(Pb) (mg/L)	mass of thiomont (mg)	Pb adsorbed (mg)	X(Pb) (mg/g)
2.87	0.08	2.5	0.070	28
5.67	1.45	2.6	0.11	41
8.52	3.44	2.6	0.13	49
11.48	6.34	2.7	0.13	48
14.29	9.04	2.8	0.13	47

Table 3.16 Adsorption of Zn(II) by ethanedithiomont.

C_i(Zn) (mg/L)	C(Zn) (mg/L)	mass of thiomont (mg)	Zn adsorbed (mg)	X(Zn) (mg/g)
4.18	2.76	3.2	0.036	11
8.04	6.48	3.6	0.039	13
12.33	10.49	3.7	0.046	12
16.49	14.21	4.6	0.057	12
21.00	18.34	5.0	0.067	13

Table 3.17 Adsorption of Pb(II) by chloromont.

C_i(Pb) (mg/L)	C(Pb) (mg/L)	mass of thiomont (mg)	Pb adsorbed (mg)	X(Pb) (mg/g)
2.87	1.69	4.1	0.030	7.2
5.67	4.45	4.4	0.031	6.9
8.52	6.30	4.4	0.056	13
11.48	9.86	4.6	0.041	8.8
14.29	12.06	6.2	0.056	9.0

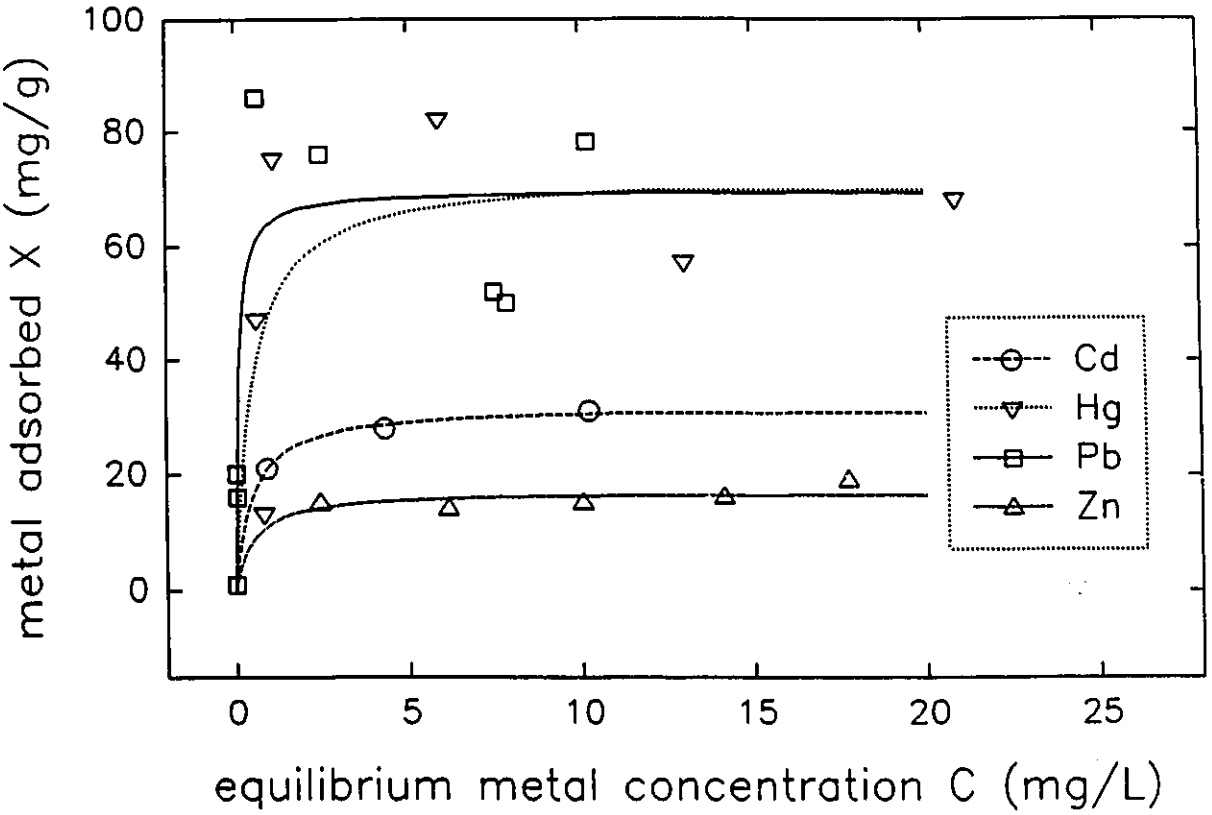

Figure 3.20 Langmuir adsorption isotherms for thiomont adsorption of (a) Pb^{2+}, (b) Hg^{2+}, (c) Cd^{2+} and (d) Zn^{2+}.

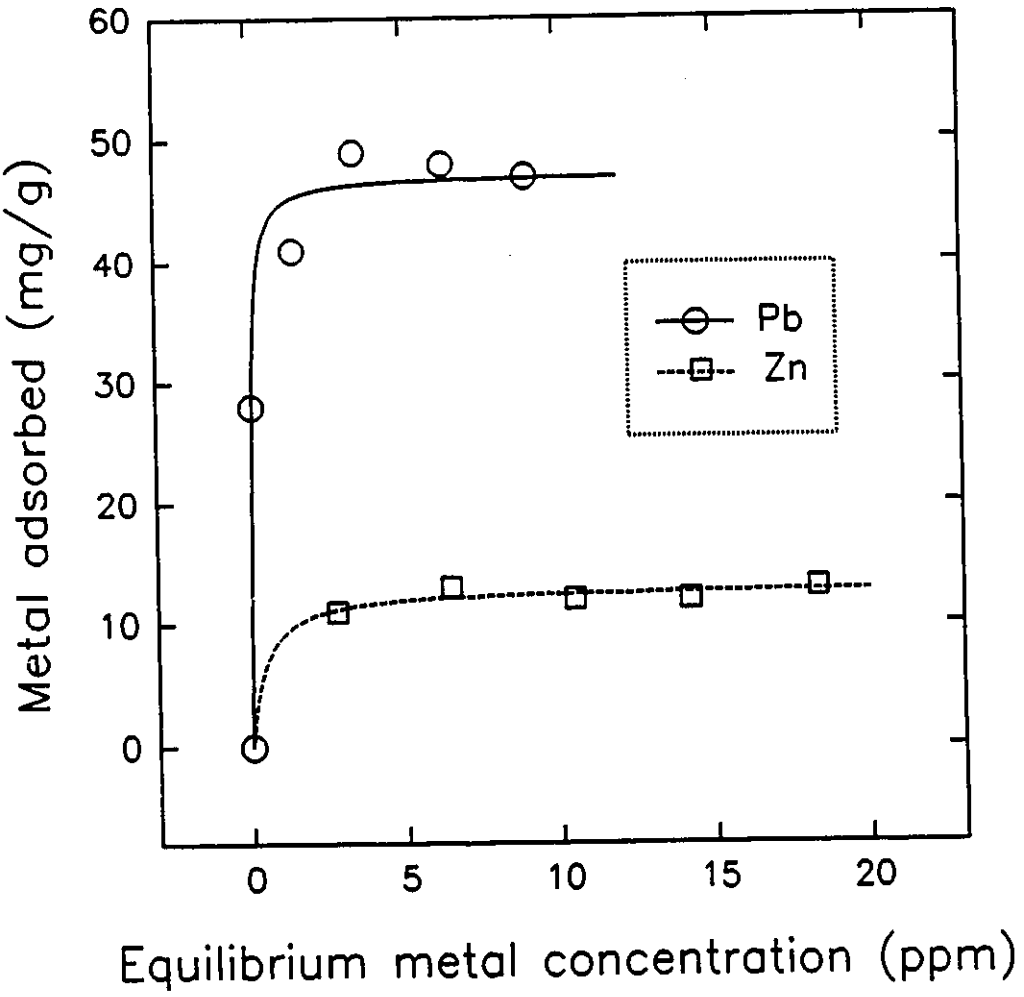

Figure 3.21 Langmuir adsorption isotherms for ethanedithiomont adsorption of (a) Pb^{2+} and (b) Zn^{2+}.

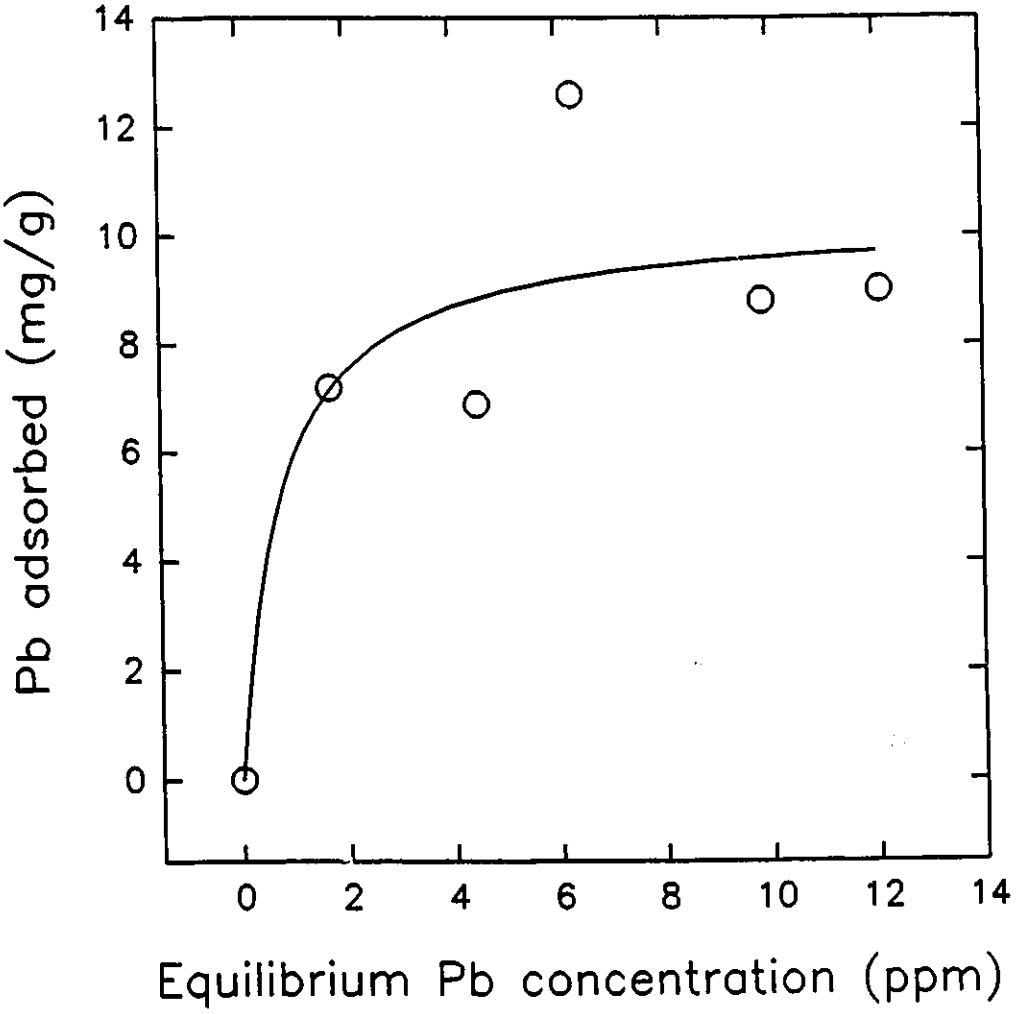

Figure 3.22 Langmuir adsorption isotherms for chloromont adsorption of Pb^{2+}.

Table 3.18 Langmuir isotherm parameters for metal adsorption (asterisks denote parameters calculated on the basis of equivalent rather than mass concentration units).

Adsorbent	Metal	b	X_m (mg/g)	X_m^* (meq/g)	K_a	K_a^*
Thiomont	Pb	11.9	70	0.68	830	8.1
	Hg	2.1	72	0.72	150	1.5
	Cd	2.1	32	0.57	67	1.2
	Zn	2.1	17	0.52	36	1.1
Ethanedithiomont	Pb	17.6	47	0.45	830	7.9
	Zn	2.4	13	0.40	31	1.0
Chloromont	Pb	1.4	10	0.097	14	0.14

Thiomont

A preliminary observation which can be made upon inspection of the isotherms (Figure 3.20) is that, in all cases, an adsorption plateau is reached on the isotherm plots following a rapid ascent at low concentration values. This profile is in agreement with the Langmuir isotherm model, so it may be claimed that the mathematical equation derived in section 3.3.3.1 is valid for these adsorption experiments.

Tables 3.11 and 3.12 show that Pb and Hg are both virtually completely adsorbed by thiomont in low concentration solutions. In comparison, Tables 3.13 and 3.14 show significant residual levels of Cd and Zn at all of the concentrations. This suggests that thiomont has a considerably higher affinity for mercury and lead than for cadmium and zinc, an observation which is substantiated by the significantly higher K_a values for Hg and Pb than for Cd and Zn (Table 3.18). Moreover, the metal saturation levels (X_m) for Pb and Hg are somewhat higher than those of Cd and Zn. It thus appears evident that "softer" metal ions are more strongly adsorbed than "harder" ones, as indicated by the decreasing K_a trend observed from Pb to Zn (Pb > Hg > Cd > Zn).

A truer comparison between the adsorption systems can be made by considering the parameters derived from the equivalent molar concentrations of the metals instead of their mass concentration (X_m^* and K_a^* from Table 3.18). Thus, it is observed that the saturation levels of the metals (X_m^*) are within close range of each other, but with those Pb and Hg still being somewhat greater than those of Cd and Zn. The adsorption constants (K_a^*), however, show that Pb has a much higher binding affinity than all of the other metals, whereas that of Hg is only slighly higher than Cd and Zn. It must be noted, however, that the Hg

solutions were at lower pH than the other metal solutions, a condition which is likely to have reduced the adsorptivity of the metal (as will be demonstrated in section 3.3.3.3). These results further demonstrate the selectivity of thiomont for Pb over Cd and Zn. It would be expected that the binding affinity of Hg, although still higher than that of Cd and Zn, be greater under neutral pH conditions.

By considering the chemical formula proposed in section 3.3.2.2, it can be calculated that thiomont has approximately 6 mmoles/g of SH functionalities. The metal adsorption values found in this study, however, show that only about 0.3 mmol/g of metal ions are adsorbed by thiomont. Thus, only one metal ion is bound for about every twenty sulfhydryl groups anchored to the clay surface. This low metal to binding site ratio can be attributed to the participation of many SH groups in the binding of a metal ion: the larger ionic radii of Pb^{2+} and Hg^{2+} compared to Cd^{2+} and Zn^{2+}, compounded with their increased "softness", would indeed favour the interaction of more sulfhydryl functionalities with these species. This situation, depicted in Figure 3.23, would also rationalize the greater binding affinity of Pb and Hg to the adsorbent. Another possible explanation for the low metal content could be that some of the binding sites are located in areas which are not accessible to the metal ions.

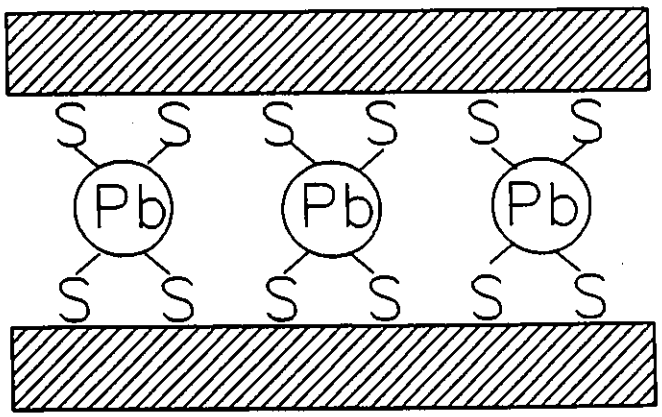

a

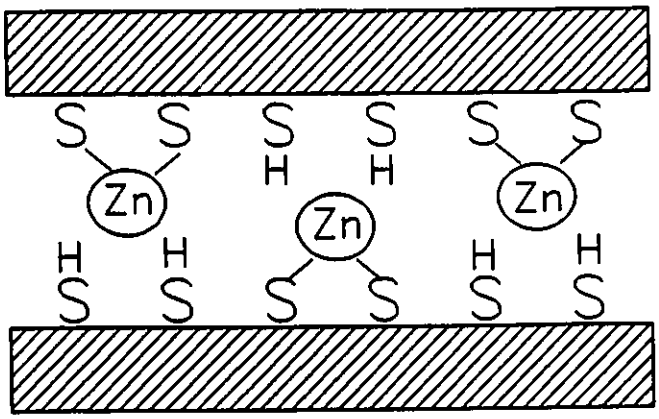

b

Figure 3.23 Representation of a binding site in thiomont interacting with (a) large ions and (b) smaller ions.

Ethanedithiomont

The data shown in Tables 3.15 and 3.16 gave adsorption isotherms (Figure 3.21) which were very similar to those of the corresponding thiomont studies. The adsorption parameters shown in Table 3.18 were also very similar to those of thiomont, showing strong adsorption of Pb and a weaker attraction towards Zn.

Similar conclusions to those of thiomont can thus be made with regards to the heavy metal adsorption by ethanedithiomont. A notable difference between thiomont and ethanedithiomont is a substantially lower maximum adsorption values (X_m) for both Pb and Zn for the latter (about 40% lower). This can be attributed to the fact that the ethanedithiomont groups are substantially larger than the thiol groups, resulting in increased steric bulk in the pores of the grafted clay and inhibiting access of the metal to the adsorption sites.

Chloromont

As expected, chloromont shows virtually negligeable adsorption of Pb, with a very weak interaction with the material (Table 3.17, Figure 3.22). It is therefore clear that the adsorption process is driven exclusively by the nature of the functional unit grafted onto the clay and not through interaction with the clay mineral surface.

3.3.4.3 Effect of pH on metal adsorption.

Lead nitrate solutions of various pH were prepared by the addition of nitric acid to a stock solution. These were treated with thiomont and the lead concentrations determine before and after treatment, as described in section 3.3.3.2. The results of this experiment are shown in Table 3.19 and Figure 3.24.

The trend of these results clearly demonstrate that acidic conditions significantly reduce the effectiveness of the adsorbent, essentially reducing the maximum adsorptivity of thiomont by 50 % upon reducing the pH to about 3. Since environmental pH values are almost always greater than 3, the usefulness of thiomont as an adsorbent would thus not be precluded.

It can be postulated that there is a competing process between H^+ and metal ions to the binding sites of thiomont which can inhibit the chelation of the metals to the SH functions, with the increased H^+ concentration of the medium shifting the following equilibrium to the left:

$$\text{Mont-SH} + M^{2+} \rightleftarrows \text{Mont-SM}^+ + H^+$$

In light of the extremely low metal concentrations targeted by this study, this hypothesis would not seem unlikely.

These observation therefore lay the groundwork for a simple method of regenerating spent thiomont by leaching the adsorbed metal via acid treatment, as will be discussed in a further section.

Table 3.19 Effect of pH on lead adsorption by thiomont.

pH	C_i(Pb) (mg/L)	C(Pb) (mg/L)	mass of thiomont (mg)	Pb adsorbed (mg)	X(Pb) (mg/g)
7.4	12.04	7.48	2.2	0.11	52
5.5	12.38	7.95	2.4	0.11	46
4.0	12.94	10.26	2.4	0.067	28
3.4	13.32	10.27	2.3	0.076	33
2.9	12.77	10.67	2.3	0.053	23

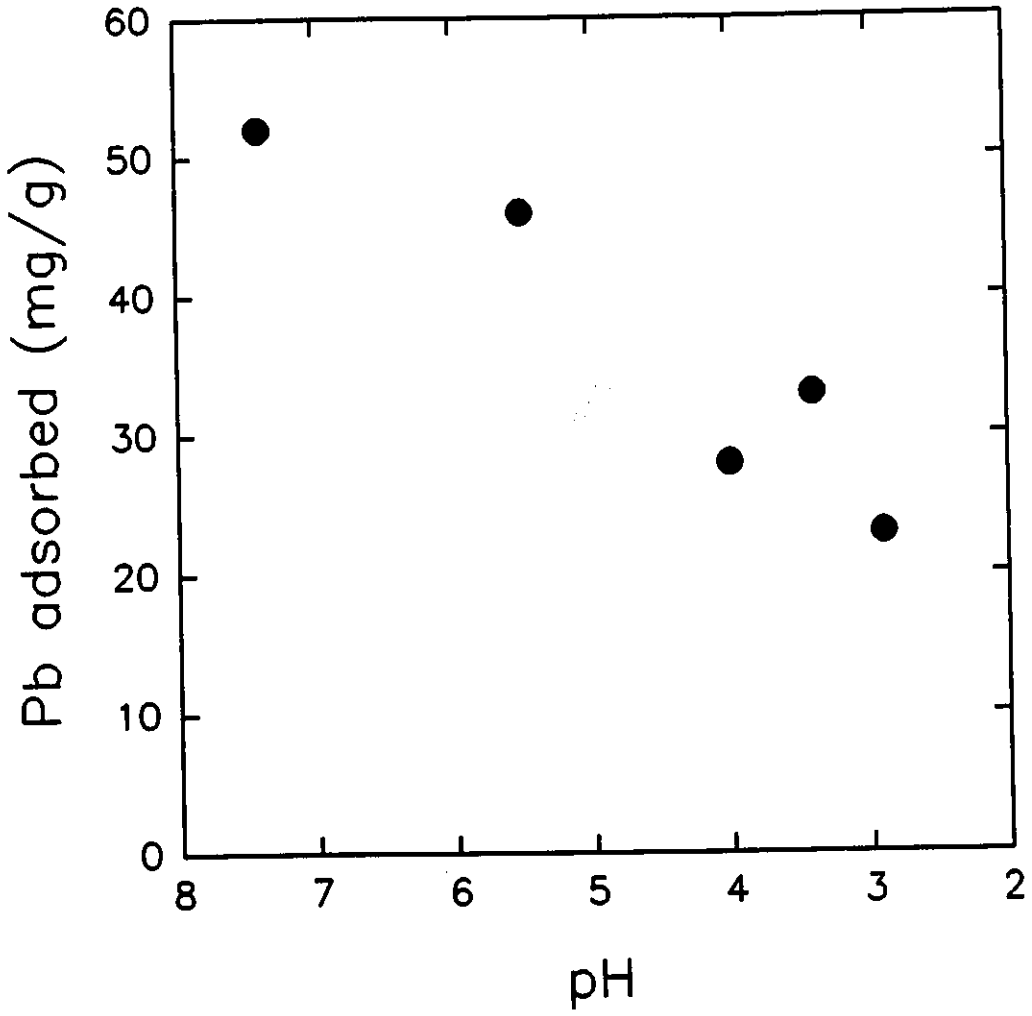

Figure 3.24 Effect of pH on lead adsorption by thiomont.

3.3.4.4 Effect of salinity on metal adsorption.

Another factor which must be taken into account if one is to consider the practical application of thiomont as a heavy metal adsorbent is that of the ambient salinity of the medium. Many ionic species such as Na^+, Ca^{2+} and K^+ are ubiquitous in the environment: in this experiment, the effect of a reasonably large concentration of NaCl on Pb adsorption will be studied.

Thus, Pb^{2+} solutions containing 100 ppm Na^+ (in the form of NaCl) were prepared and treated with thiomont. The Pb adsorption results are shown in Table 3.20 and the adsorption isotherm plotted in Figure 3.25.

The results show, in comparison with the previous Pb adsorption study, significant residual Pb levels even at low concentrations. The calculated K_a value was 76, much lower than the value of 830 calculated in Table 3.18. The maximum Pb adsorption value, however, was found to be 55 mg/g, reasonably close to the 70 mg/g value previously obtained. These results show that the presence of a comparatively large amount of sodium does not affect the total sorbability of Pb to thiomont (i.e. the Na^+ ions do not compete for the occupation of the adsorption sites) but does inhibit the accessibility of the lead ions to these sites.

Table 3.20 Adsorption of Pb(II) by thiomont in the presence of 100 ppm Na^+.

C_i(Pb) (mg/L)	C(Pb) (mg/L)	mass of thiomont (mg)	Pb adsorbed (mg)	X(Pb) (mg/g)
2.35	0.22	2.8	0.053	15
5.18	0.93	2.9	0.11	29
6.67	1.34	3.0	0.13	35
9.19	2.60	3.0	0.16	44
12.01	4.23	3.3	0.19	47

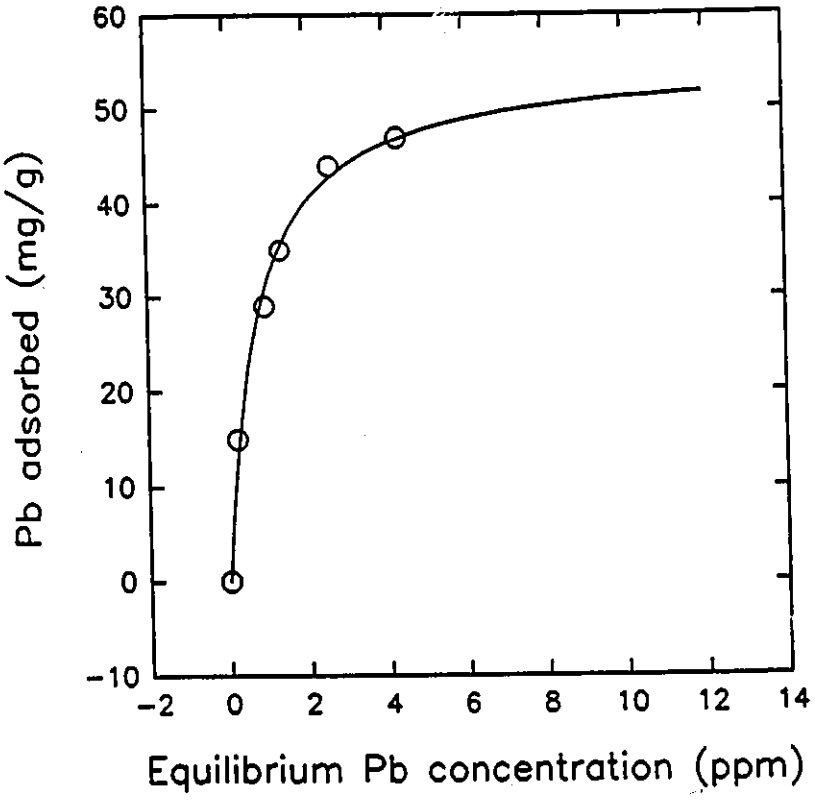

Figure 3.25 Adsorption isotherm of Pb^{2+} treated with thiomont in the presence of 100 ppm Na^+.

3.3.4.5 Regeneration of thiomont

A thiomont sample (0.5 g) was treated with a concentrated lead nitrate solution (about 2g in 50 ml) in order to produce a fully lead-loaded thiomont. The Pb-thiomont was then stirred with 1.0 and 0.10 M HCl for 18 hours in order to leach the samples of adsorbed lead. The leached thiomont was then once again put in presence of a lead solution so that the reusability of the material could be tested. At each step, after thorough water washing and drying at 130 °C overnight, the Pb content was determined (in reference to the S, Si and Al content of the material) by X-ray fluorescence (Table 3.21).

Table 3.21 thus shows that, upon treating the lead-loaded thiomont with both 1.0 and 0.10 M HCl, all of the lead is leached out of the sample. Retreating the leached sample with lead solution once again resulted in the formation of Pb-thiomont, but with only half of the lead content with respect to the first loading experiment. In both Pb-thiomont samples, the S contents were identical, showing that the thiomont structure is not altered by the acid treatment. The lower Pb uptake in the second loading experiment can be attributed to the incomplete removal of acid from the leached thiomont, resulting in some inhibition of the metal adsorption.

Table 3.21 Molar ratios of elements measured by XRF, following the regeneration process of lead-loaded thiomont by acid leaching.

Sample	Al	Si	S	Pb
Thiomont	1.00	3.29	1.86	0
Pb-thiomont	1.06	3.24	1.22	0.15
1.0 M HCl-treated Pb-thiomont	1.00	3.22	1.58	0
0.10 M HCl-treated Pb-thiomont	1.00	3.26	1.35	0
Reloaded Pb-thiomont	1.00	3.24	1.19	0.075

Synopsis of Chapter 3.

Smectite minerals were chemically modified by the ion-exchange of tetraalkylammonium cations, producing hydrophobic organoclays with affinity for the adsorption of aromatic species from aqueous media. Such exchange reaction were also found useful for the physical characterization of smectite clay minerals, particularly for the facile determination of the internal surface areas of these species.

The grafting of thiol-functionalized organosilane moieties into the interlamellar surface of smectites has yielded a novel type of environmental adsorbent suitable for the effective removal of heavy metals (lead and mercury, in particular) from contaminated water systems.

4. LAYERED SILICATE SORBENTS

In this chapter, the preparation, characterization and applications as sorbents of novel layered silicate-based compounds will be discussed. Consistent with the general goal of this research, the synthetic aim will be the covalent attachment (grafting or anchoring)of molecular species in the interlamellar space of layered silicates. The two silicates used in these experiments were Na^+-magadiite and K^+-kenyaite, both prepared by synthetic procedures. For the sake of simplicity, these two compounds will henceforth be refered to simply as magadiite and kenyaite, respectively, in the remainder of this text: it should therefore be understood by the reader that these terms refer to the minerals synthesized by the procedures described in this thesis.

The process for performing grafting reactions on the interlamellar surface of layered silicates involves three fundamental steps, as outlined in Figure 4.1. The first is the treatment of the parent alkali metal silicate with dilute acid in order to fully hydroxylate the interlamellar region, thus forming the corresponding layered silicic acid. The abundant hydroxyl sites thus generated become the minerals' reactive sites onto which functional units could be anchored. The second step of the process is the swelling of the silicic acid by treatment with polar organic molecules (POM) such as DMSO, NMF or DMF. Thus, the strong hydrogen bonding network existing between the hydroxyl units on either sides of the silicate sheets can be broken and the layers become expanded, allowing other chemical species to enter the interlamellar region and react with the silanol groups. Hence, the third and final step of the grafting process is the treatment of this POM-silicate intercalate with

suitable reagents which can condense onto the surface hydroxy units to form grafted layered silicate derivatives.

In this chapter, the covalent anchoring of organosilanes and alcohol species will be discussed, including their preparation, characterization and potential applications as sorbents.

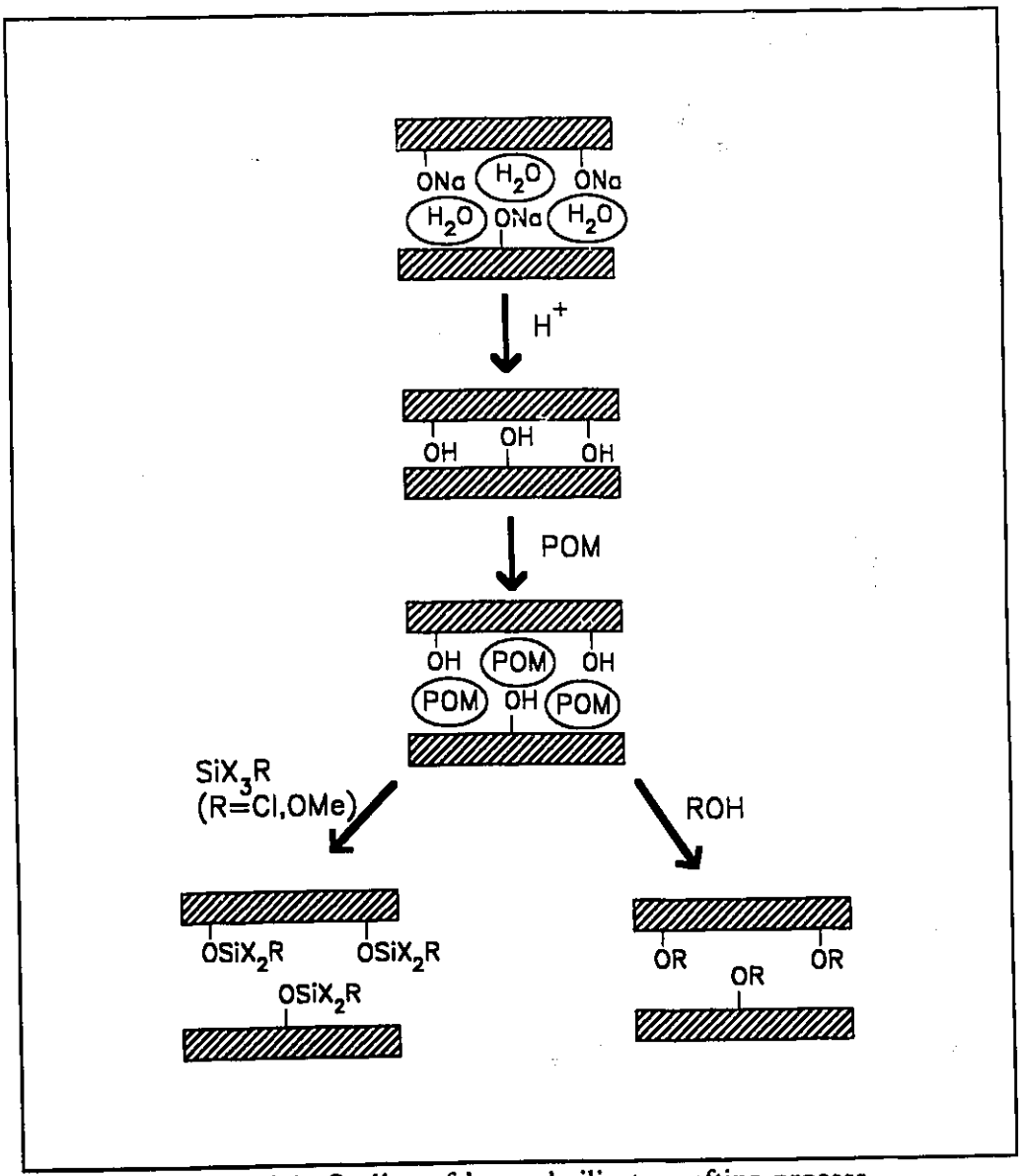

Figure 4.1 Outline of layered silicate grafting process.

4.1 Synthesis and Characterization of Na^+-Magadiite and K^+-Kenyaite

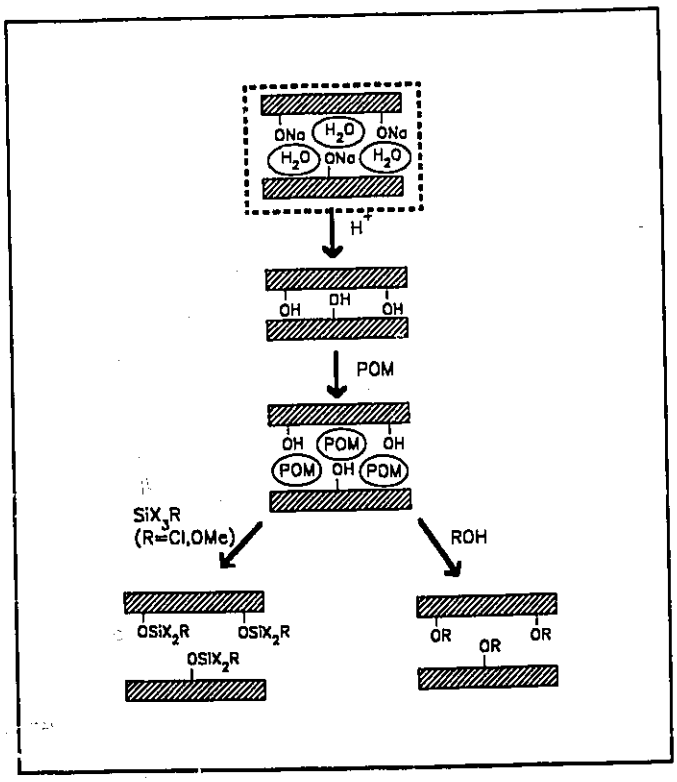

4.1.1 Synthesis

Magadiite was prepared by hydrothermal synthesis, following a similar procedure as those described in the literature.[132,135,137,140,189] Thus, 32.3 g of silica gel, 80 ml of distilled water and 4.0 g NaOH pellets were stirred in a Teflon-lined autoclave for 1 hour. The system was then sealed and heated in an oil bath at 150 to 205 °C for 19 to 120 hours (as shown in Table 4.1) with continuous stirring, the pressure inside the autoclave reaching about 100 psi (7 atm). The products thus obtained were a fine-grained white powder, in contrast to the original silica slurry which was greyish and somewhat translucent. The

magadiite was then filtered and washed with about 200 ml of pH 10 NaOH solution in order to expel excess NaOH and solubilized silica. The synthesis failed when the reaction temperature reached 205 °C, the coarse-grained white powder thus obtained being identified as a quartz-cristobalite-tridymite mixture (see section 4.1.2.1).

Table 4.1 Synthetic conditions of magadiite preparations.

Temperature	Time	Product
150 °C	120 hours	magadiite
185 °C	22 hours	magadiite
205 °C	19 hours	quartz / cristobalite /tridymite

Kenyaite was prepared by an analogous procedure to that of magadiite. Thus, 24.4 g of silica gel, 75 ml distilled water and 7.0 g KOH pellets were stirred for 1 hour in a Teflon-lined autoclave, followed by sealing and heating at 180 °C for 22 hours under autogenous pressure (about 7 atm). As in the case of magadiite, a white powder was obtained which was filtered and washed with pH 10 KOH solution.

4.1.2 Characterization

4.1.2.1 Magadiite

X-ray diffraction.

A sample of magadiite was dispersed in distilled water, verifying that the pH of the suspension remained slighly basic (so as to not leach out the sodium ions and convert the structure to H-magadiite) and the XRD pattern recorded.

The XRD pattern (Figure 4.2) confirmed the identity of the product as magadiite. The data were in excellent accordance with those of the literature for magadiite,[118,123,124,140,151,160,161] featuring a basal spacing (d_{001}) of 15.38 Å. Table 4.2 gives assignments of the observed diffraction peaks with hkl reflection planes, as well as a comparison of the observed spacing values and peak intensities with those of the literature. The match between both data sets is quite good, save for the presence of two peaks at 4.08 Å and 2.50 Å which do not correspond to any literature magadiite peak. These peaks do, however, correspond to cristobalite, a silica polymorph, which may have formed during the hydrothermal synthesis. The formation of cristobalite and quartz has been reported when magadiite is heated above 500 °C, with the subsequent transformation of these products to tridymite beyond 700 °C.[135] It is plausible that cristobalite was formed during the synthesis of magadiite, as some reports have encountered the formation of both cristobalite and quartz during the hydrothermal synthesis of layered silicates.[137,190] It may also be possible,

however, that the observed cristobalite impurity was *already* present in small quantity in the silica gel used in the preparation of the mineral.

The synthetic procedures used have thus been succesful in the preparation of essentially quantitative yields of highly crystalline magadiite, except for the case where the reaction temperature reached 205 °C. This failed reaction resulted in the formation of a mixture of quartz, cristobalite and tridymite, as identified in the XRD pattern (Figure 4.3). There thus exists an upper temperature limit for the synthesis of magadiite which lies somewhere between 185 and 205 °C.

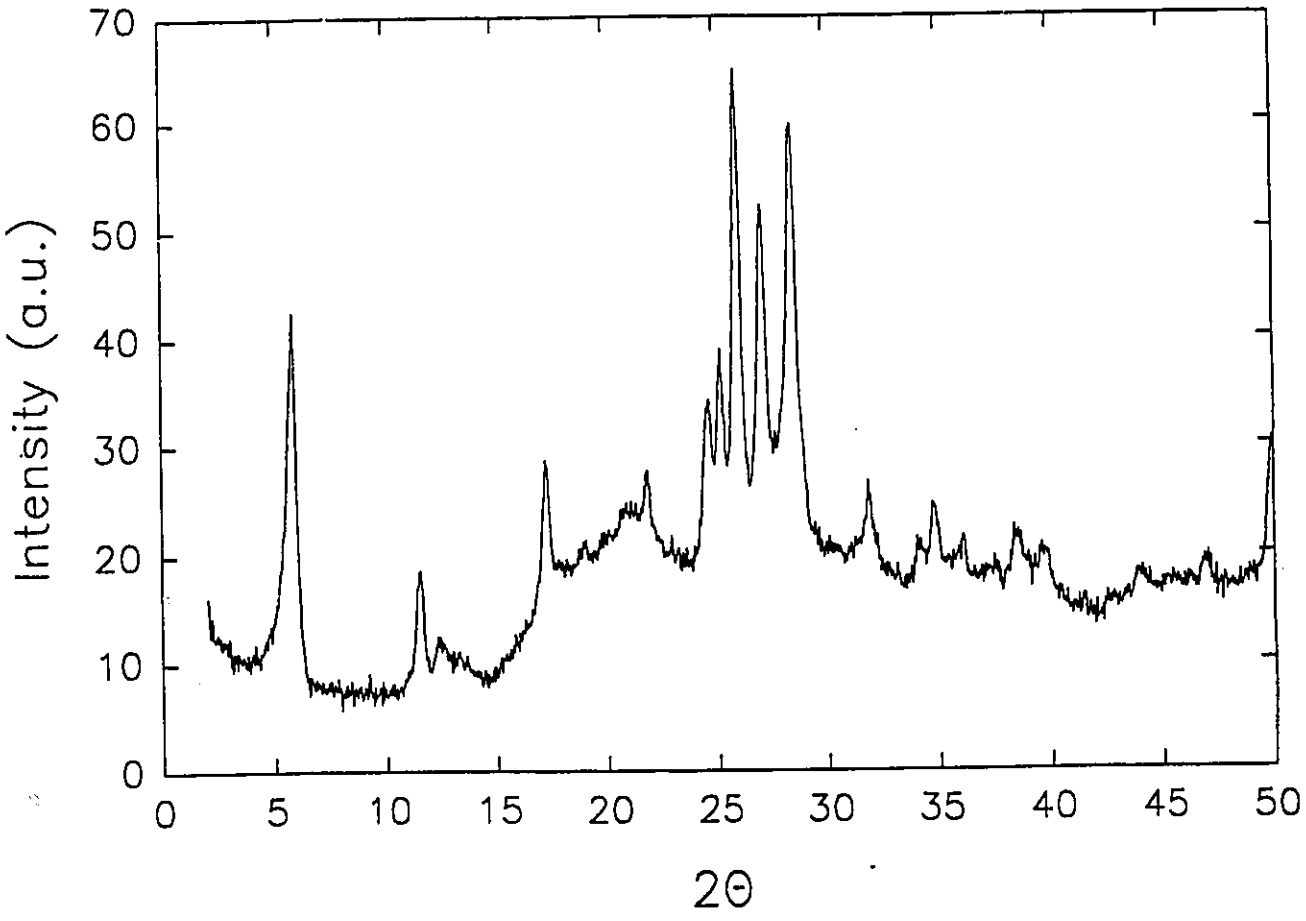

Figure 4.2 XRD pattern of magadiite

Table 4.2 Comparison of XRD patterns between magadiite prepared in this work and that obtained in the literature.

d_{obs}	I_{obs}	d_{lit}	I_{lit}	h k l	d_{obs}	I_{obs}	d_{lit}	I_{lit}	h k l
15.38	90	15.60	100	0 0 1	2.81	6	2.82	10	-1 2 3
7.75	12	7.77	10	0 0 2	-	-	2.74	4	1 0 5
7.22	4	7.24	6	0 1 0	2.63	4	2.64	2	0 2 4
-	-	5.64	4	-1 0 2	2.58	8	2.60	2	0 0 6
5.15	20	5.19	18	0 0 3	-	-	2.53	2	-1 0 6
-	-	5.01	14	1 0 2	2.50	3	-	-	Crist.
-	-	4.70	6	1 1 1	-	-	2.41	2	3 0 0
-	-	4.47	18	-1 0 3	2.35	6	2.35	4	1 0 6
-	-	4.23	4	0 1 3	2.27	3	2.27	2	3 1 0
4.08	10	-	-	Crist.	-	-	2.10	2	-1 1 7
-	-	4.01	8	1 0 3	2.06	2	2.07	2	1 3 3
-	-	3.92	4	0 0 4	-	-	2.00	4	2 0 6
3.64	20	3.63	14	0 2 0	-	-	1.97	2	2 3 1
3.56	30	3.54	20	0 2 1	1.93	4	1.94	2	-1 0 8
3.44	100	3.43	75	0 1 4	-	-	1.87	2	-1 1 8
3.30	60	3.30	40	0 2 2	1.82	14	1.82	8	1 0 8
-	-	3.20	12	-1 2 1	-	-	1.79	2	1 2 7
3.14	80	3.15	60	-2 0 3	-	-	1.74	2	-2 3 5
-	-	2.99	6	-1 0 5	-	-	1.70	2	-3 3 0
-	-	2.87	6	0 1 5	-	-	1.67	2	3 3 1

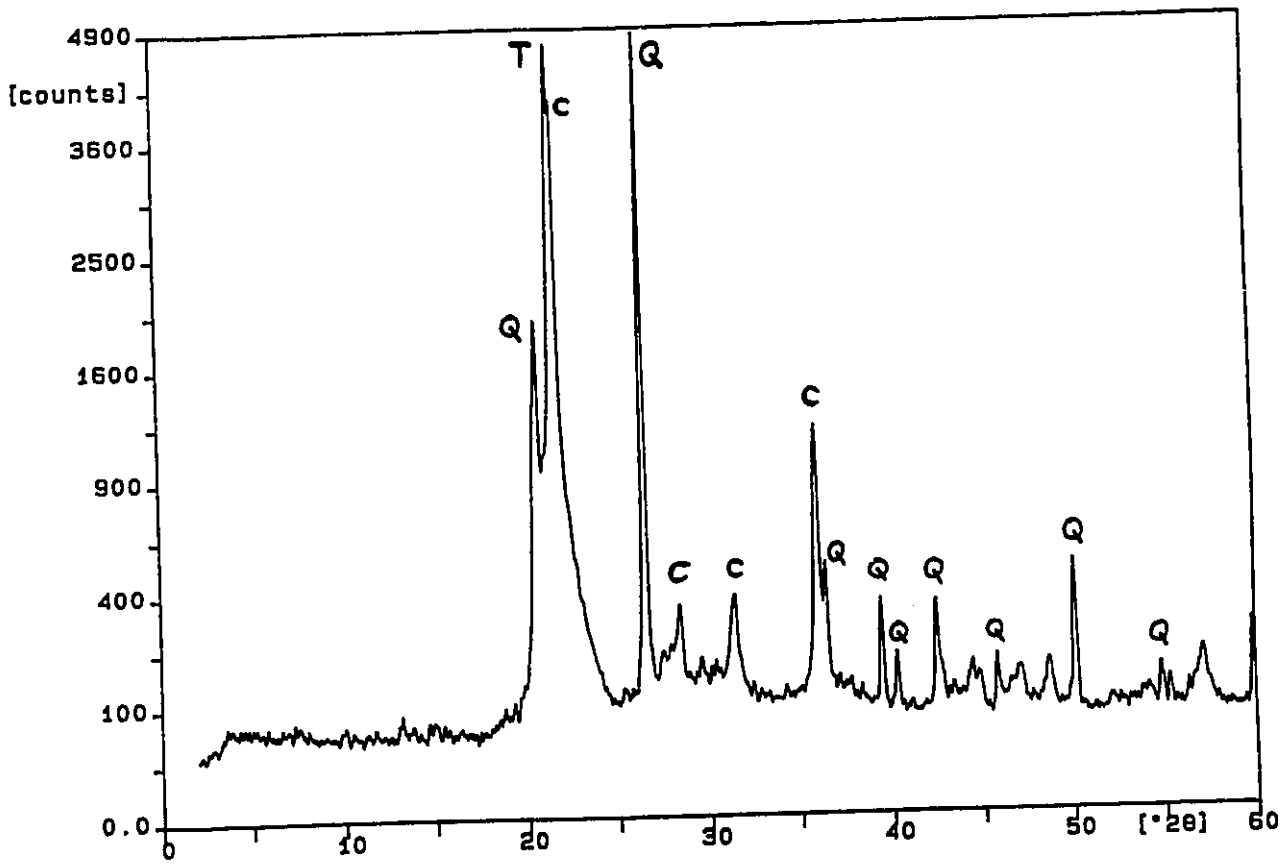

Figure 4.3 XRD pattern for failed magadiite synthesis attempt (at 205 °C). Q refers to quartz, C for cristobalite and T for tridymite.

Infrared spectroscopy

The FTIR spectrum of H-magadiite (Figure 4.4) featured a multitude of Si-O vibrational bands between 400 and 1200 cm^{-1}, a broad signal at 3400 cm^{-1} attributable to interlamellar water or hydrogen bonded OH groups and a sharper band at 3660 cm^{-1} corresponding to "free" OH stretching. All of these features were in accord with previously reported spectral data.[150-152,191]

Thermogravimetric analysis

The TGA curve of magadiite (Figure 4.5) featured a sudden mass loss of about 6% up to about 110 °C, immediately followed by a slightly more gradual drop of about 6% between 110 and 170 °C. Both of these events can be attributed to the dehydration of the structure, the former being the disappearance of physisorbed and loosely bound interlamellar water, the latter being the removal of more tightly held water molecules due to intercalative attraction force or coordination to the interlayer sodium ions. Another way of rationalizing this phenomenon is to consider the water bilayer present in the interlamellar region of magadiite: the first water layer can be considered easy to remove, whereas the second water layer can be more strongly retained through hydrogen bonding to the silicate surfaces or through hydration of the sodium ions.

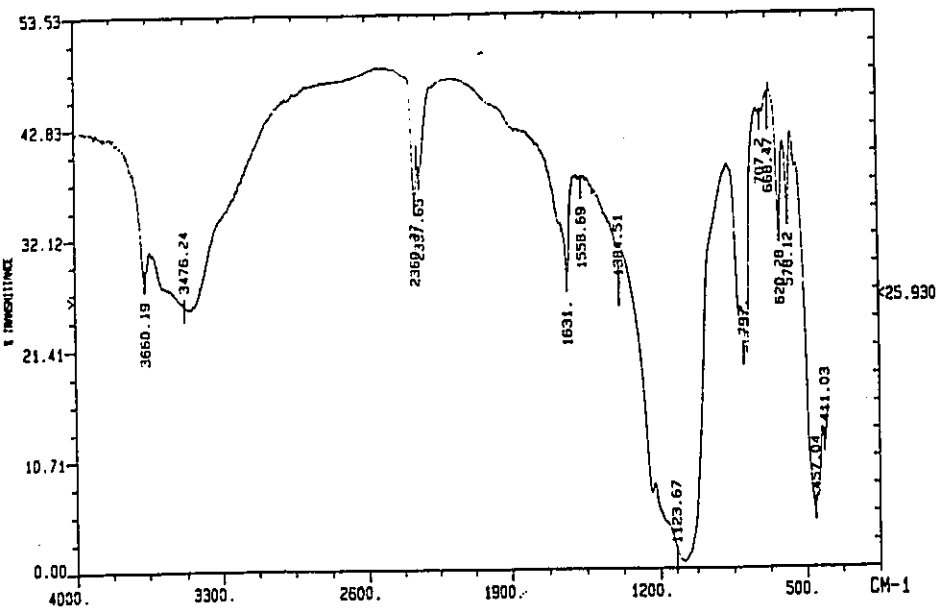

Figure 4.4 FTIR spectrum of magadiite.

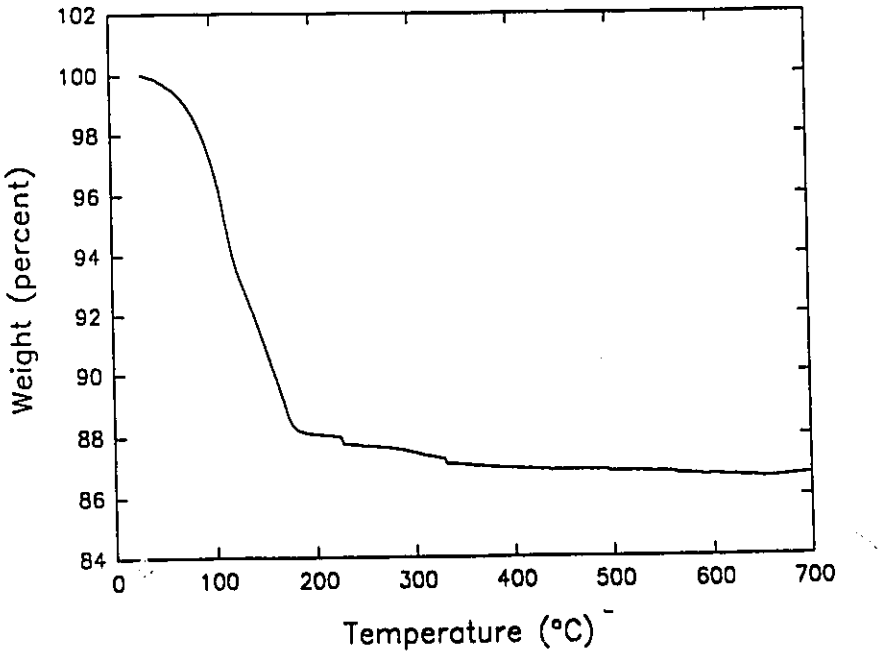

Figure 4.5 TGA curve of magadiite.

A third very gradual weight loss of 1.4% can also be observed beyond 200 °C. This can be attributed to the dehydroxylation of Si-OH groups present in the interlamellar region of magadiite. This observation, along with the 3660 cm^{-1} OH band in the FTIR spectrum, demonstrates the existence of surface silanol functionalities in magadiite.

Acid titration

9.6 g of magadiite were dispersed in 100 ml distilled water and slowly titrated with 1M HCl, adding 0.5 or 1.0 ml aliquots every 15-20 minutes. The profile thus obtained (Figure 4.6) is in good agreement with that of previous titration studies of sodium silicates.[120,191] Thus, this process causes the interlayer sodiums of magadiite to be leached out of the structure and be replaced by hydrogen ions, producing the layered silicic acid H-magadiite.[138] The strong affinity of this mineral for proton exchange is clearly demonstrated by the exchange of sodium ions even in the alkaline pH range. The ultimate end-point of the titration, however, occurs after the addition of 0.0017 mol H^+ per g of magadiite: at this stage, the pH drops to about 2 as all of the interlayer sodiums of magadiite have been exchanged.

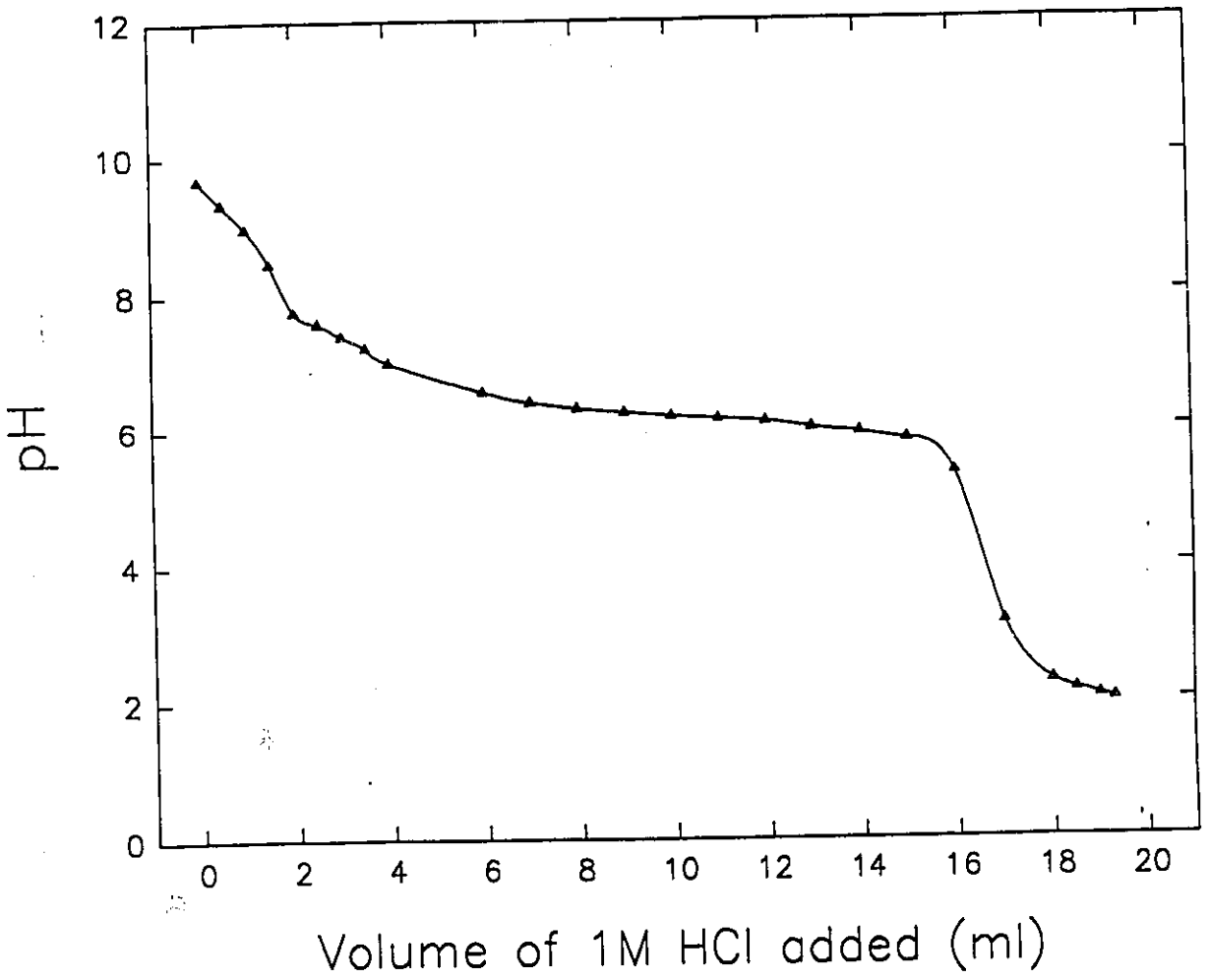

Figure 4.6 Titration curve of magadiite (9.6 g in 100 ml water) with 1 M HCl.

Chemical formula and structure of magadiite

From the TGA and titration results, the empirical composition of the magadiite used in this study can be deduced as $Na_{1.6}Si_{14}O_{28.8}(OH)_{1.6}\cdot 6.9H_2O$. This formula compares well with the approximate formula $Na_2Si_{14}O_{29}\cdot 9H_2O$ obtained by other authors[123,135,150] and corresponded very well to results recently obtained by Dailey and Pinnavaia,[161] who suggested the formula $Na_{1.7}Si_{14}O_{27.9}(OH)_{1.9}\cdot 7.6H_2O$. The problem with the commonly accepted $Na_2Si_{14}O_{29}\cdot 9H_2O$ formulation is that it cannot account for the 3660 cm^{-1} OH stretch observed by FTIR, nor can it explain the high temperature weight loss shown in the TGA curve. Thus, an alternate structural formula can be adopted for magadiite: $Na_2Si_{14}O_{28}(OH)_2\cdot xH_2O$, or $Na_2H_2Si_{14}O_{30}\cdot xH_2O$. This formalism is more useful than the previous one since it represents the chemical properties of magadiite more accurately.

From the informations obtained, it is possible to propose a structural representation of magadiite, depicted in Figure 4.7. One should, however, bear in mind that the layer structure is still unknown.

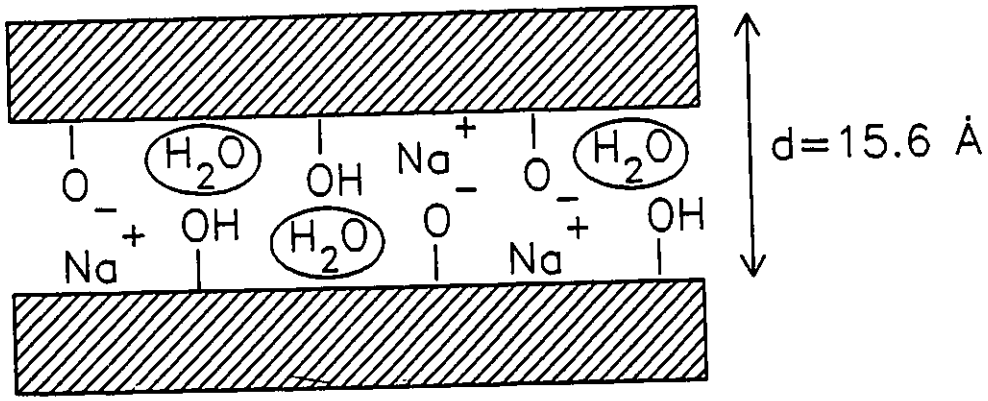

Figure 4.7 Representation of the magadiite layer.

4.1.2.2 Kenyaite

X-ray diffraction

The XRD pattern obtained for kenyaite (Figure 4.8) showed a very crystalline compound with a basal spacing of 19.24 Å (9 basal reflections could be observed) corresponding to kenyaite.[118,123] Table 4.3 gives assignments of the Miller indices, as well as a comparison of the observed spacing values and peak intensities with those of the literature.

As in the case for magadiite, this compound also showed the tridymite impurity peaks at 4.09 and 2.50 Å.

Infrared spectroscopy

The FTIR spectrum of kenyaite was recorded by the same method as magadiite. The spectrum obtained (Figure 6) was found virtually identical to that of magadiite, with a free OH stretch at 3650 cm^{-1} suggesting, as in the case of magadiite, the presence of silanol functionalities on the interlamellar surface of the mineral.

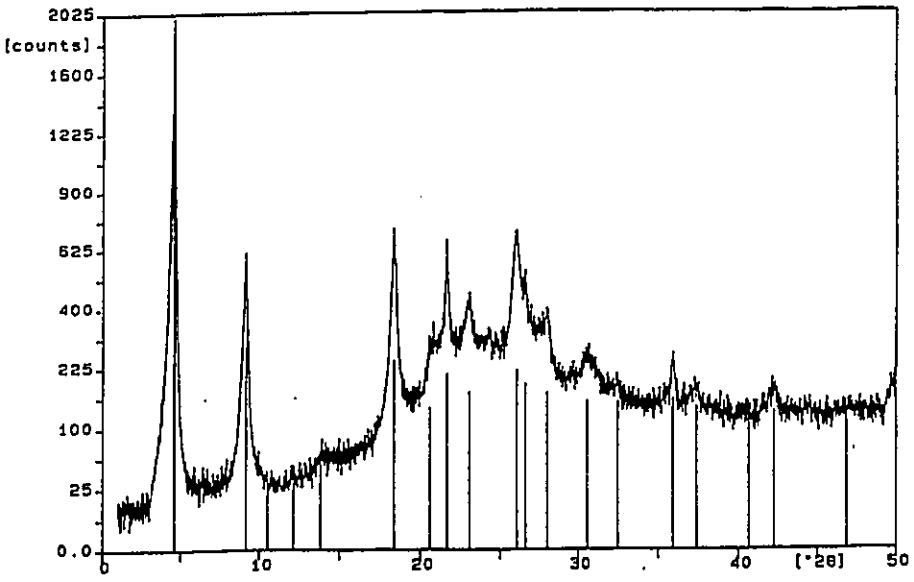

Figure 4.8 XRD pattern of kenyaite.

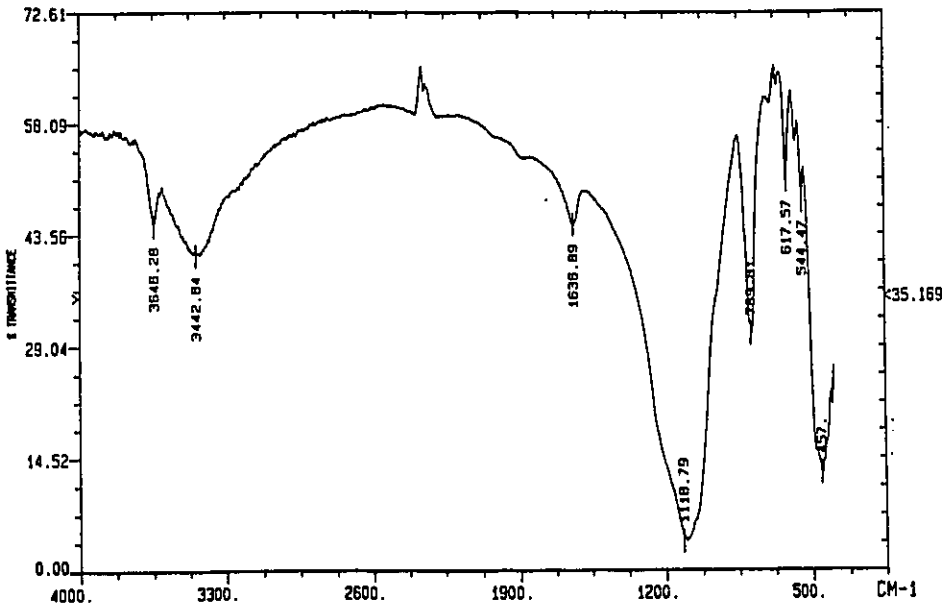

Figure 4.9 FTIR spectrum of kenyaite.

Table 4.3 Comparison of XRD patterns between kenyaite prepared in this work and that obtained in the literature.[118]

d_{obs}	I_{obs}	d_{lit}	I_{lit}	h k l	d_{obs}	I_{obs}	d_{lit}	I_{lit}	h k l
19.25	100	19.70	100	0 1 0	3.41	6	3.43	85	0 0 2
9.61	15	9.93	50	0 2 0	3.34	4	3.32	45	-2 2 1
7.27	0.2	7.78	2	1 0 0	3.18	2	3.20	55	2 1 1
6.40	0.3	6.62	6	0 3 0	2.92	2	2.93	14	-1 3 2
-	-	5.64	8	0 2 1	-	-	2.83	12	0 4 2
-	-	5.14	12	-1 1 1	2.75	0.4	-	-	0 7 0
4.82	10	4.97	35	0 4 0	-	-	2.65	4	1 7 0
4.31	2	-	-	Crist.	2.50	0.8	2.52	4	-1 5 2
4.09	6	-	-	Crist.	-	-	2.48	4	-3 1 1
-	-	4.69	30	0 3 1	2.40	0.3	-	-	0 0 8
-	-	4.47	6	1 2 1	-	-	2.42	6	-2 6 1
3.85	4	3.95	10	0 5 0	-	-	2.34	8	-3 3 1
-	-	3.75	6	2 1 0	2.14	0.3	-	-	0 0 9
-	-	3.64	20	-1 4 1	-	-	1.88	4	2 1 3
-	-	3.53	20	-2 0 1					

Thermogravimetric analysis

The TGA curve of kenyaite (recorded in an identical manner as that of magadiite) (Figure 4.10) showed a 4.4% mass drop between 50 and 180 °C due to the loss of interlamellar water. Due to instrumental malfunction at the time of this experiment, no information could be extracted beyond 200 °C.

Chemical formula and structure of kenyaite

Because of the similarity of the experimental results with those of magadiite, it is plausible to make a direct analogy between the chemical formulae of magadiite and kenyaite. Thus, the previously proposed formula $K_2Si_{20}O_{41}\cdot xH_2O$[118,137] could be replaced by $K_2Si_{20}O_{40}(OH)_2\cdot xH_2O$, or $K_2H_2Si_{20}O_{42}\cdot xH_2O$. Thus, by considering the TGA for the compound synthesized here, its structure would be $K_2H_2Si_{20}O_{42}\cdot 3.4H_2O$.

In accord with the results obtained, a proposed structure for kenyaite is given in Figure 4.11 (represented in its sodium form). As in the case of magadiite, the layer structure of this mineral remains unknown.

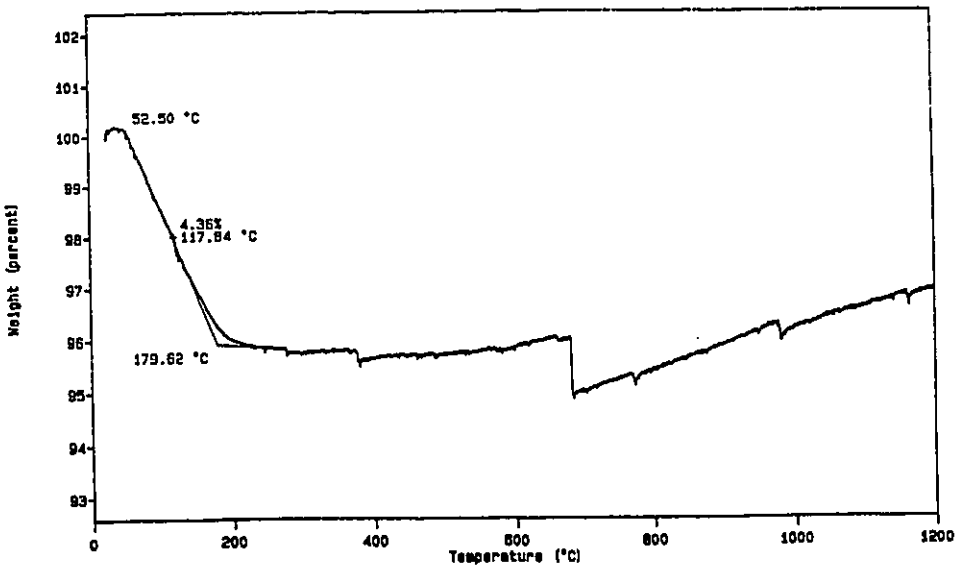

Figure 4.10 TGA curve for kenyaite

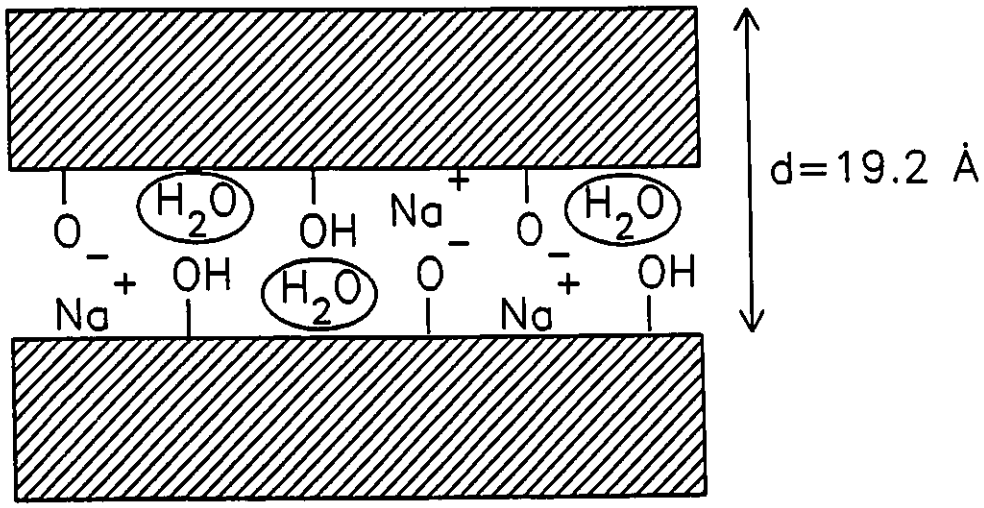

Figure 4.11 Representation of the kenyaite layer.

4.2 H-Magadiite and H-kenyaite: Layered Silicic Acid Precursors

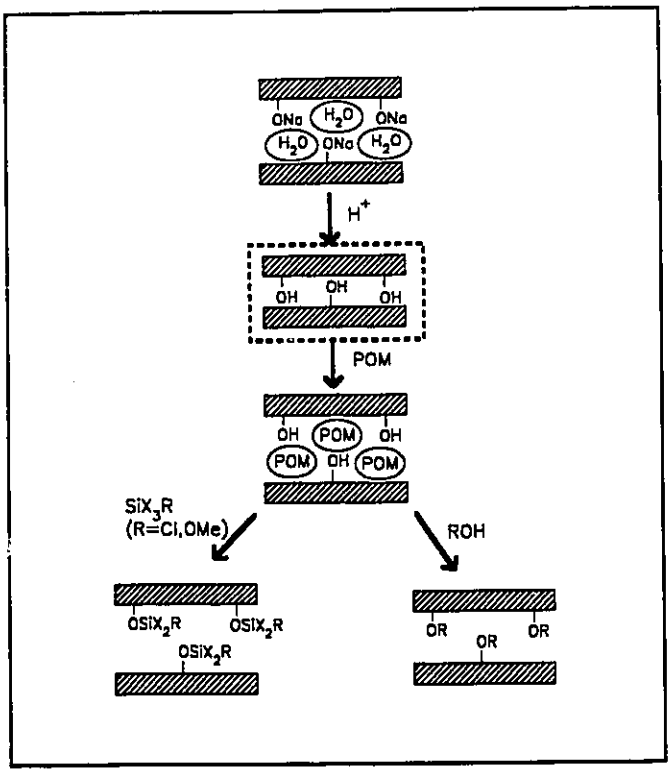

4.2.1 H-Magadiite

Preparation[120,138,140,161]

Magadiite was dispersed in distilled water (25 ml/g) and the pH of the suspension was brought to 1.5 by the dropwise addition of 18% HCl. The mixture was stirred for 24 hours, maintaining the pH within 1.5 and 2.0. The H-magadiite thus obtained was isolated either by centrifugation followed by water and methanol washings, or by dialysis of the mixture in distilled water for about 1 week followed by freeze drying. Both methods yielded

essentially identical materials, with no discernable macroscopic or structural differences, as evidenced by XRD.

In an attempt to obtain a more crystalline batch of H-magadiite, the acid titration method of Lagaly, *et al.*[138] was performed (Figure 4.6). This procedure has been described in section 4.1.2.1. The products thus obtained, however, were crystallographically identical to those produced by the more brutal acidification approach.

X-ray diffraction

The XRD pattern for H-magadiite (Figure 4.12) showed a marked decrease in crystallinity with respect to the parent magadiite, with only broad d_{001} and d_{002} peaks being observed. This amorphicity is likely due to the strong hydrogen bonding between adjacent layers causing distortions in the layer stacking.

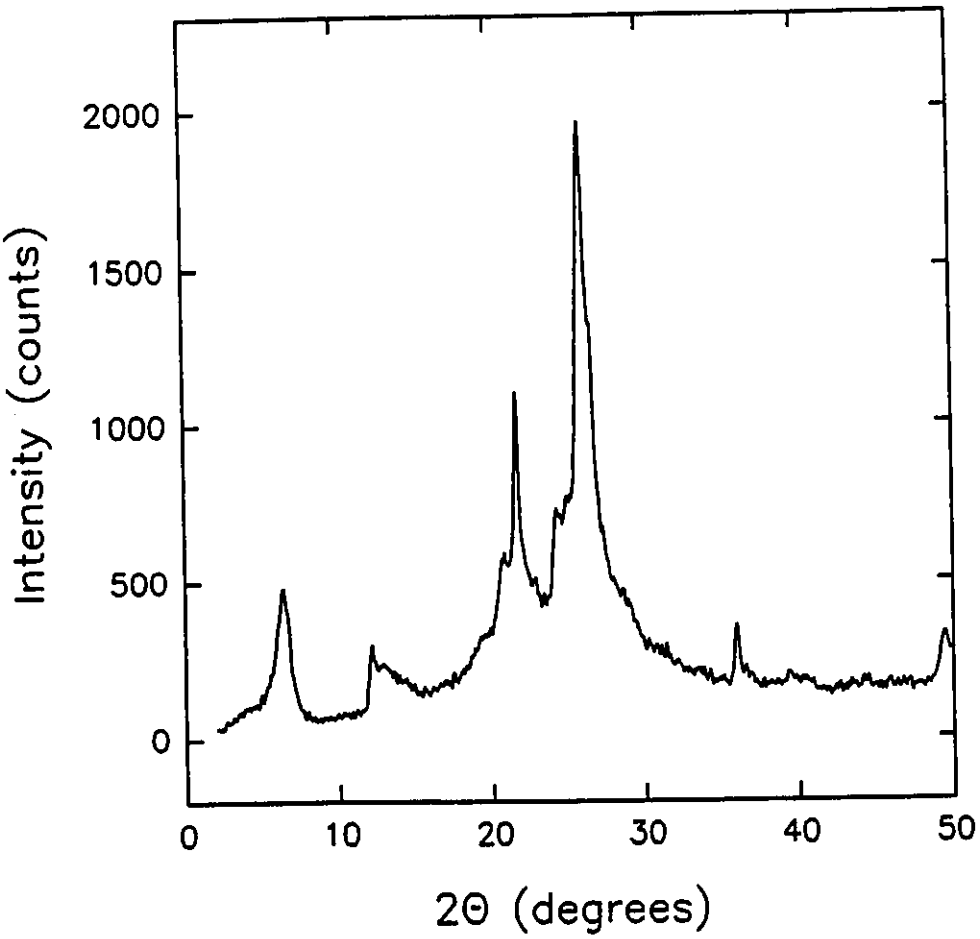

Figure 4.12 XRD pattern of H-magadiite.

The basal spacing collapsed to 11.2 Å, indicating that the structure is completely devoid of interlayer water molecules. Even the slow titration method failed to produce the 13.2 Å spacing for H-magadiite (arising from the presence of a water monolayer in the interlamellar region) claimed by other authors.[138,157,158]

Infrared spectroscopy

The FTIR spectrum of H-magadiite was virtually identical to that of the parent magadiite. The lack of any appreciable enhancement of the free OH stretch at 3660 cm^{-1} can be rationalized by the fact that most new hydroxyl sites generated by the acidification are likely to become involved in hydrogen bonding with neighboring hydroxyls , and thus their signal would become shifted in the broad band at 3400 cm^{-1}.

Since physisorbed water as well as water captured by the KBr upon recording the IR spectrum are likely to be part of the 3400 cm^{-1} band, a sample of H-magadiite was stirred in D_2O for 3 days in order to deuterate the interlamellar silanol groups (forming D-magadiite). Thus, the interlamellar hydroxyl bands could be isolated from the contaminating surface and atmospheric water. The FTIR spectrum of D-magadiite (Figure 4.13) showed two OD stretching bands at 2650 and 2550 cm^{-1}, the former corresponding to the isolated free OD groups and the latter to hydrogen bonded OD groups. This experiment clearly identifies the two dominant types of hydrogens which exist in H-magadiite: those which are isolated and those which participate in interlamellar hydrogen bonding.

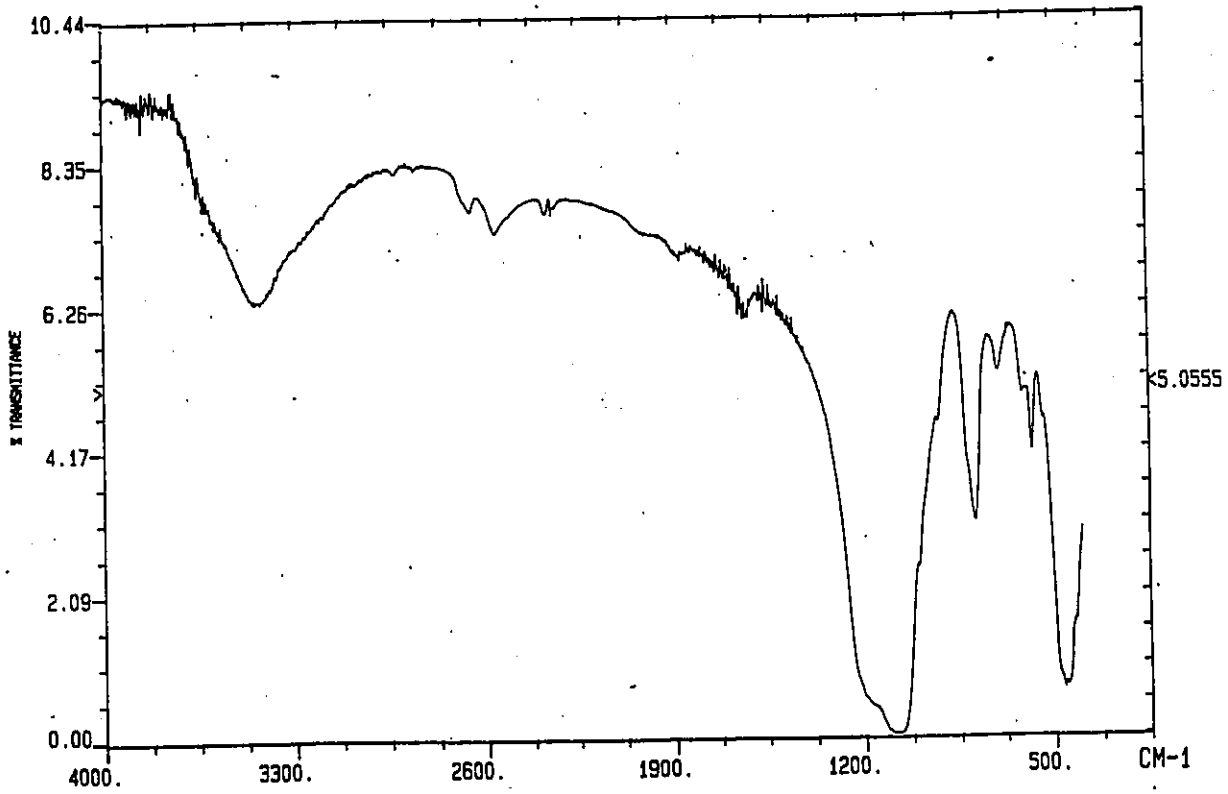

Figure 4.13 FTIR spectrum of D-magadiite.

Particle size analysis

Particle size analysis of H-magadiite showed that the bulk of the particles (about 90% by mass) were between 0.3 and 10 μm spherical diameter (Figure 4.14a). The mass population graph (Figure 4.14b) reflects this distribution and one can calculate an average particle diameter of 3.8 μm. The analysis of a second batch of magadiite gave almost identical particle size information, showing that under the synthetic conditions used the product obtained is quite reproducible. Compared with the smectite clays used in Chapter 3, the particle dimensions of magadiite are very large, possible due to the strong attractive force between adjacent layers causing a greater agglomeration of the lamella.

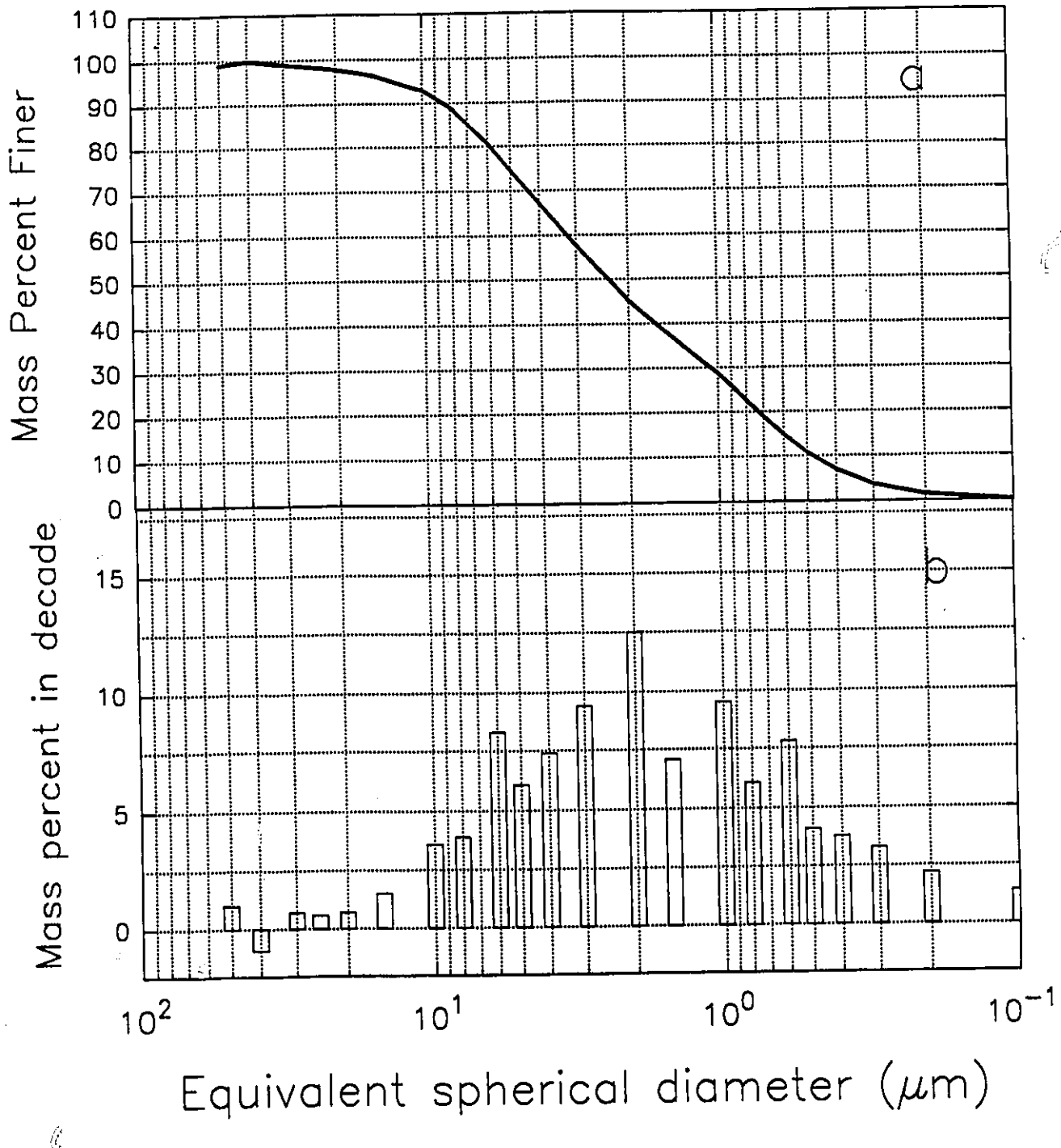

Figure 4.14 Particle size analysis of H-magadiite featuring (a) the cumulative mass percent finer plot and (b) the mass population plot.

^{29}Si solid state NMR

The ^{29}Si solid state NMR spectra of H-magadiite were recorded on a 200 MHz spectrometer at 39.76 MHz with a 3.9 μs pulse width by using both the proton decoupled MAS (acquiring 440 scans, with a pulse repetition time of 120 s) and CP-MAS (1024 scans, spin contact time 10 ms, pulse repetition time 4 s) sequences (Figures 4.15a and 4.15b, respectively). This latter technique essentially transfers the magnetization of the interlamellar hydrogens to the spatially proximate silicons of the mineral, thus greatly enhancing the signals of the silanol groups ($(SiO)_3$**Si**-OH, Q^3 silicons) of H-magadiite with respect to the more distant bulk silicon atoms ($(SiO)_4$**Si**, Q^4 silicons). The former technique (proton decoupled) does not discriminate between any type of Si environment, so the resulting spectra will quantitatively reflect the populations of Si atoms in different chemical environments (given, of course, that a sufficient delay time is allowed between each spectral acquisition so that the nuclei can fully relax): for H-magadiite, a delay time of 120 s was applied so that reliable quantitation could be achieved from the spectra[151] (T_1 relaxation times were measured as being 28 and 24 s for the Q^4 and Q^3 signals, respectively, so the recycle time for the experiment was found to be adequate for obtaining quantitative information).

Thus, four signals could be observed in these spectra whose positions and relative intensities were in accord with previously published spectra.[140,146-148,151,160,161] The first signal at -101 ppm was assigned to the silanol silicons (Q^3 sites) while the three remaining (-109, -112 and -114) were attributed to the bulk "internal" silicon atoms (Q^4 sites). For the sake of discussion, these three sites will henceforth be annotated as Q^{4a}, Q^{4b} and Q^{4c}, respectively, and have tentatively been assigned to silica tetrahedra with differing Si-O-Si bond angles.[146]

It is to be noted that layered silicates have been found to possess identical resonances to their corresponding layered silicic acids,[147] thus the silicon sites of magadiite are indistinguishable from those of H-magadiite: direct comparisons between the NMR data of magadiite with H-magadiite can therefore be made. The relative intensity ratio of the Q^4 with respect to the Q^3 signals was 2.5, in accordance with that obtained by the previously cited authors. Very recently, Almond *et al.* reported a very similar spectrum for natural magadiite[192] including the three distinct Q^4 sites at virtually the same chemical shifts (-109.5, -111.2 and -113.6 ppm). Scholzen *et al.* have also reported three magadiite Q^4 sites (-110, -111 and -114 ppm) which were reproducible among six magadiite batches prepared under various synthetic conditions.[151] The similarity between these results shows that magadiite has consistency in its molecular scale structure, whether it is prepared synthetically or naturally occuring. In both of these cited works (using proton-decoupled MAS NMR), the Q^{4b} (-112 ppm) signal usually appears to be of equal or greater intensity as the Q^{4a} (-109 ppm) signal, with the latter signal often appearing as a shoulder on the former. The Q^{4c} signal is in all cases somewhat less intense than either of the other two. In the case of the H-magadiite prepared in this work, the Q^{4b} signal is the most intense, with the Q^{4a} showing up as a shoulder, and the weaker Q^{4c} signal distinctly appearing at higher field.

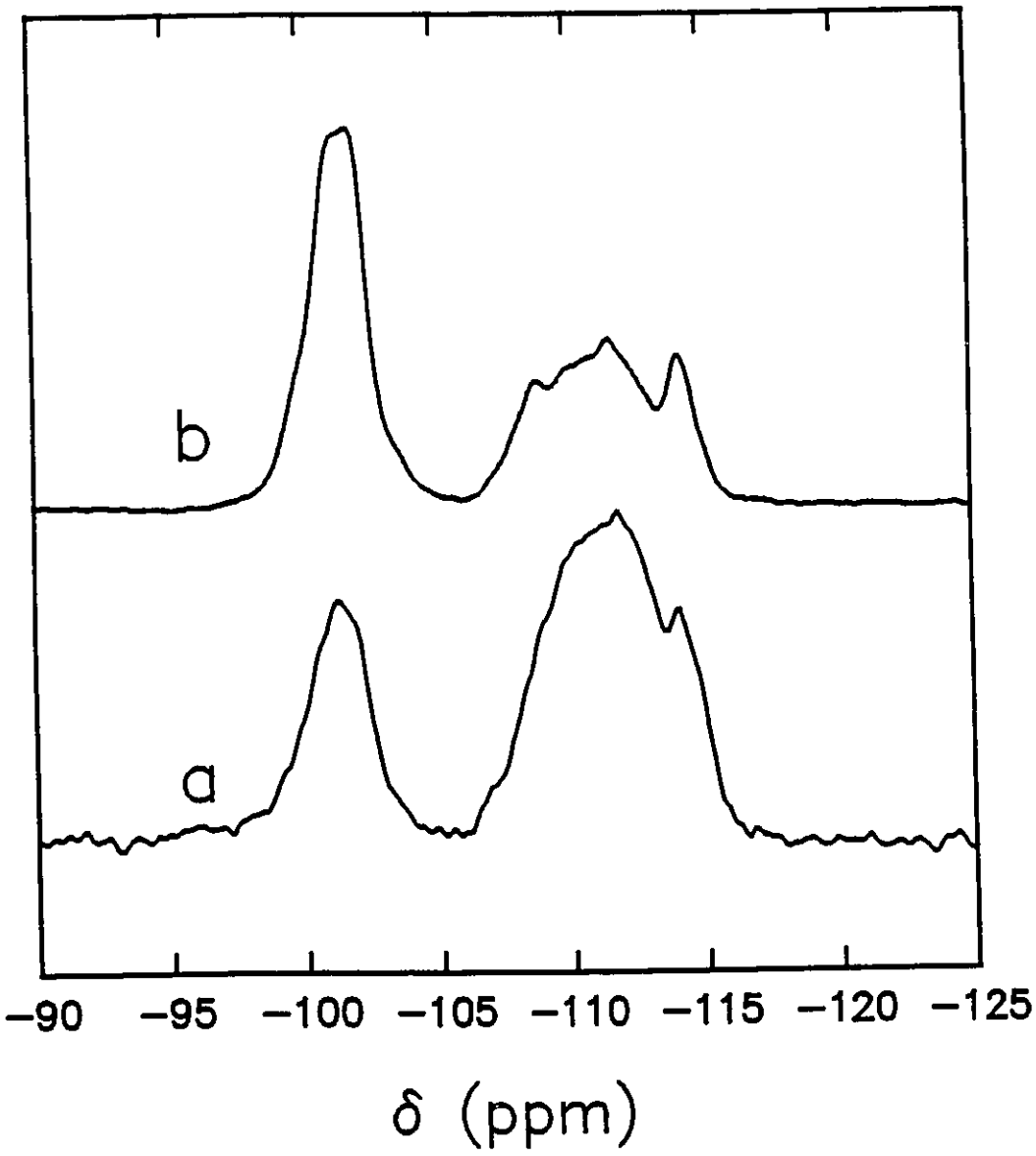

Figure 4.15 ^{29}Si NMR spectra of H-magadiite using (a) proton decoupled MAS and (b) CP-MAS sequences.

The CP-MAS spectrum showed, as expected, a strong enhancement of the proton-proximate Q^3 silicon signal with respect to that of the decoupled MAS spectrum. Noteworthy observations can also be made for the three Q^4 signals: the Q^{4a} and Q^{4c} signals show significant enhancement upon cross-polarization with respect to the Q^{4b} signal (although not to the extent of the -101 ppm signal enhancement), indicating that these two signals represent Q^4 silicons which are closer to protons than those represented by the -112 ppm signal. The hypothesis can thus be put forth that the Q^{4a} and Q^{4c} tetrahedra are neighboring to Q^3 tetrahedra, thus benefitting from some intensity enhancement from the silanol hydrogens, while the Q^{4b} tetrahedra are more isolated from the Q^3 sites, thus receiving less proton magnetization transfer.

Thermogravimetric analysis/ Differential Scanning Calorimetry

The TGA profile of H-magadiite (Figure 4.16) was comparable to that found by other authors,[120,138,140,145,191] showing a 2.1% mass drop below 100 °C corresponding to the loss of physisorbed water and a 1.6% drop between 320 and 420 °C corresponding to the condensation of adjacent hydroxyl groups in the interlamellar region. A subsequent more gradual loss of 2.2% is observed between 420 and 700 °C which may be attributed to the condensation of the remaining, more isolated, hydroxyls. From the total loss of 3.83% water from the hydroxyls in H-magadiite, one can calculate that the structure is comprised of 0.428% hydrogen per unit mass. This value is supported by elemental analysis results on dry H-magadiite, which revealed 0.40 % hydrogen.

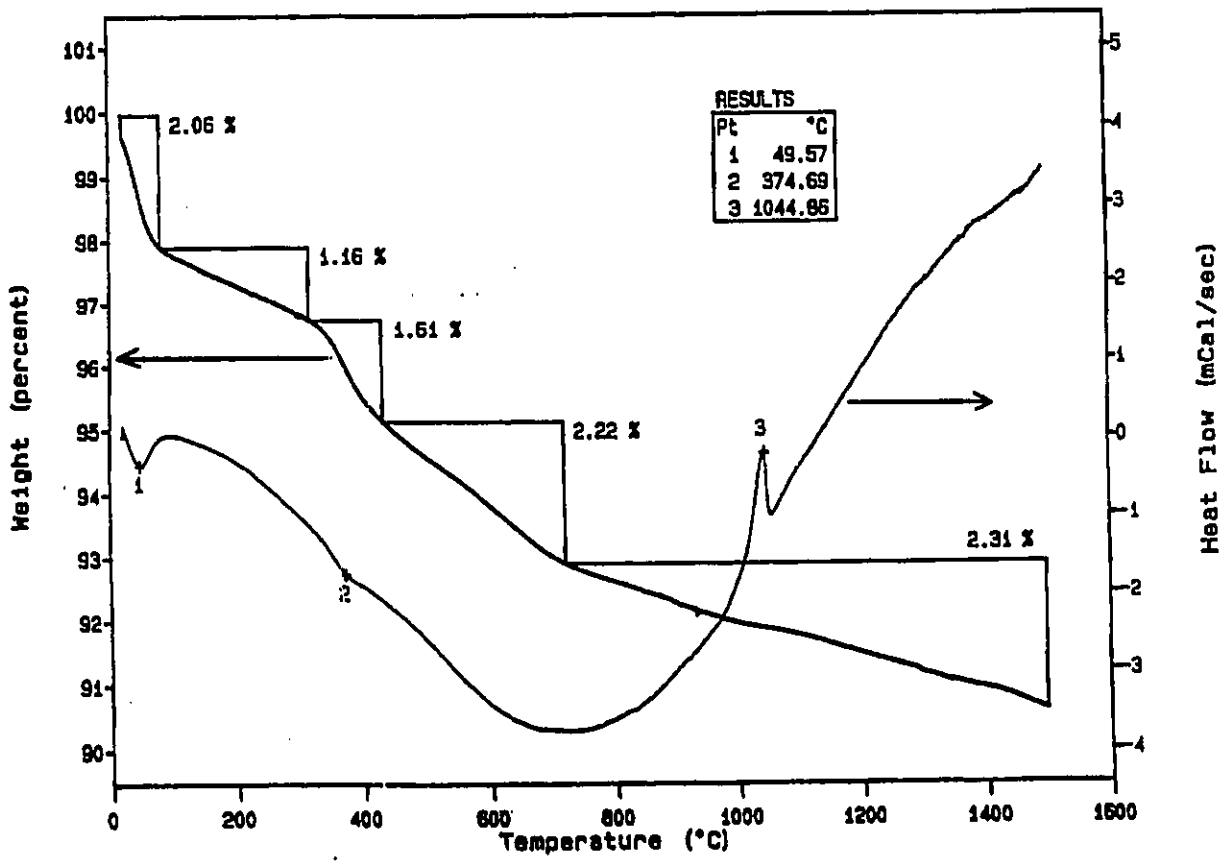

Figure 4.16 TGA (scale on left) and DSC (scale on right) profiles of H-magadiite.

The DSC profile of H-magadiite (Figure 4.16) featured exotherms at 50 and 375 °C resulting from the water loss and hydroxyl condensation. An endothermic signal could also be seen at 1045 °C which can be attributed to the phase transition of silica to cristobalite.

Chemical formula and structure of H-magadiite

Although the most commonly accepted structural formula for *dry* H-magadiite is $H_2Si_{14}O_{28}$,[138] the formula $H_4Si_{14}O_{30}$ has also been proposed.[145,161] The mass percent of hydrogen in magadiite according the former structural formulation can be calculated as 0.235%, while that of the latter formula is 0.460%. The second formulation is thus most consistent with the measured hydrogen contents for the H-magadiite used in this work, according to TGA and elemental analysis data (0.428% and 0.40%, respectively). As for the ^{29}Si MAS NMR spectra, one would expect to obtain, according to the first formulation, a Q^4/Q^3 ratio of 6 (*i.e.* 2/(14-2)); the second formula would give this ratio as being 2.5 (*i.e.* 4/(14-4)). Again, the second formulation has the best agreement with results obtained by this research, as well as with those reported by other authors.

Thus, by considering the average H-content obtained from the TGA and elemental analysis results, one can calculate the chemical formula of H-magadiite as $H_{3.6}Si_{14}O_{29.8}$ (very close to the $H_4Si_{14}O_{30}$ formulation). Moreover, if one considers that H-magadiite is formed by the simple replacement of Na^+ ions from magadiite by H^+ ions, the H-magadiite formula calculated using the magadiite formula found in section 4.1.2.1 would become $H_{3.2}Si_{14}O_{28.8}$. Thus, the consistency between these results conclusively demonstrate that $H_4Si_{14}O_{30}$ is a more

accurate structural formalism for H-magadiite than $H_2Si_{14}O_{28}$ in order to explain the physical properties as well as the chemical reactivity of this mineral.

Structures for H-magadiite can now be proposed, based on all of the results mentioned above. Following the proposals of Pinnavaia *et al.*[147] and Rojo *et al.*[148], a good starting point would be to consider the basic morphology of the magadiite layer as being composed of two sheets of silica tetrahedra fused together at each apex, with some tetrahedra being inverted to point in the interlamellar region (these would represent the silanol groups of the mineral). The thickness of this layer structure has the best accord with the XRD basal spacing of dry H-magadiite (11.2 Å) than those proposed by Schwieger *et al.*[146] and Brandt *et al.*[149] models for magadiite, from which were calculated impossibly high silicate layer thicknesses (15.06 and 12.84 Å, respectively). Moreover, it has been observed by ^1H-^{29}Si correlation spectroscopy that all of the Q^4 sites of magadiite cross-polarize with the interlamellar hydrogens:[192] this would not be the expected case if silicon atoms were located in sites deeply buried in a stack of three or four silica tetrahedra, as is the case in these two latter models. It can thus be concluded that, in a manner consistent with the Pinnavaia and Rojo models, the magadiite layer probably consists of two fused sheets of silica tetrahedra with approximately two out of every seven being inverted, resulting in interlayer Si-OH or Si-ONa groups (Figure 4.17). Note that it is a consequence of this structure that when a tetrahedron inverts, so must the corresponding one at the other side of the layer.

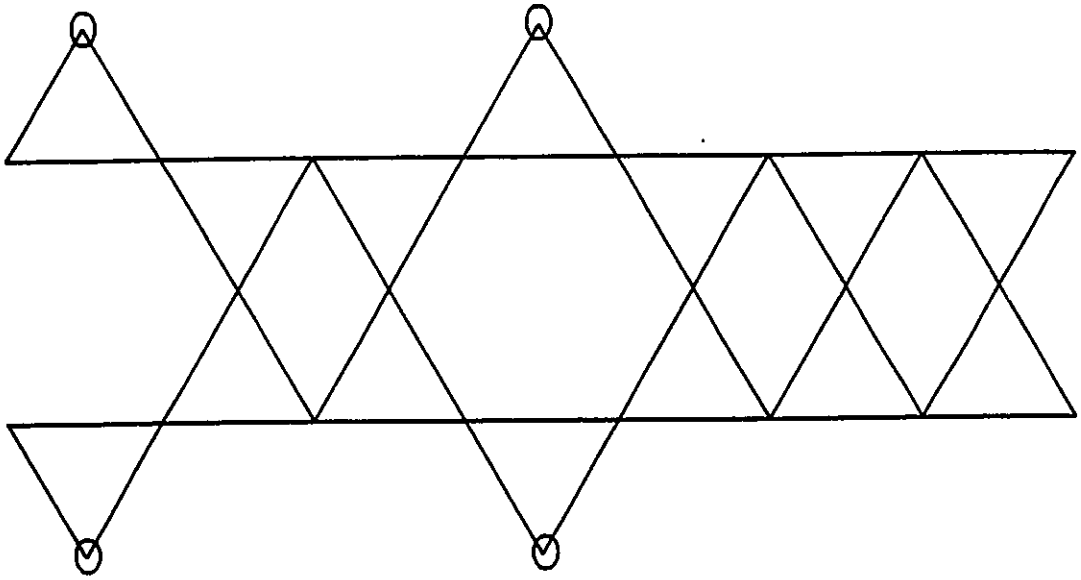

Figure 4.17 Cross-sectional view of magadiite layer.

4.2.2 H-Kenyaite

Preparation

H-kenyaite was prepared from its potassium silicate precursor following exactly the same method as for H-magadiite (see section 4.2.1).

X-ray diffraction

The powder XRD pattern of H-kenyaite (Figure 4.18a) showed a material of considerably higher crystallinity than H-magadiite, as evidenced by the sharper peaks and observation of the *00l* reflections up to $\ell = 9$. Thus, a basal spacing of 17.7 Å was found. Drying the sample at 130 °C *in vacuo* for 24 hours resulted in a reduction of crystallinity and a very slight drop of the basal spacing to 17.5 Å (Figure 4.18b). This value is in good agreement with previously reported values.[137] It can therefore be concluded that, as was the case of magadiite, acid treatment of kenyaite caused the near complete collapse of the structure by the removal of interlamellar water. The slightly higher spacing of air dried H-kenyaite can be attributed to a small amount of water remaining occluded in the structure, which is expelled by heating under vacuum.

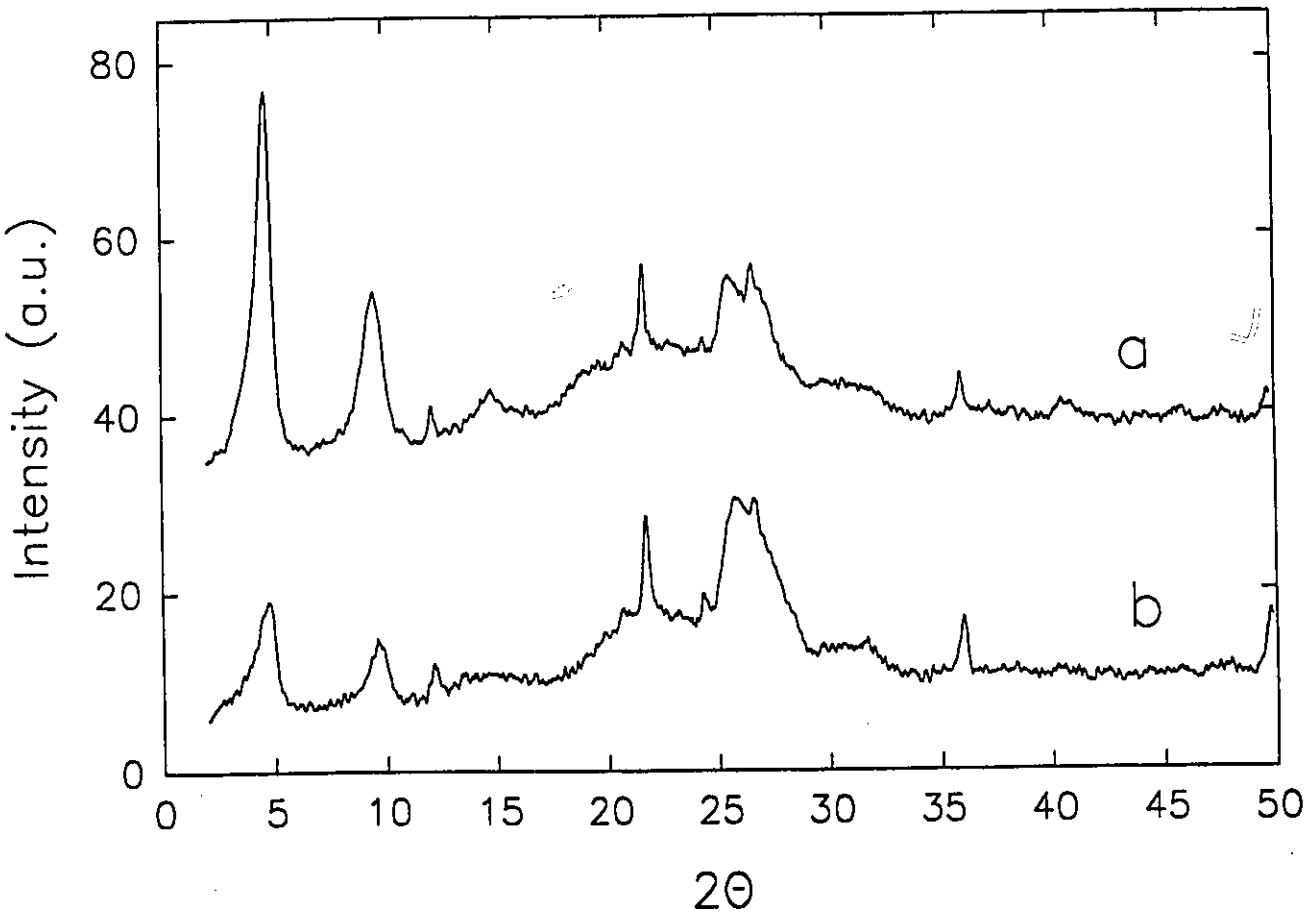

Figure 4.18 XRD pattern of (a) air dried H-kenyaite and (b) H-kenyaite dried *in vacuo* at 130 °C.

Particle size analysis

The PSA of H-kenyaite showed that, very similarly to H-magadiite, 95 % of the particles were between 0.3 and 10 μm in diameter (Figure 4.19a). From the population graph (Figure 4.19b), the average particle size was calculated as 1.9 μm, about half the size of the H-magadiite particles reported above. Thus, the mass distribution of these particles is skewed in favour of smaller particles than H-magadiite. Indeed, 50% of the H-magadiite particles were found to be smaller than about 2.5 μm whereas 50% of H-kenyaite particles were below 1 μm. This property may favour the diffusion kinetics of chemical species into the interlamellar region of H-kenyaite with respect to H-magadiite, although the study of this effect is not within the scope of this thesis.

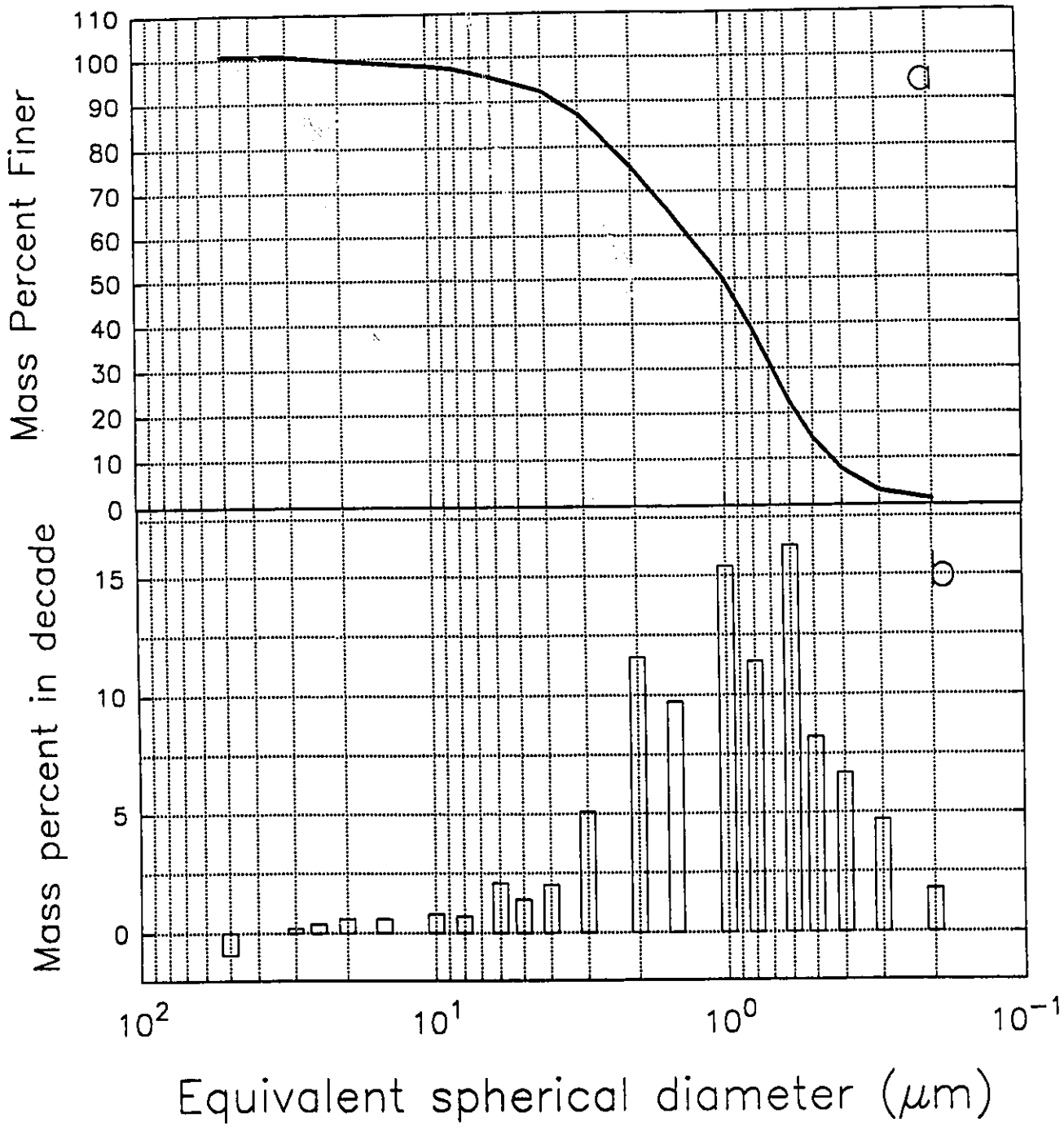

Figure 4.19 Particle size analysis of H-kenyaite featuring (a) the cumulative mass percent finer plot and (b) the mass population plot.

^{29}Si solid state NMR

The ^{29}Si solid state NMR spectra of H-kenyaite (proton decoupled MAS and CP-MAS) were recorded using the same parameters as those of the H-magadiite experiments, with 135 scans for the H-decoupled experiment and 1024 scans for the CP-MAS (Figures 4.20a and 4.20b, respectively).

Four major signals could be observed in the MAS spectrum whose positions and relative intensities were in accord with the previously published kenyaite spectrum by Schwieger *et al.*[146] In a manner analogous to that of H-magadiite, the first signal at -100.3 ppm was assigned to the Q^3 silicons while the three remaining (-107.6, -110.3 and -113.0) were attributed to the Q^4 sites (henceforth annotated as Q^{4a}, Q^{4b} and Q^{4c}, respectively). Schwieger observed the Q^3 signal at -101.1 ppm, and the Q^4 peaks at -109.7, -112.2 and -114.1 ppm: these values are all slighly shifted from those obtained in this work (perhaps due to some reference discrepancy), but the general shapes of the spectra were very similar. A small peak is also observed in the decoupled spectrum (but not in the CP-MAS) at -119.1 ppm which is also seen in the Schwieger spectrum[146] at -120.5 ppm: this signal has been assigned to yet another type of Q^4 site, henceforth denoted at Q^{4d}. The relative intensity ratio of the Q^4 with respect to the Q^3 signals was found to be 4, still in accordance with the results of Schwieger *et al.*: this result is consistent with the higher silicon content of kenyaite when compared to magadiite (with respect to hydrogen content), since the kenyaite sheet is expected to be thicker than that of magadiite resulting in a higher Q^4:Q^3 ratio. The presence of at least four distinct Q^4 sites testifies to the chemical and/or geometrical variability among these silica tetrahedra.

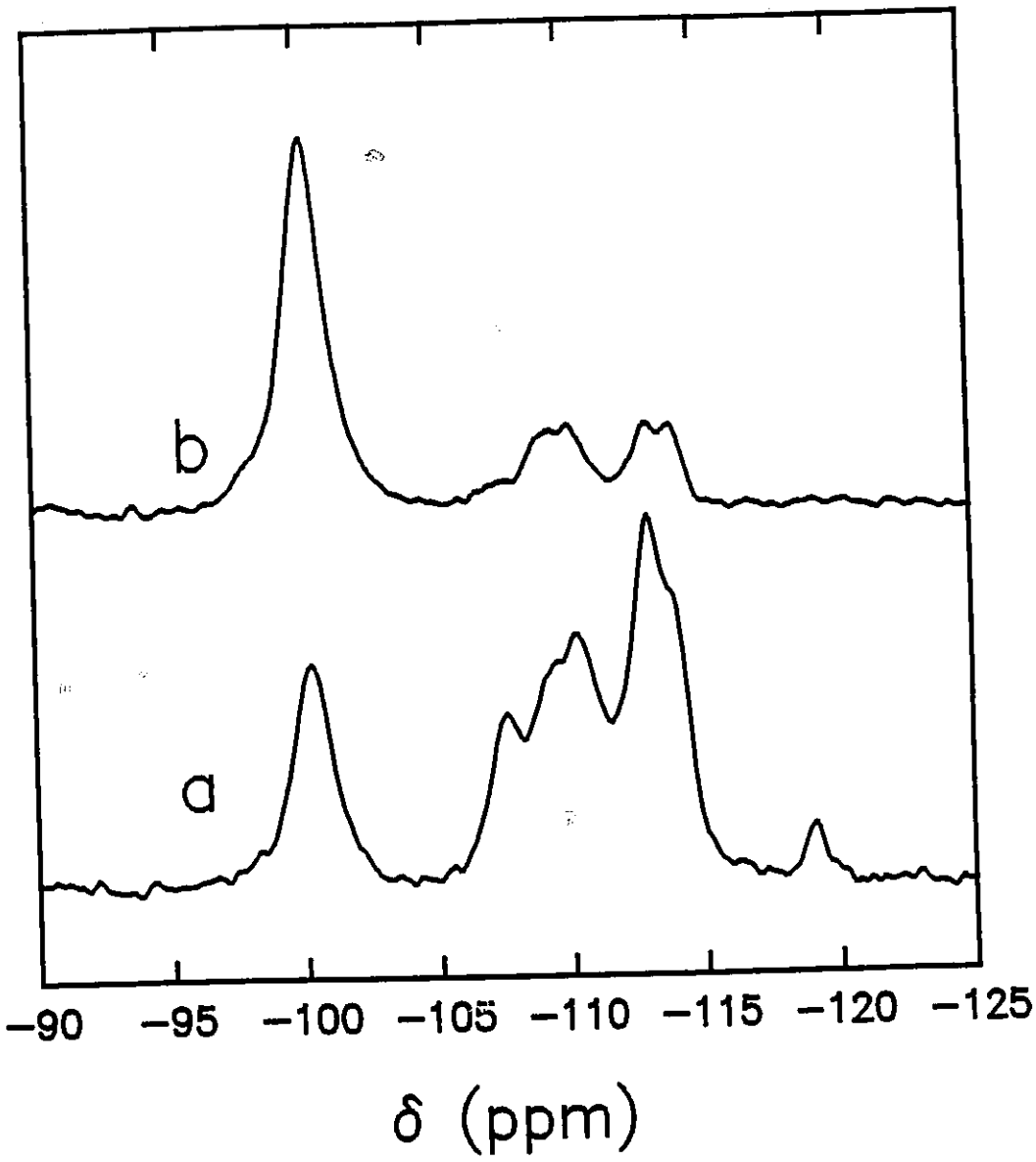

Figure 4.20 ^{29}Si NMR spectra of H-kenyaite using (a) proton decoupled MAS and (b) CP-MAS sequences.

The CP-MAS spectrum showed, as expected, a strong enhancement of the proton-proximate Q^3 silicon signal with respect to that of the decoupled MAS spectrum (it is quite mystifying that Schwieger *et al.* obtained no signal whatsoever for kenyaite using the CP-MAS sequence!). In the Q^4 region of the spectrum, a new signal appears at -113.9 ppm, revealing a fifth Q^4 site (labelled as Q^{4e}) which is likely to be located near some hydrogen atom. Also of note is the disappearance of the -119.1 ppm signal which can be attributed to the large distance of the Q^{4d} site to hydrogen sources: this fact is concurrent with the thick layer structure of kenyaite, where sites can exist deeply buried in the structure where cross-polarization to the interlamellar hydrogen becomes impossible. Finally, the appearance of a weak signal at about -91 ppm denotes the presence of Q^2 sites ($(SiO)_2(OH)_2\mathbf{Si}$): these would be expected to occur on the edge sites of the particles where Q^3 sites would otherwise reside. That Q^2 sites are observed in H-kenyaite but not in H-magadiite may be attributed to the comparatively small sizes of H-kenyaite particles with respect to those of H-magadiite which increases the number of edge sites on the sample and hence the Q^2 silicons.

Chemical formula and structure of H-kenyaite

Following the formalism described in section 4.1.2.2, the chemical structure of H-kenyaite would be $H_4Si_{20}O_{42}$. The Q^4:Q^3 ratio can be calculated on the basis of this formula as being 4 (4/(20-4)), consistent with the NMR data obtained.

The layer structure of kenyaite can thus be postulated as consisting of four silica sheets fused together in the manner shown in Figure 4.21, with approximately two fifths of the surface tetrahedra being inverted to point in the interlamellar region. This structural

model, already proposed by Brandt *et al.*[149] fits quite well with the XRD and NMR data, much better than the structure initially proposed by Schwieger *et al.*[146]

It should be noted that this proposed structure essentially consists of the condensation of two magadiite-type layers together, while magadiite itself can be said to be built up from the fusion of two makatite layers. This concept has previously been used to explain the formation of quartz from silica solutions via the intermediate generation of magadiite followed by kenyaite[118,137,139], by the subsequent condensation of layered systems:

silica solution → makatite → magadiite → kenyaite → quartz

Under the synthetic conditions used in this experiment, magadiite and kenyaite thus appear to be the thermodynamically favoured "stations" of this process. Templating conditions of the reaction solutions are likely to be the factor which drives the selection of either product, as evidenced by the variation in product by merely changing the alkali cation from sodium to potassium, or by varying the counter anion of the metal.[132]

A hypothesis can now be put forward in order to explain the selective formation of magadiite or kenyaite. It can be proposed that if, after the condensation of two makatite sheets, the resulting layer has a Q^4:Q^3 ratio of about 2.5:1 (29% inverted into Si-OH or Si-ONa), then it will not undergo any further condensation and the compound will crystallize as magadiite. If, however, the resulting "di-makatite" layer happened to bear a larger number of inverted tetrahedra (for instance, a Q^4:Q^3 ratio of 3:2, or 40% inverted), then the high number of siloxane groups on the layers might cause them to condense and form the

thicker kenyaite layer. This mechanism is plausible according to the structures proposed above for magadiite and kenyaite, since magadiite has about 29% of its surface tetrahedra inverted (as Si-OH) and kenyaite 40%.

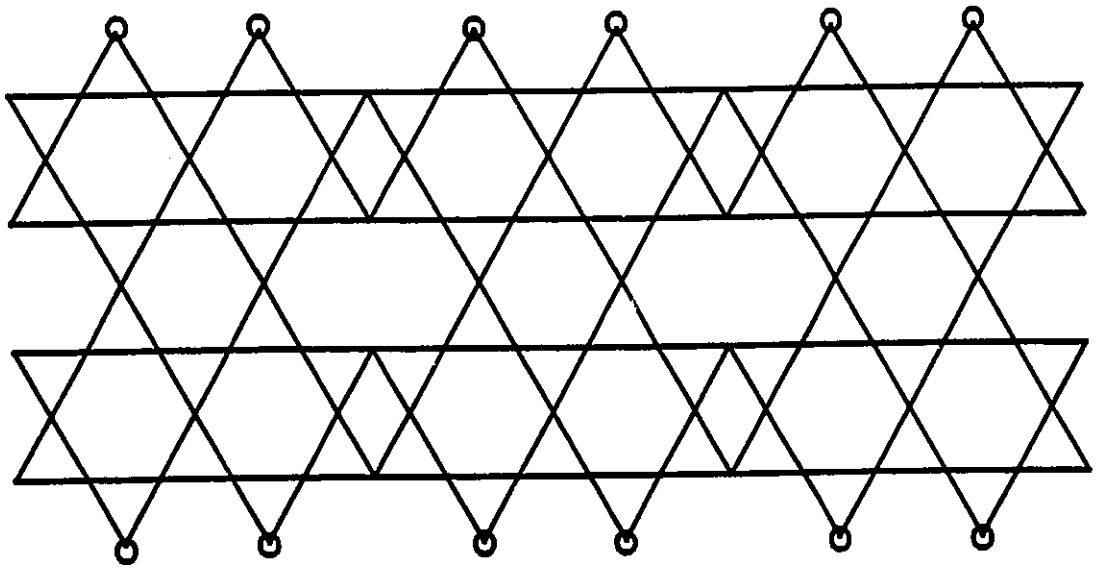

Figure 4.21 Cross-sectional view of kenyaite layer.

4.3 Swelling reactions of layered silicates

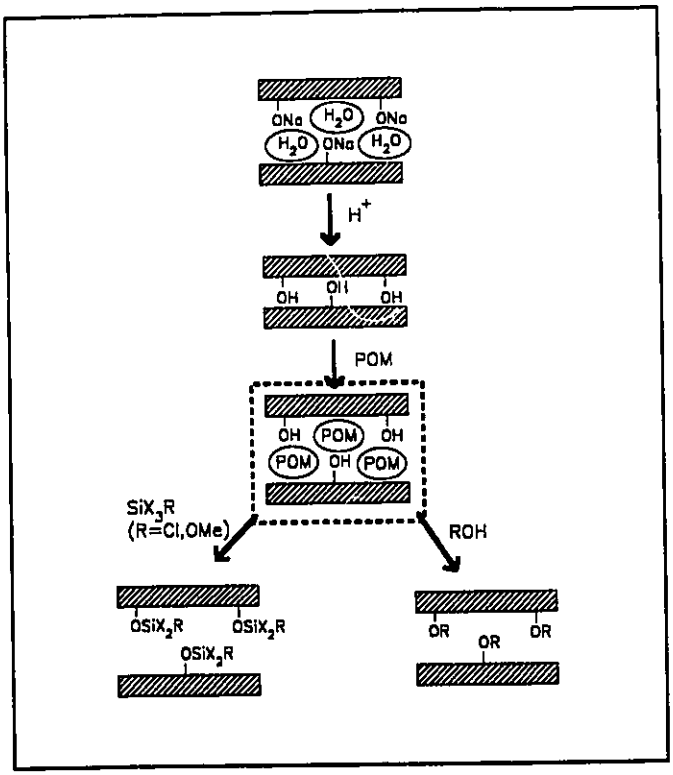

As a preliminary step before grafting of species into the interlamellar region of layered silicates, the swelling of the structure (or the expansion of the interlayer space) is necessary in order to disrupt the rather strong hydrogen bonding network between adjacent layers and enhance the diffusion of the grafting molecules into the mineral. In this section, various swelling strategies will be discussed, featuring the inclusion of *N*-methylformamide (NMF), myristyltrimethylammonium ions and *n*-octylamine.

4.3.1 *N*-Methylformamide (NMF) intercalation

4.3.1.1 H-magadiite

Preparation

H-magadiite (0.5g) was dried *in vacuo* at 110 °C for 24 hours then stirred in NMF (10 ml, dried over molecular sieves) for 3 days to obtain the intercalated species. The gel was then centrifuged and the supernatent NMF discarded. Generally, the NMF/H-magadiite thus obtained was used as-is in further reactions, without removing the excess NMF adhering to the material. In instances where dry or opaque material is preferred (such as for X-ray diffraction or thermal analysis), the NMF/H-magadiite was gently washed in dry dioxane.

Characterization

XRD data revealed a basal spacing of 16.3 Å for NMF/H-magadiite, from which a 5.1 Å interlayer separation can be determined. These values are reasonably consistent with the 15.9 Å basal spacing reported by Lagaly *et al.*[138] (4.7 Å interlayer distance) and feasibly consist of a monolayer of molecules in a perpendicular arrangement with respect to the layer planes.

The TGA curve for NMF/H-magadiite shows a gradual mass loss (about 7%) between 200 and 400 °C assigned to the removal of the intercalated NMF molecules. This sluggish desorption at temperatures well above the boiling point of pure NMF (185 °C) can be

attributed to the strong hydrogen bonding between the H-magadiite hydroxyl groups and the polar NMF molecules.

4.3.1.2 H-kenyaite

Preparation

NMF/H-kenyaite was prepared following exactly the same method as the corresponding magadiite intercalation reaction (see section 4.3.1.1).

Characterization

The XRD pattern for NMF/H-kenyaite showed a basal spacing of 21.0 Å, giving an interlayer spacing of 3.5 Å. This indicates that, unlike the case of NMF/H-magadiite, the NMF molecules are probably somewhat tilted with respect to the surface of the mineral. Nonetheless, this spacing indicates that the hydrogen bonding network within the mineral layers is broken and that further inclusion of molecules into the structure may be possible.

4.3.2 Other swelling strategies

Although the NMF swelling method was exclusively applied in all of the layered silicate grafting processes in this thesis, other reactions have been explored as potential alternative means of expanding the layers. These involved the inclusion of amines and tetraalkylammonium ions, both of which being briefly explored in this section.

4.3.2.1 Tetraalkylammonium ion intercalation

This technique involves the ion exchange of the interlayer alkali metal ions of the parent layered silicates for large tetraalkylammonium cations, bypassing the acidification process altogether. Thus, materials with large interlayer spaces can be obtained, but with only one half of the hydroxyl groups available when compared to the silicic acids (for example, $Na_2H_2Si_{14}O_{30} + 2TAA^+ \rightarrow TAA_2H_2Si_{14}O_{30} + 2Na^+$).

Thus, magadiite and kenyaite (1g) were treated with 100 ml of 0.1 M myristyltrimethylammonium bromide [$CH_3(CH_2)_{13}N(CH_3)_3Br$] solution for 48 hours. The products (TMMyrA-magadiite and TMMyrA-kenyaite) were isolated by centrifugation followed by washing with water and acetone. The XRD patterns of these compounds featured basal spacings of 15.6 Å for TMMyrA-magadiite and 34.7 Å for TMMyrA-kenyaite (shown in Figure 4.22), showing that the alkyl chains lie parallel to the mineral plane in magadiite (interlayer spacing 4.4 Å) but standing up with paraffin-type packing in kenyaite (interlayer spacing 23.5 Å, Figure 4.23). (It is to be noted that, although the 15.6 Å spacing for TMMyrA-magadiite is the same as that of the parent magadiite, FTIR confirmed the presence of CH groups in the sample and the XRD pattern signatures of both species were clearly different, with only the d_{001} peak being observed: this leads to the conclusion that the material obtained is indeed an intercalate of magadiite with, fortuitously, the same basal spacing as its predecessor.)

Lagaly *et al.* obtained a basal spacing of 35.7 Å for the same cation intercalated in magadiite,[135] giving an interlayer distance of 24.5 Å. This latter distance does not correspond to that observed in this study. It is consistent, however, with that obtained in

the kenyaite intercalation in this study. This observation illustrates the greater reactivity of the potassium silicate when compared to the sodium variety, as was noted by Beneke *et al.*[142] The lack of accord between the magadiite intercalation results supports the observation of other authors that different samples of this mineral can exhibit rather different intracrystalline reactivities.[151]

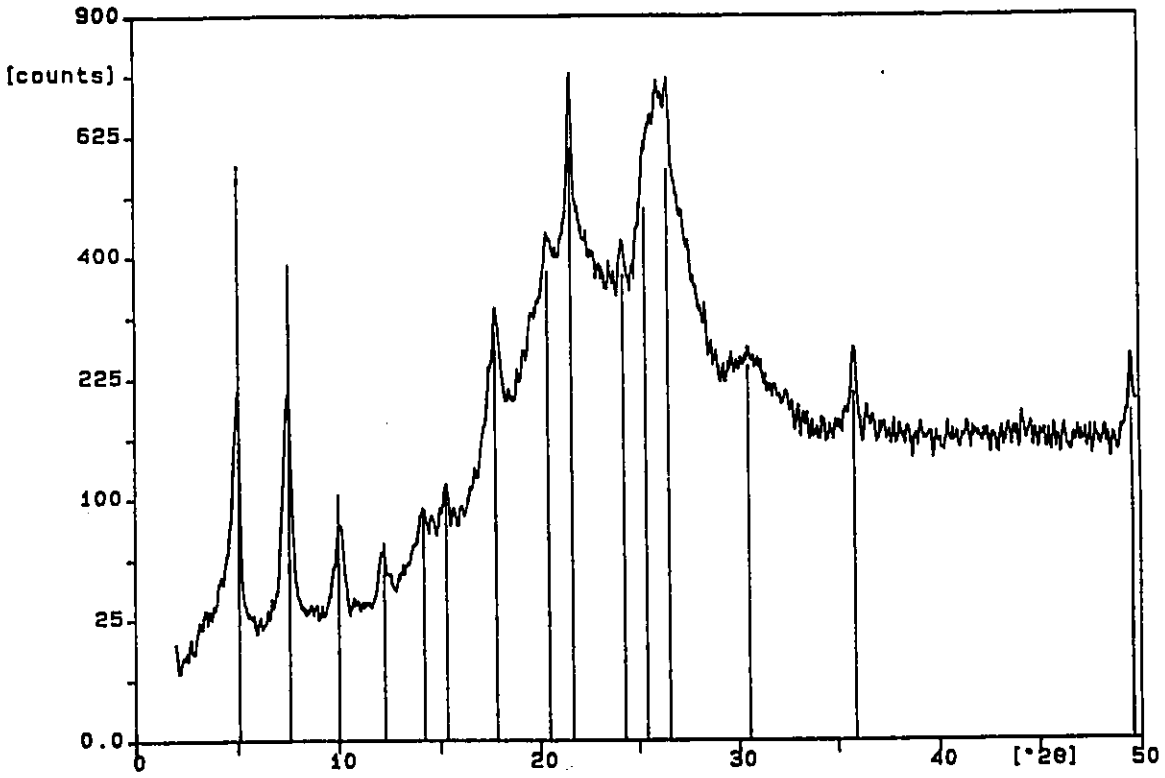

Figure 4.22 XRD patterns for trimethylmyristylammonium $[CH_3(CH_2)_{13}(CH_3)_3N^+]$ exchanged kenyaite.

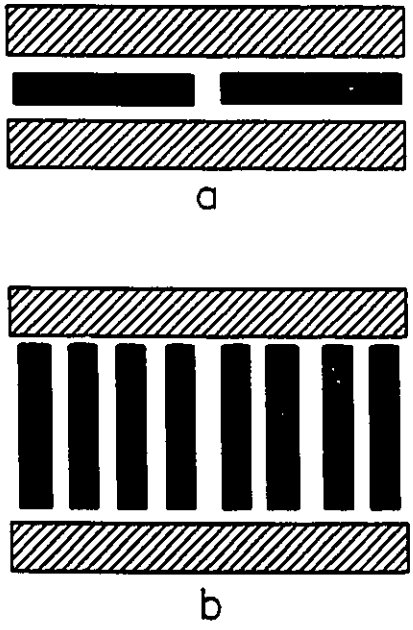

Figure 4.23 Arrangement of the alkylammonium chains of TMMyrA in the interlayers of (a) magadiite and (b) kenyaite.

4.3.2.2 Alkylamine intercalation

This technique is a useful counterpart to the tetraalkylammonium intercalation method since it can expand layered silicic acid to a similar extent as tetraalkylammonium ions do for the analogous alkali metal silicates. Thus, one can benefit from both the very high gallery expansion as well as from the increase number of hydroxyl sites on the interlamellar surfaces of the minerals.[120,138]

Thus, intercalation of H-magadiite and H-kenyaite was attempted by stirring 0.5g of the minerals in 2 ml *n*-octylamine for 72 hours at room temperature.

Characterization of the resulting intercalates by XRD was complicated by the formation of a white film upon exposure of the n-octylamine to the air (presumably its reaction with water forming octylammonium hydroxide) which exhibited strong diffraction lines and prevented the definitive observation of diffraction patterns for the layered silicic acid-amine complex. Attempts to wash or to pump the material free of excess amine resulted in the total collapse of the interlayer spaces of H-magadiite and H-kenyaite.

Therefore, due to the technical difficulties in the characterization of these intercalated complexes, this swelling technique was not utilized in any subsequent grafting experiments.

4.4 Grafting reactions of layered silicates

4.4.1 Silanation reactions

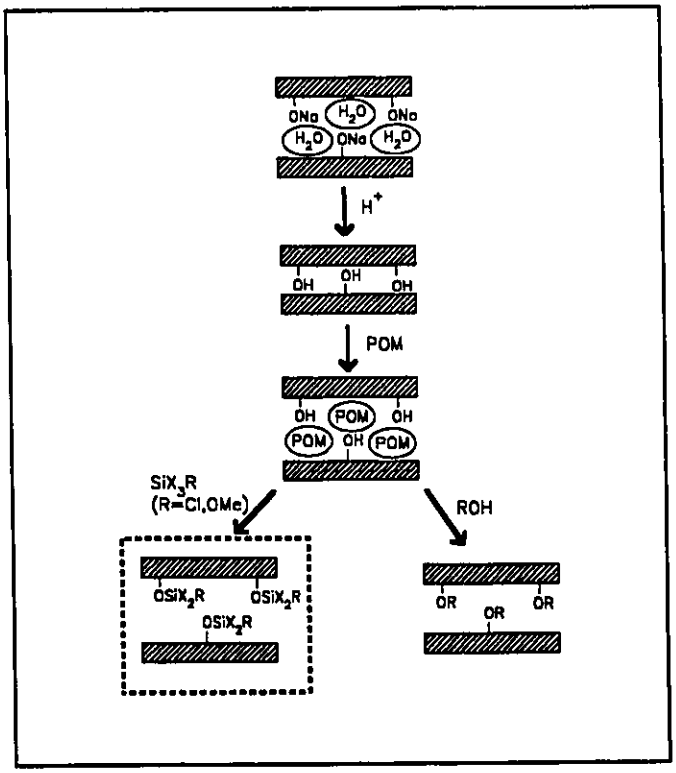

Preparation

The preparation of layered silicic acids functionalized with organosilane moieties involves drying at 110 °C *in vacuo* a sample (0.5 g) of H-magadiite or H-kenyaite and treating it with about 25 ml of NMF dried over molecular sieves. The NMF intercalate was then isolated by centrifugation and dispersed in dry dioxane. About 1 ml of an appropriate

organosilane (3-chloropropyltrimethoxysilane (CPTMS), 3-chloropropyldimethylchlorosilane (CPDMS), trimethylchlorosilane (TMS) or 3-mercaptopropyltrimethoxysilane (MPTMS)) was then added and the mixture was refluxed for 48 hours under nitrogen. The products were isolated by filtration or centrifugation followed by washing with dry dioxane. The SH-functionalized H-magadiite will henceforth be denoted as "thiomag" to avoid the usage of complex acronyms.

Thus, H-magadiite was derivatized into the following products: CPTMS-magadiite, CPDMS-magadiite, TMS-magadiite and MPTMS-magadiite. Similarly, MPTMS-kenyaite (henceforth denoted as "thioken") was prepared from the H-kenyaite precursor.

X-ray diffraction

For the silylated H-magadiite derivatives, the basal spacings increased to 14.5 Å (CPTMS-magadiite), 14.2 Å (CPDMS-magadiite) and 15.8 Å (TMS-magadiite), resulting in respective interlayer spacings of 3.3, 3.0 and 4.6 Å. All of these values are consistent with the presence of a monolayer of grafted molecules in the interlayer space.

The XRD pattern for MPTMS-kenyaite ("thioken") showed a basal spacing of 23.3 Å, or an interlayer separation of 5.8 Å. This would correspond either to a bilayer arrangement of the grafted molecules or a perpendicular arrangement of the thiopropyl chains with respect to the mineral plane. The relatively high density of hydroxyl sites on the H-kenyaite layers compared to that of H-magadiite can explain the propensity of the grafted molecules to adopt such configurations.

Thermogravimetric analysis

TGA profiles were performed for thiomag and thioken. Thiomag showed a single mass drop of 4.2% between 310 and 600 °C. Thioken showed two losses: the first between 250 and 400 °C (3.2%) and the other between 400 and 600 °C (4.8%).

Compared with thiomag, the greater total mass loss observed in thioken is consistent with the greater interlayer separation observed in the XRD pattern, indicating a denser loading of the grafted molecules in H-kenyaite. The two mass losses observed in thioken can be tentatively attributed to the presence of two types of grafting, the first resulting from silane moieties grafted to only one Si-OH group, the second to silanes attached to two Si-OH sites located adjacent to each other.

X-ray fuorescence

XRF analysis of thioken showed an Si/S molar ratio of 5. This quantity would suggest that five silane moieties have been grafted per unit formula of H-kenyaite ($H_4Si_{20}O_{42}$), which is slightly higher than the quantitative grafting of one molecule per hydroxyl group. This fact can be attributed to the possible formation of some silane clusters resulting from the cocondensation of silanes to each other due to the presence of trace amount of water in the reaction mixture.

4.4.2 Condensation of alcohols and diols

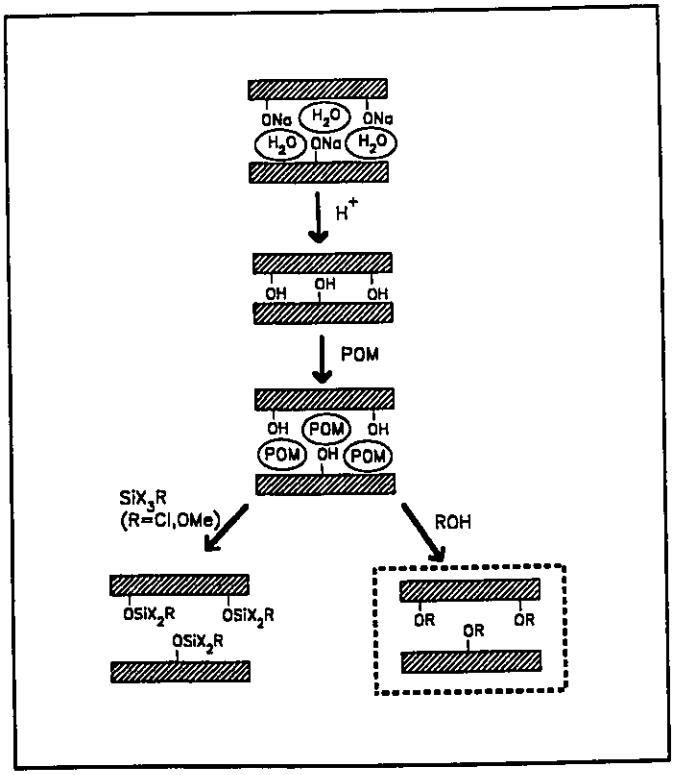

The working hypothesis of this section relies on the feasibility that alcohol functionalities, under heating, can spontaneously condense onto the interlamellar Si-OH groups of H-magadiite:

$$\text{Si-OH} + \text{HO-R} \rightarrow \text{Si-O-R} + H_2O$$

This grafting of alcohols to the silanols of activated silica gel has been reported.[193-196] Such strategies have, moreover, been used for the diols on silica gel with the purpose of generating new types of inverse-phase chromatographic columns.[197-202] This section will focus upon the interlayer covalent grafting of alcohols and diols to layered silicates. As well, the conformations adopted by these species within the mineral structure will be explored.

4.4.2.1 H-magadiite

Preparation

The procedure involved refluxing NMF/H-magadiite (prepared from about 1 g H-magadiite) in about 100 ml of neat alcohol or diol for 48 hours. The molecules chosen here all had boiling points in the range of 185 to 260 °C in order to promote their thermal condensation under reflux conditions while not being too high as to collapse the magadiite structure. The nanocomposites thus obtained were centrifuged and washed several times with acetone in order to expel physisorbed species. It was subsequently noticed, however, that some ungrafted intercalated molecules remained nonetheless trapped inside the structure which could be removed under ultra-high vacuum (UHV) or Soxhlet extraction: future samples were thenceforth washed by Soxhlet extraction over chloroform for 24 hours in order to expel all but the grafted moieties.

X-ray diffraction

For all of the grafted compounds prepared, significant increases of the basal spacings were observed with respect to that of H-magadiite. Table 4.4 shows the various species grafted in magadiite, along with their boiling points and the interlayer spacings of the nanocomposites. These results confirm the presence of the species in the interlamellar region of H-magadiite.

It is interesting that, prior to Soxhlet extraction, there is a consistent increase of the layer spacing as a function of the carbon chain length with the homologous α,ω-diol series (*i.e.* the $HO(CH_2)_nOH$ species with the hydroxyls at the terminal positions). This can be explained by the presence of ungrafted diol molecules packing with the grafted ones to form a monolayer of inclined organic chains, as depicted in figure 4.24a. Under UHV, however, the interlayer distances diminished significantly due to the removal of the ungrafted moieties, causing the chains to adopt a flat conformation in the interlamellar region of H-magadiite (Figure 4.24b).

Table 4.4 Boiling point of alcohols and diols and basal spacing of grafted magadiite derivatives.

Grafted species	Boiling point (°C)	Interlayer spacing (Å)	
		Initial	After UHV
ethylene glycol	196-198	2.3	3.0
1,3-propanediol	214	3.1	3.1
1,4-butanediol	230	4.0	3.7
1,5-pentanediol	242	5.3	3.9
1,6-hexanediol	250	5.8	4.2
1,7-heptanediol	259	7.0	6.2
1,2-propanediol	187	3.3	-
benzylalcohol	205	2.9	-
diethylene glycol	245	4.8	-
triethylene glycol	285	4.0	-
diethylene glycol monobutylether	231	3.1	-

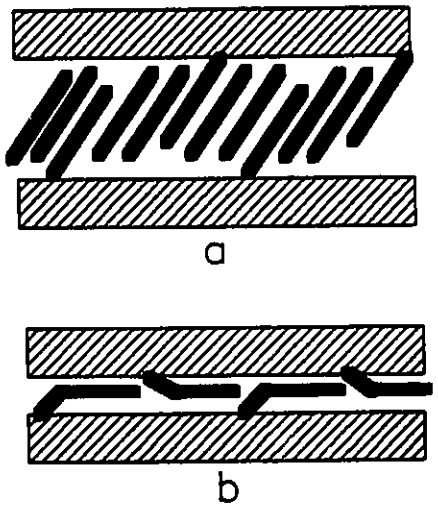

Figure 4.24 Schematic representation of diols grafted/intercalated into H-magadiite in the (a) inclined configuration and (b) monolayer configuration.

Infrared spectroscopy

In all cases, the free OH stretch at 3660 cm^{-1} in the H-magadiite spectrum is lost upon treatment with the diols and alcohols, suggesting that the OH groups are lost due to their condensation (grafting) to the included species and/or that they are hydrogen bonded to the simply intercalated (ungrafted) molecules, causing a shift of the band to the broad 3500 cm^{-1} region. This question, however, cannot be conclusively elucidated by this characterization method.

The presence of C-H stretching bands between 2850 and 3000 cm^{-1} in all FTIR spectra confirmed the presence of organic functionalities in the structure.

The characterizations which will follow were focussed solely on the diol series in order to make a thorough investigation of nanocomposites that could be readily compared with each other. Thus, ethylene glycol (EG), 1,3-propanediol (PG), 1,4-butanediol (BG) and 1,5-pentanediol (PentG) were chosen as the species for the comparative study.

Thermogravimetric analysis

TGA analysis of the diol-magadiite complexes (Figure 4.25) all featured their most significant mass losses between 400 and 600 °C, showing that the nanocomposites possess remarkable thermal stabilities. These features show that the guest molecules are very strongly held in the interlamellar region of H-magadiite, consistent with the covalent grafting hypothesis of the diols. The previous statement is clarified upon observation of the TGA of

H-magadiite intercalated (but not grafted) with ethylene glycol at room temperature,[e] where a single significant mass drop is observed between 100 and 180 °C (Figure 4.26): this is in strong support of the hypothesis that Si-O-C linkages were formed by the thermal treatment of ethylene glycol with H-magadiite. It is to be noted that the same low temperature mass loss seen in EG/H-magadiite is also observed in the grafted EG-magadiite,[f] indicating the coexistence of intercalated and grafted diols as was postulated above. After treating the material with Soxhlet extraction, the mass loss at 180 °C could no longer be seen (but the 550 °C loss remained intact), indicating the removal of the ungrafted species and leaving only the purely grafted organo-mineral compound.

---

[e]H-magadiite was stirred for 3 days in ethylene glycol at room temperature and filtered. XRD confirmed the intercalation of the guest (interlayer spacing of 4.0 Å).

[f]The following convention is used to distinguish between intercalated (host-guest complex) and grafted (the host and guest have chemically reacted and are covalently bound) species; they are respectively described by 'guest/H-magadiite' and 'guest-magadiite'.

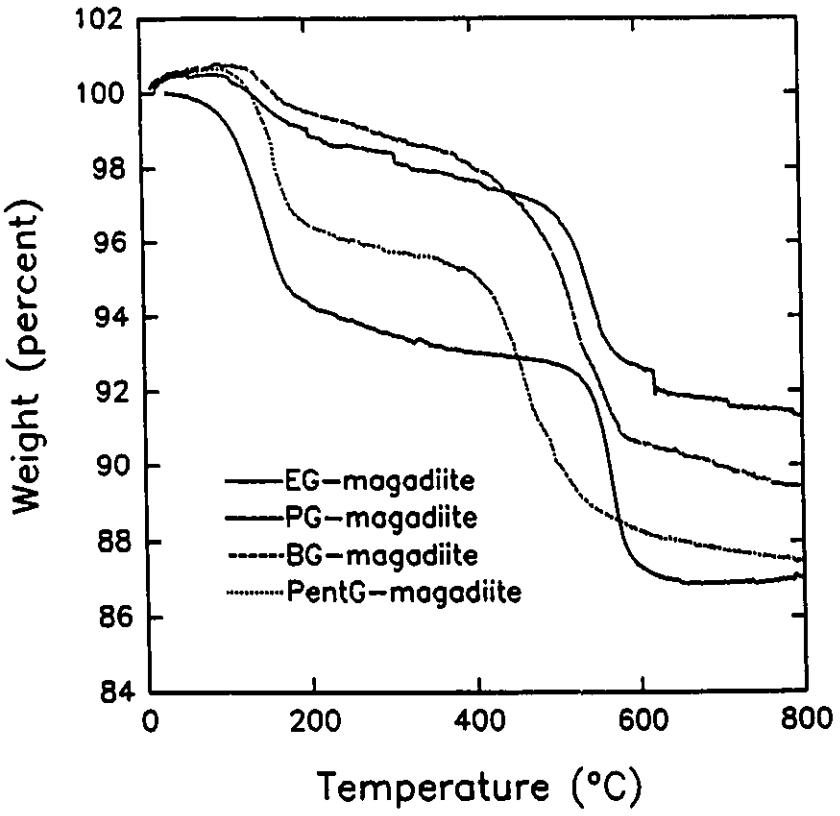

Figure 4.25 TGA curves for diol-magadiite complexes.

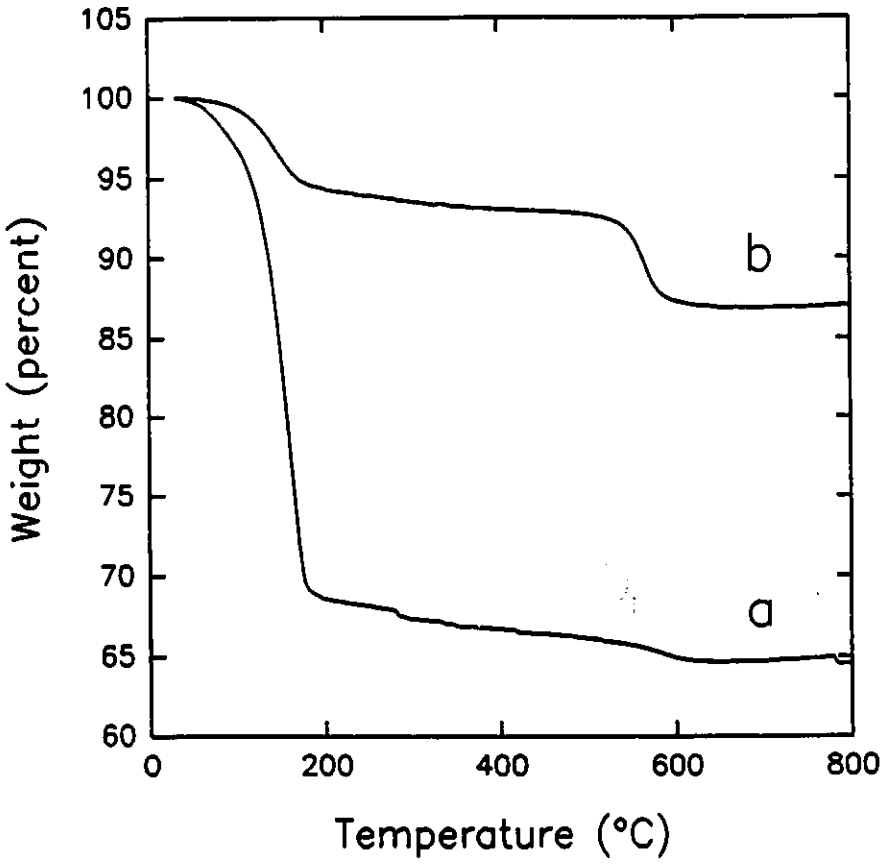

Figure 4.26 TGA profiles for ethylene glycol (a) intercalated into H-magadiite and (b) grafted into H-magadiite.

Elemental analysis

The analyses for C,H and N on the diol-magadiite samples were performed after they were washed by Soxhlet extraction and dried for 24 hours at 130 °C. The data thus obtained (quantitating the elements for compounds containing only grafted diol moieties) is shown in Table 4.5. In all cases, the N content was found to be negligeable, as expected. All of the samples were found to have an H:C ratio close to 2, slightly larger in the case of the BG and PentG grafts (2.1): these values are consistent with the presence of CH_2 groups in the materials and suggest the possibility that the diols may be grafted by both ends of their chains, since a higher H:C ratio (of 2.5 or higher) would be expected in the case of the diols being grafted from only one end (due to the presence of unreacted OH groups on both the H-magadiite surface and the diols). Due to the relatively low values of the hydrogen contents, however, it is possible that the uncertainties in the measured values make the discrimination between these cases impossible.

From the carbon content of the samples, one can calculate the percentage of H-magadiite hydroxyl sites which were grafted, assuming both one-end and two-end grafting and using the formula for H-magadiite found in this study ($H_{3.6}Si_{14}O_{29.8}$) (Table 4.6).

Table 4.5 C and H analyses for the magadiite-diol grafted complexes.

Diol	% C (by mass)	% H (by mass)
ethylene glycol	3.26	0.54
propanediol	4.79	0.65
butanediol	5.51	0.96
pentanediol	6.13	1.08

Table 4.6 Calculated percentages of grafted H-magadiite silanol groups, using the formula $H_{3.6}Si_{14}O_{29.8}$ and elemental analysis data.

Diol	percentage of H-magadiite hydroxyls grafted	
	by one end of diol	by both ends of diol
ethylene glycol	35%	69%
propanediol	35%	68%
butanediol	30%	59%
pentanediol	27%	53%

From this data, it is evident that the number of the grafted H-magadiite sites diminishes as the size of the guest diol increases. This suggests that steric factors may be involved in the grafting process, especially in light of the fact that no great increase in the interlayer spacing is observed between these materials. The confined space of the magadiite interlayers may thus preclude the complete hydroxyl grafting of larger guest molecules.

It is also of note that, according to Table 4.6, in no circumstance does the grafting seem to condense all of the H-magadiite hydroxyls, the maximum efficiency being close to 70% for EG and PG grafted at both ends. One must bear in mind, however, that a common drawback of elemental analysis with layered nanocomposites is its propensity to form unoxidizable carbonaceous residues: despite the use of copious amounts of tungsten oxide as oxidizing agent during the analysis in order to prevent this, such a problem might still have occurred during these analyses, possibly resulting in the measurement of a smaller amount of carbon than that actually contained in the sample. Moreover, in the case of EG-magadiite, the calculated H/C molar ratio is found to be exactly 2.0, suggesting that all of the interlayer Si-OH sites and all of the diol C-OH groups have been grafted: otherwise, one would expect a larger measured amount of H resulting from ungrafted Si-OH sites as well as from unbound ("dangling") C-OH groups on the diols (in a one-end grafting situation).

^{29}Si solid-state NMR spectrocopy

The ^{29}Si solid state NMR spectra of the diol-magadiite nanocomposites were recorded at 39.76 MHz with a 3.8 μs pulse width by using the CP-MAS sequence (763 to 3072 scans, spin contact time 10 ms, pulse repitition time 4 s) and are shown in Figure 4.27.

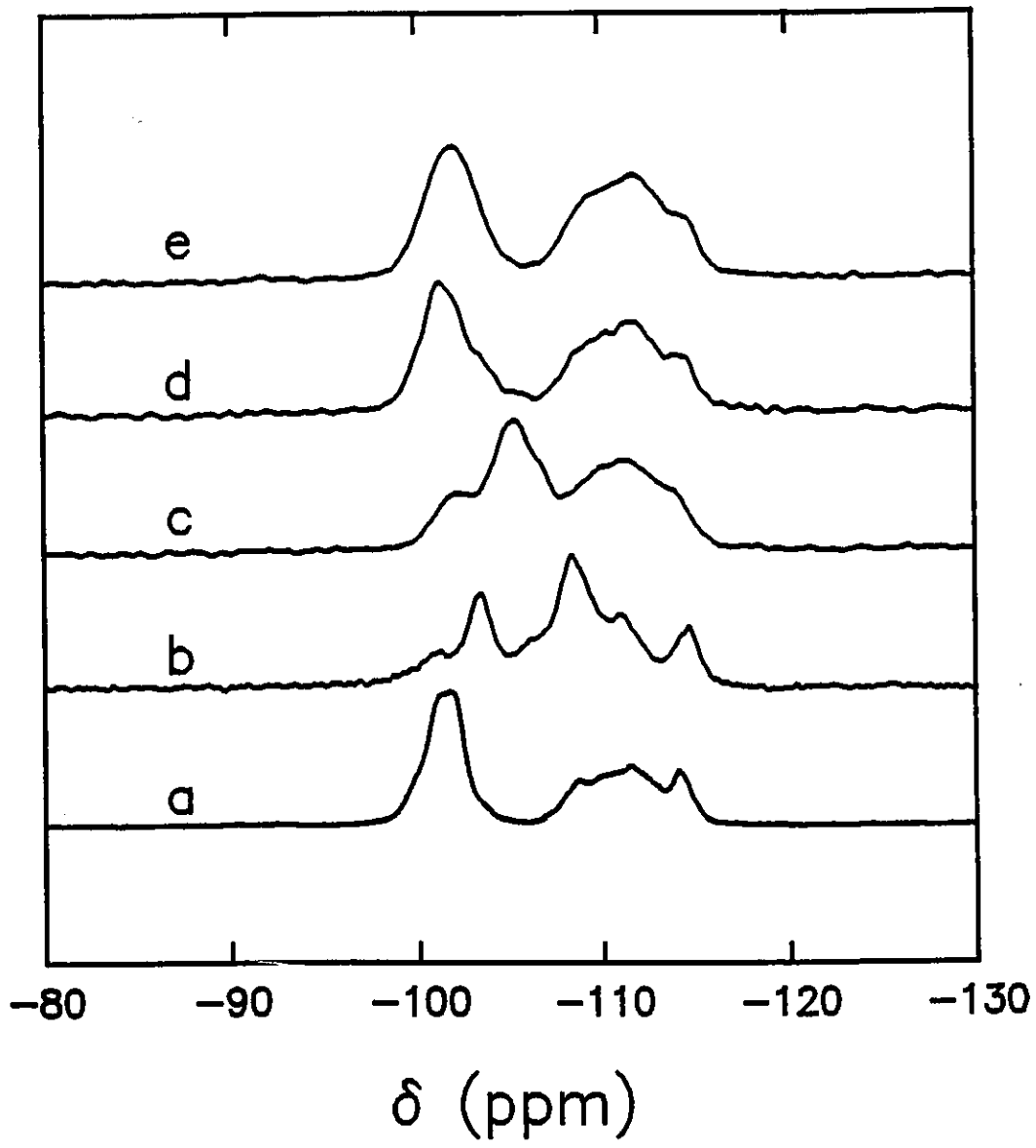

Figure 4.27 ^{29}Si NMR spectra of (a) H-magadiite, (b) EG-magadiite, (c) PG-magadiite, (d) BG-magadiite and (e) PentG-magadiite

All the spectra of diol-grafted magadiites featured a reduction in the relative intensities of the Q^3 signals, especially in the case of EG-magadiite. This effect can be attributed to the loss of the hydrogens on the H-magadiite interlayers resulting from the condensation with the diols. Thus, the Q^3 silicons no longer benefit from the great signal enhancement given by the ^1H cross-polarization. Assuming that all of the H-magadiite Si-OH groups have been grafted, the only possible source of cross-polarization becomes the hydrogens on the diol chains (or from the diol OH groups, if grafted by only one end). In contrast to H-magadiite, this situation would result in a more even distribution of ^1H magnetization transfer to **all** of the silicon sites in the structure, as the Q^3 sites would become no more proximate than the Q^4 sites to hydrogen atoms (*reminder*: the H-magadiite is composed of two Q^4 sheets which are in contact with the interlayer space, so this assumption can hold true). The outcome of this cross-polarization 'equalization' would be a similar intensity profile between the CP-MAS spectrum of the diol-magadiites and the proton-decoupled MAS spectrum of H-magadiite. This is indeed the case for EG-magadiite, and it can thus be concluded that the EG moieties are grafted to *all* of the interlayer hydroxyls of H-magadiite: if this were not the case, the remaining interlayer silanol groups would significantly increase the signal of the Q^3 site, as is the case for the other diol-grafted compounds who, as shown in Table 4.6, were found to have more residual Si-OH groups than EG-magadiite.

The chemical shifts for the diol-magadiites are given in Table 4.7, assigned according to the nomenclature used in section 4.2.1. Noteworthy is the pronounced displacement of the main Q^3 signals in the cases of EG-magadiite and PG-magadiite with respect to that of

H-magadiite (from -101.8 to -103.4 and -105.4 ppm, respectively). The same signals for BG-magadiite and PentG-magadiite do not exhibit this displacement, and are close to that of H-magadiite (although a small shoulder at higher field is observed for the BG-magadiite Q^3 signal). The isotropic chemical shifts of Q^4 sites were found by many authors to be strongly correlated with Si-O-Si bond angles in zeolites[203,204] and other silicates:[205] it has thus become apparent that the geometry of the silica tetrahedra strongly affects their NMR characteristics. On this basis, the chemical shift displacement observed for EG- and PG-magadiite can be tentatively explained by ethylene glycol and propanediol chains grafted at both ends on two adjacent Si-OH groups located either on the same side of the H-magadiite layer, resulting in bridging conformation of the diol chains (Figure 4.28b), or on silanols located across the interlamellar region, resulting in a pillared conformation (Figure 4.28a). This situation is likely to cause significant distortions in the geometry of the Q^3 silica tetrahedra with respect to that of H-magadiite, resulting in significant chemical shift displacements. Larger diols (BG and PentG) would be too long to adopt such a conformation, so they would be bound by only one end of their chains (Figure 4.28c) and the chemical shift of their Q^3 sites would remain unaltered. Smaller Q^3 signals are also present in the EG-magadiite and PG-magadiite spectra at -101 to -102 ppm which can be assigned to trace amounts of ungrafted Si-OH groups or to the presence of some unbridged diols (grafted by only one end).

It is noteworthy that the diol grafting (H to C substitution) has had little or no effect on the Q^3 chemical shift, as evidenced by the lack of any significant changes in the Q^3 signal position of either BG-magadiite or PentG-magadiite with respect to that of H-magadiite. This observation leads to the conclusion that any changes in the Q^3 chemical shifts in this system

is likely due to geometric considerations (*i.e.* Si-O-Si bond lengths and angles) rather than substituent effects.

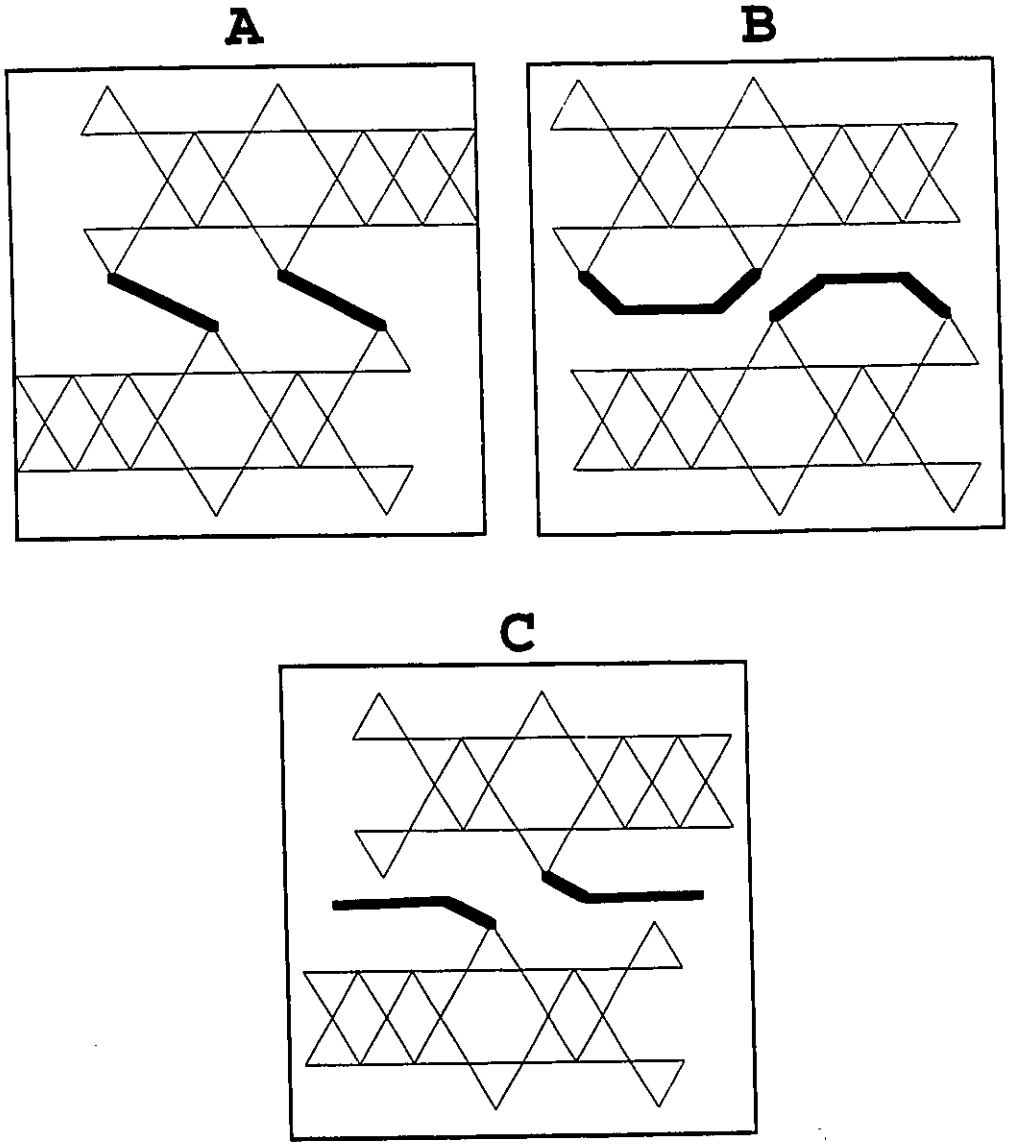

Figure 4.28 Possible grafting situations of diols in magadiite, showing (a) bridging conformation, (b) pillaring conformation and (c) one-end grafting.

Table 4.7 Chemical shifts (in ppm) of silicon sites in magadiite diol complexes (values in parentheses refer to less intense signals assigned to the same site)

Compound	δQ^3	δQ^{4a}	δQ^{4b}	δQ^{4c}
H-magadiite	-101.8	-108.8	-111.5	-114.1
EG-magadiite	-103.4 (-101.2)	-108.4	-110.9	-114.7
PG-magadiite	-105.4 (-102.2)	-110.0	-111.2	-113.7
BG-magadiite	-101.3	-108.9	-111.8	-114.0
PentG-magadiite	-102.0	-109.4	-111.8	-114.3

The Q^4 signals were mostly consistent with those observed for H-magadiite, with chemical shifts in all cases of about -109 (Q^{4a}), -112 (Q^{4b}) and -114 ppm (Q^{4c}). A striking observation, however, is the dramatic enhancement of the Q^{4a} signal at -108.4 ppm in EG-magadiite, signifying that, in the case of this material alone, this signal is in very close proximity to hydrogen protons. A possible explanation for this could be that the relative small size of the ethylene chain may have permitted it to key in a hexagonal cavity on the opposite magadiite layer, thus putting hydrogens in close proximity to Q^4 sites. This effect could not occur for larger chains, since these would be too large to fit in the cavity.

T_1 relaxation times for both the Q^3 and Q^4 sites of EG-magadiite were measured as 7.6 s and 12.0 s, respectively. The relaxation of these silicon atoms was somewhat faster than that of the parent H-magadiite, probably owing to the abundant presence of hydrogen atoms in the interlayer region which can quickly relax the Si nuclei through dipolar interactions.

Correlation between amount of grafted moieties and NMR results

A direct correlation is observed between the ratio of the Q^3 and Q^4 intensities (by ^{29}Si CP-MAS NMR) and the mass loss measured by TGA for the magadiite-glycol complexes. Figure 4.29 shows that the number of grafted diol molecules (expressed as being proportional to the TGA weight loss divided by the number of carbons in the respective diols) diminishes as a function of the relative intensities (peak areas) of the Q^3 and Q^4 signals. Thus, when EG is grafted into H-magadiite, the Q^3 signal becomes, in comparison to that of H-magadiite, very small in comparison to that of the Q^4 as a result of the abstraction of the

silanol protons. When larger diols are inserted, the amount of grafted diols diminishes and residual ungrafted Si-OH sites result in an increase of the Q^3 signal intensity. When pentanediol is grafted, the spectral characteristics become similar to that of the parent H-magadiite since there remains a significant number of ungrafted hydroxyl groups in this material.

What has been demonstrated here is that the relative intensity of the Q^3 and Q^4 signals as measured by CP-MAS NMR is diagnostic of the relative amount of Si-OH sites which are grafted into the structure and that complete grafting is likely to result in a spectral profile similar to that of the corresponding proton decoupled spectrum (as was previously discussed). Incomplete grafting would give rise to a spectrum which would appear more like that of H-magadiite (using CP-MAS).

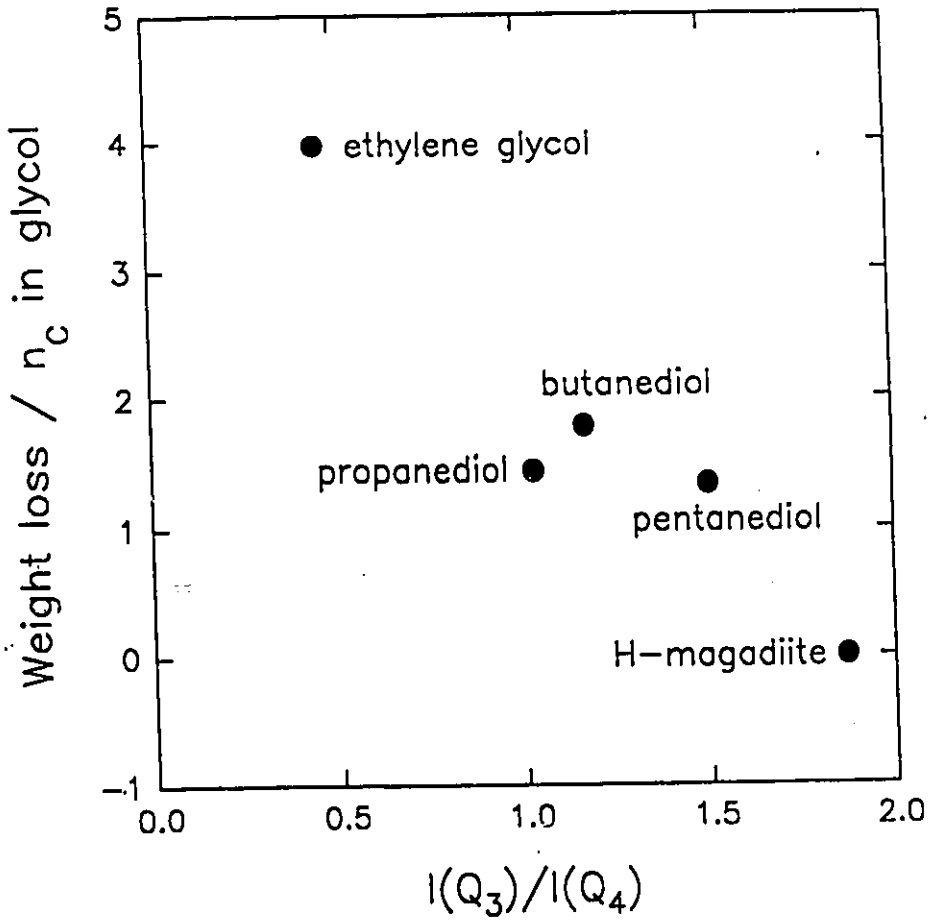

Figure 4.29 Correlation between TGA mass loss of grafted diols and the relative intensities of the ^{29}Si CP-MAS NMR sites for magadiite-diol complexes.

^{13}C solid-state NMR spectroscopy

The ^{13}C solid state NMR spectra of the diol-magadiite nanocomposites were recorded at 50.32 MHz with a 4.2 μs pulse width by using the CP-MAS sequence (2048 to 6848 scans, spin contact time 10 ms, pulse repetition time 2 s) and are shown in Figure 4.30. Spectra were also recorded for ethylene glycol and propanediol intercalated into H-magadiite at room temperature in order to compare the NMR data with their grafted analogs. Dipolar dephasing experiments were also performed on both the grafted and intercalated compounds in order to study the relative mobilities of the carbon moieties, using up to 40 μs dephasing times.

Table 4.8 shows the chemical shifts for the methylene groups for both intercalated and grafted magadiite compounds. It was found that the diols simply intercalated into H-magadiite had chemical shifts nearly identical to those of liquid state spectra. Upon grafting, however, significant differences are observed in the corresponding signals: the EG signal is shifted by 1.7 ppm to lower field, whereas the signals of propanediol were moved to higher field (by 3.2 ppm for the C-1 signal and 9.6 ppm for the C-2). This can be attributed to two phenomena: (1) the substituent effect caused by the formation of a C-O-Si bond and (2) the effect of the methylene chain configuration adopted in the grafted compounds.

It has been proposed that the ^{13}C chemical shifts of polyethylene oxyde chains shift to lower ppm when the ethylene chains adopt a predominant *gauche* conformation.[206] This is supported by the low chemical shift of dioxane (66.5 ppm),[207] whose ethylene chains are locked in a *gauche* conformation, compared to that of dimethylethylene glycol ($CH_3OCH_2CH_2OCH_3$) (72.3 ppm),[206] whose conformation is predominantly *trans*. The

chemical shift reported here for the oxoethylene units of EG-magadiite seems consistent with that of ethylene units locked in a *gauche* conformation, suggesting that the bridging configuration shown in Figure 4.28b is likely to be the case for EG-magadiite, as a much more downfield chemical shift would be expected if this molecule were to adopt a *trans* pillaring arrangement. The upfield shifts of the propylene unit signals with respect to the liquid state situation would likewise suggest a *gauche* arrangement of the methylene groups, again consistent with a bridging conformation of this species. The lack of any appreciable change in the chemical shifts of butanediol would indicate that no such "*gauche*-locking" occurs for this molecule resulting in no change from the preferred *trans* arrangement, as would be expected in a one-end grafting situation (Figure 4.28c).

The half-height line widths of the grafted carbons (EG: 75 Hz, PG: 130 and 190 Hz) were considerably larger than those of the intercalated chains (EG: 35 Hz, PG: 20 and 15 Hz), indicating faster relaxation of the carbon signals possibly resulting from enhanced dipolar relaxation resulting from the relative immobility of the grafted carbon chains in H-magadiite.

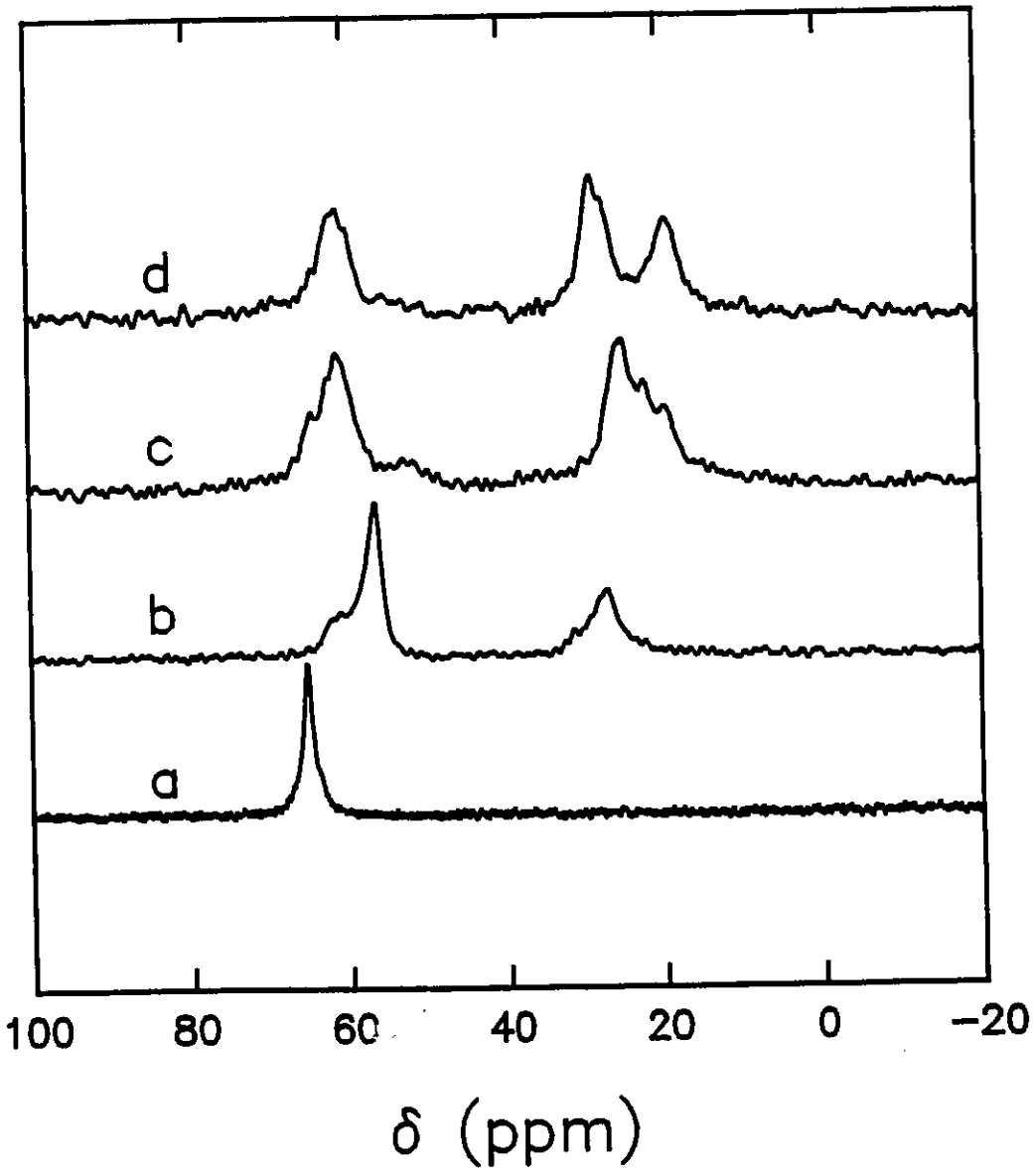

Figure 4.30 ^{13}C NMR spectra of (a) EG-magadiite, (b) PG-magadiite, (c) BG-magadiite and (d) PentG-magadiite.

Table 4.8 ^{13}C chemical shifts (in ppm) of carbon sites in grafted magadiite-diol species and in intercalated (ungrafted) compounds (numbers in parentheses refer to bulk liquid shifts). C-1 refers to methylene units adjacent to oxygen atoms, C-2 to those one carbon removed, and C-3 to those two carbons removed.

diol	C-1		C-2		C-3	
	Grafted	Ungrafted	Grafted	Ungrafted	Grafted	Ungrafted
EG	65.3	63.6 (63.4)	-	-	-	-
PG	56.3	59.5 (60.2)	26.9	35.5 (36.4)	-	-
BG	61.2	n.d. (62.1)	24.9	n.d. (29.4)	-	-
PentG	60.9	n.d.	28.5	n.d.	19.1	n.d.

It is noteworthy to observe that EG-magadiite has a single carbon signal, indicating that only one carbon environment exists in this species: this is also consistent with the case of a bridging EG species (grafted by both ends) since in the case of a molecule grafted by only one end one would observe two carbon signals, or a shoulder/assymetry on the signal. Similar conclusions can be made for PG-magadiite, but a less intense second C-1 signal is also observed at lower field, possibly the result of a small quantity of propanediol species grafted by only one end. The BG-magadiite spectrum, however, shows distinct shouldering of the signals which could be attributed to the presence of species grafted at only one end, resulting in the resolution of four signals due to the dissymetry in the diol chain. Although similar conclusions are less evidently arrived at in the case of PentG-magadiite due to the breath of the signals and high signal to noise ratio, the hypothesis that such chains are grafted by only one end cannot be precluded. ^{13}C NMR results are thus very consistent with the grafting hypothesis proposed on the basis of the ^{29}Si NMR data.

The mobilities of the carbon chains can be studied further by way of dipolar dephasing NMR. Thus, a variable dephasing period is applied between cross-polarization and acquisition in order to allow attenuation of the methylene signals. After applying a 40 μs dephasing time, the signals of very rigid methylene signals would be expected to decay completely, whereas more mobile moieties may have some residual intensity. Figure 4.31 shows the results of this experiment for the diol-magadiite series. It is thus clearly observed that the most mobile carbons (the ones with signals that decay least as a function of dephasing time) are those of the C-2 and C-3 carbons of butanediol and pentanediol. Less mobile are the C-1 methylenes belonging to these same diols, which can be explained by the

fact that one of these groups is attached to the magadiite surface (the other C-1 group is not, but the *average* motional rigidity between both would be nonetheless greater than the C-2 and C-3 methylenes). The most rigid methylenes belong to propanediol and ethylene glycol, which decay almost completely after 40 μs of dephasing: this is strong evidence supporting the bridging conformation of these species, since the grafting of both ends of these diols would expect to lead to the fixation of the chains in a very rigid conformation. The data from Figure 4.31 can be quantitated by using the expression proposed by Alemany *et al.*[208] to describe the intensity decay of methylene carbons as a function of dipolar dephasing time:

$$I = I_0 \exp[-t_1^2/(2T_2^2)]$$

Which can be tranformed to the linear form:

$$\ln(I/I_0) = -t_1^2/2T_2^2$$

Where I/I_0 is the relative signal intensity, t_1 the dephasing time and T_2 a time constant related to the carbon mobility. Thus, by plotting t_1^2 as a function of $\ln(I/I_0)$, one can obtained the T_2 parameter from the slope of the linear range of the plot. Table 4.9 shows the T_2 constants calculated for the methylene groups in the diol-magadiite series, and these values are plotted as a function of the diol chain length in Figure 4.32. Although the range of the time constants for the diols is rather small (13.8 to 20 μs), the values for the EG and PG carbons (13.8 to 15 μs) are all significantly smaller than those of BG and PentG (18 to 20

μs): this is consistent with the higher rigidity of the latter species with respect to BG and PentG.

It is notable that all of these values signify high rigidity with respect to bulk organic solids which exhibit T_2 times on the order of 200 μs: this constricted interlayer environment in which the organic species are located thus bestows a high degree of rigidity to the included molecules, regardless of their grafting conformation.

The lower field shoulder of the PG-magadiite C-1 signal was found to have a time constant of 16 μs, slighly higher than the other T_2 values for this compound and suggestive of a more mobile propanediol moiety grafted only by one end.

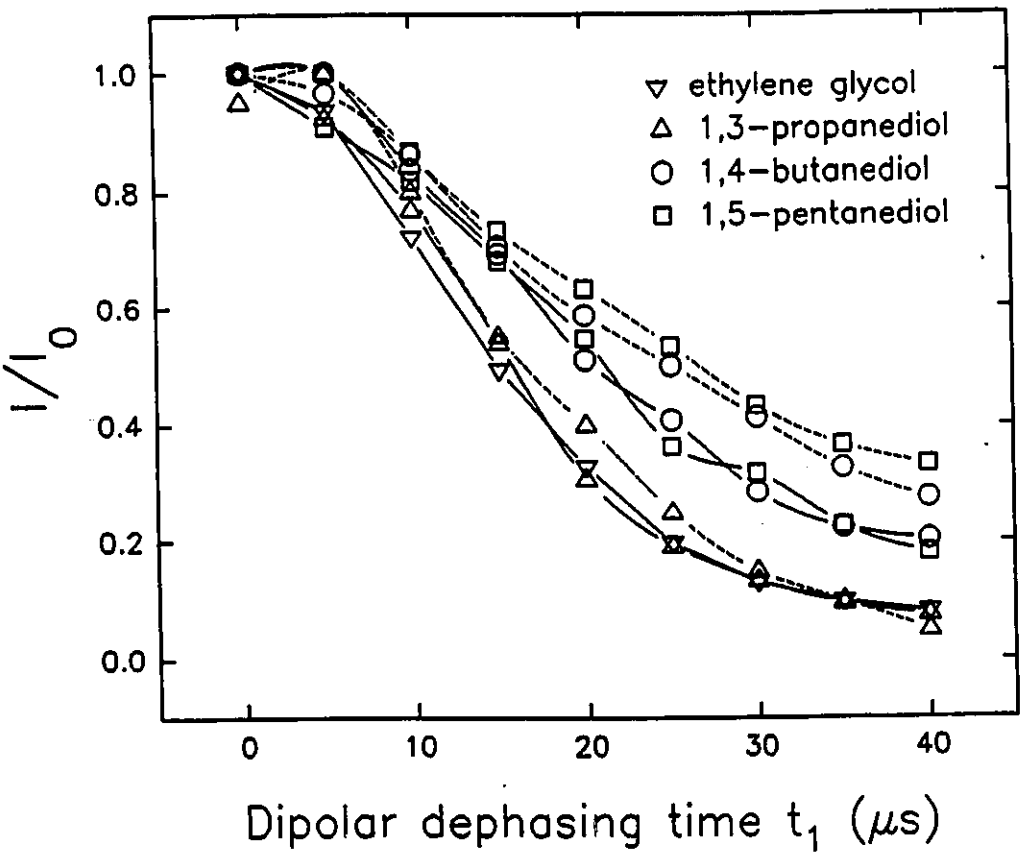

Figure 4.31 ^{13}C NMR signal intensities of diol-magadiite complexes using variable dipolar dephasing times. Solid lines correspond to C-1 and dashed lines to C-2 signals.

Table 4.9 T_2 decay time constants for diol-magadiite ^{13}C signals

Diol	Signal	T_2 (μs)
Ethylene glycol	C-1	13.8
1,3-propanediol	C-1	14
	C-2	15
1,4-butanediol	C-1	18
	C-2	19
1,5-pentanediol	C-1	18
	C-2 and C-3	20

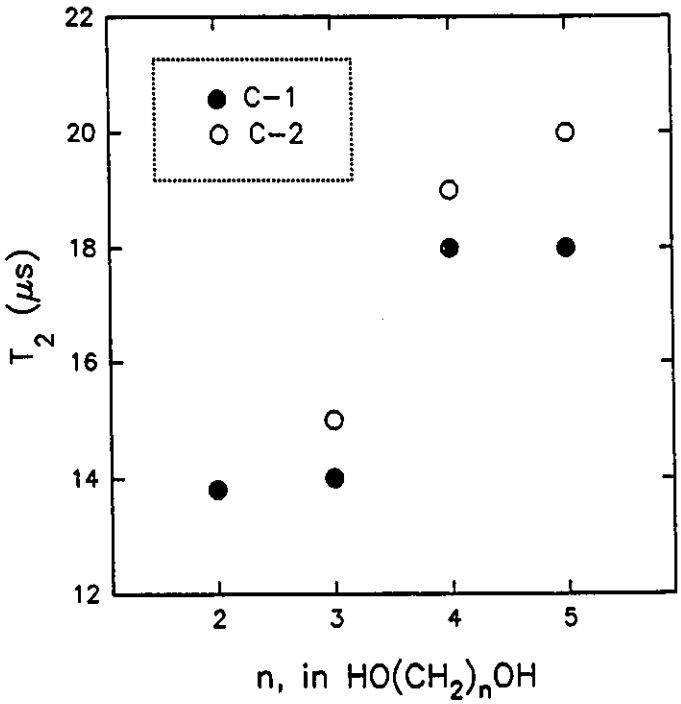

Figure 4.32 T_2 values for diol-magadiite complexes.

Porosity measurements

N_2 BET measurements were carried out on a Micromeritics ASAP 2000 instrument for H-magadiite and the diol-magadiite samples (with prior treatment under UHV). Total surface area measurements were made, as well as t-plot and Horvath-Kawazoe calculations, the results of which are summarized in Table 4.10.

Thus, an increase in surface area is observed from H-magadiite upon the grafting of EG and PG. The t-plot calculation ascertained that this surface area enhancement was the result of increased microporosity, since the external surface area remained approximately constant in all of the studied cases. The grafting of these species thus renders the interlamellar region of magadiite accessible for gas diffusion, reaching a maximum of 65 m^2/g of micropore area in PG-magadiite (effectively doubling the total surface area with respect to H-magadiite). Although appreciable, this microporosity is far from the 200-300 m^2/g micropore areas obtained by other pillared clay compounds. In contrast, BG- and PentG-magadiite featured almost no microporosity, possibly a result of the stuffing of the interlayer space with the longer diol chains. It is, however, interesting to note the increase of pore size maxima from 5.0 to 5.4 Å for EG- and PG-magadiite to 7.0 Å for BG- and PentG-magadiite: the latter two compounds may possess pockets of relatively large pores whereas the former two have more abundant pores of smaller dimensions.

The grafting of diols into layered silicates thus affords microporous materials, although the extent of this microporosity may be too small for practical separation or adsorption applications. Access to the interlayer surface has, however, been achieved to a certain degree and future applicability of such materials may not necessarily be precluded.

Table 4.10 N_2 BET information on the diol-magadiite system.

Compound	BET surface area (m^2/g)	Horvath-Kawazoe pore size maximum	t-plot data		
			micropore volume (ml/g)	micropore surface area (m^2/g)	external surface area (m^2/g)
H-magadiite	43.6	6.1 Å	0.0055	16	39
EG-magadiite	60.6	5.4 Å	0.0136	38	48
PG-magadiite	74.9	5.0 Å	0.0231	65	45
BG-magadiite	39.8	7.0 Å	0.0031	9	41
PentG-magadiite	38.5	7.0 Å	0.0039	11	41

Pyridine adsorption

Samples of H-magadiite and the diol-magadiite compounds were exposed to pyridine vapour (about 35 Torr) after prior pumping under vacuum. The FTIR spectra of the pyridine adsorbed compounds were then recorded (KBr pressed pellet).

The most striking observation within this set of spectra is the change in position of the 1439 cm^{-1} band of pyridine (shown in Table 4.11), assigned to the aromatic-ring vibration mode 19b.[209] This 1454 cm^{-1} band observed when pyridine was adsorbed on H-magadiite can be attributed to the pyridine bound to acidic sites on the mineral. The shift of this band to 1438 and 1434 cm^{-1} in EG- and PG-magadiite shows that the acidic sites are no longer present (due to the grafting of the diols) and that the adsorbed pyridine molecules (plausibly in the micropores of the materials) have liquid-like behaviour. The shift of these peaks to 1447 and 1452 cm^{-1} shows increased acidity in these materials due to the presence of Si-OH groups resulting from the incomplete grafting of these sites by the longer diols. Moreover, a band at 1604 cm^{-1} was found for H-magadiite, BG-magadiite and PentG-magadiite which could also be assigned to pyridine interacting with acidic sites.[209] Thus, the complete grafting of EG and PG moieties in H-magadiite has resulted in a virtually complete elimination of the acidic nature of the H-magadiite, whereas this occurs only partially in the case of BG and PentG-magadiite.

Table 4.11 Shifts in pyridine band upon exposure to diol-magadiite complexes.

Adsorbent	Pyridine vibrational mode 19b[209] (cm^{-1})
Liquid-state	1439
H-magadiite	1454
EG-magadiite	1438
PG-magadiite	1434
BG-magadiite	1447
PentG-magadiite	1452

4.4.2.2 H-Kenyaite

Preparation

The diol-kenyaite composites were prepared following identical procedures as for H-magadiite (see section 4.4.2.1). Thus, ethylene glycol, 1,3-propanediol and 1,4-butanediol were grafted in the interlamellar region of H-kenyaite.

X-ray diffraction

XRD patterns revealed spacings for EG-kenyaite, PG-kenyaite and BG-kenyaite of 19.5 Å. Each compound thus featured an interlayer spacing of 2.0 Å, corresponding to a monolayer of carbon chains in the interlayers of H-kenyaite.

^{29}Si NMR spectroscopy

The ^{29}Si CP-MAS spectra for the diol-kenyaite series were recorded following similar procedures as that of the diol-magadiite series (see section 4.4.2.1) and are shown in Figure 4.33.

As in the case of H-magadiite, the grafting of diols on the interlamellar region of H-kenyaite has caused an "equalization" of the Q^3 and Q^4 signals, with the relative Q^4 intensities increasing with respect to that of the Q^3. Also similar to the H-magadiite analogs, shifts in the positions of the Q^3 sites are observed for the EG and PG grafted materials, as shown in Table 4.12. This phenomenon can likewise be attributed to the presence of

bridging diol moieties causing distortion in the Q^3 tetrahedral geometries, as was proposed for the diol-magadiite system.

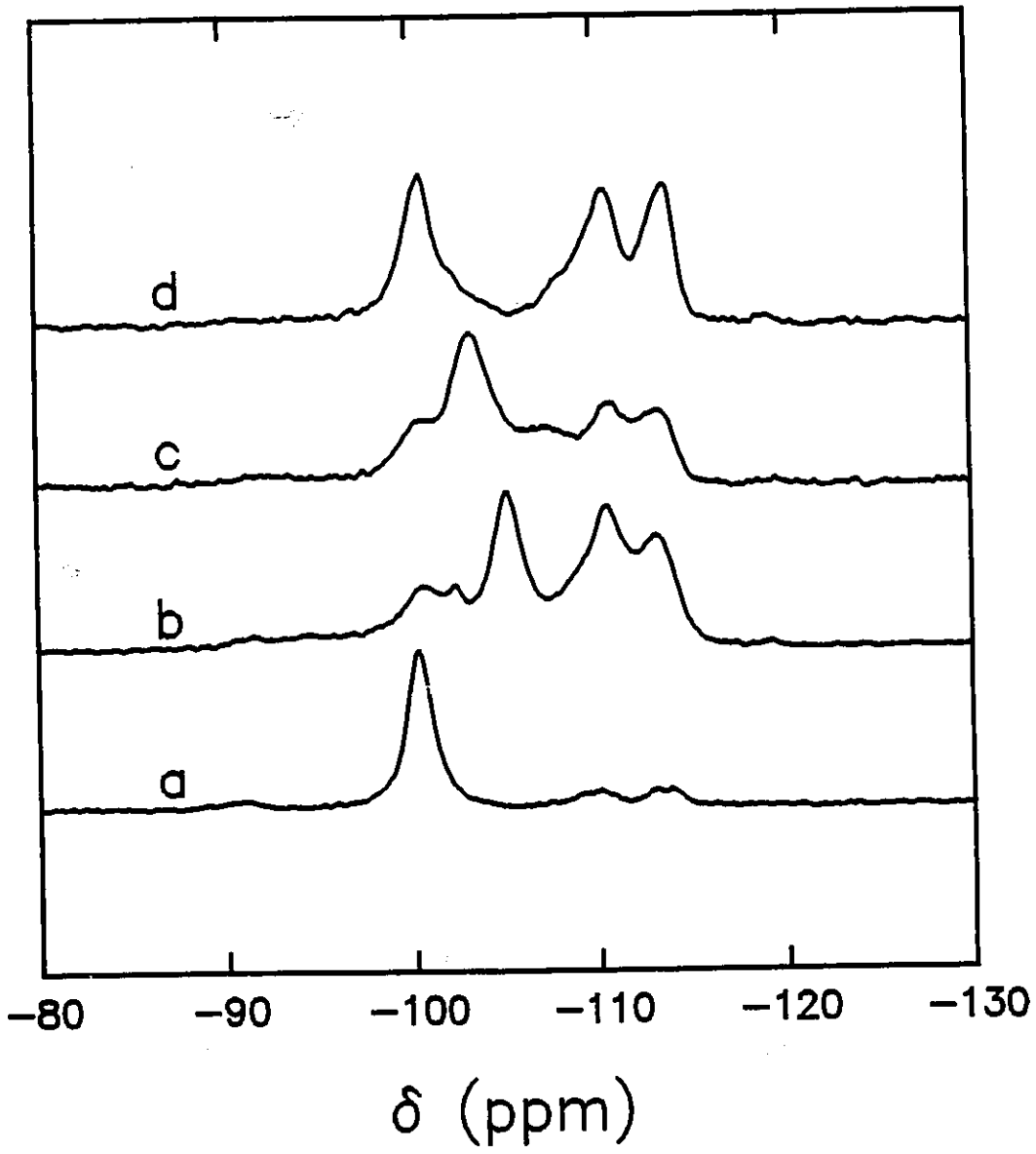

Figure 4.33 ^{29}Si CP-MAS NMR spectra of (a) H-kenyaite, (b) EG-kenyaite, (c) PG-kenyaite and (d) BG-kenyaite.

Table 4.12 Chemical shifts (in ppm) of silicon sites in kenyaite-diol complexes (values in parentheses refer to less intense signals assigned to the same site).

Compound	δQ^3	δQ^{4a}	δQ^{4b}	δQ^{4c}	δQ^{4d}	δQ^{4e}
H-kenyaite	-100.3	-107.6	-110.3	-113.0	-113.9	-119.1
EG-kenyaite	-105.2 (-100.3, -102.3)	-	-110.6	-113.2		-
PG-kenyaite	-103.3 (-100.3)	-107.2	-111.2	-113.5		-
BG-kenyaite	-100.7	-	-110.7	-113.9		-

Interestingly, the new positions of the Q^3 signals in the case of EG- and PG-magadiite seem to have switched places when compared to EG- and PG- magadiite: it can be postulated that EG affects the geometry of the Q^3 silicons of kenyaite in much the same way as PG affects that of the magadiite Q^3 sites. Consequences of these observations on the grafting conformations of the diols in both H-magadiite and H-kenyaite will be discussed in more detail in section 4.4.2.3.

^{13}C solid-state NMR spectroscopy

The ^{13}C CP-MAS spectra of EG-kenyaite, PG-kenyaite and BG-kenyaite were recorded following identical procedures to those of the diol-magadiite series. Since these compounds were not treated with UHV or Soxhlet extraction, dipolar dephasing (40 μs dephasing time) was used in order to identify the signals resulting from the mobile ungrafted diol molecules: thus, the signals corresponding to the grafted diols could be located, as shown in Figure 4.35. Spectra of EG and PG intercalated into H-kenyaite were recorded and compared with those of the grafted compounds in Table 4.13.

The chemical shift value of the EG-kenyaite complex would suggest, as in the case of EG-magadiite, a *gauche* conformation of the ethylene chains. Similar to PG-magadiite, the PG-kenyaite C-2 signal was shifted to significantly higher field (from 35.4 ungrafted to 30.0 ppm grafted), also suggesting the adoption of a *gauche* conformation. Contrary to BG-magadiite, however, the BG-kenyaite signals observed for the grafted moieties were significant shifted to higher field, suggesting that this molecule may also be in a *gauche* conformation as a result on being grafted by both ends. Figure 4.34 suggests a possible

grafting configuration which can account for the *gauche* conformation of the methylene groups of butanediol. This picture can, moreover, feasibly explain the increased signal intensity of the Q^4 sites by CP-MAS NMR shown in Figure 4.33d (with respect to that of PG-kenyaite) since the methyl hydrogens would likely be in close proximity to the Q^4 silicons as a result of their "keying" into hexagonal cavities of the kenyaite layers (a situation analogous to that of the EG-magadiite system).

These results thus clearly demonstrate the analogy which can be made between the kenyaite and magadiite diol grafting systems.

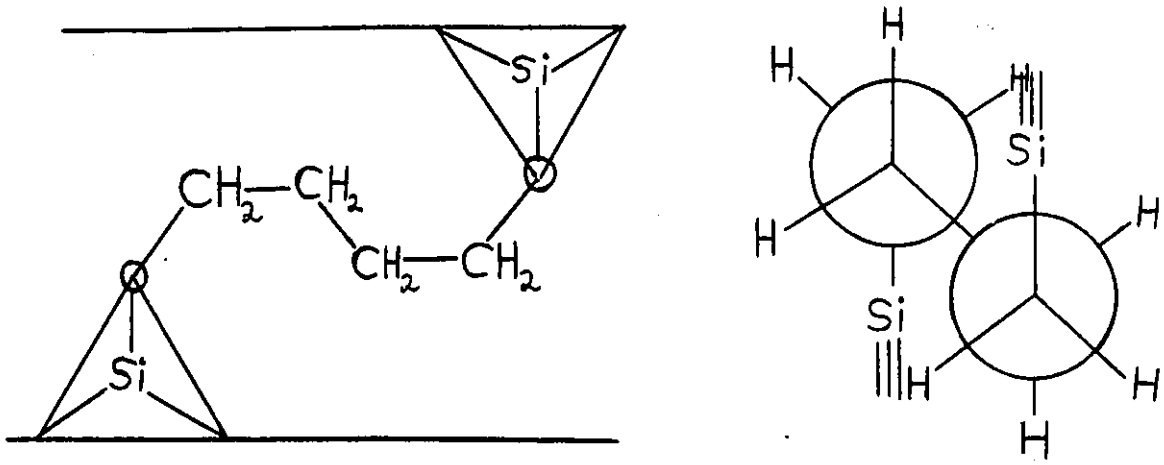

Figure 4.34 Hypothetical grafting situation of butanediol in H-kenyaite.

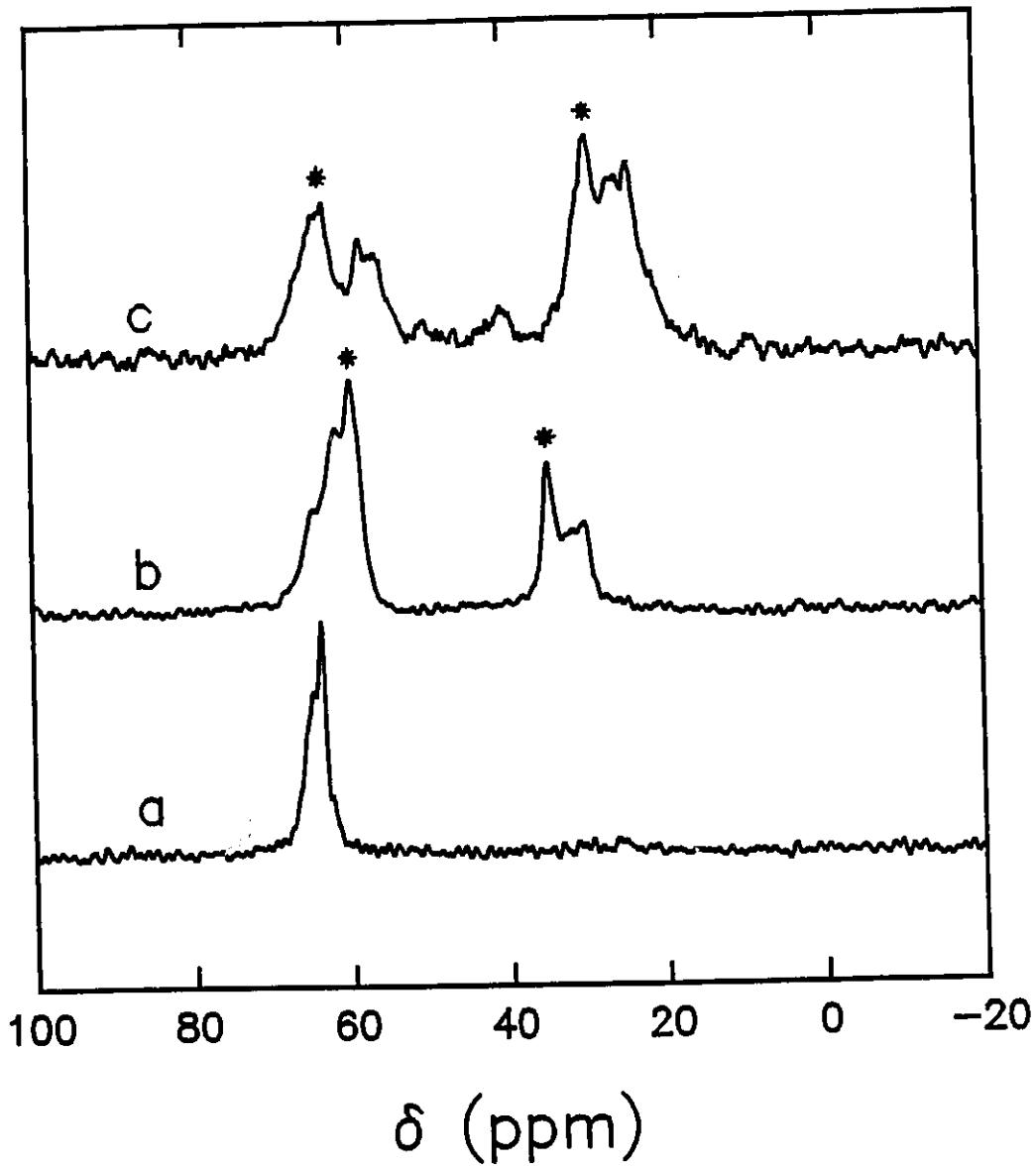

Figure 4.35 ^{13}C NMR spectra of (a) EG-kenyaite, (b) PG-kenyaite and (c) BG-kenyaite. Asterisks denote ungrafted (intercalated) diols as detected by dipolar dephasing NMR.

Table 4.13 ^{13}C chemical shifts (in ppm) of carbon sites in grafted kenyaite-diol species and in intercalated (ungrafted) compounds (numbers in parentheses refer to bulk liquid shifts). C-1 refers to methylene units adjacent to oxygen atoms and C-2 to those one carbon removed.

diol	C-1		C-2	
	Grafted	Ungrafted	Grafted	Ungrafted
EG	65.3	63.5 (63.4)	-	-
PG	61.6	59.5 (60.2)	30.1	35.4 (36.4)
BG	57.8	n.d. (62.1)	25.5 and 23.8	n.d. (29.4)

4.4.2.3 Conformations of grafted diols in layered silicates

According to the ^{29}Si chemical shifts for the Q^3 sites observed in the diol-magadiite and diol-kenyaite spectra, one can identify three distinct types of grafting characterized by Q^3 signals at -105, -103 and -101 ppm. On the basis of this and other experimental evidence, it is possible to postulate about how the diols are grafted on the interlamellar surfaces of H-magadiite and H-kenyaite. ^{13}C NMR results have suggested that EG and PG moieties are likely to be grafted by both ends and adopt a bridging configuration, grafting adjacent Si-OH groups on the same silicate layer.

The Q^3 signals at -105 ppm can be attributed to some significant alteration of the tetrahedral geometry of the Si-OH sites and could be explained by the bridging of two nearby hydroxyls on the same silicate layer such that a certain degree of strain is imparted upon the Si-O-Si bond angles. Two such situations can be envisaged, being referred to as "outward" and "inward" distortions, both of which being schematically represented in Figure 4.36. Inward distortion would be expected when diols bridge hydroxyls which are slightly farther apart than the length of the diol carbon chain, thus causing the Q^3 sites to be "pulled together". Outward distortion should occur if the bridging diol chain is slightly longer than the distance between the hydroxyl sites, resulting in a "pushing apart" of the Q^3 tetrahedra.

The Q^3 signal at -103 ppm can be assigned to a somewhat less altered tetrahedral geometry compared to the strained situation described in the previous paragraph, suggesting a more "comfortable fit" of the bridging diols. It can thus be postulated that this type of site corresponds to a bridging situation such that the Si-O-Si bond angles of the Q^3 sites are only

slightly altered by the grafting due to the favourable matching between the distance separating the hydroxyls and the length of the diol carbon chains.

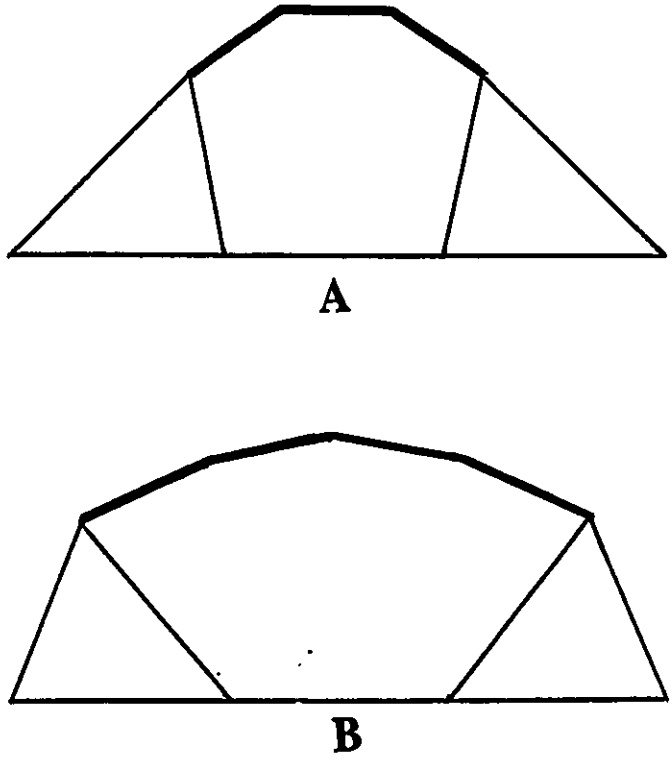

Figure 4.36 Representation of (a) inward and (b) outward Q^3 tetrahedral distortions resulting from the strain imparted by bridging diols.

The third Q^3 signal observed in the grafted silicates at -101 ppm would occur when no significant alteration of the tetrahedral geometry occurs, such that the signal is found at the same chemical shift as that of the parent H-magadiite. This should be observed in the case of unbridged diols (bound by only one end), as no strain is confered to the tetrahedra.

In EG-magadiite, the chains may be grafted to two Q^3 sites separated by one Q^4 tetrahedron, as depicted in Figure 4.37 (top picture), resulting in a strain-free bridging of the surface silanols. Those in PG-magadiite may bridge these same sites, but the longer length of the chain may force an outward distortion of the Q^3 sites.

EG chains grafted on H-kenyaite could instead be bound to two immediately adjacent Q^3 sites, resulting in outward distortion of the tetrahedra (middle of Figure 4.37). This situation would be more expected to occur in H-kenyaite than in H-magadiite since the greater concentration of Si-OH groups present on the surface of the former mineral (40% "flipped" tetrahedra, compared to 25% for H-magadiite) is likely to result in the presence of many such "geminal" hydroxyls. The PG molecules, however, would be much too long to graft geminal Q^3 sites, so they would seek out more distant Si-OH groups: one possibility could involve the bridging of Q^3 sites located across a hexagonal cavity from each other (bottom of Figure 4.37). This would result in a slightly longer distance between the Q^3 sites than that postulated for PG-magadiite (by a factor of 1.15, see figure 4.37), allowing a low-strain Q^3 geometry to be attained. These postulates allow the proposition of surface silanol group distribution models for H-magadiite and H-kenyaite which are consistent with the mechanisms proposed (Figure 4.38), based on the previously described models.

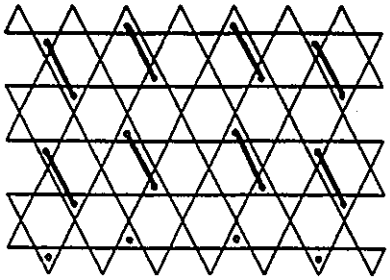

EG–magadiite and PG–magadiite

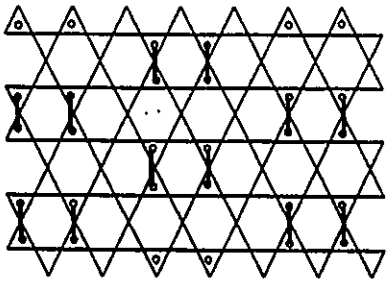

EG–kenyaite

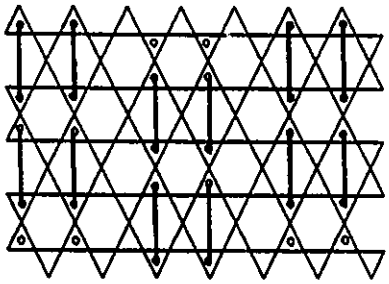

PG–kenyaite

Figure 4.37 Proposed grafting situations for EG and PG on the interlayer surfaces of H-magadiite and H-kenyaite.

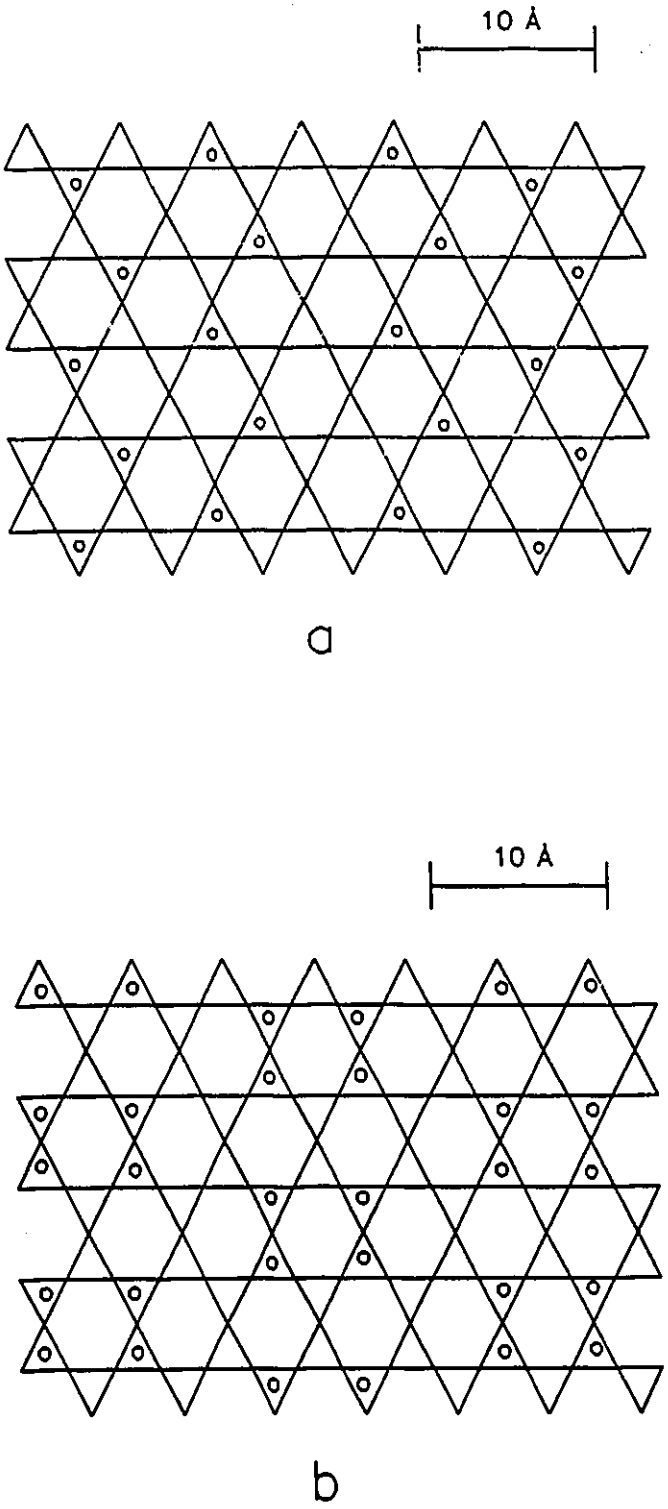

Figure 4.38 Distribution of Q^3 sites on the interlamellar surfaces of (a) magadiite and (b) kenyaite, according to the diol-grafting observations.

4.5 Heavy metal adsorption by grafted layered silicates

In a manner consistent with that of the grafted montmorillonite adsorbents (Chapter 3), the adsorption of heavy metals by thiol-grafted layered silicates was tested. Thus, Pb^{2+} solutions (0 to 20 ppm) were prepared and stirred with H-kenyaite and thioken (25 ml with 2.5 g) for 18 hours at room temperature. Pb concentration were measured before and after treatment by ICP emission spectroscopy. Tables 4.14 and 4.15 show the lead adsorption data for H-kenyaite and thioken, respectively. The adsorption isotherms are plotted in Figure 4.39 and the Langmuir parameters for both systems are given in Table 4.16.

In both cases, the lead adsorption was found to be much lower than their grafted smectite analogs. Pb was found to adsorb to a maximum of 22 mg/g in the case of H-kenyaite. The equilibrium constant for this adsorption process was quite low in comparison to those of thiomont, suggesting a very weak interaction between metal and adsorbent. In contrast, thioken was found to have a significantly lower maximum adsorption value of 12 mg/g, but had a higher K_a value than the ungrafted silicate.

It can be proposed that the grafting of thiopropyl moieties in the interlamellar region of H-kenyaite has resulted in a stuffing of the interlayer region such that metal ions do not have access to the chelation sites (SH groups). Moreover, the lower adsorption maximum in thioken with respect to H-kenyaite could be explained by the blocking of H-kenyaite adsorption sites by the grafting of the silanes. The higher K_a values for thioken can be accounted for by the greater binding affinity of Pb for thiol sites as opposed to H-kenyaite sites, although the total number of adsorption sites is lower in the case of thioken. It can

be thus concluded that only externally bound thiol moieties participate in the adsorption of metal ions.

Compared to the situation of the grafted smectite adsorbents studied in chapter 3, the grafting of chelating functionalities in the interlamellar region of layered silicates was found to be an ineffective strategy for the design of heavy metal adsorbents.

Table 4.14 Adsorption of Pb(II) by H-kenyaite.

C_i(Pb) (mg/L)	C(Pb) (mg/L)	mass of H-kenyaite (mg)	Pb adsorbed (mg)	X(Pb) (mg/g)
2.18	1.65	3.3	0.0133	4.0
5.23	3.90	2.9	0.0333	11.5
8.48	6.85	3.4	0.0408	12.0
16.41	14.37	3.2	0.0510	15.9

Table 4.15 Adsorption of Pb(II) by thioken.

C_i(Pb) (mg/L)	C(Pb) (mg/L)	mass of thioken (mg)	Pb adsorbed (mg)	X(Pb) (mg/g)
2.18	1.43	2.9	0.0188	6.5
5.23	3.39	2.8	0.0460	16.4
8.48	7.17	2.8	0.0328	11.7
19.84	18.98	2.6	0.0215	8.3

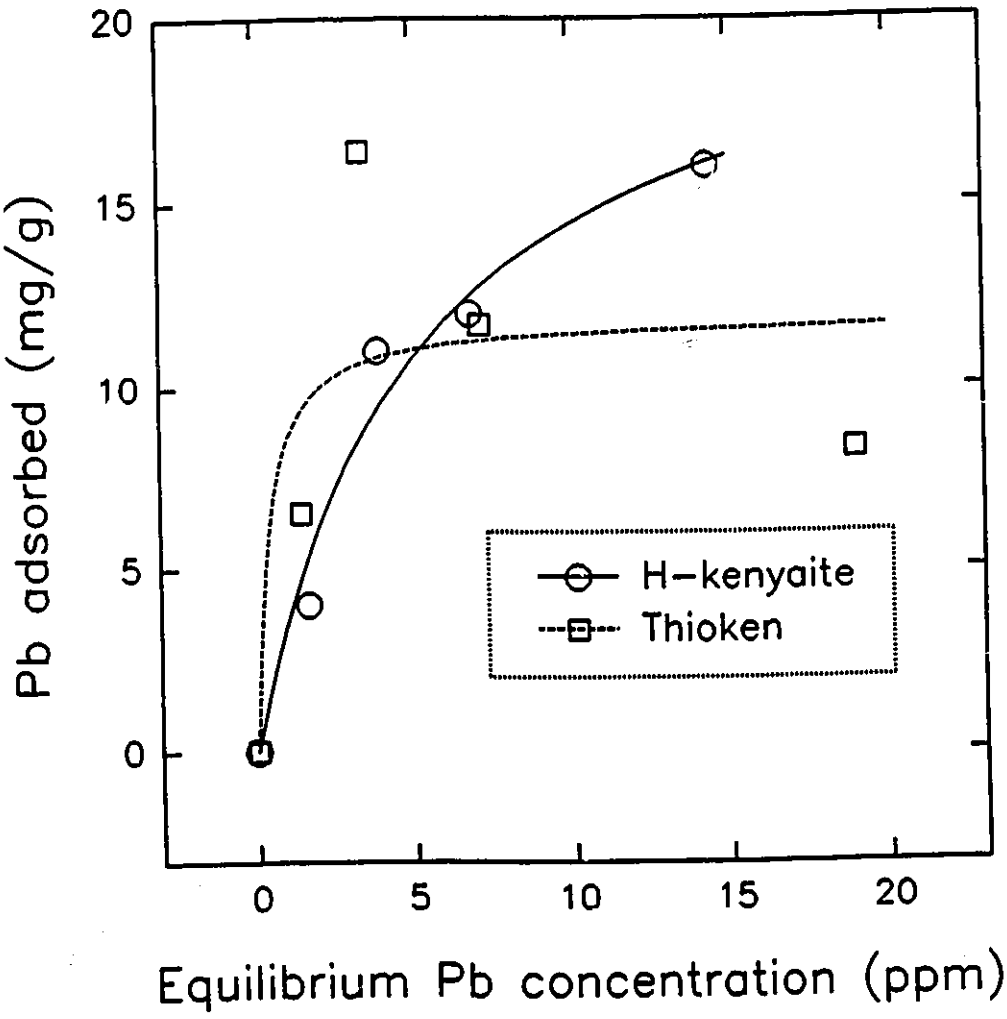

Figure 4.39 Langmuir adsorption isotherms for adsorption of Pb^{2+} by H-kenyaite and thioken.

Table 4.16 Langmuir isotherm parameters for Pb adsorption by H-kenyaite and thioken (asterisks denote parameters calculated on the basis of equivalent rather than mass concentration units).

Adsorbent	b	X_m (mg/g)	X_m^* (meq/g)	K_a	K_a^*
H-kenyaite	0.20	22	0.11	4.4	0.022
Thioken	2.6	12	0.058	31	0.15

Synopsis of Chapter 4.

The grafting of thiol-functionalized organosilane moieties onto the interlamellar hydroxyls of layered silicic acids has resulted in a stuffing of the interlayer space and hence non-microporous materials. Thus, unlike their smectite analogs, such compounds have exhibited little affinity for the adsorption of heavy metals.

Alcohols and diols were found to condense onto the hydroxyls of layered silicic acids, forming Si-O-C linkages to the mineral surfaces by a thermal condensation process. Although the nanocomposites were only slightly microporous, the process proved to be a new and alternative means of achieving covalent pillaring of such minerals. Some insight about the structural features of layered silicates were gained from the grafting of diols with variable carbon chain lengths.

5. DESIGN OF PHYLLOSILICATE-BASED MICROPOROUS NITRIC OXIDE DECOMPOSITON CATALYSTS.

In this chapter, an exploratory look at the design and potential applications of phyllosilicates as base materials for NO decomposition catalysis will be endeavoured. The results presented here are not by any means complete or exhaustive, but may provide some insights useful for further research on this subject.

5.1 Introduction

5.1.1 The need for NO decomposition catalysts

NO_x compounds (principally NO and NO_2) are of serious health and environmental concern. These gases are linked to a multitude of pulmonary diseases and immune system problems, and contribute to acid rain, urban smog and ozone depletion.[210]

These compounds find their origin in natural sources, including N_2 conversion by lightning, microbial metabolic waste and volcanic activity. The most prevalent sources of these pollutants, however, stem from anthropogenic sources primarily involving fossil fuel combustion, where bound nitrogen becomes oxidized. The most convenient way of

reducing the atmospheric content of NO_x is by preventing its release into the environment at the source. This can be achieved by the use of exhaust catalysts which can promote their decomposition to N_2 and O_2.

Three-way catalysts currently used in catalytic converters permit the effective removal of NO_x, CO and hydrocarbons from automotive exhaust. Such catalysts, however, employ the rare end expensive metals Pt, Rh and Pd as the active species. The need for cheaper technologies to achieve the effective catalysis would thus be of economic importance. Phyllosilicates would be useful for this purpose on two accounts: first, their propensity to form microporous high surface area materials may be conducive to the formation of catalysts with a high dispersion of reactive sites. Second, the cheap and ubiquitous nature of such minerals would satisfy the economic considerations for the preparation of less expensive catalytic converters.

5.1.2 Catalytic NO decomposition

The decomposition of NO into N_2 and O_2 is thermodynamically favoured under 1000 °C, but the high activation energy required precludes the spontaneity of the reaction. A catalyst is thus required in order to make the reaction proceed at an appreciable rate.

Initially, metal oxides were explored as NO decomposition catalysts, but were found to inhibited by the irreversible oxidation of the catalysts by the produced O_2, requiring the use of reducing agents in order to regenerate the active (reduced) form of the catalysts.[211]

Zeolite-based catalysts were found to be the most active NO decomposition catalysts so far known, particularly Cu(II) exchanged ZSM-5.[211-215] Although much more effective than other catalysts, such compounds still required the presence of a reductant (ammonia or hydrocarbons) in order to regenerate the catalytic centres. By such means, effective NO conversion to N_2 and O_2 can be achieved at temperatures as low as 300 °C.[216]

The success of such microporous catalysts leads one to postulate about the potential applicability of modified clays as an analogous class of catalysts to zeolites for the purpose of NO decomposition.

5.1.3 Catalyst design

5.1.3.1 Organic pillar and metal cointercalation

The first strategy in the design of phyllosilicate-based NO decomposition catalysts involves the ion exchange of interlayer cations with both an organic pillaring cation (tetramethylammonium (TMA) or tetraphenylphosphonium (TPP)) and a reactive metal ion (Cu(II) or Ce(III)). Thus, microporosity would be created in the layered minerals by exchanging the interlayer cations (Na^+) with the minimum number of organic cations necessary to expand all of the layers. The remaining Na^+ would then be exchanged for metal ions such as Ce(III) to produce a high dispersion of the catalytic sites, as shown in Figure 5.1a.

5.1.3.2 Metal doping of Al-pillared montmorillonite

The high microporosity and thermal stability of Al-pillared montmorillonite (APM) can be exploited in the preparation of NO decomposition catalysts. Thus, treatment of APM with relatively concentrated metal solution can lead to the formation of metal doped APM, as depicted in Figure 5.1b.

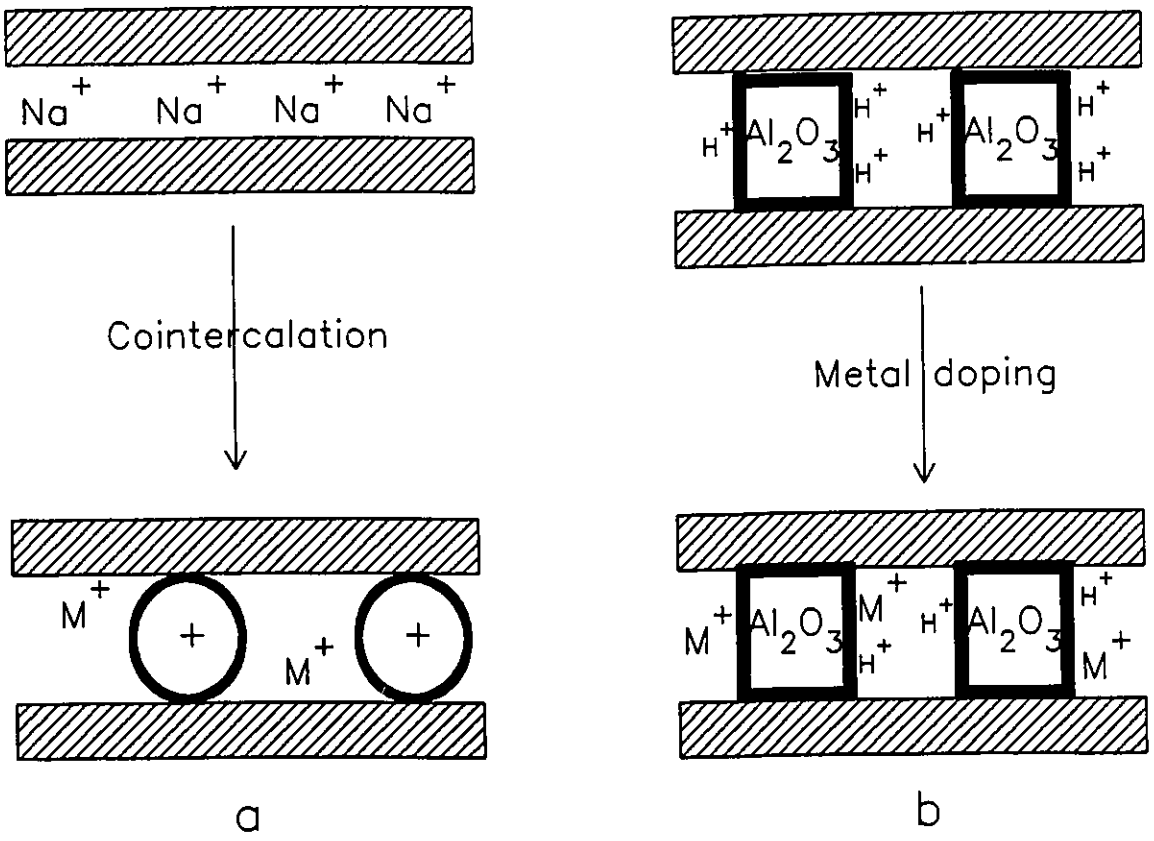

Figure 5.1 Catalyst design scheme using (a) ion-exchange route and (b) metal doping of Al-pillared montmorillonite.

5.2 Preparation and characterization of catalysts

5.2.1 Cointercalated catalysts

TPP-Ce(III)-montmorillonite

The procedure for the ion exchange process involves the treatment of a known mass of clay (SWy-1) with an equivalent stochiometric amount of a mixture of tetraphenylphosphonium bromide and $CeCl_3$. Thus, 1 g of purified homoionic Na^+ SWy-1 (CEC of 0.83 meq/g) is dispersed in water for 2 hours to allow complete delamination of the layers. A solution containing x% of the CEC (for 1 g of clay) in TPP and (1-x)% in metal salt is then added and the mixture stirred for 24 hours.

The XRD patterns of the catalysts prepared by the exchange of 10%, 30% and 33% in TPP cations (hereby refered to as TPP10-Ce90-Mont, TPP30-Ce70-Mont and TPP33-Ce67-Mont, respectively) are shown in Figure 5.2 (all samples dried at 150 °C prior to the scan). In all cases, two distinct d_{001} peaks could be seen at 9.6 Å (unexpanded layers) and at 17.6 Å (expanded layers). In the case of the 10% exchanged material, the expanded layer peak appeared only as a small shoulder in comparison to that of the unexpanded layers, indicating that most layers contained no TPP ions. At 30% intercalation, however, the expanded layer peak became somewhat more intense than that of the unexpanded layers, indicating that most layers contained intercalated TPP ions. At 33%, the unexpanded peak is almost completely gone. This organic pillar ratio is therefore optimal for the preparation

of the catalysts, as it should afford significant microporosity (with all the layers being expanded) and leave 67% of the remaining Na^+ for the exchange with Ce^{3+} ions.

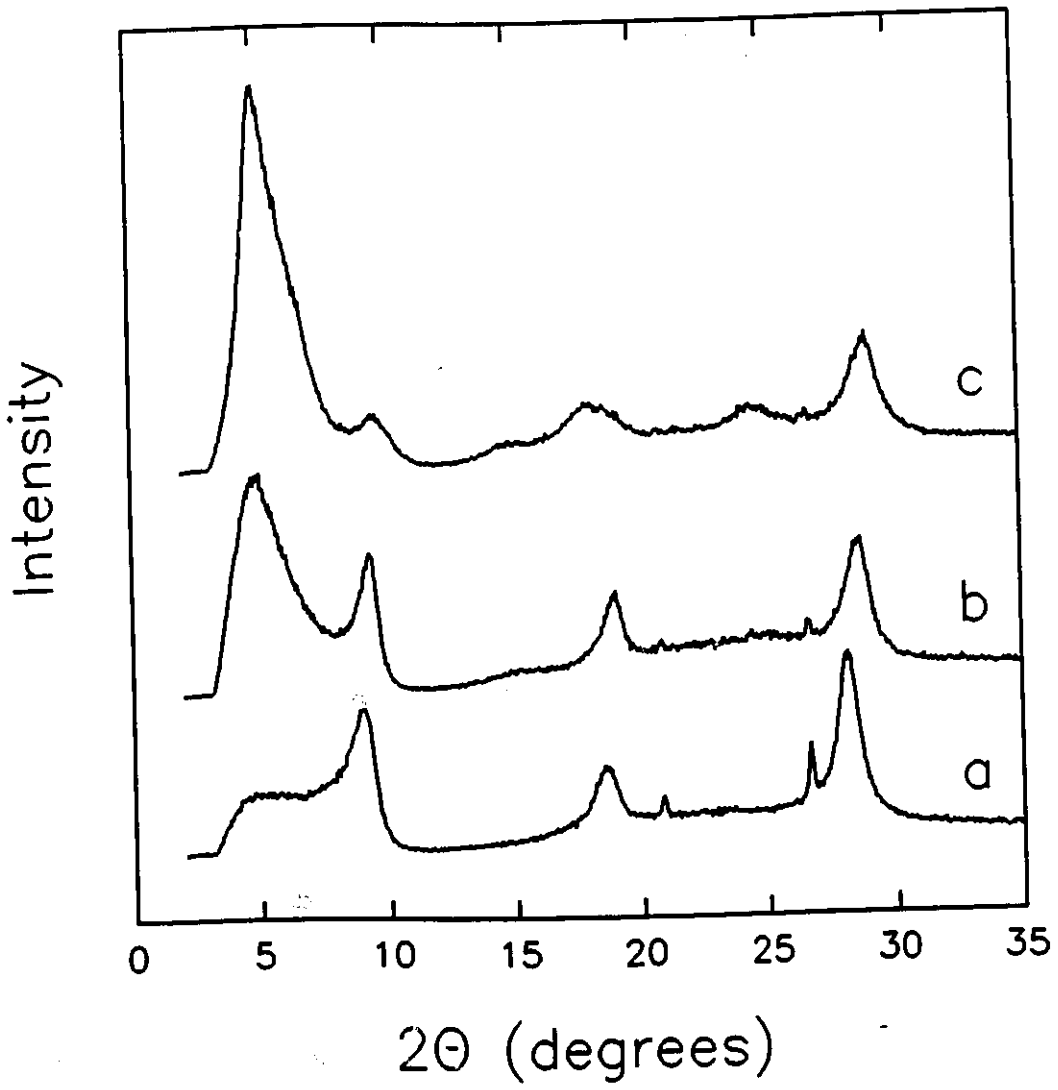

Figure 5.2 XRD patterns for (a) TPP10-Ce90-Mont, (b) TPP30-Ce(70)-Mont and (c) TPP33-Ce(67)-Mont.

Thus, TPP33-Ce67-Mont was prepared by adding 0.0543 g of $CeCl_3 \cdot 7H_2O$, 0.0903 g of tetraphenylphosphonium bromide (dissolved in about 25 ml water) to a slurry of 0.3180 g Swy-1 in about 25 ml H_2O. After 24 hours of stirring, the material was washed several times with water and ethanol and isolated by centrifugation. XRF analysis gave a Si/Ce molar ratio of 62.4 and an Al/Ce molar ratio of 26.4. The expected values, based on the structural formula of SWy-1 (7.8 Si atoms for 0.62 equivalents of exchangeable ion), would give these ratios as 56.3 and 26.4, respectively, or 1.11 that of the experimental values. The exchange is thus reasonably consistent with the stoichiometric composition of the cation exchange mixture.

TMA-Ce(III)-montmorillonite

In a manner similar to the 33% organic pillaring strategy used in the case of TPP-Ce(III)-montmorillonite, 0.0165 g tetramethylammonium bromide and 0.0214 g $CeCl_3 \cdot 7H_2O$ were stirred with 0.3034 g of SWy-1 for 24 hours and isolated. The XRD pattern (Figure 5.3) showed that all of the layers were expanded with a 4.0 Å interlayer space (d_{001} = 13.6 Å). XRF gave a Si/Ce molar ratio of 50.6 and an Al/Ce ratio of 22.7, which are 0.9 and 0.86 that of the expected value. Again, these results are consistent with the material expected on the basis of the composition of the exchange mixture.

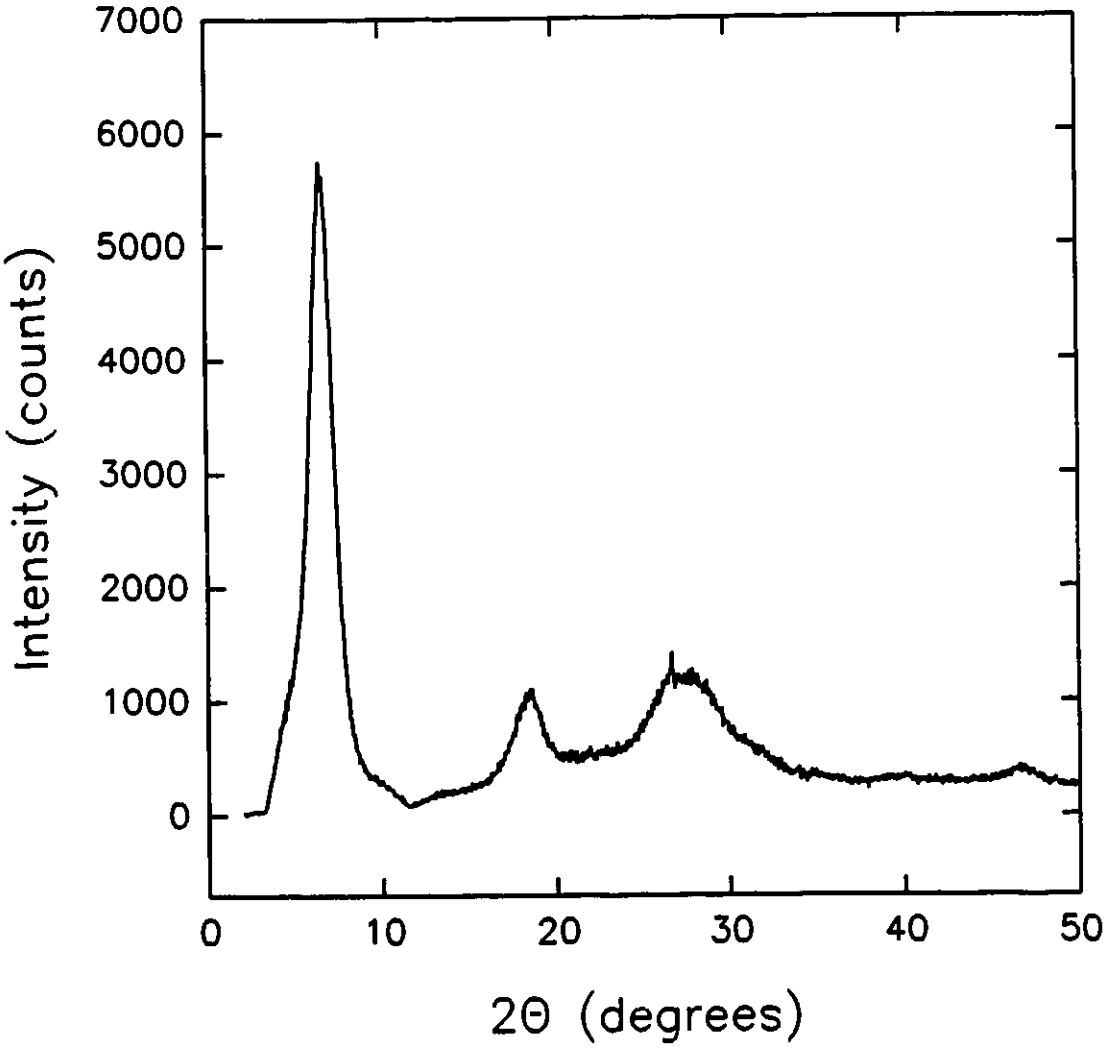

Figure 5.3 XRD pattern of TMA-Ce(III)-Mont.

5.2.2 Metal-doped pillared clay catalysts

The general procedure involves the stirring of 0.2 g samples of aluminum pillared montmorillonite (APM) (supplied courtesy of Hongbai Lao, calcined at 350 °C) with 3 g of metal nitrate salts (Ce^{3+}, Cu^{2+}, Ni^{2+} and Fe^{3+}) in 25 ml distilled water for 5 days. The resulting materials were washed by Soxhlet extraction over ethanol for 24 hours.

The XRD patterns (Figure 5.4) reveal that the layer spacings for the Ce, Cu and Ni compounds were 17.3, 15.3 and 15.4 Å, respectively. These correspond to interlayer distances ranging from 5.7 to 7.7 Å and reflect the porosity of the materials due to the interlamellar aluminum oxide pillars. The Fe-treated sample, however, showed a collapse of the basal spacing to 14.1 Å, suggesting the possibility that the pillars have been removed from the structure.

XRF analysis were performed for the Ce, Cu and Fe doped samples, the results of which are shown in Table 5.1. The quantity of doping metals which are found in the samples were similar to those of the ion-exchanged catalysts. In the cases of the Ce and Cu derivatives, the Al content was found to be significantly higher than that of the parent clay due to the presence of the aluminum oxide pillars. In the case of the Fe-doped sample, however, the Al content was close to that of the parent clay, confirming the XRD evidence that the pillars of this sample have indeed been removed upon treatment with the Fe^{3+} solution, which is likely to have resulted in the formation of Fe(III)-exchange montmorillonite.

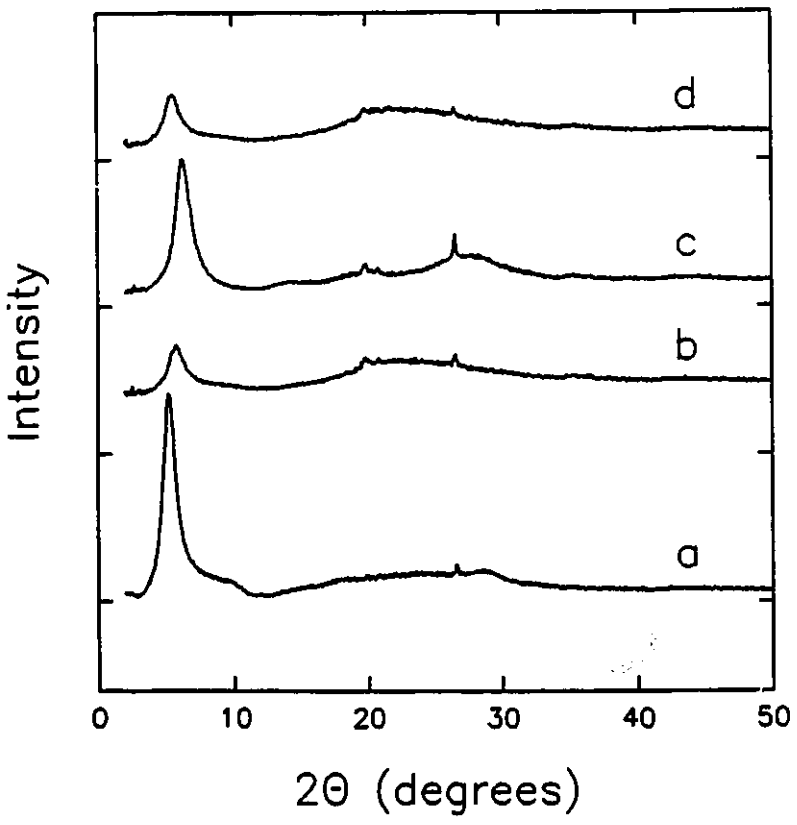

Figure 5.4 XRD patterns for Al_{13}-pillared montmorillonite doped with (a) Ce^{3+}, (b) Cu^{2+}, (c) Fe^{3+} and (d) Ni^{2+}.

Thus, the appreciable quantities of Cu and Ce which were successfully included into the APM materials would result in potential catalysts with similar reactivities but much higher thermal stability than those produced by the ion-exchange pillaring procedure.

Table 5.1 Molar ratios for metal-doped Al-pillared clays (by XRF).

Doping metal in sample	Doping metal content	Fe content	Si content	Al content
None (parent clay)	None	0.30	7.8	3.3
Ce(III)	0.12	0.64	7.8	4.8
Cu(II)	0.65	0.54	7.8	4.6
Fe(III)	0.84		7.8	3.0

5.3 Nitric oxide adsorption and decomposition

5.3.1 NO adsorption to materials

The materials prepared by the ion-exchange procedure were dried at 120 °C for 24 hours and put under vacuum in a Schlenk tube, followed by exposure to 1 atm of NO gas for 24 hours. The samples were then flushed with N_2 before exposure to the air and analyzed by FTIR spectroscopy by the KBr pressed pellet technique. As a reference compound, Ce(III)-exchanged montmorillonite (100% exchanged) was prepared and likewise exposed to NO and analyzed.

In all cases, a sharp band at 1384 cm^{-1} was observed associated with a weak band appearing at about 2430 cm^{-1}. Both of these can be assigned to NO_2^+.[217] The samples were then pumped under vacuum (about 0.01 Torr) for 30 minutes and the FTIR spectra recorded once again. Table 5.2 shows the intensities of the 1384 cm^{-1} bands (relative to the 525 cm^{-1} band of the montmorillonite structure used as an internal standard) for each compound, both before and after vacuum treatment. These experiments show the distinct improvement of NO adsorptivity, both before and vacuum treatment, of the microporous TMA exchanged material when compared to the nonporous Ce(III)-montmorillonite. Note that the TPP exchanged material showed little adsorption of NO and complete expulsion of NO under vacuum, a phenomenon which can be attributed to the effective non-microporosity of this material due to the large size of the TPP pillars.

Table 5.2 NO adsorption by Ce-exchanged montmorillonite materials.

Material	Relative intensity of 1384 cm^{-1} band	
	Before vacuum	After vacuum
Ce(III)-montmorillonite	0.50	0.22
TMA33-Ce67-Mont	1.20	0.48
TPP33-Ce67-Mont	0.37	0

5.3.2 Nitrosylation of phenol

In a sideline experiment designed to futher probe the interaction of NO with the metal-exchanged clay materials, a model reaction was explored involving the nitrosylation of phenol by NO gas in the presence and absence of the materials. It is known that NO itself is not an effective nitrosylating agent, as the presence of air or other catalysts would be required to bring about the reaction.[218] Effective catalysts which can promote nitrosylation reactions in the absence of air include iodine[219] and transition metals[220,221]. Metal salts can form nitrosyl complexes in which the NO group can be formally described as the NO^+ species. According to the FTIR data presented in section 5.3.1, such a situation

is likely to occur in the heterogeneous systems prepared in this work. The nitrosylation of phenol has thus been attempted via heterogeneous catalysis using microporous clay systems.

Experimental setup

In a typical experiment, 50 mg of phenol, 25 ml of benzene (distilled over calcium hydride) and 50 mg of "catalyst" was put in a flask equipped with a gas inlet valve and outgassed. 0.4 atm of NO was bubbled into the flask which was under constant stirring. The contents were stirred for 18 hours and the flask subsequently evacuated in order to remove the remaining NO. The contents were then filtered and the benzene removed by rotary evaporation. The isolated compound was then redissolved in petroleum ether and once again evaporated. This process was continued until the residue in the flask was completely solid. The compound was dissolved in $CDCl_3$ and immediately analyzed by ^1H NMR.

The above experiments were performed without any clay material (blank experiment) and by using TMA-montmorillonite and TMA33-Ce67-Mont. The reaction was also attempted using acetonitrile as a solvent and Ce-doped Al-pillared montmorillonite as catalyst.

Results

The results of the nitrosylation reactions have been summarized in Table 5.3. In the case of the blank experiment (no "catalyst") and that of the TMA-montmorillonite, the products of the reaction were colourless like the starting phenol and no nitrosylation could

be detected on the basis of the NMR results, which showed only the signals of phenol (broad signal at 5.48 ppm (OH), doublet at 6.84 ppm (*ortho* hydrogens), triplets at 6.94 (*para* hydrogens) and 7.24 ppm (*meta* hydrogens), which integrated for 1:2:1:2 protons, respectively).

Table 5.3 Nitrosylation of phenol by nitric oxide.

Solvent	Catalyst	% conversion	% para	% ortho
Benzene	None	0	-	-
	TMA-montmorillonite	0	-	-
	TMA33-Ce67-Montmorillonite	3	0	100
Acetonitrile	None	100	86	13
	Ce-doped APM	100	83	17

When TMA33-Ce67-Mont was used, however, the colour of the reaction solution gradually adopted a yellow-green colour. The proton NMR spectra showed that the majority of the sample was still in the form of phenol, but the presence of *ortho*-nitrosophenol could also be detected (6.97 ppm (H_4), 7.14 ppm (H_6), 7.56 ppm (H_5), 8.09 ppm (H_3) and 10.56 ppm (OH)), corresponding to a yield of about 3% of the total number of molecules.

When acetonitrile was used as a solvent, then reaction was found to proceed even without the addition of catalyst, primarily producing *para* nitrosophenol (86%) (doublets at 6.44 ppm and at 7.43 ppm) but also some of the *ortho* isomer (14%). The conversion was found to be virtually complete,as no residual phenol could be observed in the spectra. The readiness for this reaction to occur even without catalyst can be attributed with the reasonably high polarity of the solvent which can activate the NO into a reactive form. When Ce-doped Al-pillared montmorillonite was added, essentially the same reaction is found to occur, but the relative amount of *ortho* isomer was slightly enhanced to 17%.

Thus, the metal-bearing clay materials favour the selective formation of the *ortho* isomers of nitrosophenol. In both benzene and acetonitrile, the absolute yield was found to increase by 3% as a result of the addition of the catalysts. A plausible explanation for this phenomenon would be that phenol molecules interact with the catalyst through physisorption of their hydroxyl groups to the clay surface. The adsorbed NO species (plausibly in the form of NO^+), also bound to the surface (or, specifically, to a metal ion on the surface) would then be in a position which would favour an attack on the *ortho* position of the aromatic ring. Under homogeneous conditions, attack on the *para* position would be the expected preferred situation, as was observed in the acetonitrile reaction. The low

conversion yields obtained by these materials, however, suggest that they become inactivated after they have reacted.

5.3.3 Decomposition of NO

Experimental setup

100 mg of Cu(II) doped Al-pillared montmorillonite was put into a two-necked flask with a septum attached to one of the necks. The material was activated at 400 °C under vacuum for 2 hours, then cooled to room temperature. 0.2 atm of NO was introduced into the flask and gradually heated up to 600 °C for a period of 5 hours. At various temperatures, aliquots of the gas in the flask were taken with a gas syringe and analyzed by gas chromatography (using He as carrier gas and molecular sieves as stationary phase).

In another experiment, the temperature was immediately increased to 400 °C and maintained there for 5 hours. The gas conversion was then monitored as a function of time.

Results

Under all of the experimental conditions mentioned above, no nitric oxide conversion was observed at all. This would indicate that, under static conditions (i.e. no flow of the gas through the catalyst bed) and without the presence of other gases to assist in the reaction (such as oxygen, ammonia or hydrocarbons), the materials prepared were not suitable as NO decomposition catalysts.

Synopsis of Chapter 6.

By cointercalation and metal doping pathways, microporous clay materials were prepared in which potentially catalytic metal centres were dispersed. Although the experiments performed here have failed to show any decomposition of nitric oxide over these materials, the selective *ortho* nitrosylation of phenol was found to be promoted by these compounds (but only in low yield).

It is to be noted that these results were very preliminary and more work would need to be done in order to further explore the potential of such materials as NO_x decomposition catalysts.

6. CONCLUSIONS

In this thesis, various reactions were performed on two different types of phyllosilicate minerals, namely smectites (primarily montmorillonite) and layered silicates (magadiite and kenyaite). The purpose of such reactions was to design novel types of microporous adsorbents via the covalent grafting of functional units to the mineral interlayers. Thus, the condensation of organosilane and alcohol moieties to the interlamellar hydroxyls of phyllosilicates was exploited as a means of generating these new materials. In the case of smectites, tetraalkylammonium ion intercalation was also studied, resulting in useful applications to the internal surface area measurement of smectites, aromatic compound adsorption and the characterization of Alberta oil sands.

Tetraalkylammonium cation exchange into smectites

By the exchange of the interlayer sodium ions of various homoionic smectites for cations belonging to the homologous tetraalkylammonium series (ranging from tetramethylammonium to tetraoctylammonium), a series of microporous organoclay materials was prepared.

The internal surface areas of the studied smectites could be measured by relating the occurence of the monolayer to bilayer (MTB) and bilayer to pseudotrimolecular (BTP) transitions to the size of the cations which corresponded to these transitions. This method

was found to be a quicker and simpler alternative to previously used methods, but had some limitations to its applicability (see Chapter 3).

Adsorption studies of aromatic compounds (benzene, biphenyl and naphthalene) from aqueous media by these organoclays have suggested that the pore geometries and relative organophilicity of these materials were key factors affecting the affinity of these materials for organic molecules.

A brief characterization study of Alberta oil sands tailings have demonstrated the usefulness of the tetraalkylammonium ion exchange technique towards the identification of the mineral components in the sludge.

Grafted smectites as heavy metal adsorbent

The grafting of organosilane moieties bearing thiolated functionalities to the interlamellar surfaces of SWy-1 montmorillonite have resulted in an effective new class of heavy metal adsorbents.

Such materials were found to bind the metals Cd and Zn, but had strongest affinity for Pb and Hg. The materials adsorbed the metals to much higher levels than activated charcoal (about 50 times more for Hg). Treatment of the metal-loaded adsorbents with reasonably dilute acid resulted in the leaching of the metals and the non-destructive regeneration of the adsorbents. Considering all of these properties, the grafted smectite adsorbents would prove very useful as part of a contaminated water system treatment cycle, as depicted in Figure 6.1.

Thus, this thesis has demonstrated, for the first time, the application of silylated smectites for environmental remediation. Although the exact nature of these materials still remains largely controversial, it is hoped that the characterization of the grafted clays performed in this work have contributed towards their elucidation. Continued research, however, will be paramount in order to more adequately achieve this goal.

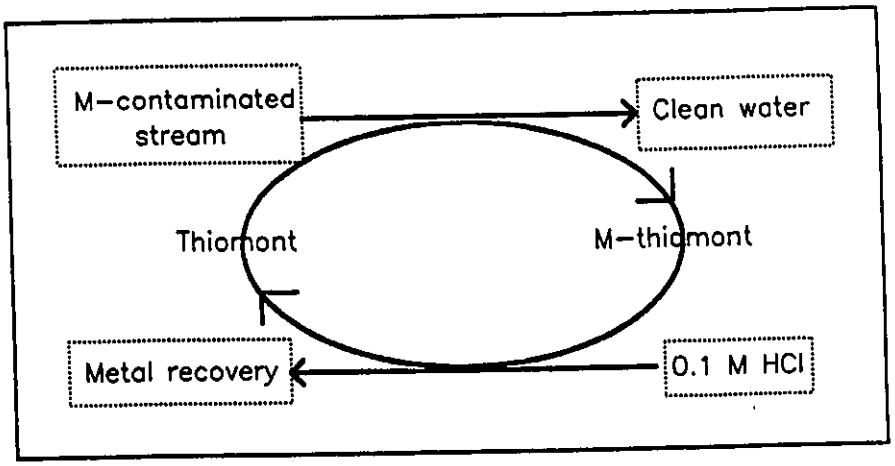

Figure 6.1 Water treatment cycle using grafted smectite adsorbents.

Grafting reactions of layered silicates

Analogous silylation reactions on layered silicates have resulted in the grafting of thiol functionalites in the interlayer region of magadiite and kenyaite. It was found, however, that such materials were ineffective as heavy metal adsorbents due to the congestion of the interlamellar region of the materials which precluded the access of the chelating functions to the metal ions.

A new class of thermally stable organo-silicate nanocomposite materials was prepared via the condensation of alcohols and diols to the interlamellar hydroxyls of magadiite and kenyaite. It was demonstrated that the organic moieties were grafted via Si-O-C linkages and that small diols (ethylene glycol and 1,3-propanediol) were likely to be bound to the mineral template by both ends, resulting in bridged configuration of the carbon chains. Analogous grafting situations were found to occur in both magadiite and kenyaite. This information gave new insight about the possible arrangement of the hydroxyl groups on the interlamellar surface of these minerals whose structures to this day remain unknown.

The microporosities of the diol-grafted magadiite series were very low due to the rather small gallery height of the materials and the relatively full stuffing of the interlayers with the organic species, precluding these compounds from any immediate use as adsorbent or catalysts. These organosilicates may exhibit, however, interesting new rheological properties which could make them useful as fillers or strengtheners for polymers and plastics.

The grafting procedure proposed in this thesis offers an alternate method of achieving the interlamellar functionalization of layered silicates without the use of labile and moisture

sensitive silanes. Thus, for the first time, the grafting of *purely organic* moieties in magadiite and kenyaite has been achieved.

Future research in this domain should focus upon controling the extent of grafting of alcohols and diols in these minerals so that adequate microporosity may be obtained in these systems. If this is achieved, adsorption and catalysis with these compounds would become possible.

Another possible application for these materials could be the preparation of mesoporous molecular sieves. It has been reported that the layered silicate kanemite can serve as a precursor for the formation of MCM-41,[222] the procedure involving the calcination of alkylammonium ion intercalated kanemite. It can thus be postulated that kanemite *grafted* with long alkyl chains may result in similar mesoporous silicates, especially considering the very high thermal stability of the grafted silicates when compared to the intercalated analogs. It may be a worthy endeavor to attempt such a synthesis using kanemite which has been grafted with long chain alcohol moities (1-dodecanol, for example).

REFERENCES

1) Bailey, S. W. *Clay Miner.* **1980**, *15*, 85.

2) Neumann, B. S.; Sansom, K. G. *Clay Miner.* **1970**, *8*, 389.

3) van Olphen, H.; Fripiat, J. J. In *Data Handbook for Clay Materials and Other non-Metallic Minerals*; van Olphen H.; Fripiat J. J. Eds.; Pergamon Press: 1979

4) Bonnin, D.; Calas, G.; Suquet, H. *Phys. Chem. Minerals* **1985**, *12*, 55.

5) Weir, A. H.; Greene-Kelly, R. *Amer. Mineral.* **1962**, *47*, 137.

6) MacKenzie, R. C. *Clay Miner.* **1984**, *19*, 669.

7) Ames, L. L.; Sand, L. B.; Goldrich, S. S. *Econ. Geol.* **1958**, *53*, 22.

8) Köster H. M. *International Clay Conference 1981*; Elsevier: 1982. pp 41-71.

9) Ross, C. S. *Amer. Mineral.* **1946**, *31*, 411.

10) Méring J. *Smectites in Soil Components 2. Inorganic Components*; Springer-Verlag: New York, 1975. pp 98-120.

11) Mamy J.; Gaultier J. P. *Proceedings of the International Clay Conference 1975 (Mexico City)*; Applied Publishing Ltd.: Wilmette, Illinois, 1976. pp 149-155.

12) Besson, G.; Gleaser, R.; Tchoubar, C. *Clay Miner.* **1983**, *18*, 11.

13) Jenny, H. *J. Phys. Chem.* **1932**, *36*, 2217.

14) Gieseking, J. E. *Soil Sci.* **1936**, *42*, 273.

15) Gieseking, J. E. *Soil Sci.* **1939**, *47*, 1.

16) Ensminger, L. E.; Gieseking, J. E. *Soil Sci.* **1939**, *48*, 467.

17) Ensminger, L. E.; Gieseking, J. E. *Soil Sci.* **1941**, *51*, 125.

18) Ensminger, L. E.; Gieseking, J. E. *Soil Sci.* **1942**, *53*, 205.

19) Hendricks, S. B. *J. Phys. Chem.* **1941**, *45*, 65.

20) Ensminger, L. E. *Soil Sci.* **1942**, *54*, 191.

21) Bradley, W. F. *J. Am. Chem. Soc.* **1945**, *67*, 975.

22) Barrer, R. M.; MacLeod, D. M. *Trans. Farad. Soc.* **1955**, 1290.

23) Barrer, R. M.; Reay, J. S. S. *Trans. Farad. Soc.* **1957**, 1253.

24) Barrer, R. M.; Hampton, M. G. *Trans. Farad. Soc.* **1957**, 1462.

25) Barrer, R. M.; Perry, G. S. *J. Chem. Soc.* **1961**, 842.

26) Barrer, R. M.; Perry, G. S. *J. Chem. Soc.* **1961**, 850.

27) Barrer, R. M.; Brummer, K. *Trans. Farad. Soc.* **1963**, 959.

28) Barrer, R. M.; Millington, A. D. *J. Colloid Interf. Sci.* **1967**, *25*, 359.

29) Barrer, R. M.; Jones, D. L. *J. Chem. Soc. (A)* **1971**, 2594.

30) Barrer, R. M. *J. Incl. Phen.* **1986**, *4*, 109.

31) Barrer, R. M. *Pure Appl. Chem.* **1989**, *61*, 1903.

32) Barrer, R. M. *Clays Clay Miner.* **1989**, *37*, 385.

33) McAtee, J. L.; Robbins, R. C. *Clays Clay Miner.* **1980**, *28*, 61.

34) Lao, H.; Latieule, S.; Detellier, C. *Chem. Mater.* **1991**, *3*, 1009.

35) Weiss, A.; Becker, H. O.; Lagaly, G. *Int. Clay Conf.* **1969**, 67.

36) Stul, M. S.; Mortier, W. J. *Clays Clay Miner.* **1974**, *22*, 391.

37) Clementz, D. M.; Mortland, M. M. *Clays Clay Miner.* **1974**, *22*, 223.

38) Nunez, L.; Rogers, R. D. *J. Cryst. Spectrosc. Res.* **1992**, *22*, 265.

39) Lagaly, G.; Fernandez Gonzalez, M.; Weiss, A. *Clay Miner.* **1976**, *11*, 173.

40) Ruehlicke, G.; Kohler, E. E. *Clay Miner.* **1981**, *16*, 305.

41) Ruhlicke, G.; Niederbudde, E. A. *Clay Miner.* **1985**, *20*, 291.

42) Stanjek, H.; Friedrich, R. *Clay Miner.* **1986**, *21*, 183.

43) Laird, D. A.; Scott, A. D.; Fenton, T. E. *Soil Sci. Soc. Am. J.* **1987**, *51*, 1659.

44) Malla, P. B.; Douglas, L. A. *Soil Sci. Soc. Am. J.* **1989**, *51*, 1362.

45) Hausler, W.; Stanjek, H. *Clay Miner.* **1988**, *23*, 333.

46) Laird, D. A.; Fenton, T. E.; Scott, A. D. *Soil Sci. Soc. Am. J.* **1988**, *52*, 463.

47) Laird, D. A.; Scott, A. D.; Fenton, T. E. *Clays Clay Miner.* **1989**, *37*, 41.

48) Olis, A. C.; Malla, P. B.; Douglas, L. A. *Clay Miner.* **1990**, *25*, 39.

49) Stanjek, H.; Niederbudde, E. A.; Hausler, W. *Clay Miner.* **1992**, *27*, 3.

50) Farfantorres, E. M.; Sham, E.; Grange, P. *Catal. Today* **1992**, *15*, 515.

51) Drljaca, A.; Anderson, J. R.; Spiccia, L.; Turney, T. W. *Inorg. Chem.* **1992**, *31*, 4894.

52) Butruille, J. R.; Pinnavaia, T. J. *Characterization. of. Catalytic. Materials.* **1992**

53) Michot, L. J.; Pinnavaia, T. J. *Chem. Mater.* **1992**, *4*, 1433.

54) Johnson, J. W.; Brody, J. F.; Alexander, R. M.; Yacullo, L. N.; Klein, C. F. *Chem. Mater.* **1993**, *5*, 36.

55) Trillo, J. M.; Alba, M. D.; Castro, M. A.; Poyato, J.; Tobias, M. M. *J. Mater. Sci.* **1993**, *28*, 373.

56) Bergaya, F.; Hassoun, N.; Barrault, J.; Gatineau, L. *Clay Miner.* **1993**, *28*, 109.

57) Auer, H.; Hofmann, H. *Appl. Catal. A-Gen.* **1993**, *97*, 23.

58) Jones, W. *Catal. Today* **1988**, *2*, 357.

59) Gonzalez, F.; Pesquera, C.; Blanco, C.; Benito, I.; Mendioroz, S. *Inorg. Chem.* **1992**, *31*, 727.

60) Bradley, S. M.; Kydd, R. A. *J. Chem. Soc. , Dalton Trans.* **1993**, 2407.

61) Zhao, D. Y.; Wang, G. J.; Yang, Y. S.; Guo, X. X.; Wang, Q. B.; Ren, J. Y. *Clays Clay Miner.* **1993**, *41*, 317.

62) Jimenez Lopez, A.; Maza Rodriguez, J.; Olivera Pastor, P.; Maireles Torres, P.; Rodriguez Castellon, E. *Clays Clay Miner.* **1993**, *41*, 328.

63) Figueras, F. *Catal. Rev. -Sci. Eng.* **1988**, *30*, 457.

64) Kikuchi, E.; Matsuda, T. *Catal. Today* **1988**, *2*, 297.

65) Bartley, G. J. J. *Catal. Today* **1988**, *2*, 233.

66) Slater, C. S.; Brooks, C. A. *Separ. Sci. Technol.* **1992**, *27*, 1361.

67) Moll, D. M.; Vestal, J. R. *Icarus.* **1992**, *98*, 233.

68) Pinnavaia, T. J. *Science* **1983**, *220*, 365.

69) Deuel, H.; Huber, G.; Iberg, R. *Helv. Chim. Acta* **1950**, *33*, 1229.

70) Deuel, H. *Kolloid Z.* **1951**, *124*, 164.

71) Deuel, H.; Huber, G.; Günthard, Hs. H. *Helv. Chim. Acta* **1952**, *35*, 1799.

72) Deuel, H. *Clay Min. Bull.* **1952**, *1*, 205.

73) Deuel, H.; Iberg, R. *Helv. Chim. Acta* **1953**, *36*, 808.

74) Edelman, C. H.; Favejee, J. C. L. Z. *Krist.* **1940**, *102*, 417.

75) Greenland, D. J.; Russel, E. W. *Trans. Farad. Soc.* **1955**, 1300.

76) Rao, Y. V. S.; Rani, S. S.; Choudary, B. M. *J. Mol. Catal.* **1992**, *75*, 141.

77) Choudary, B. M.; Subba Rao, Y. V.; Prasad, B. P. *Clays Clay Miner.* **1991**, *39*, 329.

78) Subba Rao, Y. V.; Choudary, B. M. *Syn. Commun.* **1991**, *21*, 1163.

79) Ravi Kumar, K.; Choudary, B. M.; Jamil, Z.; Thyagarajan, G. *J. Chem. Soc. , Chem. Commun.* **1986**, 130.

80) Choudary, B. M.; Bharathi, P. *J. Chem. Soc. , Chem. Commun.* **1987**, 1505.

81) Sharma, G. V. M.; Choudary, B. M.; Ravichandra Sarma, M.; Koteswara Rao, K. *J. Org. Chem.* **1989**, *54*, 2997.

82) Choudary, B. M.; Ravi Kumar, K.; Jamil, Z.; Thyagarajan, G. *J. Chem. Soc. , Chem. Commun.* **1985**, 931.

83) Butruille, J. R.; Pinnavaia, T. J. In *Multifunctional Mesoporous Inorganic Solids*; Sesqueira C. A. C.; Hudson M. J. Eds.; Kluwer Academic: 1993; pp 259-272.

84) Choudary, B. M.; Prasad, A. D.; Bhuma, V.; Swapna, V. *J. Org. Chem.* **1992**, *57*, 5841.

85) Choudary, B. M.; Bharathi, P.; Rao, K. K.; Sarma, M. R.; Kantam, M. L. *Catalysis. Lett.* **1993**, *19*, 293.

86) Shimazu, S.; Uematsu, T. *J. Syn. Org. Chem. Jpn.* **1993**, *51*, 664.

87) Habib, A. M.; El-Sheikh, M. Y.; Saafan, A. A.; Kandil, S. H. *J. Incl. Phen.* **1985**, *3*, 379.

88) Carrado, K. A.; Hayatsu, R.; Botto, R. E.; Winans, R. E. *Clays Clay Miner.* **1990**, *38*, 250.

89) Choudary, B. M.; Rani, S. S. *J. Mol. Catal.* **1992**, *75*, L7.

90) Zhao, D. Y.; Yang, Y. S.; Guo, X. X. *Mater. Res. Bull.* **1993**, *28*, 939.

91) Choudary, B. M.; Sharma, G. V. M.; Bharathi, P. *Angew. Chem. Int. Ed. Engl.* **1989**, *28*, 465.

92) Pusino, A.; Micera, G.; Gessa, C.; Petretto, S. *Clays Clay Miner.* **1989**, *37*, 558.

93) Pusino, A.; Micera, G.; Gessa, C. *Clays Clay Miner.* **1991**, *39*, 50.

94) Slabaugh, W. H.; Vasofsky, R. W. *Clays Clay Miner.* **1975**, *23*, 458.

95) Vasofsky, R. W.; Slabaugh, W. H. *J. Colloid Interf. Sci.* **1976**, *55*, 342.

96) Stul, M. S.; Uytterhoeven, J. B. *J. Colloid Interf. Sci.* **1983**, *91*, 286.

97) Lee, J. -F.; Mortland, M. M.; Chiou, C. T.; Kile, D. E.; Boyd, S. A. *Clays Clay Miner.* **1990**, *38*, 113.

98) Wolfe, T. A.; Demirel, T.; Baumann, E. R. *Clays Clay Miner.* **1985**, *33*, 301.

99) Srinivasan, K. R.; Fogler, H. S. *Clays Clay Miner.* **1990**, *38*, 287.

100) Harper, M.; Purnell, C. J. *Environ. Sci. Technol.* **1990**, *24*, 55.

101) Boyd, S. A.; Shaobai, S.; Lee, J. -F.; Mortland, M. M. *Clays Clay Miner.* **1988**, *36*, 125.

102) Zielke, R. C.; Pinnavaia, T. J. *Clays Clay Miner.* **1988**, *36*, 403.

103) Montgomery, D. M.; Sollars, C. J.; Perry, R.; Tarling, S. E.; Barnes, P.; Henderson, E. *Waste Manag. Res.* **1991**, *9*, 113.

104) Smith, J. A.; Jaffe, P. R.; Chiou, C. T. *Environ. Sci. Technol.* **1990**, *24*, 1167.

105) Siantar, D. P.; Feinberg, B. A.; Fripiat, J. J. *Clays Clay Miner.* **1994**, *42*, 187.

106) Nolan, T.; Srinivasan, R.; Fogler, H. S. *Clays Clay Miner.* **1989**,

107) Zachara, J. M.; Ainsworth, C. C.; Smith, S. C. *J. Cont. Hydrol.* **1990**, *6*, 281.

108) Sikalidis, C. A.; Alexiades, C.; Misaelides, P. *Toxicol. Environ. Chem.* **1989**, *20-21*, 175.

109) Miyake, M.; Sakata, S.; Endo, K.; Suzuki, T. *Chem. Mater.* **1994**, *6*, 1599.

110) Gonzalez Pradas, E.; Villafranca Sanchez, M.; Canton Cruz, F.; Socias Viciana, M.; Fernandez Perez, M. *J. Chem. Tech. Biotech.* **1994**, *59*, 289.

111) Siantar, D. P.; Fripiat, J. J. *J. Colloid Interf. Sci.* **1995**, (in press)

112) Keizer, P.; Bruggenwert, M. G. M. *NATO ASI Ser. , Series E* **1991**, *190*, 177.

113) Daza, L.; Mendioroz, S.; Pajares, J. A. *Clays Clay Miner.* **1991**, *39*, 14.

114) Lao, H.; Detellier, C. *Clays Clay Miner.* **1994**, *4*, 477.

115) Lao, H.; Detellier, C.; Matsuura, T.; Tremblay, A. Y. *J. Mater. Sci. Lett.* **1994**, *13*, 895.

116) Bai,J.; Master's Thesis, University of Ottawa, 1995.

117) Lao,H.; Ph.D. Thesis, University of Ottawa, 1993.

118) Eugster, H. P. *Science* **1967**, *157*, 1177.

119) Tschermak, G. *Z. Phys. Chem.* **1905**, *53*, 349.

120) Lagaly, G. *Adv. Coll. Interf. Sci.* **1979**, *11*, 105.

121) Jones, B. F.; Rettig, S. L.; Eugster, H. P. *Science* **1967**, *158*, 1310.

122) Arimura, T.; Kubota, M.; Matsuda, T.; Manabe, O.; Shinkai, S. *Bull. Chem. Soc. Jpn.* **1989**, *62*, 1674.

123) McAtee, J. L.,Jr.; House, R.; Eugster, H. P. *Amer. Mineral.* **1968**, *53*, 2061.

124) Rooney, T. P.; Jones, B. F.; Neal, J. T. *Amer. Mineral.* **1969**, *54*, 1034.

125) Sheppard, R. A.; Gude, A. J.,III *Jour. Res. U. S. Geol. Surv.* **1974**, *2*, 625.

126) Surdam, R. C.; Eugster, H. P.; Mariner, R. H. *Geol. Soc. Amer. Bull.* **1972**, *83*, 2261.

127) Zdenek, J.; Maglione, G. F. *Bull. Soc. fr. Mineral. Cristallog.* **1972**, *95*, 371.

128) Sheppard, R. A.; Gude, A. J.,III *Amer. Mineral.* **1970**, *55*, 358.

129) Gude, A. J.,III; Sheppard, R. A. *Amer. Mineral.* **1972**, *57*, 1053.

130) McCulloch, L. *J. Am. Chem. Soc.* **1952**, *74*, 2453.

131) Garofalini, S. H.; Martin, G. *J. Phys. Chem.* **1994**, *98*, 1311.

132) Fletcher, R. A.; Bibby, D. M *Clays Clay Miner.* **1987**, *35*, 318.

133) Beneke, K.; Lagaly, G. *Amer. Mineral.* **1977**, *62*, 763.

134) Iler, R.K. *J. Coll. Sci.* **1964**, *19*, 648.

135) Lagaly, G.; Beneke, K.; Weiss, A. *Amer. Mineral.* **1975**, *60*, 642.

136) Beneke, K.; Lagaly, G. *Clay Miner.* **1977**, *12*, 363.

137) Beneke, K.; Lagaly, G. *Amer. Mineral.* **1983**, *68*, 818.

138) Lagaly, G.; Beneke, K.; Weiss, A. *Amer. Mineral.* **1975**, *60*, 650.

139) Eugster, H. P. *Contr. Mineral. and Petr.* **1969**, *22*, 1.

140) Sprung, R.; Davis, M. E.; Kauffman, J. S.; Dybowsky, C. *Ind. Eng. Chem. Res.* **1990**, *29*, 213.

141) Beneke, K.; Kruse, H. -H.; Lagaly, G. *Z. Anorg. Allg. Chem.* **1984**, *518*, 65.

142) Beneke, K.; Lagaly, G. *Amer. Mineral.* **1989**, *74*, 224.

143) Brindley, G. W. *Amer. Mineral.* **1969**, *54*, 1583.

144) Annehed, H.; Fälth, L.; Lincoln, F. J. *Z. Krist.* **1982**, *159*, 203.

145) Rojo, J. M.; Ruiz-Hitzky, E.; Sanz, J.; Serratosa, J. M. *Rev. Chim. Miner.* **1983**, *20*, 807.

146) Schwieger, W.; Heidemann, D.; Bergk, K. -H. *Rev. Chim. Miner.* **1985**, *22*, 639.

147) Pinnavaia, T. J.; Johnson, I. D.; Lipsicas, M. *J. Solid State Chem.* **1986**, *63*, 118.

148) Rojo, J. M.; Sanz, J.; Ruiz-Hitzky, E.; Serratosa, J. M. *Z. Anorg. Allg. Chem.* **1986**, *540/541*, 227.

149) Brandt, A.; Schwieger, W.; Bergk, K. -H. *Rev. Chim. Miner.* **1987**, *24*, 564.

150) Garces, J. M.; Rocke, S. C.; Crowder, C. E.; Hasha, D. L. *Clays Clay Miner.* **1988**, *36*, 409.

151) Scholzen, G.; Beneke, K.; Lagaly, G. *Z. Anorg. Allg. Chem.* **1991**, *597*, 183.

152) Yanagisawa, T.; Kuroda, K.; Kato, C. *React. Solids* **1988**, *5*, 167.

153) Ledoux, R. L.; White, J. L. *Proc. Int. Clay Conf.* **1966**, *1*, 361.

154) Ledoux, R. L.; White, J. L. *J. Colloid Interf. Sci.* **1966**, *21*, 137.

155) Weiss, A.; Thielepape, W.; Orth, H. *Proc. Int. Clay Conf.* **1966**, *1*, 277.

156) Wada, K. *Amer. Mineral.* **1961**, *46*, 78.

157) Ruiz-Hitzky, E.; Rojo, J. M. *Nature* **1980**, *287*, 28.

158) Ruiz-Hitzky, E.; Rojo, J. M.; Lagaly, G. *Colloid. Polym. Sci.* **1985**, *263*, 1025.

159) Yanagisawa, T.; Kuroda, K.; Kato, C. *Bull. Chem. Soc. Jpn.* **1988**, *61*, 3743.

160) Wong, S. -T.; Cheng, S. *Chem. Mater.* **1993**, *5*, 770.

161) Dailey, J. S.; Pinnavaia, T. J. *Chem. Mater.* **1992**, *4*, 855.

162) Patterson, J.W. *Metal Speciation, Separation and Recovery*; Lewis: Chicago, 1987.

163) *World Health Organization Bulletin* **1965**, *53*,

164) Benoit, C.; Lucotte, M. *La Recherche* **1994**, *March*, 27.

165) Faust S. D.; Ali O. M. *Chemistry of Water Treatment*; Butterworth: Boston, 1983.

166) Armor, J. N. *Chem. Mater.* **1994**, *6*, 730.

167) Goeller, H. E.; Zucker, A. *Science* **1984**, *223*, 456.

168) von Laue, H. *Ann. Physik.* **1912**, *41*, 989.

169) Friedrich, W.; Knipping, P.; von Laue, H. *Ann. Physik.* **1912**, *41*, 971.

170) Bragg, W. L. *Proc. Cambridge Phil. Soc.* **1913**, *17*, 43.

171) Brevard C.; Granger P. *Handbook of High Resolution Multinuclear NMR*; Wiley-Interscience: New York, 1981.

172) van Olphen H.; Fripiat J. J. *Data Handbook for Clay Minerals and Other Non-Metallic Minerals*; Pergamon Press: Oxford, 1979.

173) Madsen, F. T. *Thermochim. Acta* **1977**, *21*, 89.

174) Favre, H.; Lagaly, G. *Clay Miner.* **1991**, *26*, 19.

175) Mercier,L.; B.Sc. Honours Thesis, University of Ottawa, 1991.

176) McAtee, J. L. *Clays Clay Miner.* **1962**, *9*, 444.

177) McAtee, J. L. *Clays Clay Miner.* **1963**, *10*, 153.

178) Lagaly, G.; Weiss, A. *Proc. Int. Clay Conf.* **1975**, 157.

179) Lagaly, G. *Clays Clay Miner.* **1982**, *30*, 215.

180) Chen, C. -C.; Turner, F. T.; Dixon, J. B. *Soil Sci. Soc. Am. J.* **1989**, *53*, 1035.

181) Ghabru, S. K.; Mermut, A. R.; St.Arnaud, R. J. *Clays Clay Miner.* **1989**, *37*, 164.

182) Pierre, A. C.; Zou, J. M.; Barker, C. *Fuel.* **1992**, *71*, 1373.

183) Ravi Kumar, K.; Choudary, B. M.; Moroz, B.; Mastikhin, V. M.; Likholobov, V. A. *J. Mol. Catal.* **1987**, *40*, 327.

184) Izatt, R. M.; Bruening, R. L.; Tarbet, B. J.; Griffin, L. D.; Bruening, M. L.; Krakowiak, K. E.; Bradshaw, J. S. *Pure Appl. Chem.* **1990**, *62*, 1115.

185) Bradshaw, J. S.; Krakowiak, K. E.; Izatt, R. M. *J. Heterocyclic Chem.* **1989**, *26*, 1431.

186) Krakowiak, K. E.; Bradshaw, J. S.; Izatt, R. M. *J. Heterocyclic Chem.* **1990**, *27*, 1585.

187) Langmuir, I. *J. Am. Chem. Soc.* **1916**, *38*, 2221.

188) Langmuir, I. *J. Am. Chem. Soc.* **1918**, *40*, 1361.

189) Muraishi, H. *Amer. Mineral.* **1989**, *74*, 1147.

190) Muraishi, H. *Bull. Chem. Soc. Jpn.* **1992**, *65*, 761.

191) Rojo, J. M.; Ruiz-Hitzky, E.; Sanz, J. *Inorg. Chem.* **1988**, *27*, 2785.

192) Almond, G. G.; Harris, R. K.; Graham, P. *J. Chem. Soc. , Chem. Commun.* **1994**, 851.

193) McDonald, R. S. *J. Phys. Chem.* **1958**, *62*, 1168.

194) Borello, E.; Zecchina, A.; Morterra, C. *J. Phys. Chem.* **1967**, *71*, 2938.

195) Borello, E.; Zecchina, A.; Morterra, C.; Ghiotti, G. *J. Phys. Chem.* **1967**, *71*, 2945.

196) Kitahara, S. *Bull. Chem. Soc. Jpn.* **1976**, *49*, 3389.

197) Balard, H.; Sidqi, M.; Papirer, E.; Donnet, J. B.; Tuel, A.; Hommel, H.; Legrand, A. P. *Chromatographia* **1988**, *25*, 707.

198) Balard, H.; Sidqi, M.; Papirer, E.; Donnet, J. B.; Tuel, A.; Hommel, H.; Legrand, A. P. *Chromatographia* **1988**, *25*, 712.

199) Walters, R. R. *J. Chromatography* **1982**, *249*, 19.

200) Czok, M.; Guiochon, G. *J. Chromatography* **1990**, *506*, 303.

201) Papirer, E.; Balard, H. *J. Adhesion Sci. Technol.* **1990**, *4*, 357.

202) Hommel, H.; Legrand, A. P.; Balard, H.; Papirer, E. *Polymer* **1983**, *24*, 959.

203) Ramdas, S.; Klinowski, J. *Nature* **1984**, *308*, 521.

204) Thomas, J. M.; Klinowski, J.; Ramdas, S.; Hunter, B. K.; Tennakoon, D. T. B. *Chem. Phys. Lett.* **1983**, *102*, 158.

205) Grimmer, A. R.; Von Lampe, F.; Tarmak, M.; Lippmaa, E. *Chem. Phys. Lett.* **1983**, *97*, 185.

206) Björling, M.; Karlström, G.; Linse, P. *J. Phys. Chem.* **1991**, *95*, 6706.

207) Breitmaier E.; Voelter W. *13C NMR Spectroscopy*; Verlag Chemie GmbH: Weiheim, 1974.

208) Alemany, L. B.; Grant, D. M.; Alger, T. D.; Pugmire, R. J. *J. Am. Chem. Soc.* **1983**, *105*, 6697.

209) Bagshaw, S. A.; Cooney, R. P. *Chem. Mater.* **1993**, *5*, 1101.

210) Armor, J. N. *Appl. Catal. B.* **1992**, *1*, 221.

211) Li, Y.; Hall, W. K. *J. Catal.* **1991**, 202.

212) Iwamoto, M.; Yokoo, S.; Sakai, K.; Kagawa, S. *J. Chem. Soc. , Faraday Trans. 1* **1981**, *77*, 1629.

213) Iwamoto, M.; Yahiro, H.; Mine, Y.; Kagawa, S. *Chem. Lett.* **1989**, 213.

214) Sata, S.; Yu-u, Y.; Yahiro, H.; Mizuno, N.; Iwamoto, M. *Appl. Catal.* **1991**, *70*, L1.

215) Iwamoto, M.; Yahiro, H.; Tanda, K.; Mizuno, N.; Mine, Y.; Kagawa, S. *J. Phys. Chem.* **1991**, *95*, 3727.

216) Zhang, Y.; Flytzani-Stephanopoulos, M. *ACS Symp. Series* **1994**, *552*, 7.

217) Hadjiivanov, K.; Bushev, V.; Kantcheva, M.; Klissurski, D. *Langmuir* **1994**, *10*, 464.

218) Challis, B. C.; Kyrtopoulos, S. A. *J. Chem. Soc. , Perkin Trans. 1* **1979**, 299.

219) Challis, B. C.; Outram, J. R. *J. Chem. Soc. , Perkin Trans. 1* **1979**, 2768.

220) Brackman, W.; Smit, P. J. *Recl. Trav. Chim. Pays-Bas* **1965**, *84*, 357.

221) Brackman, W.; Smit, P. J. *Recl. Trav. Chim. Pays-Bas* **1965**, *84*, 382.

222) Yanagisawa, T.; Shimizu, T.; Kuroda, K.; Kato, C. *Bull. Chem. Soc. Jpn.* **1990**, *63*, 988.

PUBLICATIONS

1. L. Mercier, C. Detellier and J.A. Ripmeester, "Characterization of gel-forming fractions from the Athabasca tailings ponds fine tails" Report to Sludge Fundamentals Consortium, IEC Internal Report EC-1250-92S, 1992 (unrefereed)

2. L. Mercier and C. Detellier, "Intercalation of tetraalkylammonium cations into smectites and its application to internal surface area measurements" *Clays and Clay Minerals* **42**, 71-76 (1994)

3. L. Mercier, G. Facey and C. Detellier, "Organo-layered silicates. Interlamellar intercalation and grafting of ethylene glycol in magadiite" *J. Chem. Soc., Chem. Comm.* 2111-2112 (1994)

4. L. Mercier and C. Detellier, "Preparation, characterization, and applications as heavy metal sorbents of covalently grafted thiol functionalities on the interlamellar surface of montmorillonite" *Environ. Sci. Technol.* **29**, 1318-1323 (1995)

5. L. Mercier, G. Facey and C. Detellier, "Interlamellar grafting of diols in the layered silicates magadiite and kenyaite" *Chem. Mater.* (submitted)

CONFERENCE PRESENTATIONS

1. *Access in Nanoporous Materials Symposium*; East Lansing, Michigan, U.S.A.; June 7-9, 1995: Interlayer Grafting of Diols in Layered Silicates (Poster); L. Mercier, G. Facey and C. Detellier.

2. *27th Annual Inorganic Discussion Weekend*; McMaster University, Hamilton, Ontario, Canada; November 4-6, 1994: Interlayer Pillaring and Grafting of Layered Silicates: Preparation, Characterization and Environmental Applications (Oral Presentation); L. Mercier, G. Facey and C. Detellier (Awarded prize for best presentation in session).

3. *8th International Symposium on Molecular Recognition and Inclusion*; Carleton University, Ottawa, Ontario, Canada; August 1-5, 1994: Organic Functionalization of the Interlamellar Region of the Layered Silicate Magadiite (Poster); L. Mercier, G. Facey and C. Detellier.

4. *77th Canadian Society for Chemistry Conference and Exhibition*; Winnipeg, Manitoba, Canada; May 29-June 2, 1994: MAS NMR Studies of Organic Intercalates in Layered Minerals (Oral Presentation); C. Detellier, G. Facey, L. Mercier, L. Raki, J. Tunney.

5. *Ottawa NMR Discussion Group*; Ottawa, Ontario, Canada; Feb 5, 1994: Solid State NMR Characterization of Layered Silicate-Glycol Complexes (Oral Presentation); L. Mercier, G. Facey and C. Detellier.

6. *26th Annual Inorganic Discussion Weekend*; University of Guelph, Guelph, Ontario, Canada; November 19-21, 1993: Modified Layered Minerals: the Design of a Novel Class of Sorbents (Poster); L. Mercier, G. Facey and C. Detellier. (Awarded prize for best poster)

7. *76th Canadian Society for Chemistry Conference and Exhibition*; Sherbrooke, Québec, Canada; May 30-June 3, 1993: Chemically Modified Layered Minerals (Poster); L. Mercier and C. Detellier.

8. *25th Annual Inorganic Discussion Weekend*; University of Ottawa, Ottawa, Ontario, Canada; October 31-November 1, 1992: Layered Organo-Mineral Compounds: Incorporation of Alcohols and Diols into Magadiite (Poster); L. Mercier, G. Facey and C. Detellier.